Investigation of Electron Transfer in the α-Helical Protein Cytochrome b_{562}

A Thesis

Submitted by

Neil Farrow

In Partial Fulfilment of the Requirements

for the Degree of Doctor of Philosophy in Chemistry

Division of Chemistry and Chemical Engineering

California Institute of Technology

Pasadena, California

1999

Acknowledgements

For being invested with an unusual amount of patience, understanding and humour, I am very grateful to Professor Jack Richards, my thesis advisor. His support and interest in my well being helped make it possible for me to join the graduate program at Caltech and to emerge from it with a much increased knowledge of chemistry and biochemistry. Many thanks to Professor Harry Gray and Dr. Jay Winkler for their instruction and expertise in the field of electron transfer. To the other members of my committee, Professor Peter Dervan and Professor Carl Parker, I am very grateful.

Many colleagues supported and supplied much inspiration, advice and instruction towards this thesis. Thanks to all those in Jack's group, especially Yun Sun, Cynthia Kizer, Danny Casimiro, Curtis Bloom and Phoebe Ray. Special thanks to Ralf Langen and Claire Slutter for training in molecular biology and biophysical techniques. Thanks to all members in Harry's group, especially Ofer Blum, Angel Di Bilio and Gary Mines. Also Dr. Jeff Regan, Professor Mike Hill and Tom Dunn. Thanks also to Jon Forman, Michael Murray, Chris Kenyon and Ailsa Webster for advice and friendship.

A very large thank you to Dr. Brian Ross, my advisor and friend at Huntington Medical Research Institutes who started this exciting journey by offering me the chance to 'pop-over' and become involved with his fascinating *in-vivo* magnetic resonance research. Many thanks to Dr. Keiko Kanamori for her instruction in the use of NMR. Also at HMRI, thanks to Frank Parivar, Jim Narasiman, Basam Mora, Roland Kreis, Else Danielsen, Stephan Blum, David Dubowitz, Thomas Ernst, Jennifer Bellinger, Jose Jiminez and Lesley Watts.

Thank you to my canyon-carving stress relieving buddies, Jon Forman and Chris Claypool, and all up at Newcombes Ranch. Thanks to all the Wednesday night crowd, especially Mick, Chris, Jon, and the rager regulars.

Thanks to all those members at Caltech Karate Club and Shotokan Karate of America. It was a wonderful experience and honour to be instructed by Mr. Oshima, one of the most inspirational people I have met.

I've saved the best till last. Thank you to my wife Jacky for her enormous support, patience and love and to my son Elliot who could always make me smile.

Abstract

Electron transfer rates in the α-helical protein cytochrome b_{562} are investigated using the photoexciteable luminescent labelling compound ruthenium(II)bis(2,2'-bipyridine)(imidazole) attached to surface accessible histidine residues. Three residues on helices A and D and two on helix C were replaced with histidine by site directed mutagenesis to form eight mutant proteins which, together with a wild-type histidine on helix C, were labelled with ruthenium(II)bis(2,2'-bipyridine)(imidazole). Laser excitation of ruthenium(II)bis(2,2'-bipyridine)(imidazole) formed the highly reducing species *ruthenium(II)bis(2,2'-bipyridine)(imidazole) which was either quenched by the heme directly and the back rate (k^b_{ET}) to the RuIII monitored by transient absorbance, or was oxidized by an external quencher and the rate from the reduced protein then monitored. Mutants spanned a metal-metal distance range from 14.2 Å to 25 Å with the rates ranging from 2.5 x 10^2 s^{-1} to 2.2 x 107 s^{-1}. A β value of 1.09 $Å^{-1}$ is calculated from the data which agrees well with data from azurin and *cytochrome c*. The results show that the α-helices together with the extended heme plane provides an efficient homogenous barrier to electron transfer.

A mutant of cytochrome b_{562} with a covalently attached heme via one thioether linkage was expressed. The unfolding characteristics of this protein show it to be more stable to guanidinium unfolding than wild-type protein. The electron transfer rate for this mutant was identical to wild-type indicating minimal perturbation of the heme binding pocket by the mutation. It can be inferred that the side chain of the carboxyl terminal arginine residue and not Arg98 is responsible for stabilizing the His102 ligand histidinate charge.

Table of Contents

List of Figures

List of Tables

Chapter 1

Electron Transfer in Biological Systems

Introduction

Electron transfer reactions, or redox reactions, involve the movement of electrons from a reductant (or donor), to an oxidizing agent (or acceptor). The chemistry involved in these reactions has been harnessed by nature and is incorporated into the most vital of cell processes. Photosynthesis[1, 2] and oxidative phosphorylation[3, 4] are two of the more prominent examples of electron transfer (ET) reactions in biological systems. Both involve the transfer of electrons along a chain of redox partners (metalloproteins) of decreasing reduction potential to a final acceptor, O_2 in the case of oxidative phosphorylation and NADPH+ in the case of photosynthesis. Extraction of energy from the electron during its transfer is used to form a pH gradient across a cellular membrane which is subsequently used to generate ATP, as described by Mitchell's chemiosmotic hypothesis[5]. Cells use ATP as an immediate source of energy to drive most biological processes. The transfer of the electron proceeds along a chain of oxidizing agents, rather than just a donor acceptor pair, so that the reaction may be controlled both temporally and spatially, allowing for more specific interactions and increasing the efficiency of translating the electrons potential energy into energy the cell can utilize.

The movement of electrons in the above examples involves both intra- and intermolecular transfers, both of which necessarily involve fine tuning of the pathways in order that the reactions proceed at the required rate and also in the desired direction without short circuiting via an unwanted pathway or via random interaction with another molecule. Like enzymes, the design of ET proteins are optimized to prevent such problems. In the case of metalloproteins [6-12], a large percentage of the proteins bulk plays no direct role in the ET process, which cover distances of the order of 10-20Å [13-19], but serves to orientate the

protein with respect to its redox partners, orientates the metal centre in the protein and, in the case of intermolecular ET, directs binding of the protein with redox partners through specific interactions on its surface. Orientation of the metal centre optimizes the metal centre both spatially and also electrostatically by modulation of metal ligands [20-23] and solvent accessibility [24, 25] . It is now widely accepted that the protein plays a direct role in propagating the wave functions of the donor and acceptor by the so called through-bond mechanism[26-28], rather than ET relying solely on the overlap of the wave functions through space, the through-space mechanism. For long-distance ET it is unlikely that the through-space mechanism would provide enough overlap, and hence electronic coupling, to give the rates observed[29, 30]. The through bond mechanism can be described as electron transfer or hole transfer depending on whether the path of the electron is from donor LUMO to spacer LUMO s and finally to acceptor LUMO, or from donor LUMO to spacer HOMO s and finally acceptor LUMO, respectively. The choice of pathway is dependant on the relative energies of the spacer and electron orbitals. How the spacer affects the rate of ET can be explained by two theories. One explanation, described by Dutton from experimental results from a variety of biological and chemical systems[31], is that the intervening protein matrix presents a homogenous barrier to ET and so the rates of ET are independent of secondary structure. In such a model, termed the square barrier model, the electronic-coupling strength is a function of donor-acceptor separation and results in an exponential distance dependence of the rate of ET[32, 33]. The electronic coupling is a parameter defined in ET rate theory which describes the degree of wave function overlap between donor and acceptor. The other explanation, supported by a growing body of evidence, suggests that the intervening protein matrix secondary structure has a direct effect on the rate of ET between redox centres by modulation of the electronic-coupling strength. Experimental results by Langen[34] show that the ET distance decay rate along a β-strand of the blue copper protein azurin is slower than that predicted by Dutton. The reduced distance decay rate results in faster than expected ET

for a given donor acceptor distance. Extensive studies[35-37] using cytochrome *c* also support the results found in azurin. Theoretical analysis of couplings [14, 38-51] also suggests that the intervening protein structure can attenuate or enhance the coupling between redox sites. The work described in this thesis concerns a further analysis of the effect of protein secondary structure by examining the rate of ET via protein α-helical structures. Models have been developed to explain quantitatively how the electronic coupling decays with distance between redox partners in a protein. The most prominent of these is the tunnelling pathway model developed by Beratan and Onuchic[39, 40, 43, 52, 53] whereby the known structure between redox sites in a protein is analyzed by a search algorithm to calculate electronic couplings and hence to determine the optimal pathway, or pathways, for ET. The algorithm considers sigma bonds, hydrogen bonds and through space jumps when searching, with each type of linkage assigned a coupling decay factor. Beratan et al.[42] have calculated a covalent bond decay factor (ε^C) of 0.6 from ET studies of model compounds and proteins, and Langen has shown that this value agrees well with experimental results for reactions in which oxidants have potentials of approximately 1.0 V *versus* NHE[34]. The hydrogen bond decay factor (ε^H) is 0.36 x exp[-1.7(R-2.8)] and derived by considering an H bond as two stretched covalent bonds, and likewise the through space decay constant (ε^S) is 0.6 x exp[-1.7(R - 1.4)], derived by consideration of typical binding energies for localized states. This model only considers sigma bonds despite π-systems having a more favourable coupling due to the extended π electron system. This advantage is lost, however, when considering the mixing between σ-π and π-σ bonds, a theory in agreement with the experimental results of Casimro et al.[54]. Once the coupling between two redox sites has been calculated using the pathways algorithm, the pathway can be standardized by calculating the number of covalent bonds (coupling decay 0.6) required to give the coupling calculated from the algorithm. By multiplying this number of bonds by an average bond length of 1.4Å, the tunnelling pathway is determined. This parameter can then be compared

with other results. To fully understand how tunnelling lengths can be used to analyze ET rates in proteins, it is necessary to consider ET theory, a brief overview of which is presented in the following section.

Electron Transfer Theory

The electron transfer reactions considered here are outer-sphere redox reactions; the inner coordination spheres remain intact. An example of this is a self-exchange reaction such as

$$Fe(H_2O)_6^{3+} + {}^*Fe(H_2O)_6^{2+} \rightarrow {}^*Fe(H_2O)_6^{3+} + Fe(H_2O)_6^{2+}$$

Although not directly relevant to ET in proteins, this relatively simple reaction highlights many of the important features of ET transfer in proteins. Before the reaction can take place, the first and second coordination spheres have to reorganize to accommodate the new charge. The reorganization in the above example involves a change in the $Fe\text{-}OH_2$ bonds lengths and a subsequent rearrangement of the solvation shell, both of which require energy expenditure and are the main contributors to the reactions activation energy barrier. Once these distortions have occurred, ET can take place and the products can form, thus satisfying the Frank Condon Principle and the conservation of energy. The problem of considering the distortions of many nuclear coordinates was simplified by the theoretical work of Marcus[15, 55-58] who realized that the reaction can be described by a one-dimensional reaction profile of the energy of the reactants and products versus the nuclear coordinates of the reactants and products. Parabolas are used to approximate the potential energy curves, as shown in Figure Chapter 1-1. The reaction proceeds from the reactant (R) potential energy well to the product (P) potential energy well which, for a self-exchange reaction, have the same shape and energy ($\Delta G^\circ = 0$). The reaction shown can be described as adiabatic in that upon gaining activation energy to reach the transition state geometry at

the curve crossing point, there is sufficient mixing of reactant and product wave functions so that the reaction proceeds to form products with a high probability. ET in proteins however, is described as nonadiabatic. The consequence of the donor and acceptor being at a relatively large separation (> 10 Å) to one another is that there is little mixing of their wave functions and subsequently there is a low probability of the reaction proceeding from reactants to products. This situation leads to ET being described as a tunnelling process which typically occur when the 'barrier' is greater than 5Å and the medium is a vacuum or material with low electron affinity compared to the electron donor. Tunnelling is a general term used to describe situations where particles are found in classically forbidden energy zones. It is more important for lighter particles such as the electron than heavier particles such as the proton, since the wavefunction of a heavier particle decays (exponentially) more rapidly inside a barrier and thus the probability of successfully tunnelling is reduced. The equivalent schematic for such a tunnelling reaction is shown in Figure Chapter 1-2. The rate of ET for such a system of donor and acceptor separated by a fixed distance can be calculated from the theory described by Marcus.

$$k_{ET} = \frac{2\pi}{\hbar} H_{DA}^2 FC \qquad [1]$$

FC is the 'Frank-Condon' or nuclear factor and is the sum of products of overlap integrals of the vibrational and solvational wavefunctions of the reactants with those of the products, suitably weighted by Boltzmann factors. H_{AB} is the electronic matrix element coupling reactant and product electronic wavefunctions. Further analysis led Marcus to his famous semiclassical equation which calculates the first order ET rate constant:

$$k_{ET} = \sqrt{\frac{4\pi^3}{h^2 \lambda k_B T}} H_{DA}^2 \exp\left(-\frac{(\Delta G^\circ + \lambda)^2}{4\lambda k_B T} \right) \qquad [2]$$

where $-\Delta G^\circ$, called the Driving force, is the free energy difference between reactant (donor) and product (acceptor).

$$\Delta G^\circ = zF(E_D - E_A) \qquad [3]$$

where E_D and E_A are the reduction potentials of the donor and acceptor. λ is the reorganization energy mentioned above and has contributions from both inner and outer sphere ligands.

From the geometry of parabolas, the activation energy is

$$\Delta G^* = (\lambda + \Delta G°)^2/4\lambda \qquad [4]$$

Inspection of equation [2] shows that the rate of ET increases with increasing Driving force, reaches a maximum when $-\Delta G° = \lambda$, and then decreases with further increases in Driving force. A plot of driving force versus rate of ET is shown in Figure Chapter 1-3 and illustrates the 'inverted region' where increases in the Driving force surprizingly decrease the rate of ET. Theoretical and experimental analysis[59-61], however, have shown that in the inverted region the decrease in K_{ET} has a linear rather than a quadratic profile. This may be due to the formation of excited state ET products which effectively lowers the driving force of the reaction and therefore produces faster ET rates. For systems where $-\Delta G° = \lambda$, $k_{ET} = k_{max}$, and the rate of ET is proportional to H_{AB}. As mentioned previously H_{AB} is a measure of the efficiency of the coupling between donor and acceptor and so the study of ET in such systems will characterize the medium between the donor and acceptor towards ET.

Electron Transfer Theory and Small Molecules

Much of current understanding of the parameters and experimental techniques for studying ET has been learned from studies of small linear synthetic organic molecules. Studies by Miller and co-workers [62-64] involving intermolecular ET between randomly distributed molecules in rigid glasses provided the first experimental evidence of the Marcus inverted region. Further studies by Miller using a steroid spacer linked to a biphenyl group provided

experimental evidence for the Marcus inverted region in solution using a fixed distance donor/acceptor system. Various electron acceptors attached to the end opposite the biphenyl group were used to produce donor/acceptor systems with a range of free energy's for the ET reaction, which subsequently gave a gaussian ET rate graph similar to diagram 3. ET rate experiments in which the solvent dielectric was varied were also used to provide further experimental evidence. Changing the solvent dielectric caused a change in the reorganization energy of the acceptor resulting in k_{max} at lower values of $-\Delta G^{\circ}$ for solvents of lower dielectric. Many other synthetic molecules have also been used to study the distance dependency of ET rates[65-67].

At the closest distance between donor and acceptor (approximately van der Waals contact, taken as 3Å), the rate is expected to be 10^{13} s^{-1} and to decay exponentially with increasing distance as the electronic coupling and wave functions decay exponentially, as in the through-space mechanism.

$$H_{DA} = H_{DA}^{0} \exp\left\{-\beta\left(R_m - R_0\right)/2\right\} \qquad [5]$$

R_m is the distance between donor and acceptor, R_0 is the close contact distance (3Å) and β is the rate of decay of the electronic coupling with distance. The analogous equation for the ET rate decay with distance is

$$k = k_0 \exp\left\{-\beta\left(R - R_0\right)\right\} \qquad [6]$$

[5] ignores the relatively small distance dependency of the reorganization energy[56, 68]. An equivalent expression for the through-bond mechanism, in which all bonds are equivalent and hence contribute equally to the decay of the electronic coupling, is

$$V = V_0' \exp\left[-\beta'\left(N-1\right)/2\right] \qquad [7]$$

where N is the number of bonds. For small linear molecules both the through-space and through-bond mechanisms will provide similar results since distance is approximately

proportional to the number of bonds in these systems and so it is difficult to distinguish between the through-space and through-bond mechanisms. Results from two studies of small linear molecules gave β and β‘ values of 0.95 $Å^{-1}$ and 1.12 per bond respectively[67, 69], and 0.85 $Å^{-1}$ and 1.15 per bond respectively[65, 66]. A study by Closs[69], however, using the decalin isomers **1** and **2,** has provided some evidence for the through-bond mechanism. They found similar electronic coupling values (63 cm^{-1} and 58 cm^{-1} for **1** and **2** respectively), deduced from the rates of ET, despite the donor acceptor distance in **1** (12.5 Å) being twice the distance in **2** (6.2 Å). They commented, however, that the through-space mechanism may contribute or even dominate for situations in which donor and acceptor were in direct face-to-face contact.

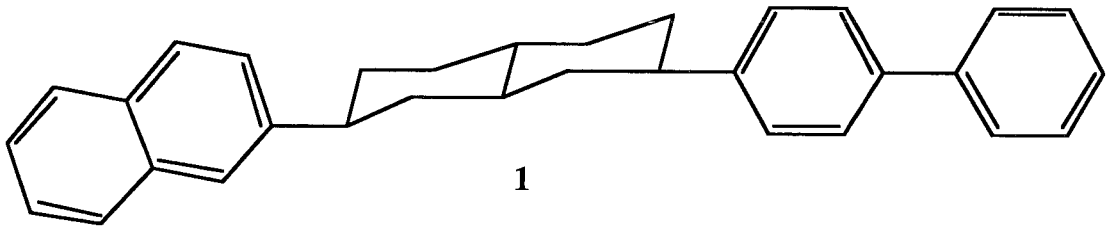

1

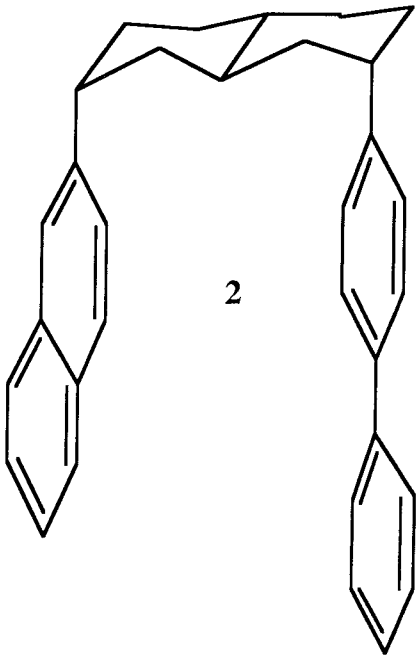

2

ET in Metalloproteins

When considering the through-bond mechanism in the highly inhomogenous interior of a protein, the distance between redox centres is not necessarily proportional to the number of bonds. If a protein can be described as a homogenous medium in the context of ET, the decay rate should satisfy a range of distances between donor and acceptor for a variety of proteins. The β value, describing the decay of the ET rate with distance, found by Dutton, is 1.4 $Å^{-1}$ and is midway between the values given for synthetic systems (β=0.85-0.95 $Å^{-1}$) and a vacuum (β approx. 2.8 $Å^{-1}$)[70]. The decay constant found for the β-strands in Azurin was 1.1 $Å^{-1}$ and is very close to that predicted from theory for an idealized β-strand (β=1.0 $Å^{-1}$) using the pathways model[71]. The theoretical decay rate for an ideal α-helix, assuming hydrogen bonds contribute to the coupling, was calculated to be 1.26 $Å^{-1}$ and thus rates of ET are expected to be slower in α-helices than in β-strands for similar distances.

The most versatile method used in this laboratory for studying ET in metallo proteins exploits the chemistry of the photoexcitable bis(bipyridine)imadazoleruthenium [$Ru(bpy)_2(im)^{2+}$] complexes, first used by Matthews et al. [72], which can be covalently attached to histidine residues on the solvent accessible surfaces of proteins. The histidines are either the natural wild-type residues or histidine residues introduced by site-directed mutagenesis reactions, usually in conjunction with mutagensis of wild-type solvent accessible histidines to alternate residues. In this way complexes can be engineered into a variety of single sites and distances from the metallo centre. The use of ruthenium complexes has evolved from initial studies which used the pentaammineruthenium complex in horse heart cytochrome *c* [73, 74]. The inner sphere reorganization energy of these complexes are relatively low owing to the small changes which accompany the conversion from Ru(II) to Ru(III). The outer sphere reorganization energy provides the major contribution to the reorganization energy and for the pentaammineruthenium complexes

described in the bimolecular system above $-\Delta G^\circ < \lambda$ and so maximal ET rates are not observed. The use of $Ru(bpy)_2(im)^{2+}$ complexes with their more hydrophobic ligands lowers the reorganization energy associated with reorientation of the solvent and the π-acidic ligands also raize the reduction potential to > 1.0 V and thus providing systems at or near the activationless region (where $-\Delta G^\circ = \lambda$) and leading to greater accessibility of the inverted region (where $-\Delta G^\circ > \lambda$). Photoexcitation of $Ru(bpy)_2(im)^{2+}$ leads to the long lived (lifetime 70 ns in H_2O) luminescent MLCT state $*Ru(bpy)_2im^{2+}$ which appears to result from a t_{2g} to ligand π^* orbital transition[75]. The triplet decay of $*Ru(bpy)_2im^{2+}$ is the sum of the intrinsic decay rate and k^f_{ET}, the 'forward' rate provided by the quenching of luminescence by the metallosite. The reduction potential of this excited species is approximately - 1.0 V which upon oxidation and relaxation to the ground state Ru^{3+}, then acts as a strong oxidant to reform Ru^{2+}. In this way the ET in a metalloprotein may be observed from $*Ru(bpy)_2(im)^{2+}$ to the metallosite (k^f_{ET}) and also from the reduced metallosite to $Ru(bpy)_2(im)^{3+}$ (the back rate k^b_{ET}). Techniques for monitoring ET can be arranged into two groups depending on whether the ET is initiated directly by photostimulation of the ruthenium label or by the use of a quencher used to form the strongly oxidizing species. Direct 'photo-induced' observation using $Ru(bpy)_2im^{2+}$ is limited to k^f_{ET} rates > $2x10^6$ owing to the lifetime of the excited state species, and means that only $k^b_{ET} \geq 1 \times 10^5\ s^{-1}$ may be observed by this technique. This window of observation may be extended to observe slower rates by the 'flash-quenched' method. A quencher of sufficient potential is used to oxidize $*Ru(bpy)_2im^{2+}$ which subsequently oxidizes the reduced protein with rate k^b_{ET}. The limit of such quenchers is then reached when k^b_{ET} becomes comparable to the rate of recombination of the reduced quencher with the oxidized ruthenium label (the back reaction is effectively bypassed). Under such circumstances the use of irreversible quenchers can be employed to extract ET rates. Figure Chapter 1-4 shows a schematic of the two methods.

Laser photoexcitation of $Ru(bpy)_2(im)^{2+}$ can be followed by monitoring the time resolved emission at 670 nm and also the absorption at 370 nm. The absorption of $Ru(bpy)_2(im)^{3+}$ can be monitored at 315 nm together with the $*Ru(bpy)_2(im)^{2+}$ absorption. Combined with time resolved monitoring of the oxidation state of the metalloprotein, the ET rates may be determined. In addition, monitoring quencher absorption may also be used to monitor ET.

Chapters 2, 3 and 4 of this thesis report such experiments using $Ru(bpy)_2im^{2+}$ labelled cytochrome b_{562}, a four helix bundle protein from Eschericia coli. Both direct photoinduced and indirect methods using quenchers (reversible and irreversible) were employed to observe ET between the non-covalent heme group of b_{562} and the ruthenium labile positioned at various solvent accessible sites on the proteins surface. Chapter 5 describes ET in a mutant in which the heme group has been covalently attached by introduction of one thioether linkage.

Bibliography

1. Deizenhofer, J., Epp, O., Miki, K., Huber, R. & Michel, H. *Nature* **318**, 618 (1985).

2. Blankenship, R.E. & Prince, R.C. *Trends Biochem. Sci.* **10**, 383 (1985).

3. Hatefi, Y. *Annu. Rev. Biochem.* **54**, 1015 (1985).

4. Wikstrom, M. & Saraste, M. in *Bioenergetics* (ed. Ernster, L.) 49-54 (Elsevier, New York, 1984).

5. Mitchell, P. *Nature* **191**, 144-148 (1961).

6. Dreyer, J.L. *Experientia* **40**, 653-675 (1984).

7. Marcus, R.A. & Sutin, N. *Biochim. Biophys. Acta.* **811**, 265-322 (1985).

8. McLendon, G. *Acc. Chem. Res.* **21**, 160-167 (1988).

9. Williams, R.J.P. *Biochem. Int.* **18**, 475-499 (1989).

10. Huber, R. *Eur. J. Biochem.* **187**, 283-305 (1990).

11. Boxer, S.G. *Annu. Rev. Biophys. Biophys. Chem.* **19**, 267-299 (1990).

12. Bowler, B.E., Raphael, A.L. & Grey, H.B. *Progr. Inorg. Chem.* **38**, 259-322 (1990).

13. Farrid, R.S., Moser, C.C. & Dutton, P.L. *Curr. Opin. Struct. Biol* **3**, 225-233 (1993).

14. Siddartth, P. & Marcus, R.A. *J. Phys. Chem* **97**, 2400-2405 (1993).

15. Marcus, R.A. & Sutin, N. *Biochim. Biophys. Acta.* **811**, 265-322 (1985).

16. DeVault, D. *Quantum-Mechanical Tunnelling in Biological Systems* (Cambridge University Press, Cambridge, 1984).

17. Canters, G.W. & Kamp, M.v.d. *Curr. Opin. Struct. Biol.* **2**, 859-869 (1992).

18. Bertrand, P. *Struct. Bonding* **75**, 1-47 (1991).

19. Hoffman, B.M., Natan, M.J., Nocek, J.M. & Wallin, S.A. *Struct. Bonding* **75**, 85-108 (1991).

20. Quin, R., Mercer-Smith, J., Burstym, J.N. & Valentine, J.S. *J. Am. Chem. Soc.* **106**, 4136-4144 (1984).

21. Goodin, D.B. & McRee, D.E. *Biochmeistry* **32**, 3313-3324 (1993).

22. Safo, M., Gupta, G.P., Walker, F.A. & Scheidt, W.R. *J. Am. Chem. Soc.* **113**, 5497-5500 (1991).

23. Sarma, S., et al. *Biochemistry* **36**, 5658-5668 (1997).

24. Langen, R., *et al. J. Mol. Biol.* **224**, 589-600 (1992).

25. Zhou, H.X. *J. Am. Chme. Soc* **116**, 10362-10375 (1994).

26. Anderson, P.W. *Phys. Rev.* **79**, 350 (1950).

27. McConnell, H.M. *J. Chem. Phys.* **35**, 508 (1961).

28. Halpern, J. & Orgel, L.E. *Discuss. Faraday Soc.* **29**, 32 (1960).

29. Ohta, K., Gloss, G.L., Morokuma, K. & Green, N.J. *J. Am. Chem. Soc.* **108**, 1319 (1986).

30. Hoffmann, R., Imamura, A. & Hehre, W.J. *J. Am. Chem. Soc.* **90**, 1499 (1968).

31. Moser, C.C., Keske, J.M., et al. *Nature* **355**, 796-802 (1992).

32. Hopfield, J.J. *Proc. Natl. Acad. Sci.* **71**, 3640 (197).

33. Marcus, R.A. & Sutin, N. *Biochim. Biophys. Acta* **811**, 265-322 (1985).

34. Langen, R., *et al. Science* **268**, 1733-1735 (1995).

35. Karpishin, T.B., Grinstaff, M.W., Komar-Panicucci, S., McLendon, G. & Gray, H.B. *Structure* **2**, 415 (1994).

36. Wuttke, D.S., Bjerrum, M.J., Winkler, J. & Gray, H.B. *Science* **256**, 1007-1009 (1992).

37. Wuttke, D.S., Bjerrum, M.J., Chang, I., Winkler, J. & Gray, H.B. *Biochim. Biophys. Acta* **1101**, 168 (1992).

38. Beratan, D.N., Onuchic, J.N. & Hopfield, J.J. *J. Chem. Phys.* **86**, 4488-4498 (1987).

39. Onuchic, J.N. & Beratan, D.N. *J. Chem. Phys.* **92**, 722-733 (1990).

40. Onuchic, J.N., Beratan, D.N., Winkler, J.R. & Gray, H.B. *Annu. Rev. Biophys. Biomol. Struct.* **21**, 349-377 (1992).

41. Beratan, D.N., Betts, J.N. & Onuchic, J.N. *J. Phys. Chem.* **96**, 2852-2855 (1992).

42. Beratan, D.N., Betts, J.N. & Onuchic, J.N. *Science* **252**, 1285-1288 (1991).

43. Skourtis, S.S., Regan, J.J. & Onuchic, J.N. *J. Phys. Chem.* **98**, 3379-3388 (1994).

44. Siddarth, P. & Marcus, R.A. *J. Phys. Chem.* **94**, 8430-8434 (1990).

45. Siddarth, P. & Marcus, R.A. *J. Phys. Chem.* **94**, 2985-2989 (1990).

46. Siddarth, P. & Marcus, R.A. *J. Phys. Chem.* **96**, 3213-3217 (1992).

47. Siddarth, P. & Marcus, R.A. *J. Phys. Chem.* **97**, 13078-13082 (1993).

48. Gruschus, J.M. & Kuki, A. *Chem. Phys. Lett.* **192**, 205-212 (1992).

49. Gruschus, J.M. & Kuki, A. *J. Phys. Chem.* **97**, 5581-5593 (1993).

50. Friesner, R.A. *Structure* **2**, 339-343 (1994).

51. Evenson, J.W. & Karplus, M. *Science* **262**, 1247-1249 (1993).

52. Beratan, D.N., Betts, J.N. & Onuchic, J.N. *Science* **252**, 1285 (1991).

53. Onuchic, J.N., Andrade, P.C.P. & Beratan, D.N. *J. Chem. Phys.* **95**, 1131 (1991).

54. Casimiro, D.R., Richards, J.H., Winkler, J.R. & Gray, H.B. *J. Phys. Chem.* **97**, 13073-13077 (1993).

55. Marcus, R.A. *J. Chem. Phys.* **24**, 966 (1956).

56. Marcus, R.A. *Annu. Rev. Phys. Chem.* **15**, 155-196 (1964).

57. Marcus, R.A. *J. Chem. Phys.* **43**, 679 (1965).

58. Marcus, R.A. & Sutin, N. *Comments Inorg. Chem.* **5**, 119 (1986).

59. Siders, P. & Marcus, R.A. *J. Am. Chem. Soc.* **103**, 748 (1981).

60. Bjerrum, M.J., *et al. J. Bioenerg. Biomem.* **27**, 295-302 (1995).

61. Mines, G.A., *et al. J. Am. Chem. Soc.* **118**, 1961-1965 (1996).

62. Miller, J.R. & Beitz, J.V. *J. Chem. Phys.* **74**, 6476 (1981).

63. Miller, J.R. & Beitz, J.V. *J. Chem. Phys.* **71**, 4579 (1979).

64. Miller, J.R. & Huddleston, R.K. *J. Am. Chem. Soc.* **106**, 5057 (1984).

65. Overing, H., et al. *Science* **109**, 3258 (1987).

66. Leland, B.A., et al. *J. Phys. Chem.* **89**, 5571 (1985).

67. Closs, G.L. & Miller, J.R. *Science* **240**, 440-447 (1988).

68. Marcus, R.A. *Can. J. Chem* **37**, 155 (1959).

69. Closs, G.L., Calcaterra, L.T., Green, N.J., Penfield, K.W. & Miller, J.R. *J. Chem. Phys.* **90**, 3673 (1986).

70. Gamow, G.Z. *Phys.* **51**, 204-212 (1928).

71. Langen, R. in *Dept. Chemistry and Chemical Engineering* (California Institute of Technology, Pasadena, 1995).

72. Matthews, C.R., Erickson, P.M., Vliet, D.L.V. & Petersheim, M. *J. Am. Chem. Soc.* **100**, 2260-2262 (1978).

73. Nocera, D.G., et al. *J. Am. Chem. Soc.* **106**, 5145-5150 (1984).

74. Winkler, J.R., Nocera, D.G., Yocom, K.M., Bordignon, E. & Gray, H.B. *J. Am. Chme. Soc* **104**, 5798 (1982).

75. Houten, J.V. & Watts, R.J. *Inorg. Chem.* **17**, 3381 (1978).

Figure Chapter 1-1: The free energies for the reactants (R) and products (P) for electron transfer reactions.

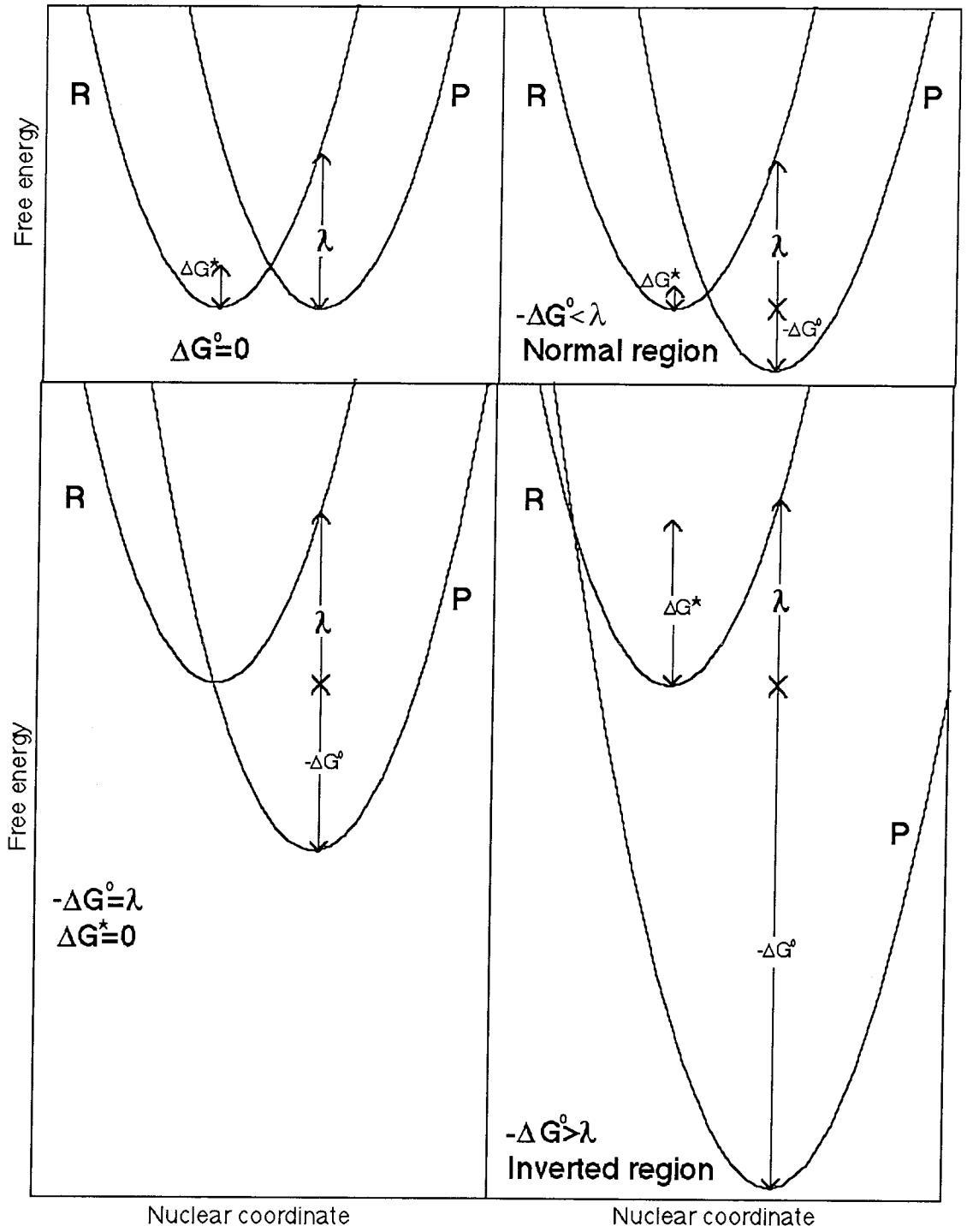
Free energy
R
P
λ
ΔG*
ΔG°=0
-ΔG°<λ
Normal region
-ΔG°
-ΔG°=λ
ΔG*=0
-ΔG°>λ
Inverted region
Nuclear coordinate
Nuclear coordinate

Figure Chapter 1-2: Schematic of a particle incident on a barrier.

The wavefunction of a heavy particle decays more rapidly inside a barrier than that of a light particle. Consequently a lighter particle has a greater probability of tunnelling through the barrier. If the barrier is not too thick, the wave function is non-zero at its opposite face which corresponds to the particle penetrating the barrier.

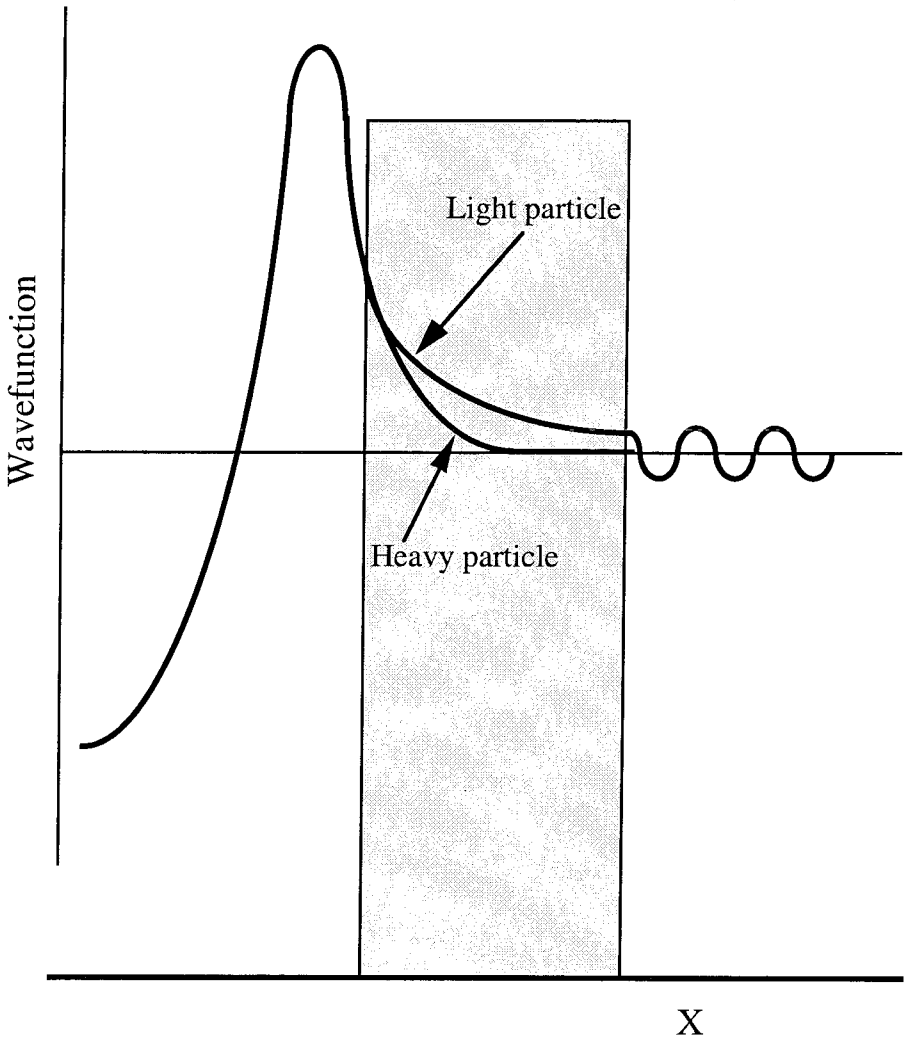
Wavefunction
Light particle
Heavy particle
X

Figure Chapter 1-3: The log of the rate constant for electron transfer *versus* the reaction free energy.

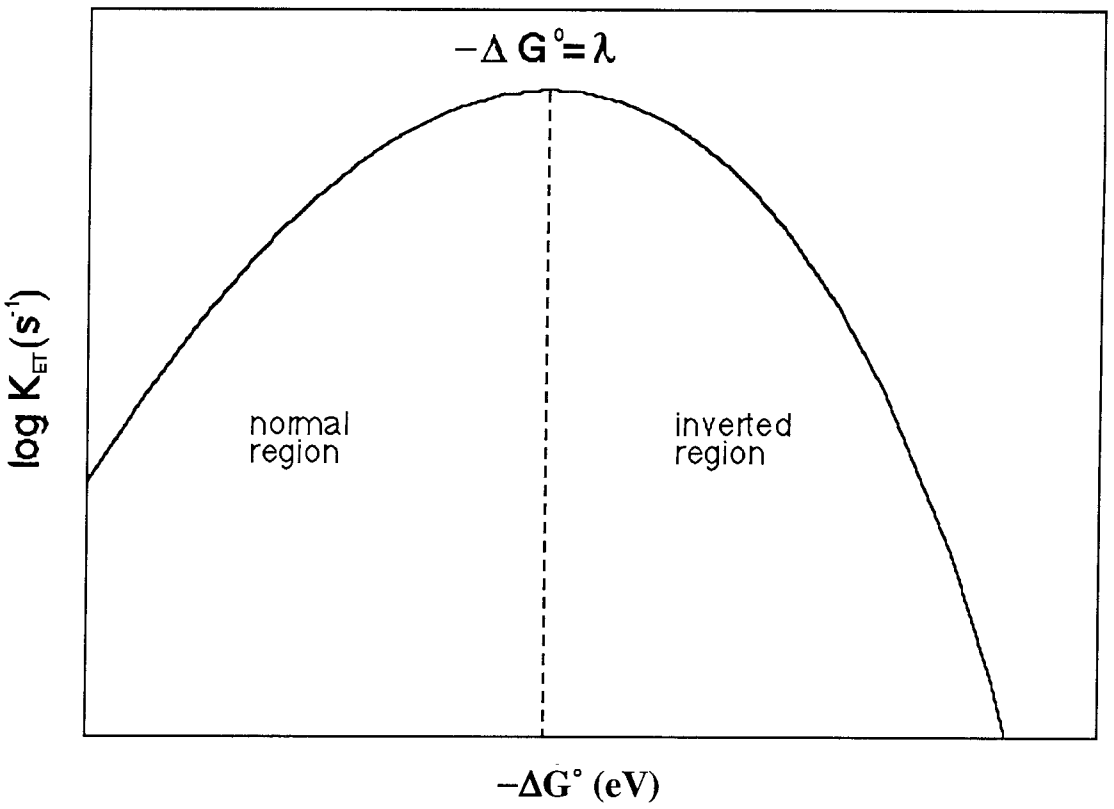
−Δ G°= λ
log K_ET(s^-1)
normal region
inverted region
−ΔG° (eV)

Figure Chapter 1-4: Schematic of the photo-induced and flash-quench methods for observing electron transfer in proteins.

Flash quench technique

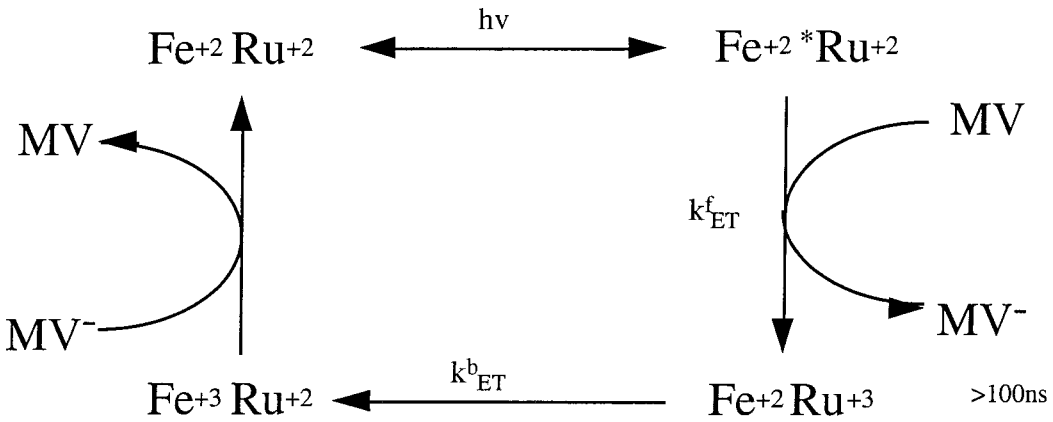

Photo induced technique

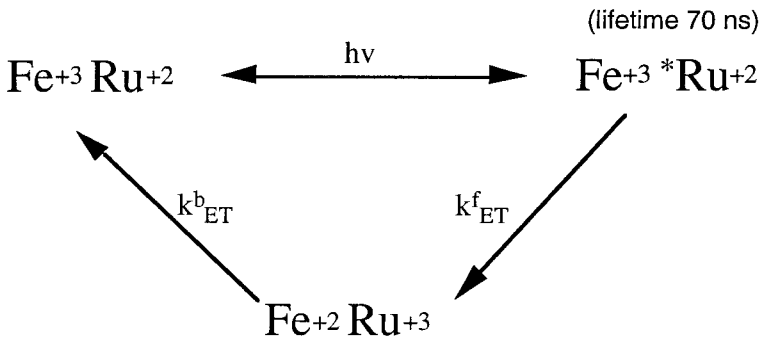

hv = excimer-dye laser pulse of 20 ns at 480nm, 1.6 m joules

MV = methyl viologen

Chapter 2

Electron Transfer Through Helix A of Cytochrome b_{562}: Labelling of Residues 12, 15 and 19

Introduction

In order to examine the distance dependence effect of protein α-helical structures on the rate of electron transfer (ET), we selected the protein cytochrome b_{562}. Single histidine residues were introduced along the length of the protein by site-directed mutagenesis and ET investigated between the proteins heme group and the photoexcitable ruthenium(II)bis(2,2'-bipyridine)(imidazole) attached to the histidine sites. Cytochrome b_{562} (b_{562}) is a well characterized[1-3] soluble 106 amino acid four α-helical bundle protein (see Figure Chapter 2-1) secreted to the periplasmic space of *Escherichia coli* during which time an N-terminal leader sequence is removed. The function of (b_{562}) is unknown[4, 5] but it is believed to function as an electron transport protein[6]. B_{562} meets the criteria for ET studies since it contains a heme group close to one end of the molecule with α-helices extending to the opposite end, and contains only one solvent exposed histidine residue with the only other histidine residue forming one of the axial ligands to the heme iron. Labelling of b_{562} with photoexcitable reducing agents is therefore possible via the wild-type histidine or by the introduction of mutant histidine sites without extensive changes to the protein. B_{562} contains the protoporphyrin IX prosthetic group towards one end of the four-helical bundle ligated with Met 7 and His 102 axial ligands. It has a large molar absorbance of 117,400 (at 418 nm) for the oxidized form and 180,100 (at 427 nm) for the reduced protein[5] (see Figure Chapter 2-2) and a pH dependent oxidation/reduction potential of approximately 180 mV (pH 7.0)[7] with the ferrous protein being more stable by 4.6 kcal mol^{-1}[8]. The pH dependence of the potential has been proposed to be modulated via the His 102 axial ligand

which has a reduced pk_a in the ferric state. B_{562} has an isoelectric point of approximately 5 and a predicted charge of -1 at pH 7. The x-ray structure[1, 3, 9] of b_{562}, crystalized as a dimer, complements circular dichroism calculations which show the protein to be 82% α-helix and 18% random coil in solution. Cytochrome b_{562} contains five prolines, situated between helical regions, and has no cysteine or tryptophan residues. The amino acid sequence of wild-type (WT) cytochrome b_{562} and a backbone representation of its structure is shown in Figure Chapter 2-1. Helix C (residues 56-80) is the longest of the four helices and contains within its length a section of 3_{10} helix from residues 61-63. Helix D (residues 84-105) also maintains a 3_{10} helix conformation between residues 89-93. The average of the dimeric crystalized protein iron to Met 7 SD and iron to His 102 NE2 distances found in the refinement of the 1.4 Å x-ray structure converged to 2.38 Å and 2.02 Å respectively which are similar to those of yeast[10], tuna[11] and rice[12] cytochrome *c*. The Met 7 side of the heme plane is faced with hydrophobic residues whilst the other side together with the histidine ligand is solvent exposed. The packing of the helices is very close such that no water molecules were found in the interior of the protein's x-ray structure.

Cytochrome b_{562} is structurally quite similar to cytochrome *c*'[1], a 128 residue four α-helical bundle electron transfer protein from *Rhodospirulum molishianum.*[13]. Overlaying the heme groups of each protein reveals close correspondence between their α-helical bundles with 65 residues having an r.m.s. distance deviation of 1.05 Å at the α-carbon position, and 11 of these residues being identical. The heme orientation is the same in each protein and they also have similar lengths (approximately 50 Å). Figure Chapter 2-3 shows the backbone structure and heme orientation of b_{562} and cytochrome *c*'. B_{562}, however, is predominately (see below) low-spin, hexacoordinate, monomeric with a non-covalent heme whilst cytochrome *c*' has only one axial ligand, His122, is high spin and has a covalently

attached heme. The porphyrin plane is flat in b_{562}, but in cytochrome *c*' it is distorted into a saddle shape. B_{562} has similarities to cytochrome *c*, which also has a hexacoordinate iron with histidine and methionine axial ligands. Both display two sets of heme NMR hyperfine shifts which in cytochrome *c* is explained by alternate axial met-16 chiralities. In b_{562} the hyperfine pattern may also be attributed to the disorder in the Fe-met-7 bond, but a more likely explanation is that there is heme orientational disorder by a 180° rotation about the hemin α,γ-meso axis[2]. Wu et al. estimate a 2:1 ratio of isomers. Wu also discovered that b_{562} displays rapid equilibrium with a thermally accessible high-spin state, a property not usually found in cytochromes with axial his/met ligands. This high-spin state is expected to be six-coordinate but only represents 12% of protein at 45°C. Earlier studies by Bullock[14] in which resonance Raman spectra recorded at 2°C were compared to data of Spiro and co-workers[15, 16] provide evidence that both ferric and ferrous b_{562} at pH 7 exist as low-spin hemoprotein.

Material and Methods

A Design of Mutants

The particular method chosen for labelling b_{562} with an electron donor moiety necessitates replacing amino acids with histidine residues to which the ET donor will be attached. The wild-type histidine residue at position 63 was replaced with a glutamate residue prior to formation of new mutant histidine sites. Electron donor labelling sites on b_{562} were designed with the following criteria. The sites must be located on an α-helical region of the protein, at a surface exposed residue to enable efficient labelling, and at a distance of interest from the

heme with no aromatic residues in the sequence between the intended labelling site and the heme. The site of mutation must also be located to minimize secondary label interactions with the protein, and at a position not likely to compromize the structure of b_{562}. The x-ray crystallography structure of dimeric b_{562} (256B[1]) was downloaded from the Protein Data Bank database, displayed as a monomer (monomer A) and sites suitable for labelling identified using RasMac v2.5 molecular display software. Further examinations of the b_{562} structure were performed on a Silicon Graphics work station using the Insight software package. The mutants listed in Table Chapter 2-2 were identified as labelling sites for helix A which fulfilled the selection criteria. Table Chapter 2-1 also lists the Cα - Fe, Cα - heme edge and the ruthenium-heme distances as calculated using RasMol and Insight II. All mutants were constructed from the H63E gene, and this mutation is implied when referring to mutant proteins.

B DNA

The gene for wild-type cytochrome b_{562} was kindly provided by Professor Stephen Sligar. The gene and flanking regions were in the multi-cloning site of a derivative of a pUC18 plasmid (via the Sma I and Sal I restriction sites) called pNS207 and under control of the pUC *lac* promoter and in *E coli* TB1 cells. Boiling mini preps and $_{max}$i preps of cultures were performed to supply plasmid for subsequent mutagenesis reactions. Prior to mutagenesis reactions expression of cytochrome b_{562} using the TB1/pNS207 cells was performed to validate the integrity of the gene.

C Mutagenesis Reactions

The "overlap extension" polymerase chain reaction (OE-PCR) mutagenesis technique was chosen and involves the synthesis of four DNA oligonucleotide primers to introduce a

mutation at the target site. Briefly, one primer is located at the 5' (antizense strand) end of the target sequence and another at the 3' (sense strand) end, in this case the flanking regions either side of the b_{562} gene, and contain a restriction site for subsequent reincorporation of the DNA into a plasmid. Each of these two primers is used in two mutagenesis reactions, PCR reaction 1 and 2. The other two primers are peculiar to the specific mutation being introduced. The two separate PCR reactions generate the 5' and 3' regions of the mutated gene with a common overlap region at the site of the mutation. The products of PCR reactions 1 and 2 are then combined in a third reaction (PCR reaction 3) to generate the full length gene.

For mutagenesis in b_{562}, the 5' and 3' flanking primers, named b_{562}prom and b_{562}term respectively, are shown below.

b_{562}prom 5'-AGT GAA TTC GAG CT*C GGT ACC C^GG

b_{562}term 5'-TGC CTG CAG GTC GA~C GGC AAA TT

^ denotes the Sma I site, the site of ligation of the N terminus of the DNA sequence containing the b_{562} gene and flanking region, and ~ the Sal I site to which the 3' end of this sequence was ligated. * denotes the Sac I site of the multi-cloning site in pUC18 and was used in preference over the SmaI site during mutagenesis reactions since the Sma I site is blunt ended and can be problematic during ligation and digestion reactions.

Similar sized oligos were constructed for incorporation of mutated residues. The sense strand oligos were named xtop and the antizense oligos named xbott (x is the residue number to be mutated). To accommodate *Taq* polymerases anomalous behaviour of occasionally inserting an additional adenosine residue at the end of extension reactions, oligos were chosen so that if the oligo were one nucleotide longer at the 5' end, the extra residue would be a thymine. Oligos were ordered from the California Institute of

Technology Biopolymer Synthesis Facility at a 2 μmole scale and purified by ethanol precipitation prior to mutagenesis reactions.

The mutation sites with their two respective oligos are listed in Table Chapter 2-1 with the mutation italicized. Initially the H63E mutant was constructed and subsequently used in the synthesis of all the non-covalent attached heme group mutants.

PCR mutagenesis reactions 1 and 2 each contained 59 μl H_2O, 10 μl each of top or bott oligos (25 pmol/μl), 10 μl each of prom or term oligos (25 pmol/ml), 10 μl 10 mM deoxynucleotide triphosphates, 10 μl PCR reaction buffer (Boehringer Mannheim), 0.125 μl Taq polymerase (Boehringer Mannheim), and 1 μl of plasmid pNS207 (approx. 0.1 mg). PCR reaction 3 contained 40 μl H_2O, 10 μl each of purified (see below) product from PCR reaction 1 and 2, 10 μl each of prom and term oligos (25 pmol/μl), 10 μl 10 mM deoxynucleotide triphosphates, 10 μl PCR reaction buffer (Boheringer Mannheim), and 0.125 μl Taq polymerase (Boehringer Mannheim). PCR reactions were carried out using a Perkin Elmer thermal cycler with the following cycle after an initial 2 minute denaturation at 95°C: denaturation at 95°C for 30 secs, primer annealing at 55°C for 30 secs and extension for 1 minute at 72°C. After the final extension reaction, the mixture was cooled to 4°C. PCR products were purified and checked for correct size on 1% agarose gels with TAE (tris-acetate-EDTA) buffer. Correct bands were excized from the gel, purified from gel matrix and concentrated using the Qiaex Gel Extraction kit (Qiagen Inc.) Purified PCR products were used for PCR reaction 3 or, in the case of PCR reaction 3 products, for endonuclease digestion and subsequent ligation into a plasmid for protein expression. 20 μl of purified PCR reaction 3 product was digested with 1 μl of Sac 1 and Sal 1 (Boehringer Mannheim) and 3 μl of buffer M (Boehringer Mannheim) for approximately 6-12 hours at room temperature. Digestion products were purified and checked for correct size on 1% agarose gels. The correct bands were excized from the gel and concentrated using the Qiaex Gel Extraction procedure.

Stocks of plasmid pNS207 were grown in the non-expression cell strain DH10B initially transformed with plasmid obtained from boiling mini preps of the WT b_{562} TB1/pNS207 cells. 100 ml cultures of DH10B cells were processed with the maxi-prep plasmid purification protocol (Qiagen Inc.) to produce the stocks. Purified plasmid was digested with the endonucleases Sal 1 and Sac 1 to remove the WT b_{562} gene, and the product then gel purified.

Ligation of the mutant gene into the multi cloning site of pNS207 was carried out as follows. 6 µl of Sal l/Sac1 digested pNS207 plasmid, 10 µl of digested PCR reaction 3 product, 2 µl of buffer M and 1 µl of T7 DNA ligase were incubated at room temperature for approximately six hours. The ligation solution was desalted and concentrated using Qiaex resin (Qiagen Inc.).

DH10B cells were transformed with purified ligation reaction products by either electroporation or incubation/temp shock method. Cells were plated on LB agar containing ampicillin at 60 µg/ml. A number of colonies were tested for inserts of the gene by a PCR screen as follows. 2.5 µl each of prom and term oligos (25 pmol/µl), 2.5 µl 10 mM deoxynucleotide triphosphates, 2.5 µl PCR reaction buffer (Boheringer Mannheim), 5 µl cell suspension, 0.125 µl Taq polymerase (Boehringer Mannheim), and 10 µl of H2O. The PCR reaction was run for 55 cycles and the products loaded onto a 1% agarose gel. Colonies showing bands of the correct size were grown up for plasmid production using the maxi-prep plasmid purification protocol (Qiagen Inc.)

D Protein Expression

Mutant proteins were expressed in either the BL21 or BL21(DE3) cell lines after electroporation or chemical transformation of competent cells. The following expression protocol was used for all cell lines with the omission of IPTG for the BL21 cells. 3 ml starter cultures in LB broth with 60 µg/ml ampicillin were grown o/n at 37°C and used to

inoculate 3 l of 2xYT broth in 6 l flasks. Cells were grown in an incubated shaker at 37°C to an OD_{600} of 0.6 and then induced by the addition of 0.1 mM IPTG. Incubation was continued until the culture became pink/red coloured (6-18 hours). Protein was released from the cell periplasm by osmotic extrusion as follows. Cells were spun down in 1 l centrifuge bottles at 4k rpm in a Beckman centrifuge and the pellet was resuspended in 100 ml/l of lysis buffer (20% sucrose, 1 mM EDTA pH8.0, 30mM Tris pH 8.0) by gentle shaking for 30 minutes. The cells suspension was then centrifuged at 5k rpm in 250 ml bottles in a GSE rotor and the pellet resuspended in 100 ml cold H_2O and then shaken to resuspend the cell pellet for another 30 minutes at 4°C. Protein released into the solution was separated from cells and debris by a final centrifugation at 10k rpm for 30 minutes. Very often the protein was released into the lysis buffer solution and the subsequent steps modified. When protein was released into the lysis buffer, the solution was centrifuged at 10k for 30 minutes to remove remaining debris and incubated with 40 mg/L DNase and 20 mg/l RNase. In all cases the final centrifugation resulted in a cell pellet with a lower red layer from which protein could not be released either by physical (shaking, ultrasound, stirring) or chemical (extended lysozyme digestion, high salt buffers) techniques.

E Protein Purification

Initial purification of the red periplasmic solution from the above expression method was carried out using Q Sepharose anion exchange fast flow resin (Pharmacia Biotech). The periplasmic fraction was suction filtered through Whatman 541 filter paper over a Buchner funnel and then approximately 50 ml of Q Sepharose resin in 100 ml of TEA buffer (25 mM triethanolamine pH 7.6) was added per 500 ml of periplasmic solution. The pH was checked and adjusted to pH 7.6 if necessary and the solution shaken gently at 4°C for a minimum of 20 minutes to allow complete binding of b_{562} to the resin. The resin was poured into a coarse glass frit funnel and washed twice with approximately 100 ml of TEA

buffer. Protein was released from the resin by washing twice with 100 ml 1 M NaCl/TEA buffer. The OD_{418}/OD_{292} was checked and used as an indicator of purity of the protein solution. After diafiltration using an Amicon unit with a 10k cut-off filter (YM10) and TEA buffer, the solution was concentrated to approximately 30 ml/per 6l culture volume and purified further by FPLC (fast protein liquid chromatography). The protein solution was loaded onto an anion exchange column, HR 10/10 MonoQ™ (Pharmacia), and the column washed with TEA. Protein was eluted from the column with a salt gradient of buffer B (TEA, 1 M NaCl). Fractions containing b_{562} were pooled, diafiltered and concentrated (using Amicon apparatus and YM10 membranes) in TEA buffer and reloaded onto the column. Fractions containing apo b_{562} were treated with hemetin (Sigma). A stoichometric amount of 1 mM hemetin in 50 mM NaOH was added to the apo protein solution drop-wise with stirring. This solution was purified using FPLC. After three or four consecutive rounds of FPLC, the OD_{418}/OD_{292} of the protein solution was checked and a sample analyzed by SDS/PAGE (see below).

F Labelling of b_{562} with ruthenium(II)bis(2,2'-bipyridine)carbonate

(1) Synthesis of ruthenium(II)bis(2,2'-bipyridine)carbonate.

2 g of cis-Dichlorobis(2,2'-bipyridine) ruthenium(III)dihydrate (Strem Chemicals) in 150 ml of degassed H_2O was refluxed under CO_2 for 15 minutes. 6.6 g of Na_2CO_3 was added and the reflux continued for two hours. After cooling purple needle-like crystals of ruthenium(II)bis(2,2'-bipyridine)carbonate formed with a yield of 19%. These were washed three times with H_2O and allowed to air dry.

(2) Labelling of Histidine residues with ruthenium(II)bis(2,2'-bipyridine)carbonate.

A 0.1 mM solution of b_{562} in freshly prepared 300 mM $NaHCO_3$ pH 7.4 was treated with an equimolar amount of ruthenium(II)bis(2,2'-bipyridine)carbonate for 6-12 hours at room temperature during which time the reaction was monitored by UV using the ratio of the Soret band to the ruthenium absorption band (418 nm and 292 nm respectively) after passing samples through a small gel filtration column (G-25 sephadex/PD10 Pharmacia). Extinction coefficients used were 117.4 mM^{-1} cm^{-1} for ferric b_{562} at 418 nm and 52.635 mM^{-1} cm^{-1} for ruthenium at 292 nm.

The reaction was stopped by diafiltration and concentrating the solution in 20 mM Na_2HPO_4/1 M NaCl pH 7.2. Labelled protein was separated from unlabelled using a 5 ml HiTrap™ metal chelating column (Pharmacia Biotech) together with FPLC apparatus. The column was pre-equilibrated with copper ions using 0.1 M $CuSO_4$ and unbound copper eluted. The diafiltered and concentrated labelling reaction solution was loaded onto the column and eluted with a gradient of 20 mM Na_2HPO_4/1 M NH_4Cl pH 7.2 to give ruthenium(II)bis(2,2'-bipyridine)(H_2O) labelled b_{562}.

Labelled b_{562} from above was diafiltered in 400 mM imidazole pH 8.0 and left at room temperature in the dark for 24-48 hours during which time the majority of the heme was precipitated by the imidazole and the ruthenium(II)bis(2,2'-bipyridine)(im) complex formed (im is imidazole). After the reaction the unreacted imidazole was removed by diafiltration in TEA buffer and the solution treated with 1 mM Hemin in 50 mM NaOH to restore the correct ratio of the 418 nm Soret to the ruthenium 292 nm absorbance. After heme addition the solution was diafiltered and concentrated in HiTrap column load buffer (20 mM Na_2HPO_4/1 M NaCl pH 7.2) and purified by FPLC. Fractions containing correctly labelled protein, as ascertained by gel chromatography and UV, were then diafiltered and concentrated against 100 mM potassium phosphate pH 7.0 for characterization and measurement of electron transfer rates.

G Characterization of Expressed Protein

Various methods were employed to ascertain the purity, size, site and degree of ruthenium labelling, stability and correct folding of b_{562} and its mutants.

(1) UV spectroscopy

UV spectroscopy was performed on a Hewlett Packard 8420 diode array spectrophotometer using approximately 13 μM solutions of protein in 100 mM sodium phosphate buffer at pH 7.0. The 418 nm to 280 nm absorption ratio was used to quantitate the purity of unlabelled protein, with a value of 5.5-6.0 considered to be close to homogenous. For labelled protein the 418 nm to 292 nm absorption ratio was used to judge the degree of ruthenation, with a value of 1.6 taken as a molar ratio of 1:1 protein to label.

(2) Gel Electrophoresis

Protein samples were run on 15% polyacrylamide SDS gels using both self poured and pre-cast mini gels (Biorad) and Tris/glycine/SDS running buffer. Samples were loaded in a glycerol/SDS/2-mercaptoethanol sample buffer and ran for 6-12 h at 10 mA or 2 h at 100 V for mini gels. Protein molecular weight markers were run to determine molecular weights of sample proteins and protein bands visualized by Coomassie staining.

(3) Electrochemistry

Cyclic voltammetry of 0.5-0.8 mM samples in 100 mM P_i pH 7.0 at 25°C with a Ag/AgCl/KCl(saturated) reference electrode and a platinum counter electrode. A Princeton Applied Research potentiostat was used to control the potential and a Houston Instruments recorder used to record the current output. The potential was swept at 5 mV/s over a range of 50-300 mV.

(4) Tryptic Digestion/Peptide sequencing

400 µl of a 1 mg/ml solution of the K19H Ru(bpy)$_2$(im) labelled mutant was denatured by the addition of 400 µl of 8M urea. The digestion of the sample was initiated by the addition of 20 µl of 2 mg/ml trypsin in 1 mM HCl. After 12 h an additional 20 µl of trypsin solution was added and the digestion continued for another 12 h at 27°C. The reaction was stopped by flash freezing. TFA was added to the solutions to a concentration of 0.1% and the sample then loaded onto a reverse-phase column (PepRPC HR 5/5 Pharmacia) for separation by FPLC. The load buffer for FPLC was 0.1% aqueous solution of TFA and peptides were eluted with an acetonitrile gradient containing 0.1% TFA. Fractions containing ruthenium, as indicated by absorption at 292 nm, were sent for N-terminal sequencing on an Applied Biosystems 473A sequencer at the Caltech Protein/Peptide Micro Analytical Laboratory.

(5) Protein stability / unfolding

The effect of the various mutations and labelling on the stability of b_{562} were assessed by analysis of the unfolding curves for the labelled and unlabelled mutants. Thermal unfolding of ferrous and ferric proteins was monitored by UV/vis at the wavelength of the Soret peak (418 and 428 nm respectively). 4 - 15 µM solutions of protein in 100 mM phosphate buffer pH 7 were heated or cooled over the range of 20-80°C, allowed to equilibrate for a few minutes until the absorption was stable, and the absorbance recorded on a Hewlett Packard 8420 spectrophotometer equipped with a Peltier sample cuvette holder. Samples of 0.5 ml were placed in a quartz 1 cm cuvette with a cover to prevent evaporation. Ferrous samples were prepared by the addition of 2-5 µl of a freshly prepared solution of sodium dithionate. Unfolding data was processed according to a two-state transition model.

In addition, the far-UV CD spectra of some mutants was recorded and compared to that of wild-type. 5-15 µM protein samples in a 1 cm path length cell were scanned using a Jasco

J600 polarimeter from 200-300 nm at 50 nm /minute, band width 1 nm and a time constant of 1 sec. Four scans were averaged and spectra recorded at room temperature.

H Electron Transfer Rate Measurements

Rates of intramolecular electron transfer were measured by both the photo-induced and flash quench methods. An outline of these methods is shown in Figure Chapter 2-4.
In the photo-induced experiment a 1-3 mJ 20 ns laser pulse at 480 nm is used to excite the Ru(II)$(bpy)_2$im bound to a surface histidine. In addition to the intrinsic decay and other processes (e.g., energy transfer), the excited state *Ru$(bpy)_2$im can be quenched by Fe(III) with rate k^f_{ET} to form the ferrous protein. The system can then return to equilibrium by charge recombination between the heme and ruthenium complex with a rate k^b_{ET}. This electron transfer rate (k^b_{ET}) was monitored by changes in the transient absorption signal at 430 nm, characteristic of ferrous heme, and also at 414 nm, characteristic of ferric heme. The rate was also monitored at 315 nm characteristic of the excited state *Ru$(bpy)_2$im and Ru(III). The excited state emission signal was monitored at 670 nm. At least 500 traces were averaged to produce the final kinetic traces. Comparison of rates and intensities at these frequencies provided evidence of the electron transfer process from iron to the ruthenium complex.

In the flash quench experiment, reduced protein in the presence of a degassed quencher, either 5 mM methyl viologen (-450 mV vs. NHE) or the irreversible quencher $Co(NH_3)_5Cl$, was added to the protein solution just before acquizition from a side arm of the laser cuvette flow cell to a concentration of 1 mM. As in the photo-induced experiment, a 1-3 mJ 20 ns laser pulse at 480 nm is used to excite the Ru(II)$(bpy)_2$im bound to a surface histidine which is then quenched at a rate of approximately 4.9×10^8 M^{-1} s^{-1}[17] and the transient

absorption signals at 430 and 414 nm monitored. In addition, the signals at 315 nm (*RuII and RuIII), and for the reduced methyl viologen quencher at 390 - 400 nm, were monitored. The system returns to equilibrium when the reduced quencher reduces the oxidized heme, a reaction which takes place in the ms time scale. Two ml samples of 10-20 μM protein in 100 mM sodium phosphate buffer pH 7.0 were degassed in vacuum cells with 1 cm fluorescence cuvettes containing a stir bar. For flash-quench experiments samples were prepared in a glove bag under nitrogen to a concentration of approximately 25 μM. The sample was reduced by addition of a freshly made concentrated solution of sodium dithionate and desalted through a PD-10 Sephadex G-25 column (Pharmacia). Degassed methyl viologen was added to a side arm of the vacuum cell and added to the sample after initial laser analysis. Alternatively, small aliquots (1-2 μl) of a freshly made concentrated solution of sodium dithionate were added until the protein sample was just reduced, as determined by UV/vis analysis, and the sample then degassed. Temperature and protein concentration effects were also studied for a number of the mutants.

Laser experiments were performed using a XeCl excimer-pumped dye laser (Lamda Physik LPX 210I, FL-3002) at the Beckman Institute Laser Spectroscopy Facility. Samples were analyzed by UV/vis spectroscopy before and after experiments to inspect sample integrity. Experiments were carried out at room temperature (20°C) except in the case of temperature dependence studies where the sample cuvette was placed in a water jacketed cuvette holder through which water was continuously recirculated at the required temperature. Transient data was analyzed and ET rates determined using the program KINFIT.

Results

A Design of mutants

The chosen sites for attachment of ruthenium(II)bis(2,2'-bipyridine)(im) gave the distances listed in Table Chapter 2-1. The ruthenium to iron distances are seen to range from 14 to 25 Å. Distances were measured using the molecular modelling programs Insight II and RasMac v2.5 using the 1.4Å x-ray crystallographic structure 256B downloaded from the Brookhaven data base. Analysis of Ru to Fe^{3+} tunnelling lengths using the Pathways program and the same wild-type crystal structure showed that tunnelling lengths, initially determined as the Cα to Fe^{3+} ligand distance, for the D12H, K15H and K19H were 24.6, 26.7 and 36.9 Å respectively (see Table Chapter 2-1).

B DNA/Mutagenesis reactions

The gene used in the mutagenesis reactions was isolated from TB1 cells containing the pNS207 plasmid donated by the Laboratory of Professor Stephen Sligar. Before mutagenesis reactions were carried out, protein was prepared from these cells and were found to overexpress a red protein which had the correct molecular weight as determined by SDS/polyacrylamide gel electrophoresis of the cells.

PCR mutagenesis reactions progressed as planned with PCR reactions 1 and 2 producing the correct size of gene fragments for each of the mutants. Figure Chapter 2-8 shows a photograph of a typical gel used to analyze and harvest products from the PCR mutagenesis reactions. The gel provides both a convenient method to check that the reactions gave the

correct products, as seen by comparison to DNA molecular weight markers, and also as a method to isolate the required products which can be excized from the gel for use in subsequent reactions. These products were excized from gels and purified by Qiaex resin (Qiagen) and used in PCR reaction 3. Products from this reaction were analyzed and isolated as above and after endonuclease digestion with Sal I and Sac I, ligated into the pNS207 plasmid which had been digested with the same enzymes. The purified and desalted (Qiaex resin) ligation product was used to transform DH10B cells. Overnight growth of transformed cells on ampicillin agar plates produced isolated colonies which displayed a pink colour to varying degrees of intensity. PCR screening of the isolated colonies confirmed that a gene of the correct size was present and positive colonies were grown for plasmid Maxi Prep (Qiagen) preparations. Sequencing of plasmid preps confirmed in all cases the correct DNA sequence.

C Protein Expression and Purification

Protein was expressed at 2 -20 mg/L of culture and varied between different protein preparations of the same mutant. Usually if the culture was of deep red colour a good yield could be expected. All mutants were eluted from the MonoQ anion exchange FPLC column at approximately 11% buffer B and from the HiTrap chelating column at approximately 80% B. A small percentage of reduced protein (<10%) was found in the initial purification steps and eluted after oxidized protein. With both FPLC columns labelled and unlabelled apo-protein, present at 10-30%, was eluted before the labelled or unlabelled holo protein. Sequential rounds of FPLC (3 to 4 rounds) produced holo protein which, when viewed by SDS PAGE was homogenous for most mutants and with others faint bands due to other proteins were seen on overloaded SDS/PAGE gels. Figure Chapter 2-13 shows a photo of an SDS/PAGE gel of WT, D12H, K15H and K19H FPLC purified b_{562} proteins.

D Protein Labelling

Labelled protein eluted from the MonoQ FPLC column at 10% B and was resolved from unlabelled protein. This holoprotein was then further purified on a HiTrap column and eluted at 5% buffer B. Labelling reaction yields of the $Ru(bpy)_2.H_2O$ (monoaqua) were 30-90% efficient depending on the length of the reaction and mutant with 36 hours being optimal. Purification of labelling reactions by FPLC using MonoQ and HiTrap columns produced samples homogenous for labelled b_{562} as determined by SDS gel electrophoresis. The labelled samples ran slightly above unlabelled samples on a 15% SDS/PAGE gels (see Figure Chapter 2-13). Addition of 400 mM imidazole pH 8.0 to $Ru(bpy)_2.H_2O$ labelled protein for 48 hours resulted in formation of the $Ru(bpy)_2$(im)labelled protein as shown by fluorescence spectra and electron transfer rates. The labelling reaction was assumed to be greater than 80% efficient since electron transfer rates for the monoaqu and imidazole species are different and electron transfer rates for the imidazole species were found to be mostly monoexponential with occasionally a second exponential component at the monoaqua rate present at approximately <20%. Anion exchange FPLC sometimes revealed a peak shoulder that eluted after the imidazole complex. Electron transfer experiments showed that the smaller peak was the monoaqua species. Additionally, for proteins labelled with these complexes where the aqua and imidazole species was resolved by FPLC/UV, the yield was found to be greater than 80%. In all cases addition of imidazole resulted in most of the heme being extracted from the protein and so after removal of the imidazole and precipitated heme by dialysis, fresh hematin was added drop-wise with stirring to reconstitute the protein. Addition of hematin as a single volume often resulted in the formation of a green protein possibly due to the alkaline pH of the hematin solution. Purification of the reconstituted protein by FPLC revealed a small fraction of apo protein. Yields of the imidizolation step were similar for all mutants and approximately 70%.

E Characterization of Expressed Protein

(1) UV Spectroscopy

The UV/vis spectra of the ferric mutants D12H, K15H and K19H are shown in Figure Chapter 2-10, Figure Chapter 2-11 and Figure Chapter 2-12 respectively. The spectra of both the ferrous and ferric proteins were identical to that of published spectrum of WT b_{562} and that of WT b_{562} expressed in this laboratory. Labelling of the WT and mutants with $Ru(bpy)_2(im)$did not perturb the UV/vis WT spectra with the difference spectra appearing identical to those of unlabelled protein (not shown). The 720 nm absorption assigned to a Met to Fe charge transfer band was very weak (molar absorbance 235[18]) and not resolved in all samples of protein. It was, however, observed for all mutants in some samples. From these results we can infer that the electronic environment surrounding the heme is not perturbed by mutation of the His63Glu and ruthenium labelling site mutations or by labelling with of $Ru(bpy)_2im$.

(2) Gel Electrophoresis / Mass spectroscopy

Figure Chapter 2-13 shows a pictures of an SDS-PAGE gels of ruthenium labelled and unlabelled D12H, K15H and K19H proteins, and also the WT b_{562}. Protein was loaded onto the gels in amounts close to being overloaded (approximately 15 μg), and it can be seen that labelled samples are essentially homogenous, with any contaminants present at minute concentrations. The proteins band in the gel at the same position as WT b_{562} which runs at a molecular weight of 12-13 kD, the reported weight for apo b_{562}. In addition, a sample of purified K15H mutant was submitted for mass spectral analysis. Figure Chapter 2-9 shows that the sample is pure and has a mass of 11,778.7 (calculated mass of apo K15H is 11,781.2 - a sample with internal standards gave a weight of 11,779.9).

(3) Electrochemistry

Analysis of the K19H and K19H Ru(bpy)$_2$(im) yielded potentials (vs. NHE) of 137 mV and 152 mV receptively, similar to the WT b_{562} and WT Ru(bpy)$_2$(im) values of 165 mV and 143 mV respectively. The published value for the oxidation-reduction midpoint potential of WT b_{562} is "approximately" 180 mV at pH 7.0 [7, 19]. Whilst slightly reduced from the published value, the results here for the wild type and mutants were all within experimental error of one another, apart from the D73H mutant (see chapter 3), and so are considered to be accurate. The difference in values to the published value may reflect a slight pH difference, slight differences in experimental technique or subtle changes induced by the mutations.

(4) Tryptic digestion / Peptide Sequencing

The tryptic digestion reaction of the labelled K19H was FPLC purified and a fraction showing an absorption for ruthenium at 292 nm was submitted for N-terminal amino acid sequencing. The results of sequencing are shown in Figure Chapter 2-14. The sequence determined is that of residues 16 to 27 inclusive and contains the K19H mutation. The characteristic decrease in the intensity of the sequencing at the histidine residue is indicative of a ruthenium modified residue. This result showed that the K19H mutant was only modified at the site of the histidine mutation.

(5) Unfolding

Results from thermal unfolding experiments are shown in Figure Chapter 2-15. It can be seen that the ferrous protein is more stable than the ferric protein. T_m values for wild-type ferric and ferrous protein are 69°C and 87°C respectively, and are similar to published results of 67°C and 81°C[8]. T_m values for the ferrous and ferric labelled K15H mutant are 65°C and 84°C respectively and for the labelled K19H mutant are 66°C and 83°C.

respectively. In all cases the unfolded spectra of the proteins resembled the spectra of free heme. It can be concluded that the introduction of the mutations and labelling with ruthenium does not perturb the environment surrounding the heme.

F Rate Measurements

Rates for the D12H, K15H and K19H mutants were determined by both the photo induced and flash quenched methods. The observed rates were for the D12H mutant (2.2±0.4) x 10^7 s^{-1}, for the K15H mutant (1.6±0.1)x10^6 s^{-1} and for the K19H mutant (5.8±0.3)x10^4 s^{-1} as shown in Table Chapter 2-3. Uncertainties are expressed as standard errors of the mean. k_{max} values were determined by the following equation:

$$k_{obs} = k_{max} \exp\left[\frac{-(\Delta G^\circ + \lambda)^2}{(4\lambda K_b T)}\right]$$

which gave values of (2.6±0.4) x 10^7 s^{-1}, (1.9±0.1)x10^6 s^{-1} and (6.7±0.3)x10^4 s^{-1} for the D12H, K15H and K19H mutants respectively.

Figure Chapter 2-16 - Figure Chapter 2-23 show examples of some typical transients from such experiments at observation wavelengths of 430 nm (Fe^{2+} absorption), 414 nm (Fe^{3+} absorption), 315 nm (Ru(III) and *RuII absorption) and 670 nm (*RuII emission). A transient difference spectrum from a flash-quench experiment using wild-type protein was recorded and shown in Figure Chapter 3-13 lower. It shows the decrease in Fe(II) heme at 430 nm and the increase of methyl viologen quencher radical at 400 nm. The increase in Fe(III) is the shoulder at approximately 414 nm. A transient decay spectrum of the apo E86H mutant (Figure Chapter 3-13 upper) shows none of the absorbencies associated with the holo proteins.

Included in the back rate for the D12H mutant was a slower rate that was assigned to the monoaqua species. For this mutant the imidazole and monoaquo species co-purified and could not be resolved. Doping of a sample with monoaqua species to increase its relative concentration also increased the relative intensity of the signal corresponding to the slower decay rate in photo-induced experiments. Transients in which the slower component represented only 10% of the total signal were recorded (but are not shown in this report due to loss of the stored data - hard copies of this data are available and were included in the analysis). D12H transients recorded at 432 nm showed only a slight decrease in signal intensity despite this being an isosbestic point for the $*Ru(bpy)_2.im/Ru(bpy)_2im^{2+}$ couple. The D12H mutant had the fastest rate of all the mutants studied with a rate of $(2.2 \pm 0.3) \times 10^7$ s^{-1}. This is also the rate of excited state emissions, but since transients were seen at both 430 and 414 nm, it confirms that this is the ET rate and not excited state emissions.

Interestingly, the emissions decay rate for K15H, 1.2×10^7 s^{-1}, is slower than that of the model compound $Ru(bpy)_2(im)_2$ excited state emission decay rate (1.4×10^7 s^{-1}). This would seem to indicate that there was little quenching by the protein but direct photo-induced ET was observed with a rate of 1.6×10^6 s^{-1}. The flash quench method gave the same rate. It may be that this particular mutant is partially shielded by the protein from the effects of solvent collizional quenching or that a small population of apo and/or reduced protein is contributing to the emissions decay. Such components would give a slower emissions decay rate. The ET rate for the K19H mutant was found to 5.8×10^4 s^{-1}. This is the same rate observed for the monoaqua species. However, the intensity of absorption of this species at 430 nm were 50% reduced relative to the imidazole species and the rate of excited state emissions decay increased over four-fold. Observation of the 430 absorption intensity and a monoexponential decay rate for the excited state emission suggested that the monoaquo species, if present in the sampl,e was at a low concentration.

In all cases the relative intensity changes at the various observation wavelengths were in accord with absorbance coefficients. Control experiment to observe the transient signals of solvent, quencher and apo-protein were carried out to rule out these species as a source of spurious signals. The effect of protein concentration on the rate of ET was measured in a number of mutants. An example using the K19H mutant is shown in Figure Chapter 2-25. It can be seen that there is no dependence on the ET rate at the concentrations used in these experiments.

Discussion

The reorganization energy for b_{562} was estimated to be similar to that of horse heart cytochrome *c*, another electron transfer metalloprotein of 104 residues with the same axial ligands. The electron-self exchange rate for b_{562} calculated by Moore from NMR analysis is $4 \times 10^6\ M^{-1}\ s^{-1}$ at 42°C and pH 7.0[7]. From this relatively fast rate Moore concluded that the reorganization energy for b_{562} is small which is in accord with the idea of Gray and Malmstrom that the reorganization energy for electron transfer proteins is minimal[20]. The reorganization energy for the Ru^{3+}/Ru^{2+} couple is not expected to differ significantly between similar electron transfer proteins since outer-sphere reorganization dominates the overall reorganization energy. Even in the blue copper protein azurin, the reorganization energy is approximately 0.8 eV[21], similar to that of cytochrome *c*. It would, seem, therefore that this estimate for the reorganization energy for b_{562} is reasonable. Comparing the value to the driving force of $\Delta G^\circ = -0.86$ eV, the reaction is in the Marcus 'inverted region' of the rate vs. $-\Delta G^\circ$ plot.

The plot of ruthenium histidine ligand to porphyrin iron ligand tunnelling distance (σl) versus the metal-metal distance (R_m) is shown in Figure Chapter 2-26. The linear relationship between R_m and σl indicates that the electron transfer rate will have an exponential dependence on R_m and the slope of this graph (1.76) predicts a distance decay of 1.29 $Å^{-1}$. The $\sigma l/R_\beta$ ratio for an ideal α-helix which includes hydrogen bond interactions is 1.72 and predicts a similar distance decay rate of 1.26 $Å^{-1}$ ($R\beta$ is the β-carbon separation). Figure Chapter 2-28 shows a plot of $R_m - R_0$ vs. log k_{max} (upper) and also σl vs.

k_{max}; R_0 = 3Å, the close contact distance. It is surprizing that both graphs are able to fit the data so well since theory predicts that ET in an α-helix will be better described by the pathways analysis due to the tortuous geometry of the α-helix backbone. No improvement is obtained by consideration of edge-edge distances, defined as ruthenium ligand bond to heme edge, and couplings as shown by Figure Chapter 2-29. In these plots the data is scattered with no obvious correlation. It can be assumed that in cytochromes there is mixing of the donor and acceptor orbitals onto the ligand orbitals with the π* orbitals of the porphyrin ring extending the influence of the Fe d-electrons to the whole of the heme surface and thus the reaction approaches the adiabatic limit at the edge of the heme. Analysis of the self-exchange reactions of $Ru(NH3)_6^{3+/2+}$ and $Fe(OH_2)_6^{3+/2+}$, however, indicate nonadiabatic rates due to minimal delocalisation of donor and acceptor orbitals onto ligands[22]. Furthermore, Casimiro obtained slightly improved correlation between k_{max} and tunnelling length for some ruthenium modified cytochrome *c* [23]and human myoglobin[24] mutants when the sigma tunnelling pathway was extended to the metal atom redox centres. The distance decay β calculated from the metal-metal distance graph where the y-intercept is constrained to the close contact rate of 10^{13} s^{-1} is 1.13 $Å^{-1}$ and the $\sigma l/R_m$ value is 1.54. The sigma bond decay rate is 0.69. These values do not agree with the theoretical predictions of 1.26 $Å^{-1}$ for the distance decay and 0.6 for the bond decay and deviate in opposite directions; the distance decay is decreased but the through bond decay is increased. The theoretical predictions are based on an ideal α-helical structure and so the discrepancy in the distance decay can be considered to be due in part to deviations from the ideal structure, inaccuracies in H-bonds decay rates and also to the pathway involving the non-helical porphyrin bonds and predicted non-helical pathways. Decay factors measured for synthetic donor-acceptor systems, as mentioned in chapter 1, have values between 0.85-0.95 $Å^{-1}$ and so it may seem surprizing that the predicted distance decay factor is not smaller than the theoretical value predicted from the ideal structure. However, the pathway of each of the

mutants involves a through space jump which will have the effect of increasing the distance decay rate and thereby reducing the effect of the improved coupling of the heme bonds. Factoring in the decreased decay rate for the heme bonds (0.9 $Å^{-1}$) yields a distance decay rate for the helix A mutants of 1.12 ±0.02 $Å^{-1}$ which compares well with the experimental value of 1.13 $Å^{-1}$. The sigma bond decay rate increase may be due to the different geometry of the bonds found in the α-helical structure and which impose a coupling that is different to that found in the synthetic ET systems. Using the experimental bond coupling (0.69/bond) and the experimental distance decay (1.13 $Å^{-1}$) and also taking the increased heme coupling into account, a σl/Rβ of 2.33 ±0.03 is calculated. This value is between that of 1.72 where H-bonds are considered as a path for ET and the value of 2.7 where H-bonds interactions are ignored. The strength of the H-bond interactions will ultimately decide this value. That it deviates from the expected value that yields the σl/Rβ value of 1.72 may be explained by the infrared analysis of the amide bonds in α-helices and β-sheets which indicates that in α-helices the H-bonds are weaker[25, 26].

The pathways for the helix A mutants are shown in Figure Chapter 2-5 to Figure Chapter 2-7. The Pathway program predicts that only the D12H mutant will have an ET pathway through the Met 7 axial ligand, which is preceded by a through-space jump of 1.57 Å from a Leu 10 Cδ1-H orbital. Both the K15H and K19H pathways are predicted to pass through a Leu 14 Cδ2-H orbital and enter the heme via a through-space jump of 1.84 Å to the heme CMβ-H bond. Only one H-bond is utilized in the pathways for these mutants. The K19H pathway involves an H-bond from Glu 18 N to Leu 14 O. The D12H mutant does not utilize the Asn 11 to Met 7 H-bond despite the pathway passing through the Asn 11 nitrogen. The D12H pathway also ignores the Leu 10 to Asn 6 H-bond by diverting from the Leu 10 Cα to the Leu 10 Cβ. The K19H mutant ET pathway also fails to utilize a His 19 to Lys 15 H-bond and also a Leu 14 to Leu 10 H-bond. In all cases the pathways appear

to follow the most direct route to the heme and only utilize H-bond interactions if actually on this route.

The best pathways generated for these mutants follow the most direct line to the heme. For the K15H and K19H mutants, entry to the heme via the Met 7 axial ligand would involve a pathway along the α-helical backbone which is adjacent to the plane of the heme. The data suggests that for these mutants at least the influence of the structure of the α-helix is not as considerable as the theory predicts, possibly because the heme provides a large and high coupling media for tunnelling. The tunnelling length to distance correlation predicts a distance decay of 1.26 $Å^{-1}$, but the experimental value is 1.13 $Å^{-1}$ indicating that the pathways are shorter than those predicted. A number of explanations can account for which include multiple pathways, a reduced sigma bond decay rate for α-helical structures and the large influence of the relatively large size of the heme group for facilitating direct pathways. These and the issue of ET to the heme edge or heme iron will be discussed in chapter 4 together with data from other mutants of b_{562}.

Bibliography

1. Hamada, K., Bethge, P.H. & Mathews, F.S. *J. Mol. Biol.* **247**, 947-962 (1995).

2. Wu, J., Gerd, N. & al, e. *Biochemistry* **30**, 2156-2165 (1991).

3. Mathews, F., Bethge, P. & Czerwinski, E. *J. Biol. Chem.* **254**, 1699-1706 (1979).

4. Fujita, T. & Sato, R. *Biochem. Biophys. Acta.* **77**, 690-693 (1963).

5. Itagaki, E. & Hager, L. *J Biol. Chem.* **241**, 3687-3695 (1966).

6. Nikkila, H., Gennis, R. & Sligar, S. *Eur. J. Biochem.* **202**, 309-313 (1991).

7. Moore, G., Williams, R., Perterson, J., Thompson, A. & Mathews, R. *Biochem. Biophys. Acta* **829**, 83-96 (1985).

8. Fisher, M. *Biochemistry* **30**, 10012-10018 (1991).

9. Ledere, F., Glatigny, A., Bethge, P.H., Bellamy, H.D. & Mathews, F.S. *J. Mol. Biol.* **148**, 427-448 (1981).

10. Louie, G.V. & Brayer, G.D. *J. Mol. Biol.* **214**, 527-555 (1990).

11. Takano, T. & Dickerson, R.E. *J. Mol. Biol.* **153**, 79-94 (1981).

12. Ochi, H., *et al. J. Mol. Biol.* **166**, 407-418 (1983).

13. Weber, P.C. & al, e. *Nature* **286**, 302-304 (1980).

14. Bullock, P.A. & Myer, Y.P. *Biochemistry* **17**, 3084-3091 (1978).

15. Spiro, T.G. & Strekas, T.C. *J. Am. Chem. Soc.* **96**, 338-345 (1974).

16. Spiro, T.G. & Loehr, T.M. in *Advance in Infrared and Raman Spectroscopy* (eds. Clark, R.J.H. & Hester, R.E.) 98-142 (Hayden, London, 1975).

17. Chang, I.J., Gray, H.B. & Winkler, J.R. *J. Am. Chem. Soc.* **113**, 7056-7057 (1991).

18. Myer, Y.P. & Bullock, P.A. *Biochemistry* **17**, 3723-3729 (1978).

19. Barker, P.D. & et al. *Inorganica Chimica Acta* **252**, 71-77 (1996).

20. Gray, H.B. & Malmstrom, B.G. *Biochemistry* **28**, 7499-7505 (1989).

21. Langen, R., *et al. Science* **268**, 1733-1735 (1995).

22. Newton, M.D. *J. Phys. Chem.* **92**, 3049 (1988).

23. Casimiro, D.R. in *Divizion of Chemistry and Chemical Engineering* (California Institute of Technology, Pasadena, 1994).

24. Casimiro, D.R. & al, e. *J. Am. Chem. Soc.* **115**, 1485-1489 (1993).

25. Susi, H. *Meth. Enzymol.* **26**, 455-472 (1972).

26. Schellman, J.A. & Schellman, C. in *The Proteins* (ed. Neurath, H.) 1 (Academic Press, New York, 1962).

Figure Chapter 2-1: The backbone structure and amino acid sequence of cytochrome b_{562}.

The amino acid sequence of cytochrome b_{562} and the N-terminal signal sequence (residues -1 to -22). The four alpha helices are underlined.

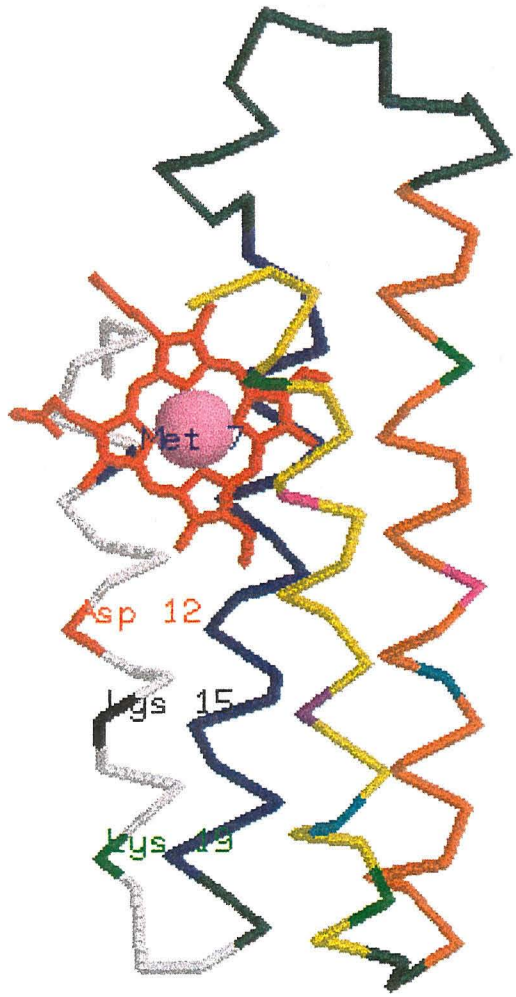

-1 -10 -22
met arg lys ser leu leu ala ile leu ala val ser ser leu val phe ser ser ala ser phe ala

1 10 20
ala asp leu glu asp asn met glu thr leu asn asp asn leu lys val ile glu lys ala asp asn

30 40
ala ala gln val lys asp ala leu thr lys met arg ala ala ala leu asp ala gln lys ala thr pro

50 60
pro lys leu glu asp lys ser pro asp ser pro glu met lys asp phe arg his gly phe asp ile

70 80 90
leu val gly gln ile asp asp ala leu lys leu ala asn glu gly lys val lys glu ala gln ala ala

91 100 106
ala glu gln leu lys thr thr arg asn ala tyr his gln lys tyr arg

Figure Chapter 2-2: UV/vis spectra of ferric and ferrous cytochrome b_{562}.

Ferric (upper) and ferrous (lower) protein at 6 μM in 100 mM potassium phosphate buffer.

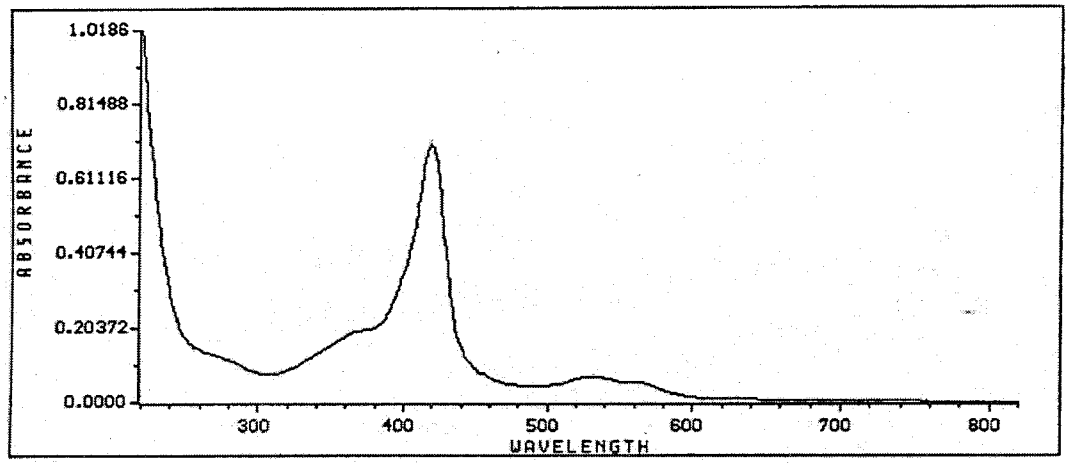
1.0186
0.81488
0.61116
0.40744
0.20372
0.0000
ABSORBANCE
300
400
500
600
700
800
WAVELENGTH

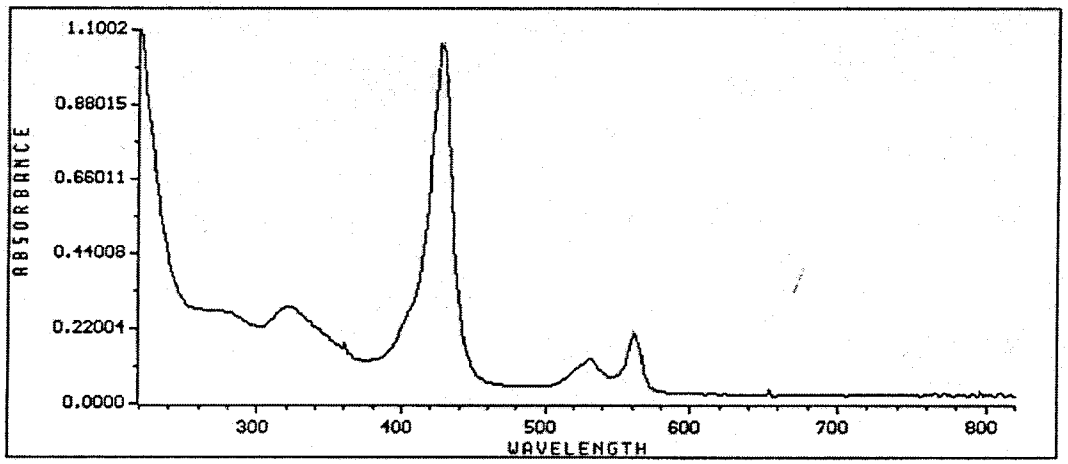
1.1002
0.88015
0.66011
0.44008
0.22004
0.0000
ABSORBANCE
300
400
500
600
700
800
WAVELENGTH

Figure Chapter 2-3: The backbone structures of cytochrome b_{562} and cytochrome *c*'.

Cytochrome b_{562}

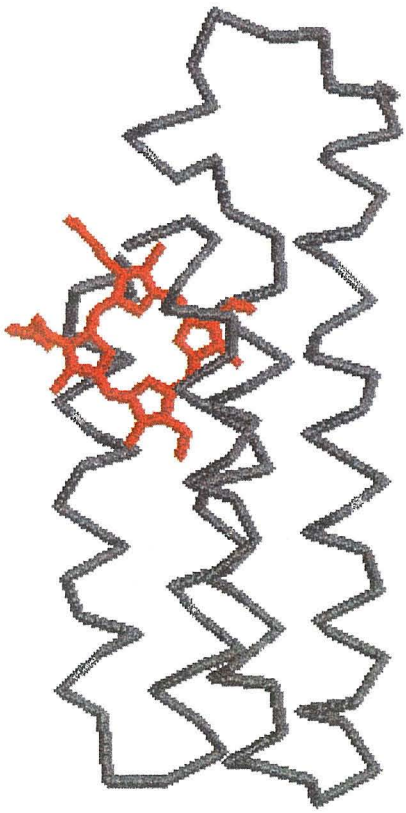

Cytochrome c'

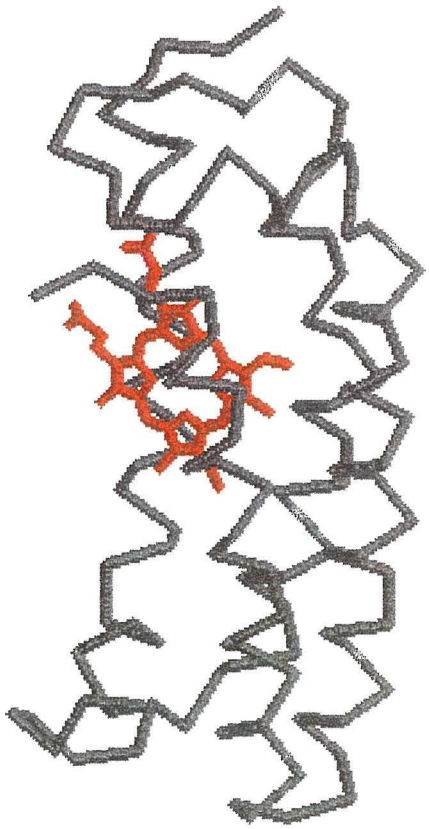

Figure Chapter 2-4: Schematic showing the flash-quench and photo induced laser techniques used for initiating electron transfer in b_{562}.

Flash quench technique

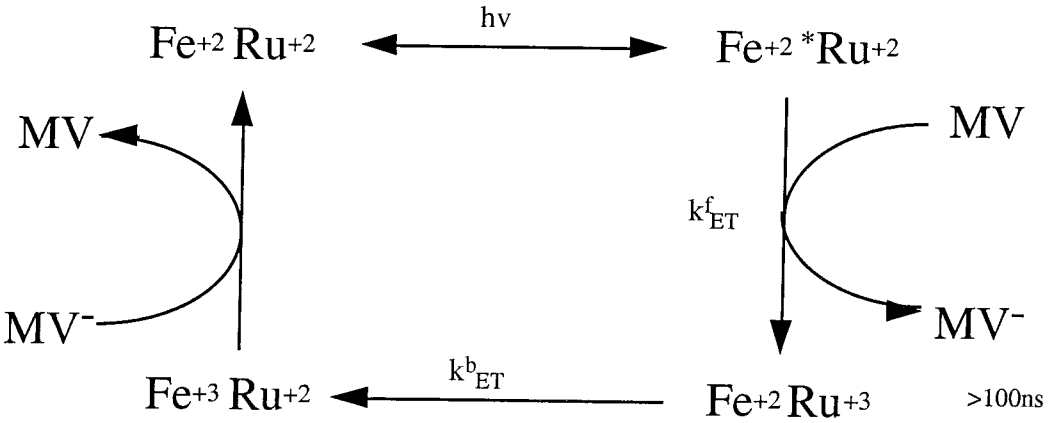

Photo induced technique

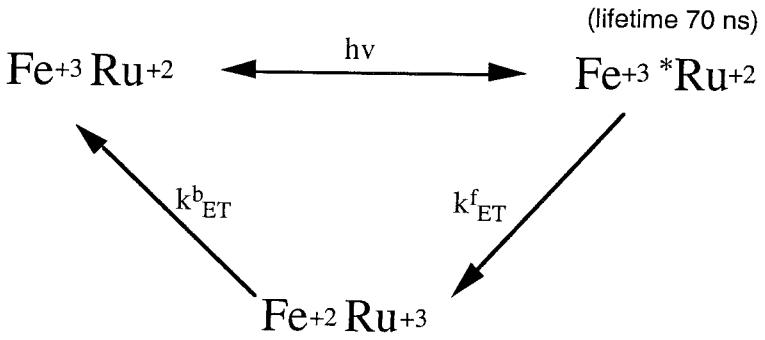

hv = excimer-dye laser pulse of 20 ns at 480nm, 1.6 m joules

MV = methyl viologen

Figure Chapter 2-5: The ET pathway of the D12H mutant of b_{562} calculated from the Pathways program.

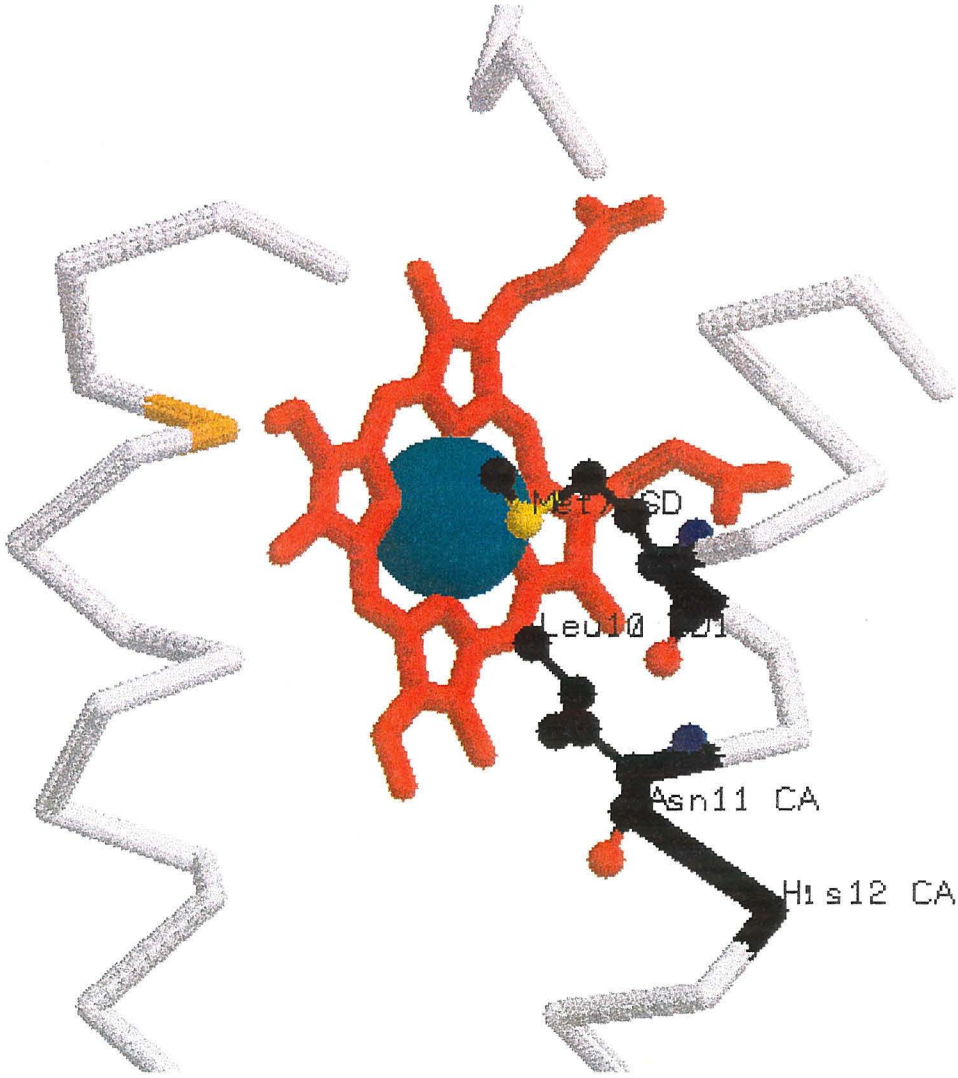
Asn11 CA
His12 CA

Figure Chapter 2-6: The ET pathway for the K15H mutant of b_{562} calculated from the Pathways program.

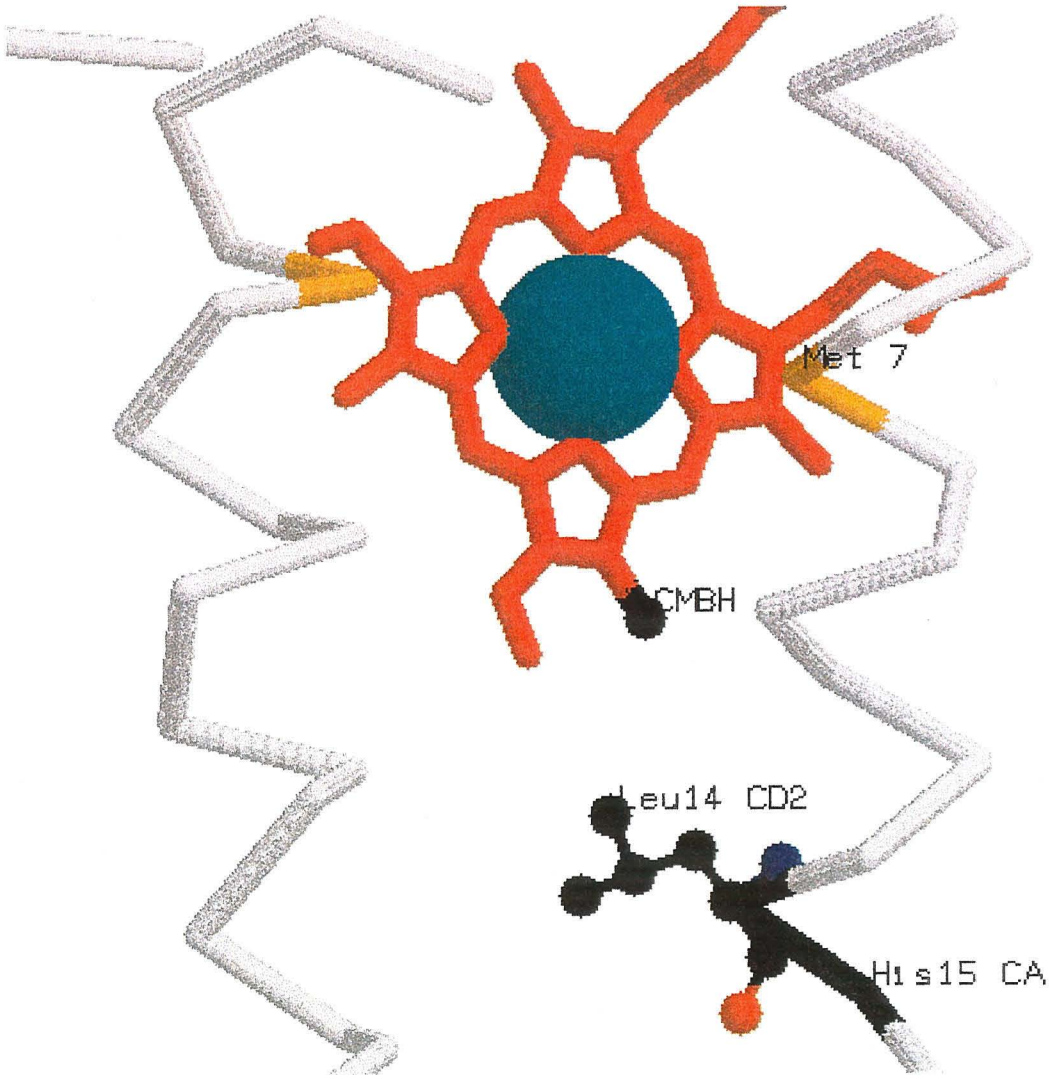
Met 7
CMBH
Leu14 CD2
His15 CA

Figure Chapter 2-7: The ET pathway for the K19H mutant of b_{562} calculated from the Pathways program.

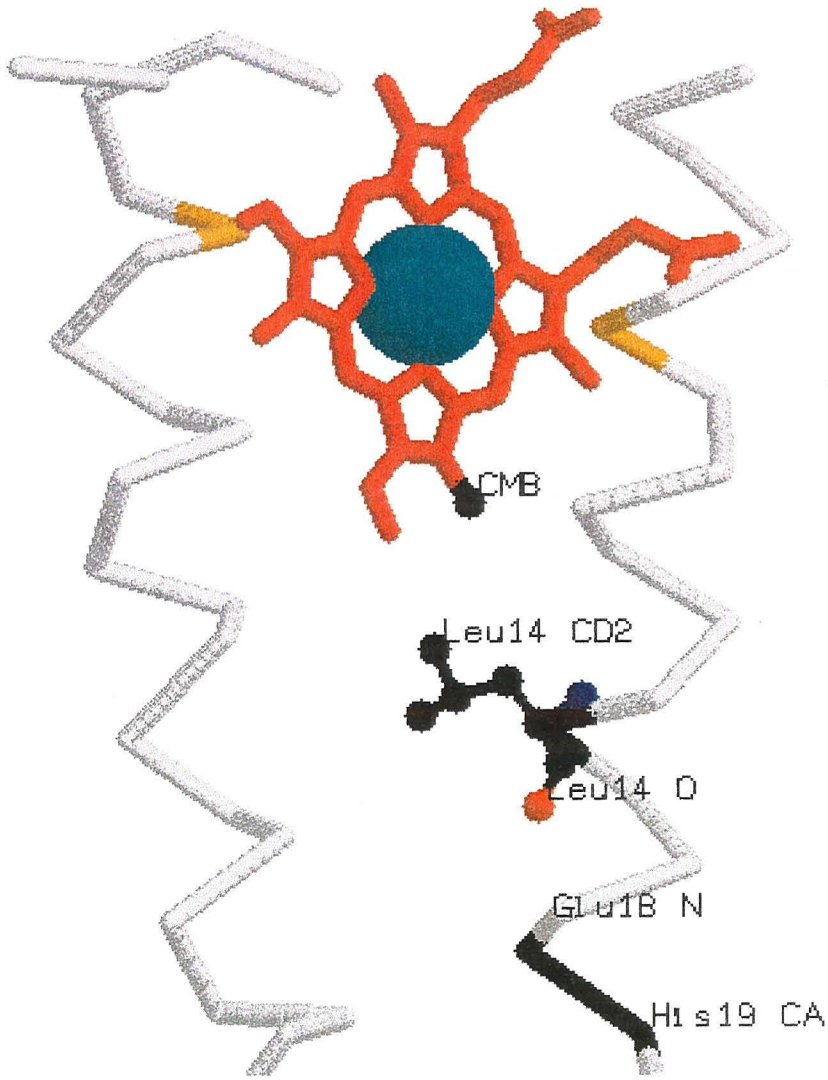
CMB
Leu14 CD2
Leu14 O
Glu1B N
His19 CA

Figure Chapter 2-8: Agarose gel showing PCR mutagenesis products.

Agarose gel showing products of PCR reactions 1 and 2 for mutants K19H, K15H and WT b_{562}. The size in base pairs of some of the molecular weight markers is shown.

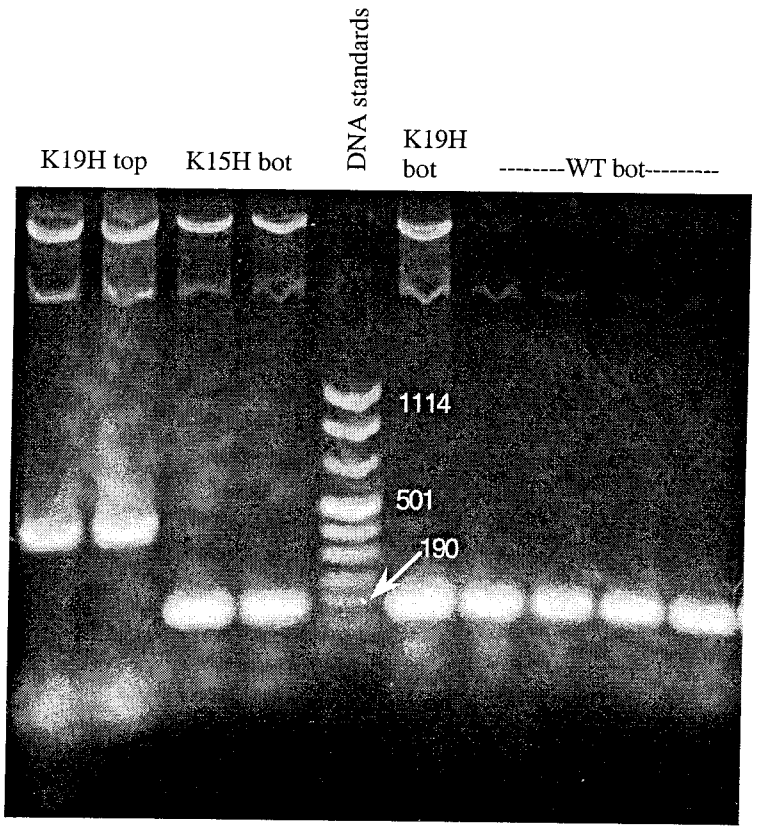
K19H top
K15H bot
DNA standards
K19H bot
--------WT bot---------
1114
501
190

Figure Chapter 2-9: MALDI mass spectrum of the purified K15H b_{562} mutant.

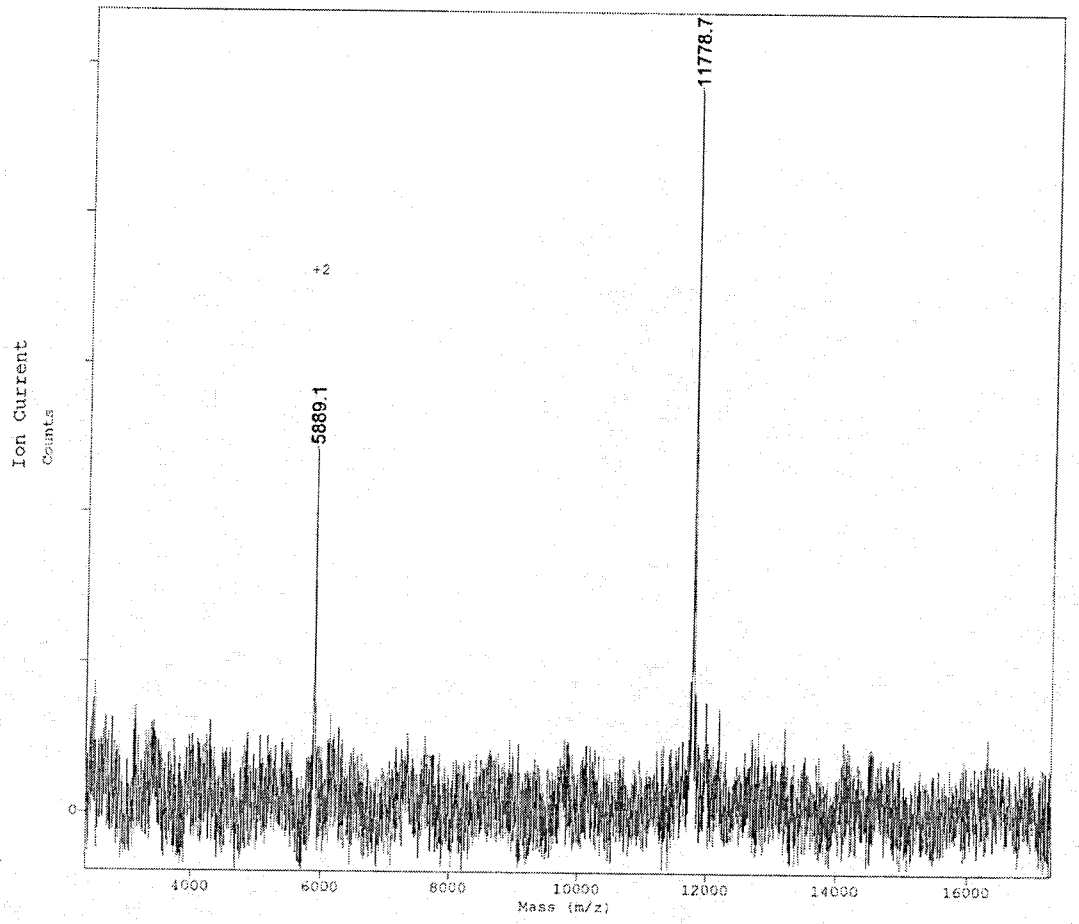

Comment: 15

Cal. Standards: Ac-angio Anf Cyt-C +Na+ +3 +2 lysozyme dimer [M+H]+1

Method: DEL12KD

Accel. Volts: 20000

Laser : 990

Mirror Ratio: 1.060

Mode: Linear

Grid Voltage: 89.400 %

Scans Averaged: 97

PSD Mirror Ratio:

Neg.Ions: OFF

Guide Wire Voltage: 0.100 %

Pressure: 2.68e-07

Low Mass Gate: 1000.0

Timed Ion Selector: 19.8

Figure Chapter 2-10: UV/vis absorption spectra of unlabelled and $Ru(bpy)_2(im)$ labelled D12H compared to WT b_{562}.

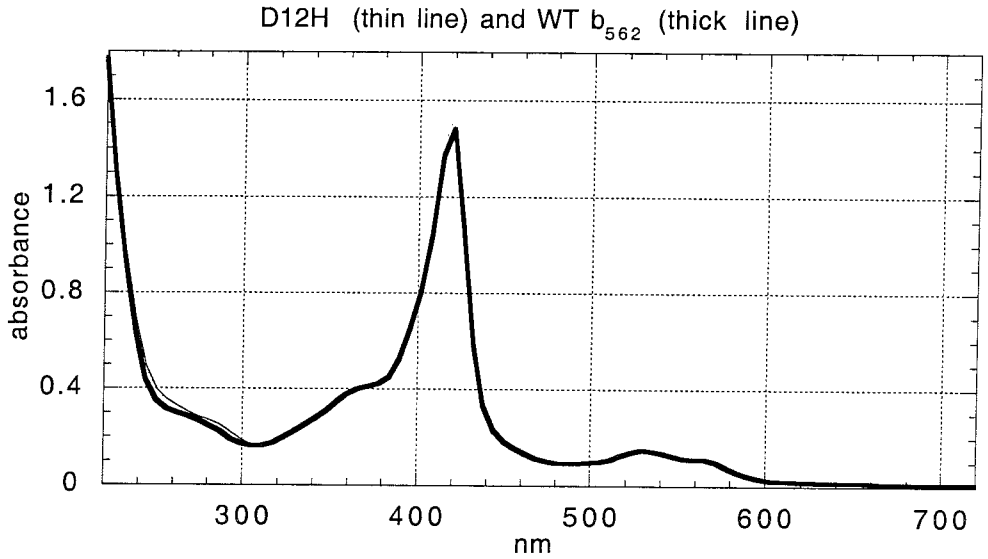
D12H (thin line) and WT b_{562} (thick line)
absorbance
1.6
1.2
0.8
0.4
0
300
400
500
600
700
nm

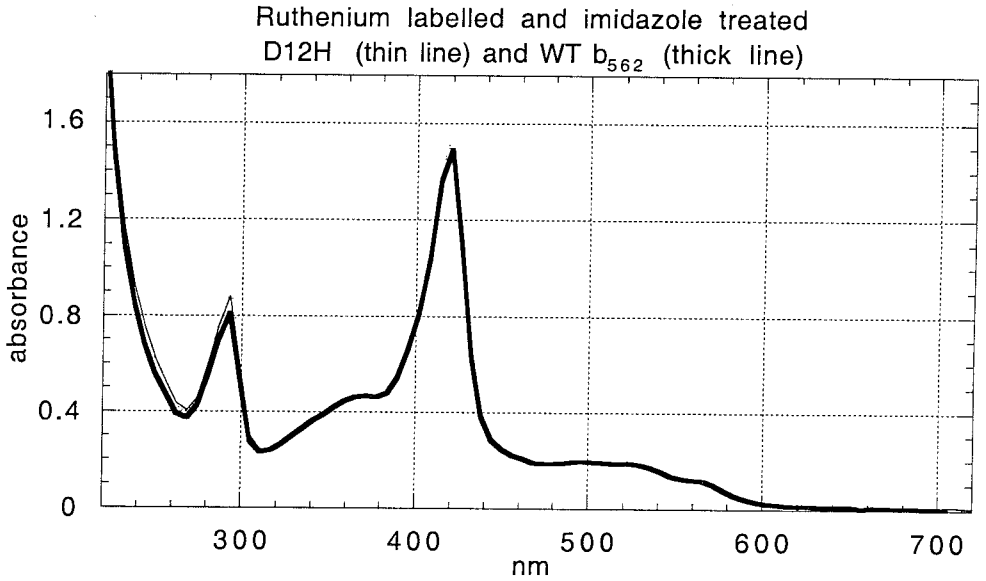
Ruthenium labelled and imidazole treated
D12H (thin line) and WT b_{562} (thick line)
absorbance
1.6
1.2
0.8
0.4
0
300
400
500
600
700
nm

Figure Chapter 2-11: UV/vis absorption spectra of $Ru(bpy)_2(im)$ labelled K15H compared to WT b_{562}.

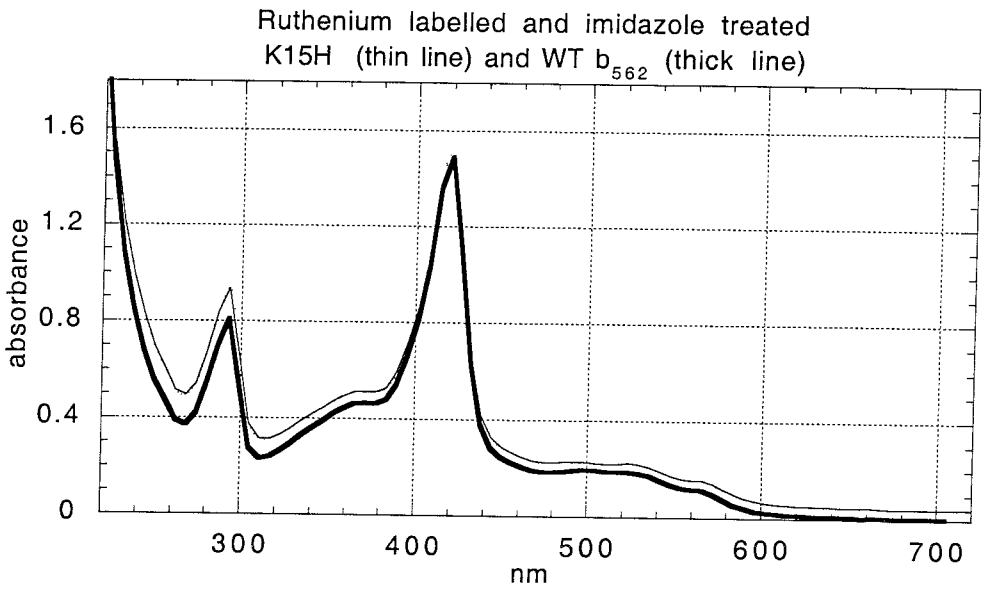
Ruthenium labelled and imidazole treated
K15H (thin line) and WT b562 (thick line)
absorbance
1.6
1.2
0.8
0.4
0
300
400
500
600
700
nm

Figure Chapter 2-12: UV/vis absorption spectra of unlabelled and $Ru(bpy)_2(im)$ labelled K19H compared to WT b_{562}.

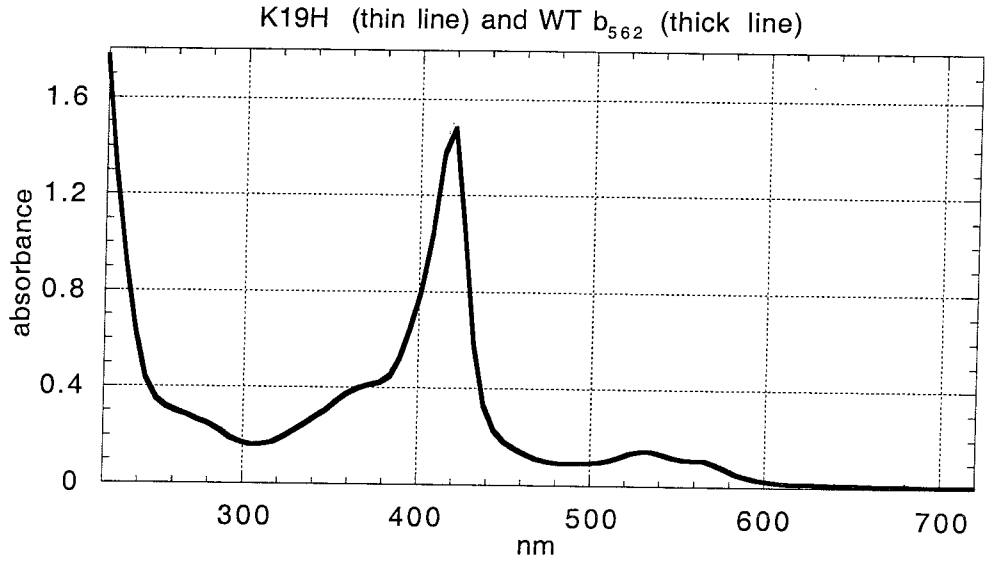
K19H (thin line) and WT b_{562} (thick line)
absorbance
1.6
1.2
0.8
0.4
0
300
400
500
600
700
nm

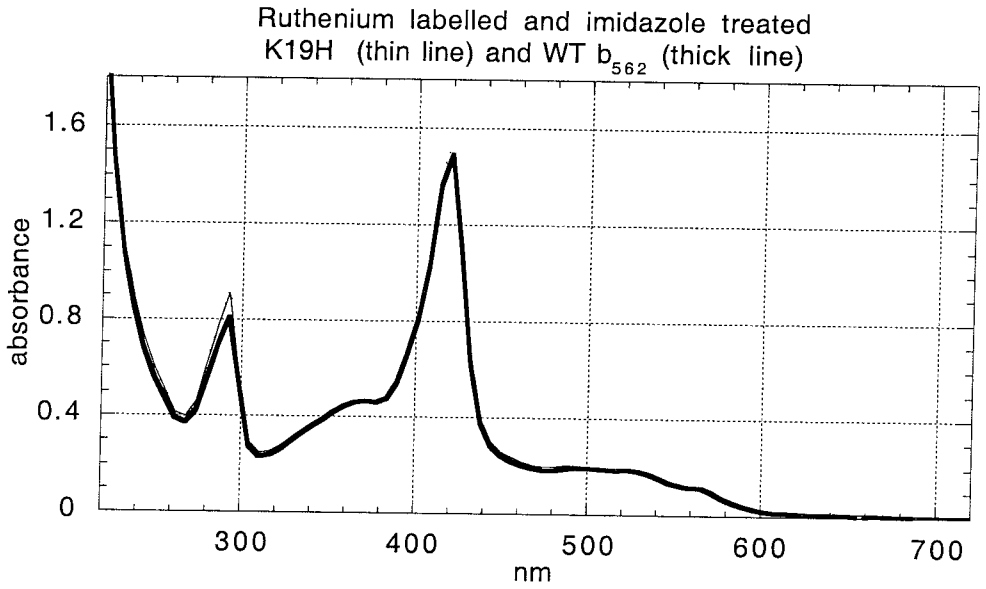
Ruthenium labelled and imidazole treated
K19H (thin line) and WT b_{562} (thick line)
absorbance
1.6
1.2
0.8
0.4
0
300
400
500
600
700
nm

Figure Chapter 2-13: SDS-PAGE protein gel of labelled/unlabelled b_{562} proteins.

Protein bands were visualized by Coomassie staining.

SDS-PAGE gel of unlabeled and labeled b_{562} proteins. The molecular weights (in kDa) of protein molecular weight standards are shown.

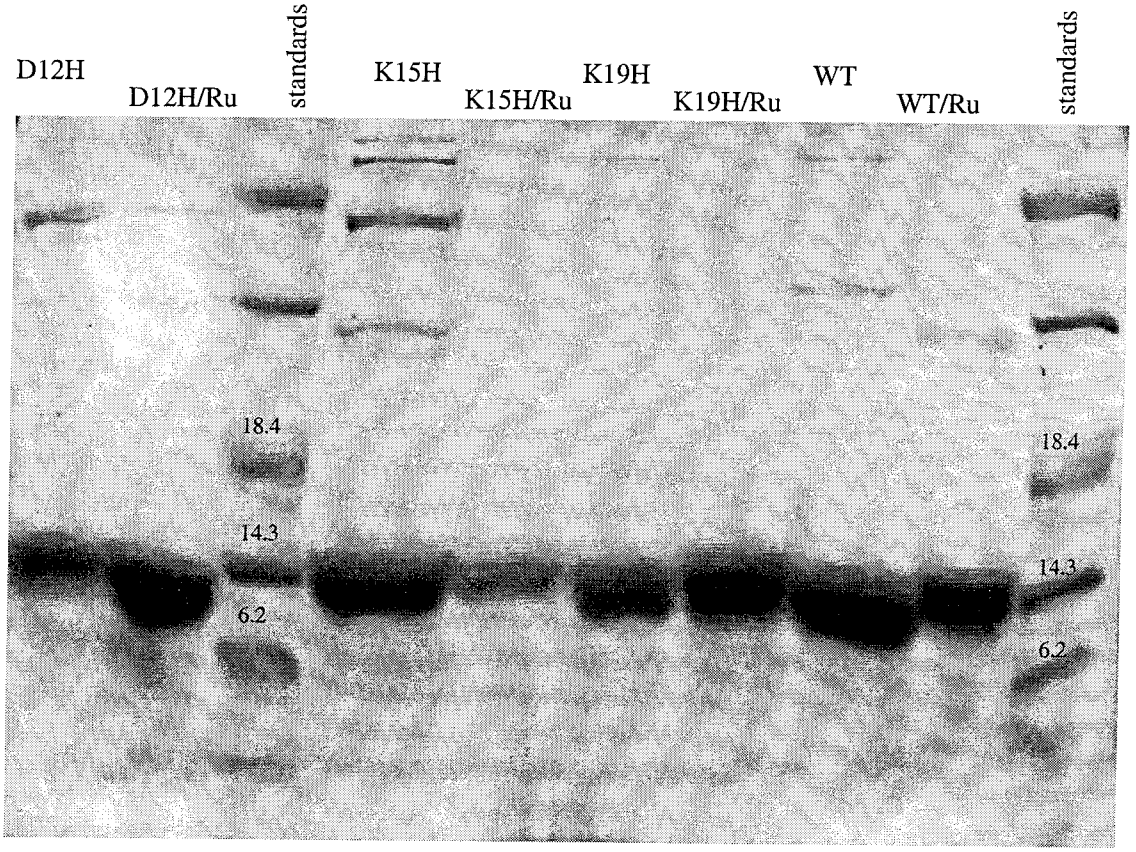

Figure Chapter 2-14: Peptide sequencing results from a ruthenium labelled fraction of the digestion of the ruthenium labelled K19H mutant.

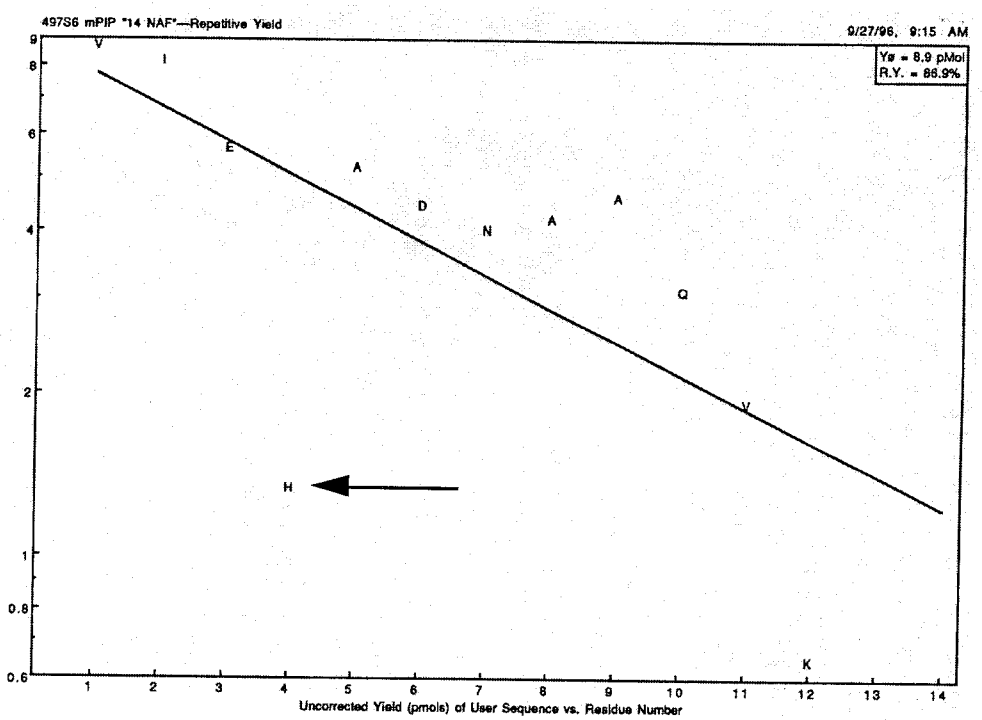
497S6 mPIP "14 NAF"—Repetitive Yield
9/27/96, 9:15 AM
Ys = 8.9 pMol
R.Y. = 88.9%
V
I
E
A
D
N
A
A
Q
V
H
K
9
8
6
4
2
1
0.8
0.6
1
2
3
4
5
6
7
8
9
10
11
12
13
14
Uncorrected Yield (pmols) of User Sequence vs. Residue Number

Figure Chapter 2-15: Thermal unfolding curves for ferric and ferrous WT b_{562} and labelled K15H and K19H mutants.

The unfolding of ferric (open symbols) and ferrous (filled symbols) wild-type (circles), $Ru(bpy)_2(im)$ labelled K15H (diamonds) and K19H (squares) was monitored using the absorbance of the Soret peak.

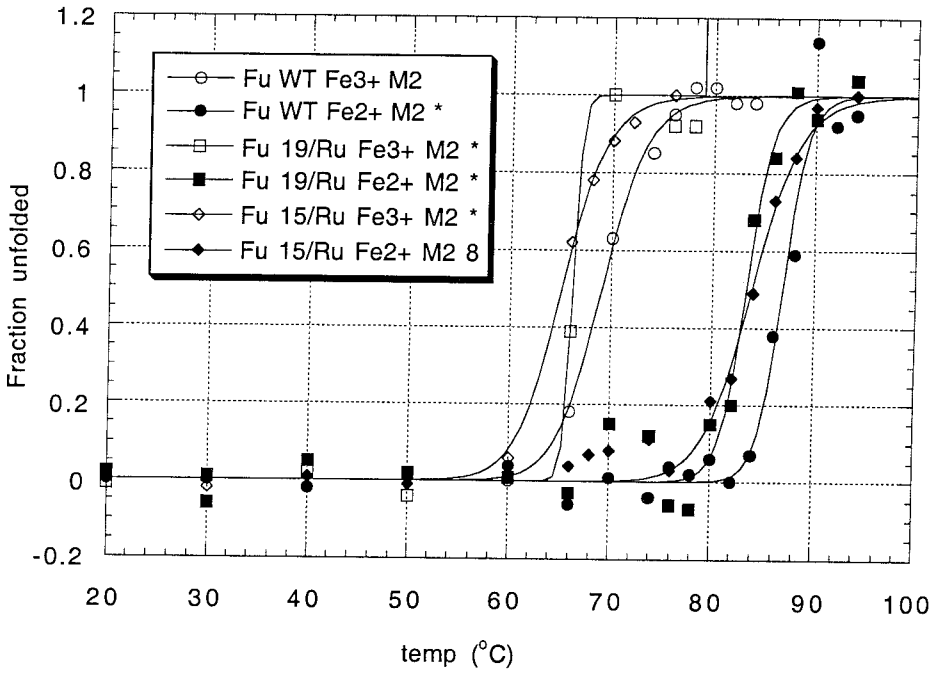
Fu WT Fe3+ M2
Fu WT Fe2+ M2 *
Fu 19/Ru Fe3+ M2 *
Fu 19/Ru Fe2+ M2 *
Fu 15/Ru Fe3+ M2 *
Fu 15/Ru Fe2+ M2 8
Fraction unfolded
1.2
1
0.8
0.6
0.4
0.2
0
-0.2
20
30
40
50
60
70
80
90
100
temp (°C)

Figure Chapter 2-16: D12H photo-induced transient absorbencies.

D12H (12μM) photo-induced transient absorbance monitored at (A) 430 nm and (B) 414 nm, showing the reduction of Fe^{3+} and the fit to the trace. The residual (signal minus fit) is shown above the traces.

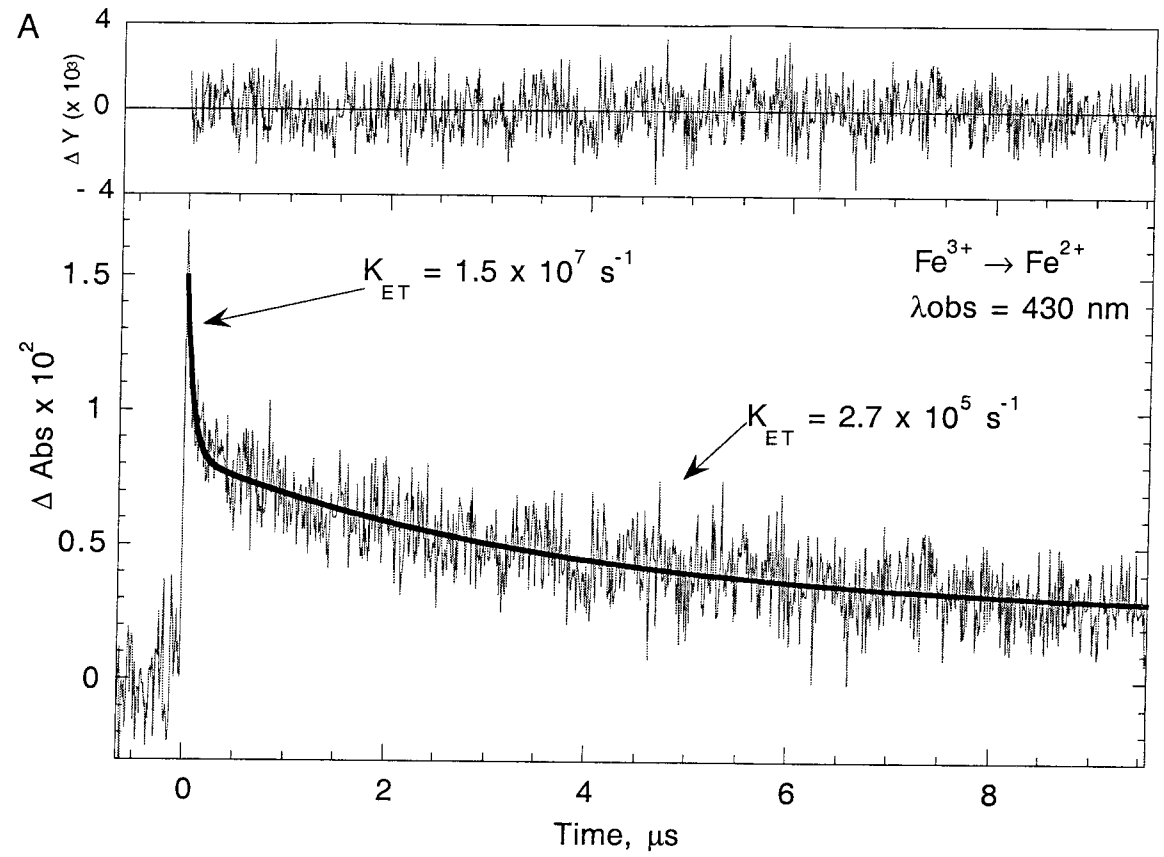
A
Δ Y (x 10⁸)
4
0
- 4
1.5
1
0.5
0
Δ Abs x 10²
K_ET = 1.5 x 10⁷ s⁻¹
Fe³⁺ → Fe²⁺
λobs = 430 nm
K_ET = 2.7 x 10⁵ s⁻¹
0
2
4
6
8
Time, μs

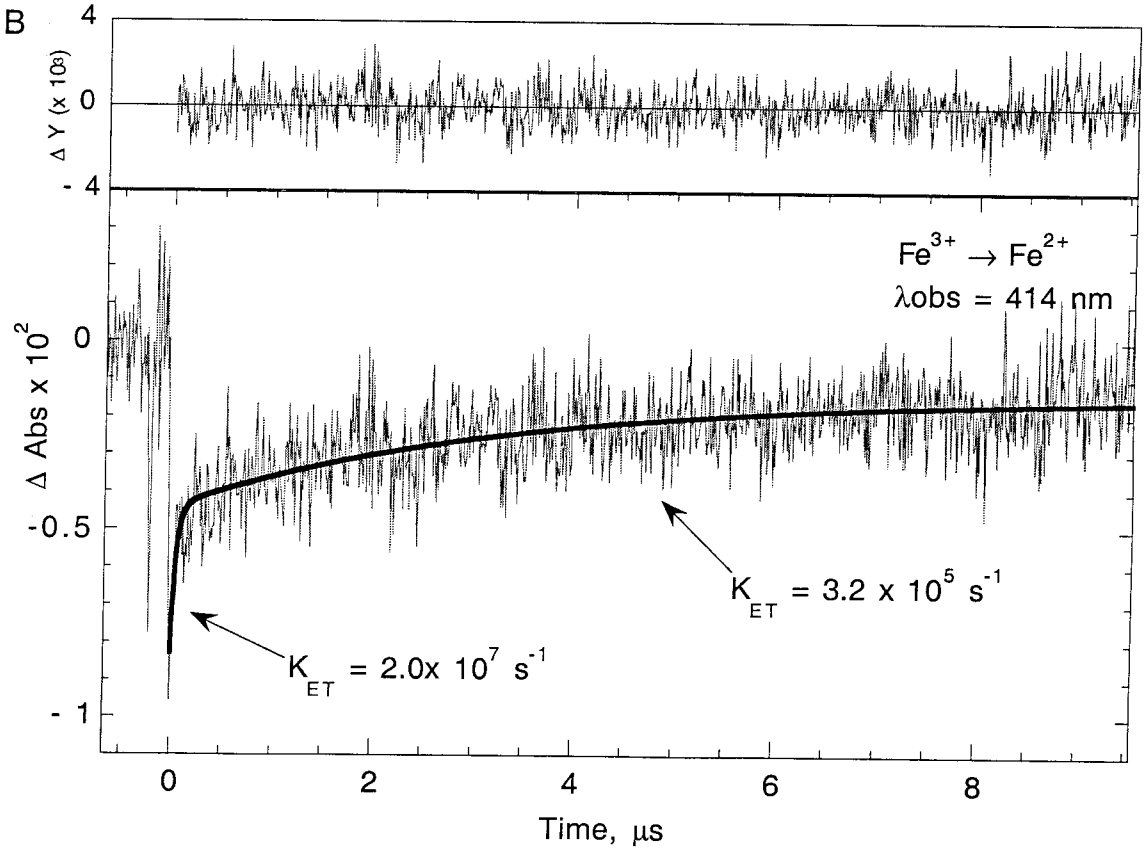
B
Δ Y (x 10⁸)
4
0
- 4
0
-0.5
- 1
Δ Abs x 10²
Fe³⁺ → Fe²⁺
λobs = 414 nm
K_ET = 3.2 x 10⁵ s⁻¹
K_ET = 2.0x 10⁷ s⁻¹
0
2
4
6
8
Time, μs

Figure Chapter 2-17: D12H flash-quench transient absorbencies.

D12H (12μM) flash-quench transient absorbencies monitored at (A) 430 nm and (B) 414 nm, showing the oxidation of Fe^{2+} and the fit to the trace. The residual (signal minus fit) is shown above the traces.

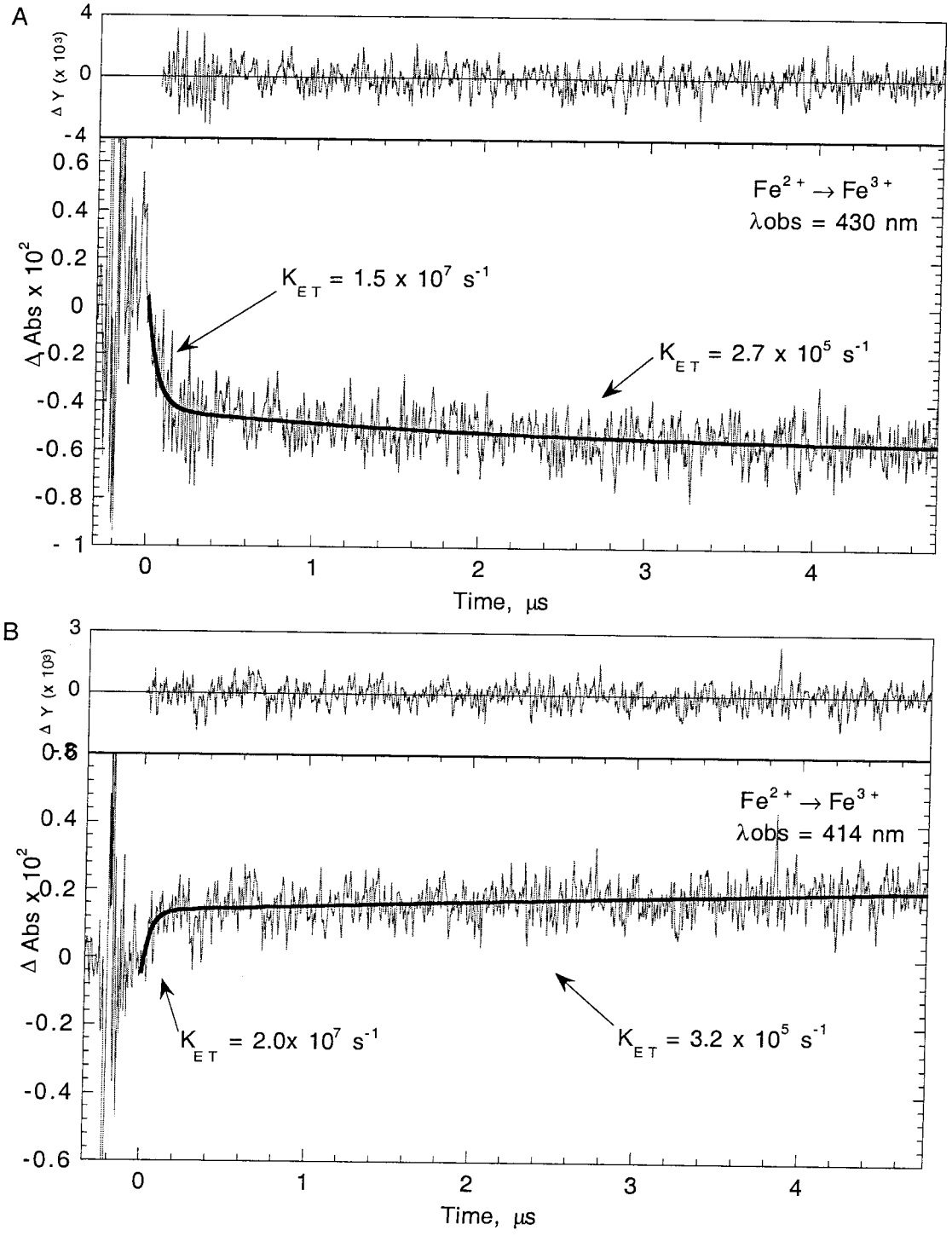
A
Δ Y (x 10³)
Δ Abs x 10²
Fe²⁺ → Fe³⁺
λobs = 430 nm
K_ET = 1.5 x 10⁷ s⁻¹
K_ET = 2.7 x 10⁵ s⁻¹
Time, μs
B
Δ Y (x 10³)
Δ Abs x 10²
Fe²⁺ → Fe³⁺
λobs = 414 nm
K_ET = 2.0x 10⁷ s⁻¹
K_ET = 3.2 x 10⁵ s⁻¹
Time, μs

Figure Chapter 2-18: 670 nm emissions and 315 nm absorption for D12H.

D12H (16μM) emissions monitored at (A) 670 nm and (B) flash-quenched transient absorbance monitored at 315 nm showing the reduction of Ru^{3+} and *Ru absorbance. The fit to the traces is shown and the residual (signal minus fit) is shown above the traces.

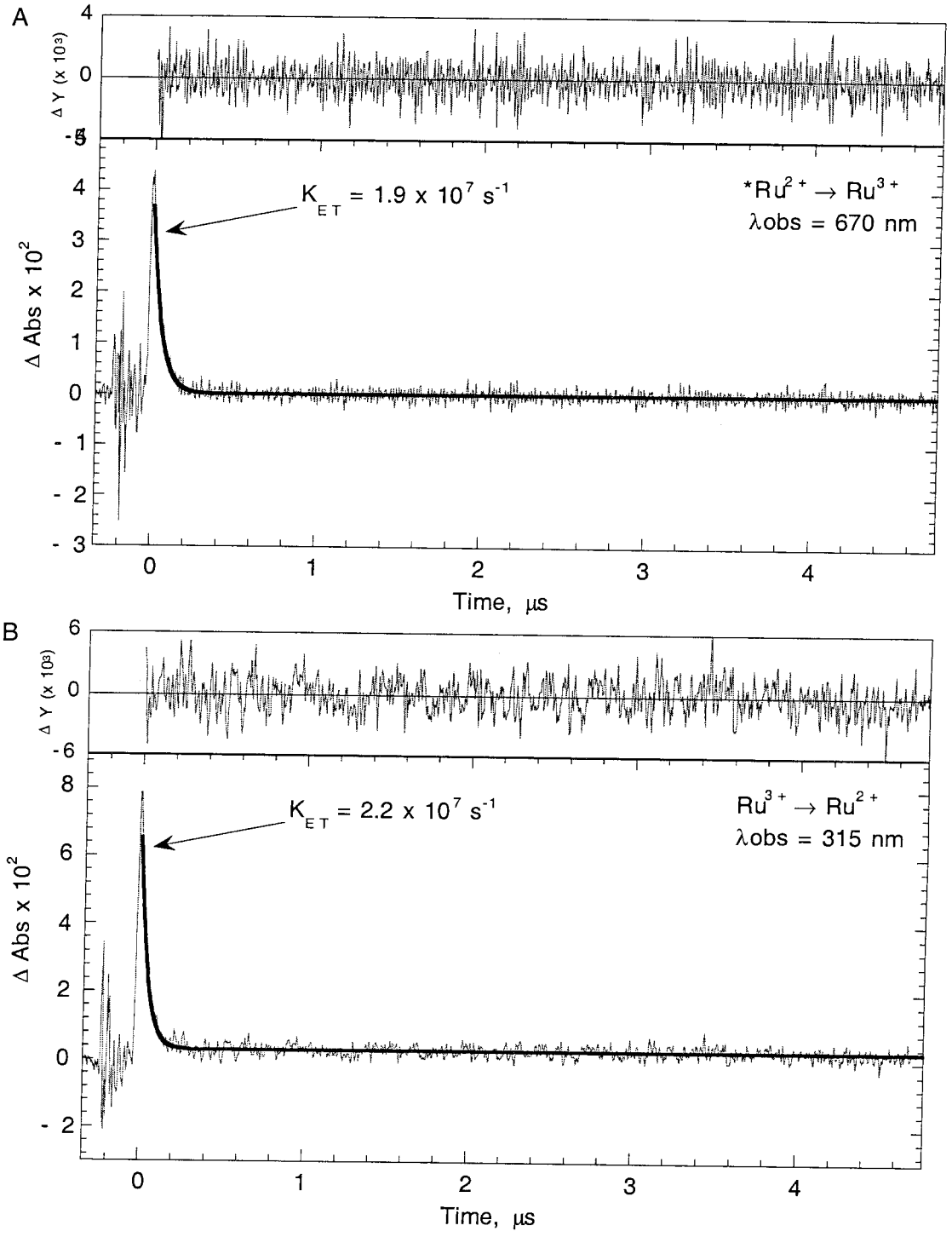
A
Δ Y (x 10³)
Δ Abs x 10²
K_{ET} = 1.9 x 10⁷ s⁻¹
*Ru²⁺ → Ru³⁺
λobs = 670 nm
Time, μs
B
Δ Y (x 10³)
Δ Abs x 10²
K_{ET} = 2.2 x 10⁷ s⁻¹
Ru³⁺ → Ru²⁺
λobs = 315 nm
Time, μs

Figure Chapter 2-19: K15H photo induced transient absorbencies.

K15H (13μM) photo-induced transient absorbencies monitored at (A) 430 nm and (B) 414 nm, showing the reduction of Fe^{3+} and the fit to the trace. The residual (signal minus fit) is shown above the traces.

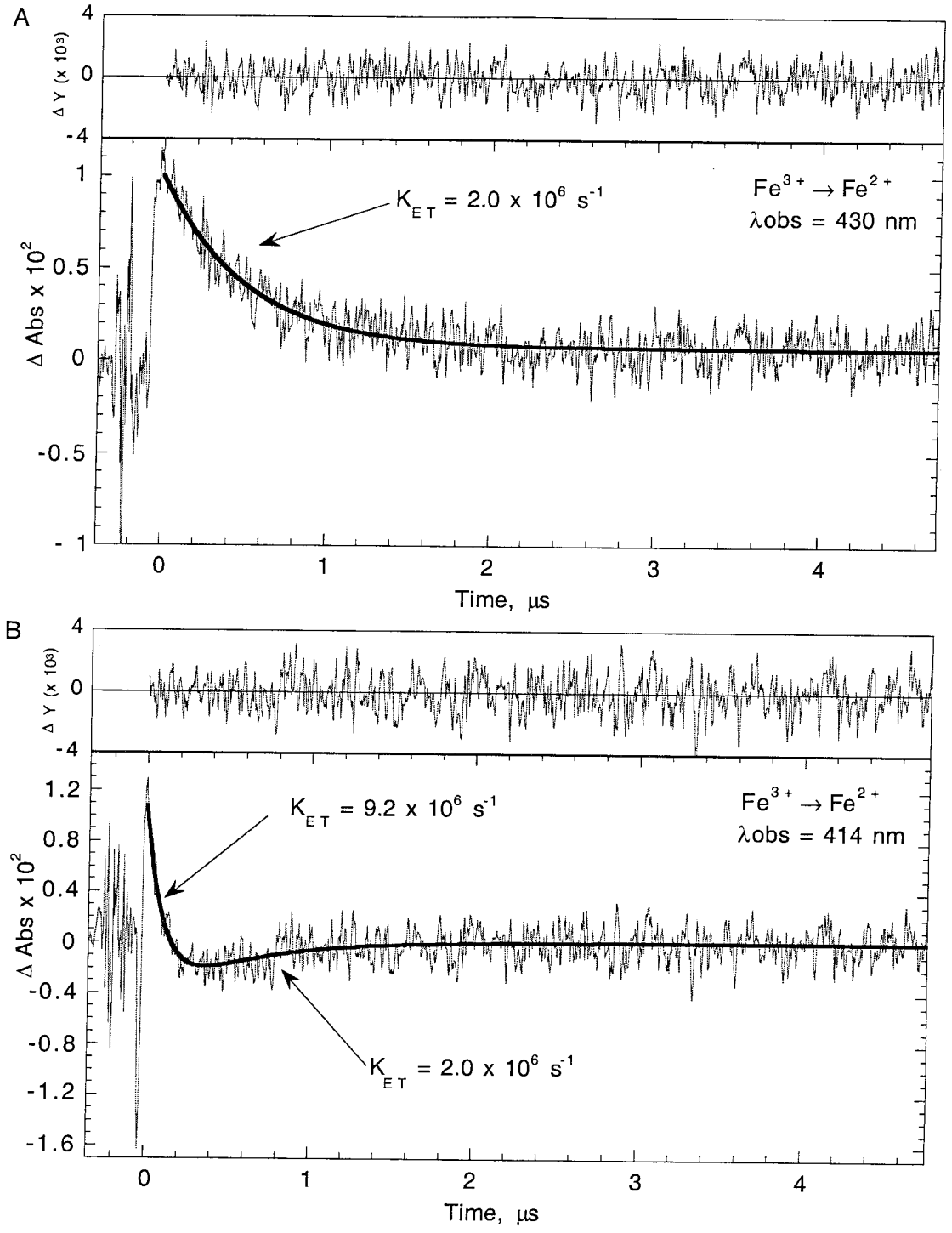
A
Δ Y (x 10³)
4
0
-4
1
0.5
0
-0.5
- 1
Δ Abs x 10²
K_ET = 2.0 x 10⁶ s⁻¹
Fe³⁺ → Fe²⁺
λobs = 430 nm
0
1
2
3
4
Time, μs
B
Δ Y (x 10³)
4
0
-4
1.2
0.8
0.4
0
-0.4
-0.8
-1.2
-1.6
Δ Abs x 10²
K_ET = 9.2 x 10⁶ s⁻¹
Fe³⁺ → Fe²⁺
λobs = 414 nm
K_ET = 2.0 x 10⁶ s⁻¹
0
1
2
3
4
Time, μs

Figure Chapter 2-20: K15H flash-quench transient absorbencies.

K15H (17μM) flash-quenched transient absorbencies monitored at (A) 430 nm and (B) 413 nm, showing the oxidation of Fe^{2+} and the fit to the trace. The residual (signal minus fit) is shown above the traces.

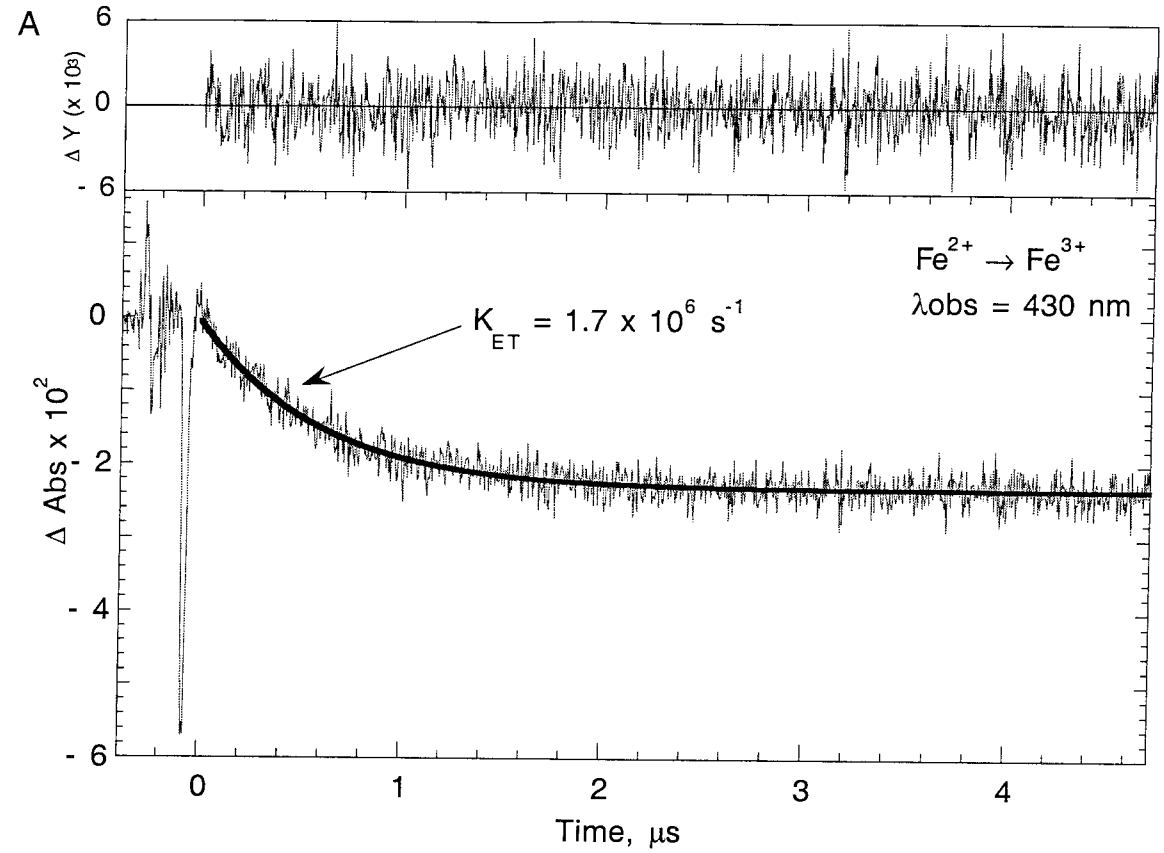
A
6
0
- 6
Δ Y (x 10⁸)
0
- 2
- 4
- 6
Δ Abs x 10²
K_{ET} = 1.7 x 10⁶ s⁻¹
$Fe^{2+} \rightarrow Fe^{3+}$
λobs = 430 nm
0
1
2
3
4
Time, μs

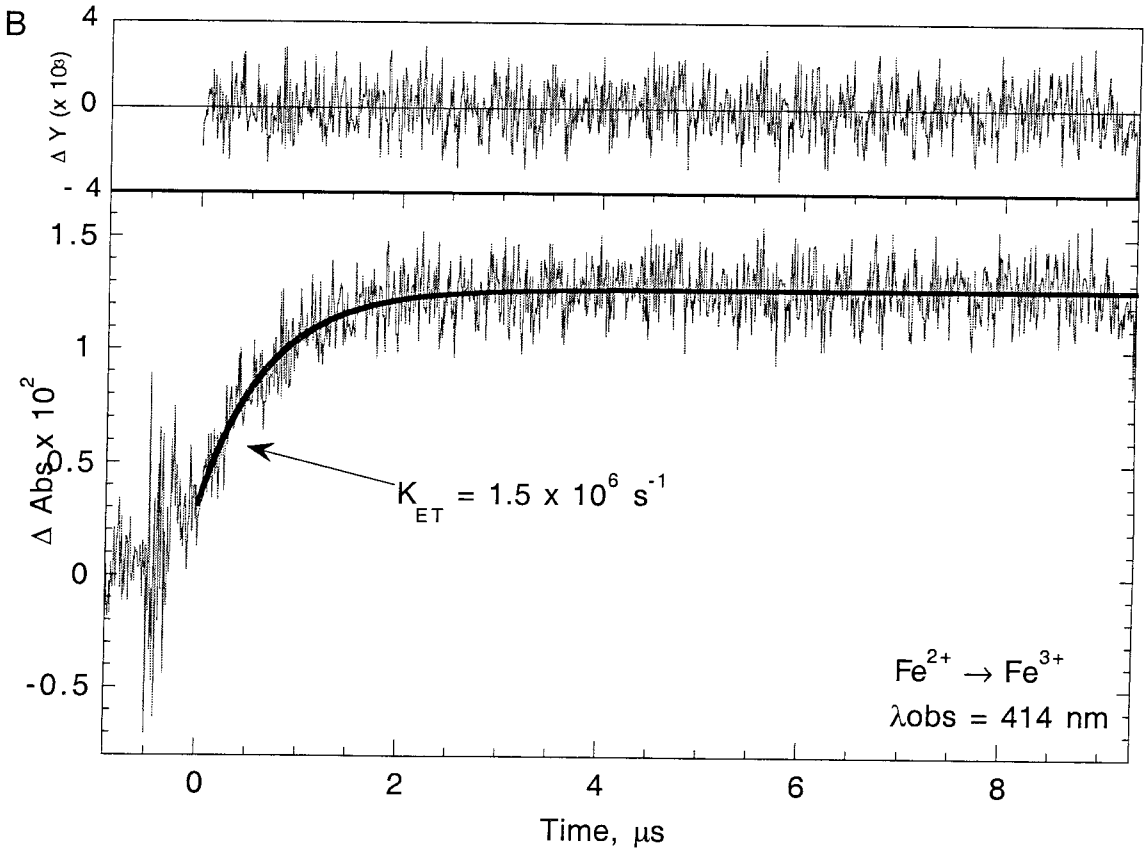
B
4
0
- 4
Δ Y (x 10⁸)
1.5
1
0.5
0
-0.5
Δ Abs x 10²
K_{ET} = 1.5 x 10⁶ s⁻¹
$Fe^{2+} \rightarrow Fe^{3+}$
λobs = 414 nm
0
2
4
6
8
Time, μs

Figure Chapter 2-21: 670 nm emissions and 315 nm absorption for K15H.

K15H (15μM) emissions monitored at (A) 670 nm and (B) flash-quenched transient absorbance monitored at 315 nm showing the reduction of Ru^{3+} and *Ru absorbance. The fit to the traces is shown and the residual (signal minus fit) is shown above the traces.

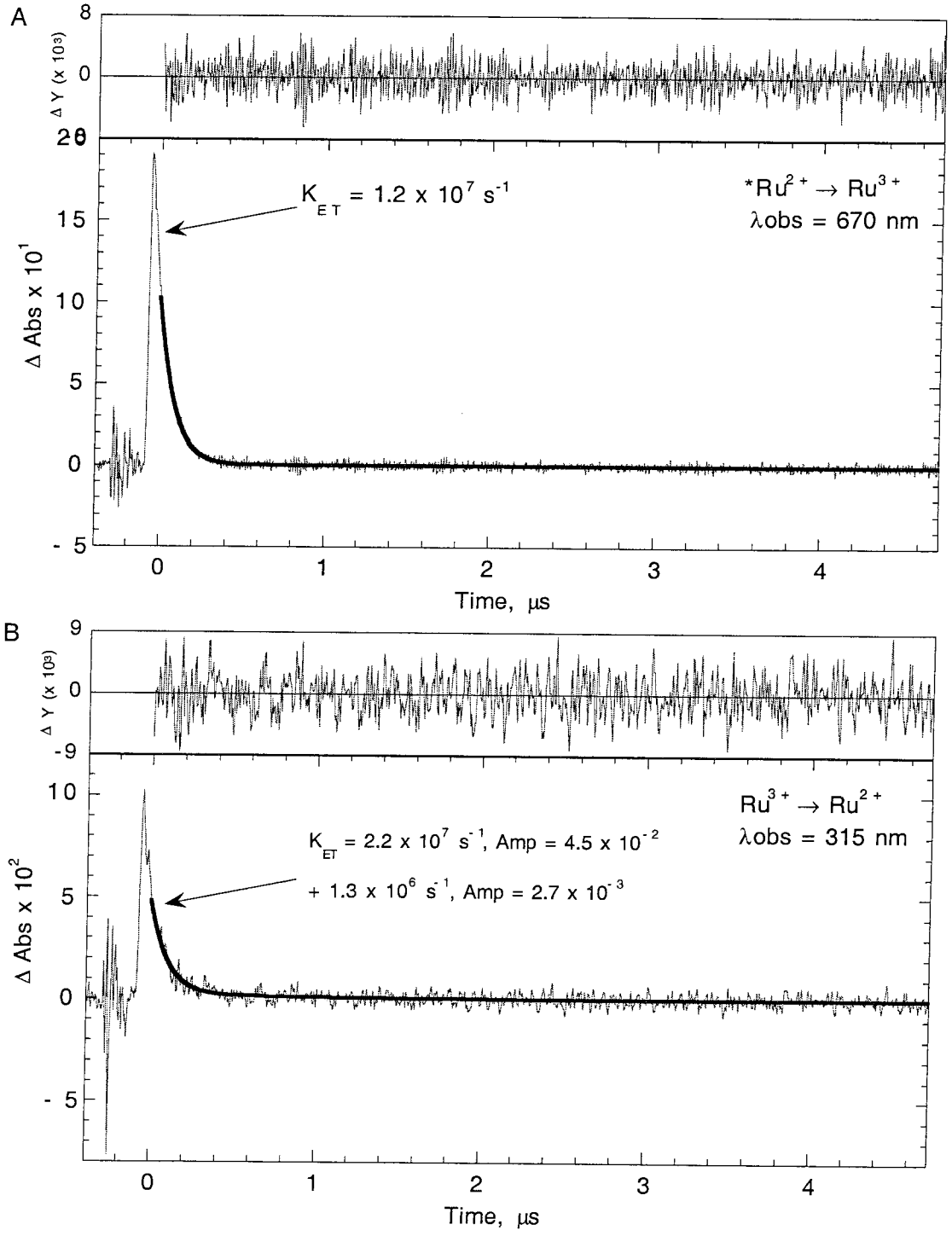
A
Δ Y (x 10³)
8
0
-8
Δ Abs x 10¹
15
10
5
0
- 5
K_{ET} = 1.2 x 10⁷ s⁻¹
*Ru²⁺ → Ru³⁺
λobs = 670 nm
0
1
2
3
4
Time, μs
B
Δ Y (x 10³)
9
0
-9
Δ Abs x 10²
10
5
0
- 5
Ru³⁺ → Ru²⁺
λobs = 315 nm
K_{ET} = 2.2 x 10⁷ s⁻¹, Amp = 4.5 x 10⁻²
+ 1.3 x 10⁶ s⁻¹, Amp = 2.7 x 10⁻³
0
1
2
3
4
Time, μs

Figure Chapter 2-22: K19H photo induced transient absorbencies.

K19H (13μM) photo-induced transient absorbance monitored at (A) 430 nm and (B) 414 nm, showing the reduction of Fe^{3+} and the fit to the trace. The residual (signal minus fit) is shown above the traces.

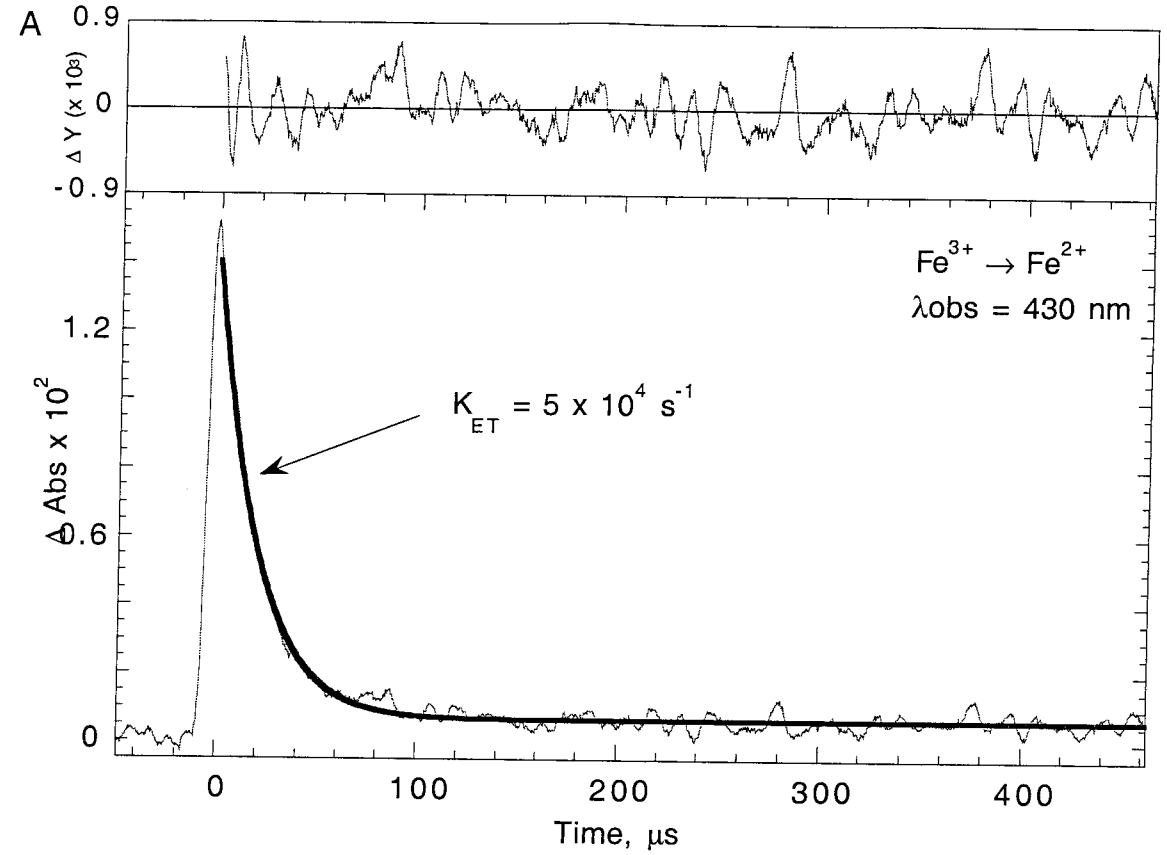
A
0.9
0
-0.9
Δ Y (x 10⁸)
Fe3+ → Fe2+
λobs = 430 nm
K_ET = 5 x 10^4 s^-1
1.2
0.6
0
Δ Abs x 10^2
0
100
200
300
400
Time, μs

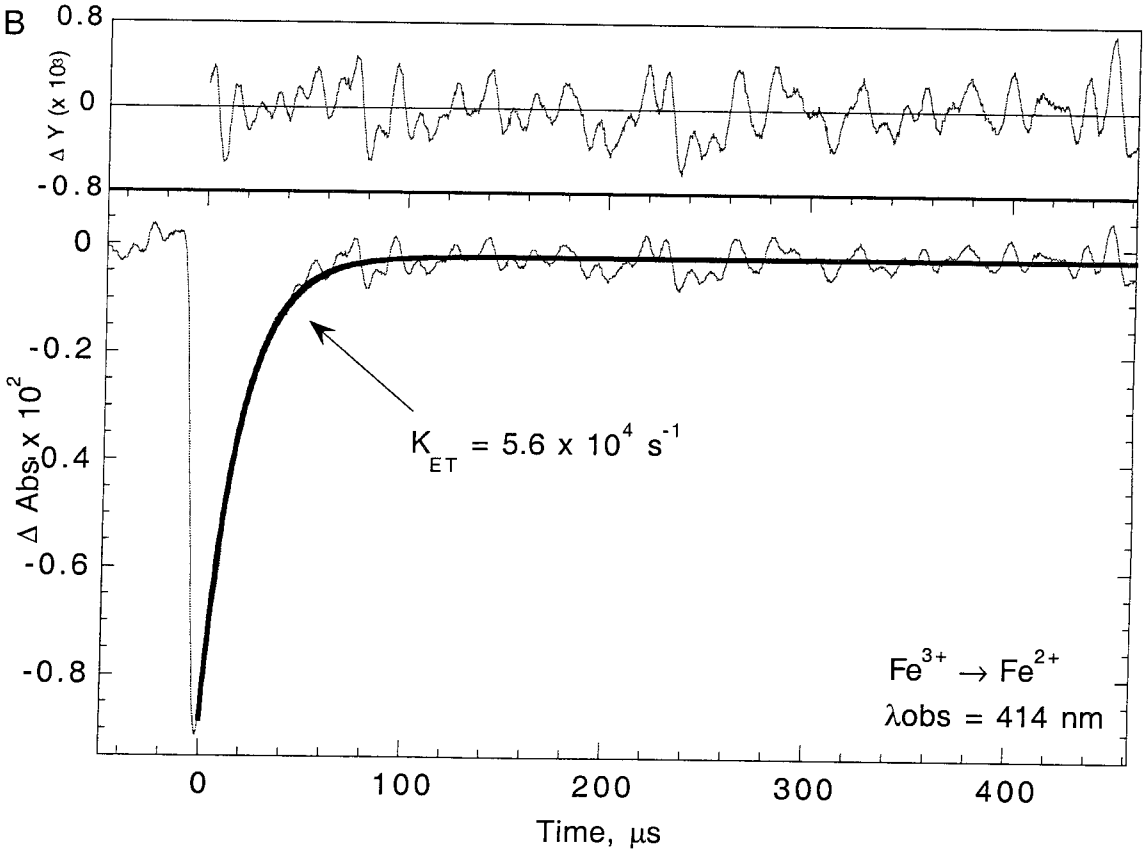
B
0.8
0
-0.8
Δ Y (x 10⁸)
0
-0.2
-0.4
-0.6
-0.8
Δ Abs x 10^2
K_ET = 5.6 x 10^4 s^-1
Fe3+ → Fe2+
λobs = 414 nm
0
100
200
300
400
Time, μs

Figure Chapter 2-23: K19H flash-quench transient absorbencies.

K19H (12μM) flash-quenched transient absorbance monitored at (A) 430 nm and (B) 414 nm, showing the oxidation of Fe^{2+} and the fit to the trace. The residual (signal minus fit) is shown above the traces.

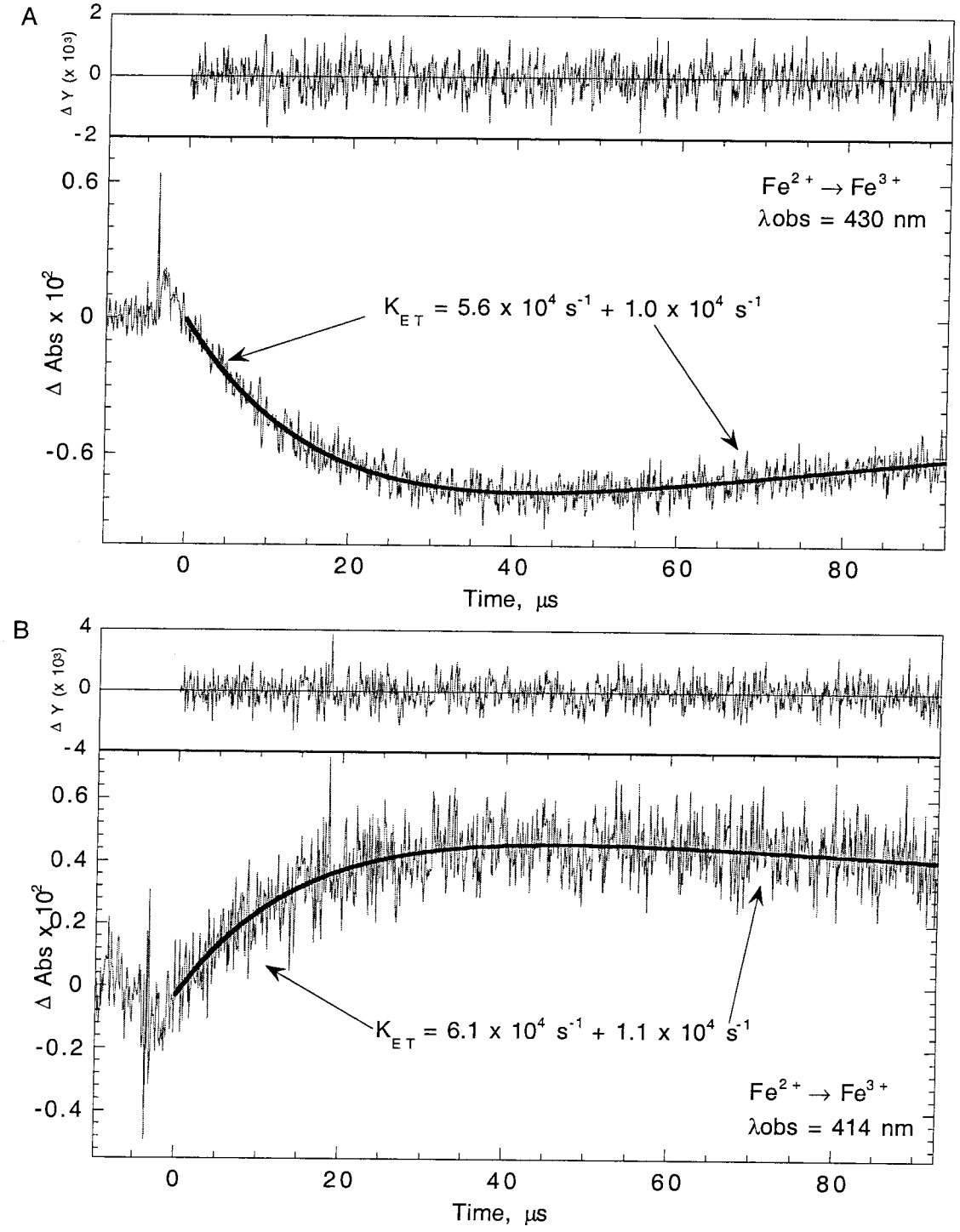
A
Δ Y (x 10³)
2
0
-2
0.6
0
-0.6
Δ Abs x 10²
Fe²⁺ → Fe³⁺
λobs = 430 nm
K_ET = 5.6 x 10⁴ s⁻¹ + 1.0 x 10⁴ s⁻¹
0
20
40
60
80
Time, μs
B
Δ Y (x 10³)
4
0
-4
0.6
0.4
0.2
0
-0.2
-0.4
Δ Abs x 10²
K_ET = 6.1 x 10⁴ s⁻¹ + 1.1 x 10⁴ s⁻¹
Fe²⁺ → Fe³⁺
λobs = 414 nm
0
20
40
60
80
Time, μs

Figure Chapter 2-24: 670 nm emissions and 315 nm absorption for K19H.

K19H (19μM) emissions monitored at (A) 670 nm and (B) flash-quenched transient absorbance monitored at 315 nm showing the reduction of Ru^{3+} and *Ru absorbance. The fit to the traces is shown and the residual (signal minus fit) is shown above the traces.

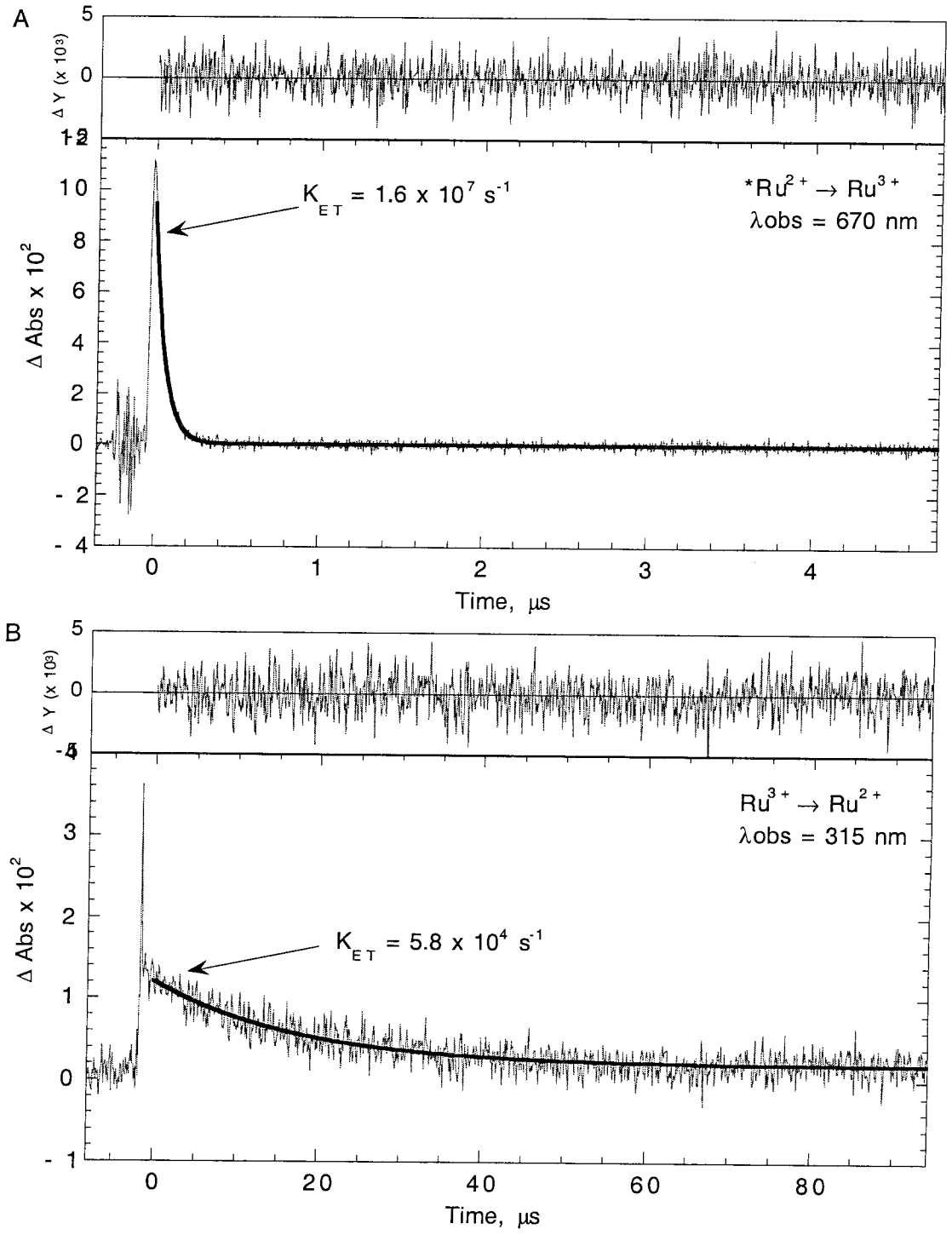
A
Δ Y (x 10³)
Δ Abs x 10²
K_{ET} = 1.6 x 10⁷ s⁻¹
*Ru²⁺ → Ru³⁺
λobs = 670 nm
Time, μs
B
Δ Y (x 10³)
Δ Abs x 10²
Ru³⁺ → Ru²⁺
λobs = 315 nm
K_{ET} = 5.8 x 10⁴ s⁻¹
Time, μs

Figure Chapter 2-25: The photo-induced ET rate vs. protein concentration for the K19H mutant.

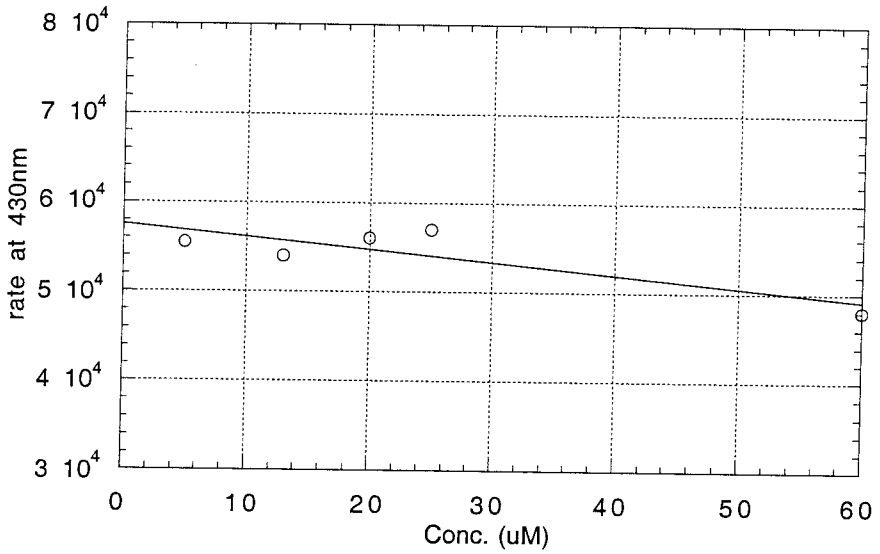
8 10^4
7 10^4
6 10^4
5 10^4
4 10^4
3 10^4
rate at 430nm
0
10
20
30
40
50
60
Conc. (uM)

Figure Chapter 2-26: The metal-metal distance (R_m) vs. the tunnelling length (σl) for helix A of cytochrome b_{562}.

R_m is the distance from the N2 His-X (X = mutation) to the porphyrin iron and σl is the Cα-X bond to iron ligand bond tunnelling length (as calculated via the Pathways program) plus 4 bond lengths.

The predicted distance decay rate for this helix is 1.29 $Å^{-1}$.

Calculation: plot rate vs. number of sigma bonds → ln y = -0.511(#bonds)
convert to distance R (multiply by bond length 1.43 Å)
→ ln y = -0.73 x R
factor in the σl/R ratio (1.76) → ln y = -1.29 $Å^{-1}$ → (log y = -0.56 $Å^{-1}$)

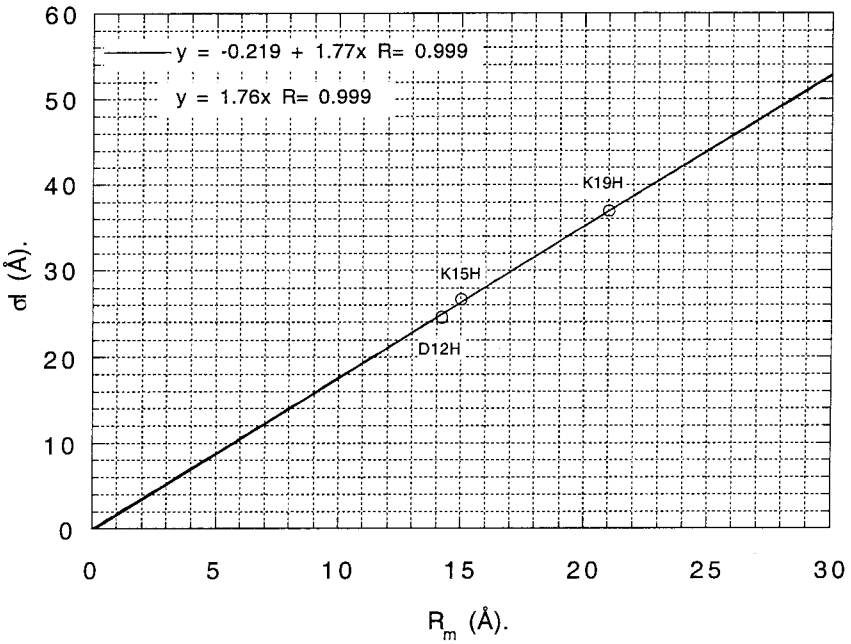
y = -0.219 + 1.77x R= 0.999
y = 1.76x R= 0.999
K19H
K15H
D12H
σ (Å).
R_m (Å).
0
10
20
30
40
50
60
0
5
10
15
20
25
30

Figure Chapter 2-27: The metal-heme distance - R_0 (R_h-R_0) vs. the metal-heme tunnelling distance (σl heme) for helix A of cytochrome b_{562}.

R_0 is the close contact distance, taken as 3Å.

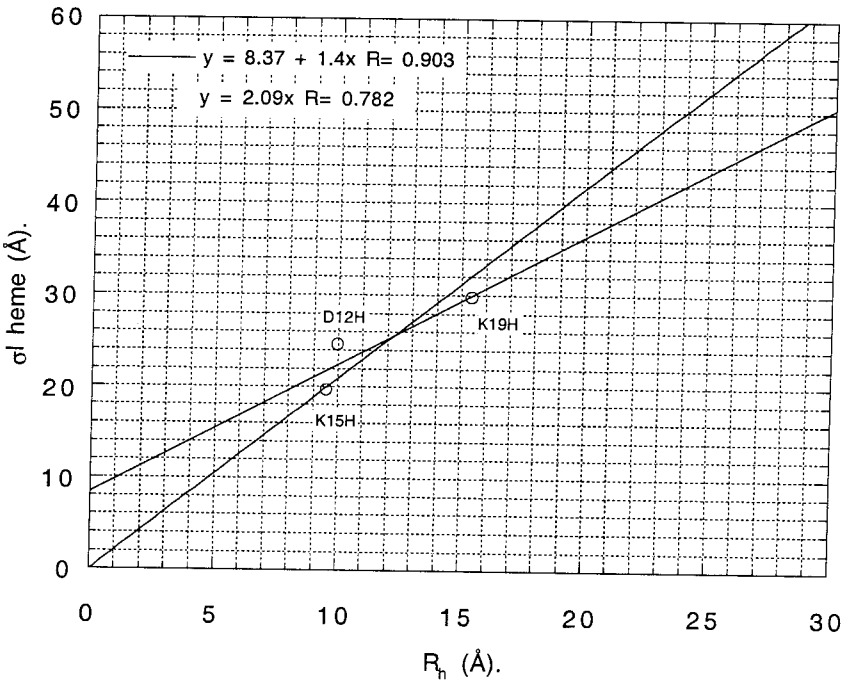
y = 8.37 + 1.4x R= 0.903
y = 2.09x R= 0.782
D12H
K19H
K15H
σI heme (Å).
R_h (Å).
0
10
20
30
40
50
60
0
5
10
15
20
25
30

Figure Chapter 2-28: Plots of metal-metal distance-R_0 (R_m-R_0) vs. log k_{max} (upper) and metal-metal sigma tunnelling length (σl) vs. log k_{max} (lower) for helix A.

R_m is the distance from the N2 His-X (X = mutation) ruthenium bond to the Fe atom and σl is the His-X Cα-Cβ bond to the Fe ligand bond tunnelling length (as calculated by the Pathways Program) plus 4 bond lengths.

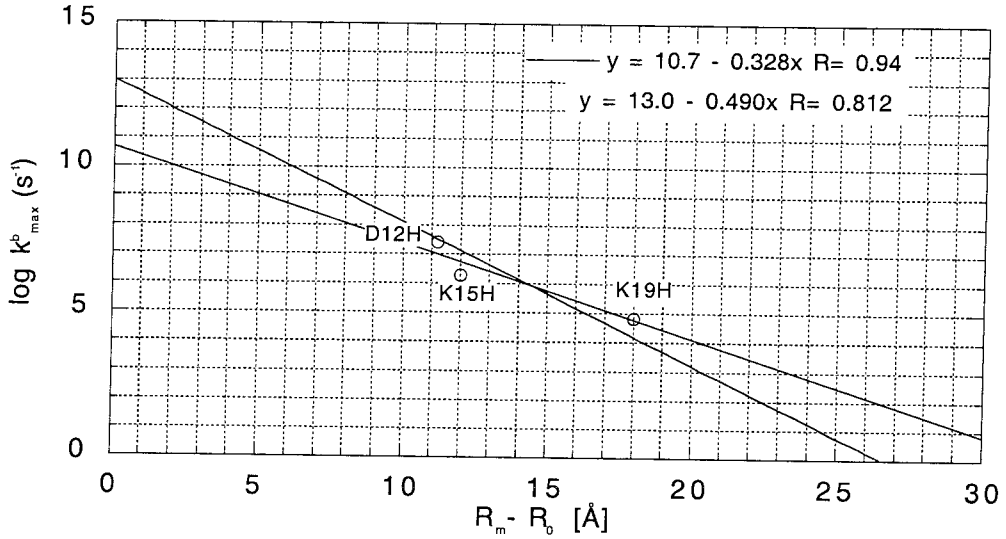
y = 10.7 - 0.328x R= 0.94
y = 13.0 - 0.490x R= 0.812
D12H
K15H
K19H
log k^b_{max} (s^{-1})
R_m - R_0 [Å]
0
5
10
15
20
25
30

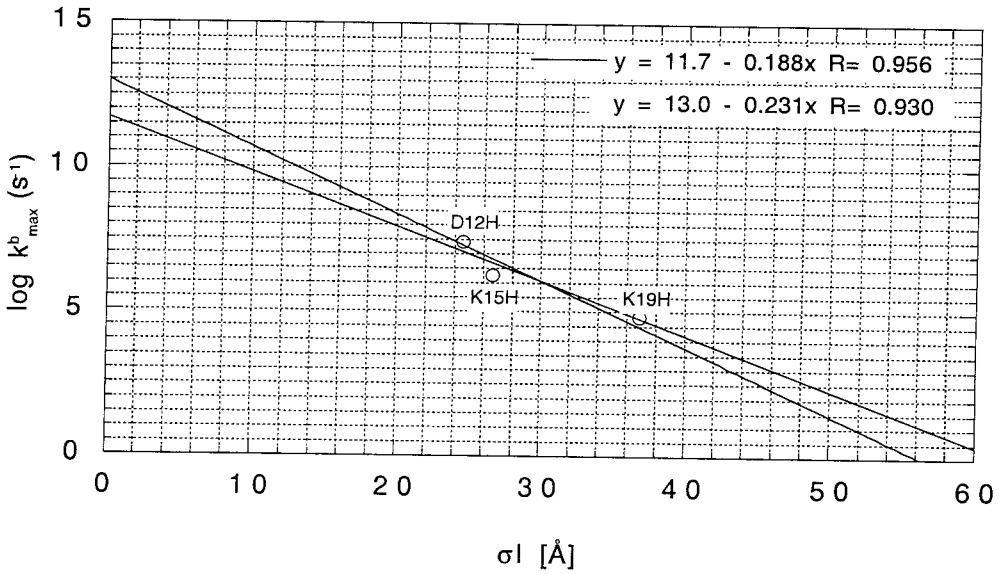
y = 11.7 - 0.188x R= 0.956
y = 13.0 - 0.231x R= 0.930
D12H
K15H
K19H
log k^b_{max} (s^{-1})
σI [Å]
0
5
10
15
20
30
40
50
60

Figure Chapter 2-29: Plots of metal-heme distance-R_0 (R_h-R_0) vs. log k_{max} (upper) and metal-heme sigma tunnelling length (σl heme) vs. log k_{max} (lower) for helix A.

R_h is the distance from the N2 His-X (X = mutation) ruthenium bond to the closest porphyrin ring atom and σl heme is the His-X Cα-Cβ bond to the closest porphyrin ring bond tunnelling length (as calculated by the Pathways Program) plus 4 bond lengths.

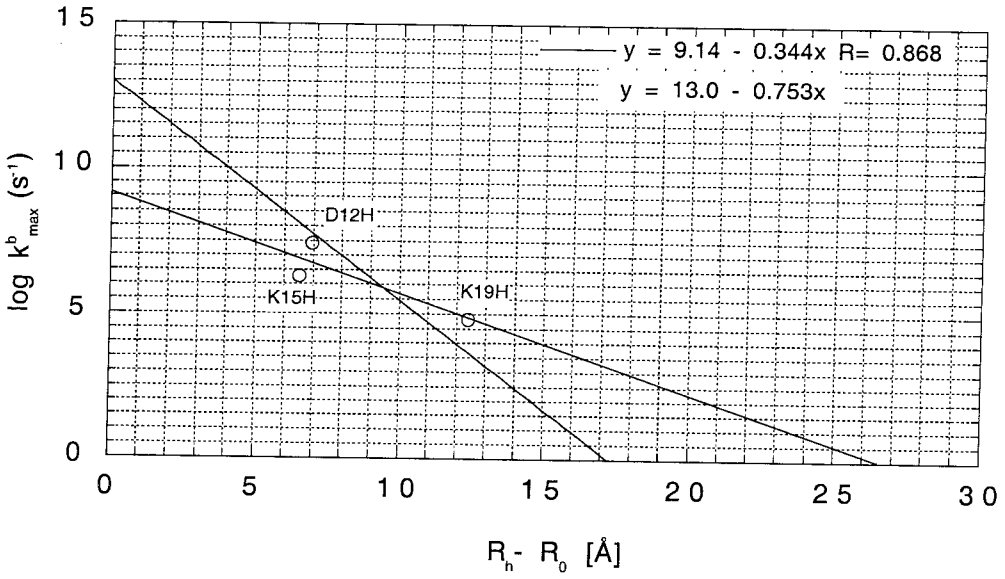
y = 9.14 - 0.344x R= 0.868
y = 13.0 - 0.753x
D12H
K15H
K19H
log k^b_max (s^-1)
R_h- R_0 [Å]
0
5
10
15
20
25
30

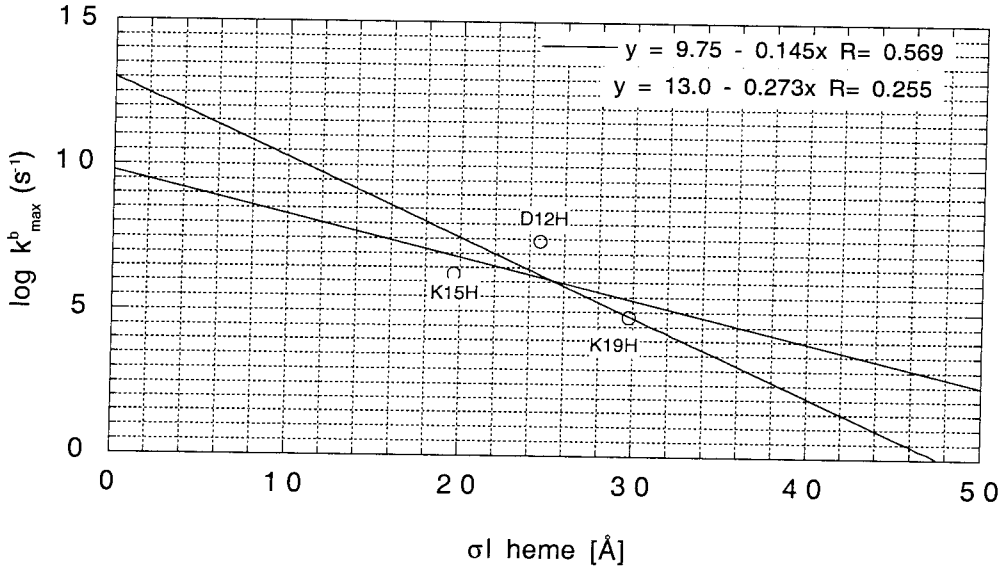
y = 9.75 - 0.145x R= 0.569
y = 13.0 - 0.273x R= 0.255
D12H
K15H
K19H
log k^b_max (s^-1)
σI heme [Å]
0
5
10
15
20
30
40
50

Table Chapter 2-1: Distance measurements (Å) for the D12H, K15H and K19H b_{562} mutants, and the couplings calculated from the Pathways program.

labelled residue/mutation	Cα-Fe distance	Cα-heme distance	Ru-Fe distance	Ru-heme distance	Ru-Fe tunnelling distance	Ru-heme tunnelling distance
Asp 12His	11.8	-	14.2	10.0	24.6	24.6
Lys 15His	14.2	8.7	15.0	9.5	26.7	19.63
Lys 19His	20.4	14.8	21.0	15.4	36.9	29.8

b_{562} coupling constants calculated using the Pathways Program.

mutant	Cα-Fe ligand coupling	Cα-heme edge coupling
12	1.6×10^{-3}	1.6×10^{-3}
15	4.6×10^{-4}	5.97×10^{-3}
19	1.1×10^{-5}	1.47×10^{-4}

Table Chapter 2-2: Mutations of b_{562} helix A and oligos used in PCR mutation. All mutants were constructed from the H63E gene, and this mutation is implied when referring to mutant proteins.

mutation	oligo name	oligo sequence
D12H	D12H top	3' -T TGG GAG TTG *GTG* TTA AAT TTT CAC TAG
	D12H bot	5' -G GAA ACC CTC AAC *CAC* AAT TTA AAA GTG
K15H	K15H top	3'-TG CTG TTA AAT *GTG* CAC TAG CTT TTT CG
	K15H bot	5'-CTC AAC GAC AAT TTA *CA*G TGA TCG AAA A
K19H	K19H top	3' -TT CAC TAG CTT *GTG* CGC CTA TTG CGC
	K19H bot	5' -A AAA GTG ATC GAA *CAC* GCG GAT AAC GC
H63E	H63E top	3' -C TTT CTA AAG GCG *CTT* CCA AAG CTG
	H63E bot	5' -G AAA GAT TTC CGC *GAA* GGT TTC GAC

Table Chapter 2-3: Observed rates of electron transfer for the D12H, K15H and K19H b_{562} mutants.

Rates measured at 670 nm are for excited state emissions.

Mutant	Observed Rates (s^{-1})*	430 nm PI	414 nm PI	430 nm FQ	414 nm FQ
D12H	$(2.2\pm0.4)\times10^{7}$	$(2.1\pm0.1)\times10^{7}$	$(3.3\pm0.6)\times10^{7}$	$(1.4\pm0.4)\times10^{7}$	$(2.1\pm0.4)\times10^{7}$
K15H	$(1.6\pm0.1)\times10^{6}$	$(1.6\pm0.1)\times10^{6}$	$(1.5\pm0.1)\times10^{6}$	1.8×10^{6}	1.4×10^{6}
K19H	$(5.8\pm0.3)\times10^{4}$	$(5.5\pm0.1)\times10^{4}$	$(5.6\pm0.3)\times10^{4}$	$(5.8\pm0.2)\times10^{4}$	$(6.1\pm0.6)\times10^{4}$

Mutant	430 mono PI	414 mono PI	670 nm PI	670 nm mono PI
D12H	$(2.9\pm0.1)\times10^{5}$ $(5.0\pm0.5)\times10^{4}$	na	$(2.0\pm0.1)\times10^{7}$	7.7×10^{7}
K15H	$(3.1\pm0.5)\times10^{4}$		$(1.2\pm0.02)\times10^{7}$	$(6.5\pm1.1)\times10^{7}$
K19H	$(6.0\pm0.1)\times10^{4}$	-	$(1.6\pm0.02)\times10^{7}$	7.4×10^{7}

*average of 430 and 414 nm PI and FQ experiments (where available)
nd - not detected

Chapter 3

Electron Transfer Along Helix C of Cytochrome b_{562}: Labelling of Residues 63, 70 and 73

Introduction

This chapter describes the analysis of electron transfer in helix C of the protein cytochrome b_{562} (b_{562}) by labelling of residues 63, 70 and 73 with the photoexcitable bis(bipyridine)imadazoleruthenium [$Ru(bpy)_2(im)^{2+}$] complexes. Cytochrome b_{562}, described in detail in chapter 2, a four-helix bundle protein isolated from *Escherichia coli*, contains 106 amino acids and the prosthetic group protophorphyrin IX ligated non-covalently towards one end of the helical bundle by Met 7 and His 102 axial ligands to the iron[1-3]. The function of b_{562} is unknown, but it is believed to be involved in electron transport[4]. It has a pH dependent redox potential with a value of 180 mV at pH 7[5] and a large molar absorbance of 117,400 (at 418 nm) for the ferric protein and 180,000 (at 427 nm) for the ferrous protein[6]. Helix C lies in the plane of the heme group and contains the second naturally occurring histidine residue at position 63. Helix C, the longest helix of b_{562}, contains in its centre from Phe61 to His63 a section of 3_{10} helix. Labelling of the WT histidine on helix C residue with $Ru(bpy)_2(im)^{2+}$ was carried out to examine the electron transfer (ET) from the ferrous protein back (the back reaction) to the ruthenium complex. Two such reaction methods, known as the photo-induced and flash-quench reactions, are available for initiating ET and are shown schematically in Figure Chapter 1-2. Labelling of residues 70 and 73 was performed by further mutation of a gene in which the wild-type histidine at position 63 had been replaced by glutamate. In this way mutants were constructed with only one histidine (other than the axial ligand at position 102) which were solvent accessible and available for labelling with $Ru(bpy)_2(im)^{2+}$. Figure Chapter 3-1 shows the structure of wild-type b_{562} and the labelling sites chosen for helix C. Position 63 is located transaxially and in the plane of the heme whilst positions 70 and 73 occupy locations distal to the heme which lie close to the plane of the heme.

Material and Methods

Most of the techniques and methods employed to make, purify and label the mutants with $Ru(bpy)_2(im)^{2+}$ for helix C are the same as those described in detail in the materials and methods section in chapter 2 and so only deviations from these protocols will be discussed here.

A DNA

The DNA oligonucleotides used to synthesize the G70H and D73H mutants are listed in **Error! Reference source not found.**. Construction of mutants and sequencing of genes was performed as described in chapter 2. All non wild-type mutants were constructed from the H63E gene and this mutation is implied when referring to mutant proteins. In addition to the G70H and D73H mutants, attempts were made to express G70H/L68G and D73H/L68G mutants. Analysis of Pathways coupling data indicated that the leucine at position 68 provide a short cut for ET through its side chain to the heme edge. The reduced coupling of the L68G mutation was predicted to remove this pathway and redirect the pathway to residues further up α-helix C.

B Electron Transfer Rate Measurements

Rates of intramolecular electron transfer were measured using both the photo-induced and the flash-quench methods by monitoring changes in the transient absorption signal at 430 nm, characteristic of ferrous heme, and also at 414 nm, characteristic of ferric heme. Absorption of the $Ru(bpy)_2(im)$-His label were monitored at 315 nm (RuIII and *RuII) together with the excited state emission at 670 nm. For flash-quench experiments the

absorption of the quencher methyl viologen was monitored at 390-400 nm. Figure Chapter 1-2 shows a schematic of the two reaction methods. Samples were approximately 2 ml 8-15 μM protein in 100 mM KP_i and a 1 cm path length laser vacuum cuvette. The samples were degassed and purged with nitrogen for 5-10 cycles prior to analysis.

The temperature and protein concentration dependence on the rate of ET for some of the mutants were analyzed. Temperature dependence was monitored with a water jacketed laser cuvette holder and the temperature varied between 10°C and 48°C with 20 minutes for equilibration for each temperature point. After measuring the ET rate at 48°C, the rate was measured at a number of points back towards room temperature (20°C). Multiple sets of laser acquizitions were measured at each temperature point and analyzed using the Kinfit program. Concentration dependence was measured for samples between 5 μM and 139 μM. For samples over 60 μM measurements were made in a 1 mm pathlength cuvette to allow adequate transmission of laser and probe light.

For the D73H mutant the irreversible quencher $Co(NH_3)_5Cl^{2+}$ was used due to the slow back rate. Under such conditions and using the reversible quencher methyl viologen, the ET back rate was in competition with reduction of Ru^{3+} by methyl viologen radical (see Figure Chapter 2-4). This places an upper limit on the rate of approximately 1×10^3 s^{-1}. Also, since photolysis of $Co(NH_3)_5Cl^{2+}$ promoted slow oxidation of the reduced protein used in these experiments, the quencher and proteins samples were mixed just prior to laser excitation by pumping sample from separate protein and quencher reservoirs into a laser flow cell. Additionally, experiments were carried out in the dark with cut-off and band-pass filters (see Figure Chapter 3-2) to block light of unnecessary wavelengths from the probe light reaching the sample. Data was collected from samples immediately after protein/quencher mixing and the flow cell refilled with another aliquot of fresh sample before averaging of further transients.

The concentration of $Co(NH_3)_5Cl^{2+}$ used was either 0.1 or 1 mM.

Results

A Design of Mutants

The chosen sites for attachment of ruthenium(II)bis(2,2'-bipyridine)(im) gave the distances listed in Table Chapter 3-1. The ruthenium to heme iron distances (R_m) are seen to range from 17 Å to 21 Å. Distances were measured using the molecular modelling programs Insight II and RasMac v2.5 using the 1.4 Å x-ray crystallographic structure 256B[7] downloaded from the Brookhaven data base. χ_1 and χ_2 angles were rotated manually to minimize Van de Waals and electrostatic interactions.

B DNA/Mutagenesis Reactions

The gene used in the mutagenesis reactions was isolated from TB1 cells containing the pNS207 plasmid donated by the Laboratory of Professor Stephen Sligar. Before mutagenesis reactions the protein was expressed from these cells and was found to give a red protein which was over expressed and had the correct molecular weight as determined by SDS/polyacrylamide gel electrophoresis of the cells.

PCR mutagenesis reactions 1 and 2 produced the correct size of gene fragments for each of the mutants. Figure Chapter 2-8 shows a typical gel with the results of PCR reaction 1 and 2. These products were excised from gels and purified by Qiaex resin (Qiagen) and used in PCR reaction 3. Products from this reaction were analyzed and isolated as above and, after

endonuclease digestion with Sal I and Sac I, ligated into the pNS207 plasmid which had been digested with the same enzymes. The purified and desalted (Qiaex resin) ligation product was used to transform DH10B cells. Overnight growth of transformed cells on ampicillin agar plates produced isolated colonies which displayed a pink colour to varying degrees of intensity. PCR screening of the isolated colonies confirmed that a gene of the correct size was present and positive colonies were grown for Maxi Prep (Qiagen) preparations. Sequencing of these plasmid preps confirmed in all cases the correct DNA sequence.

C Protein Expression and Purification

Protein was expressed at 10 -30 mg/L of culture for the wild-type protein and the G70H mutant. The D73H mutant yields were on average much lower at approximately 4 mg/L. Proteins containing the L68G mutation could not be isolated as holo-protein; neither could apo protein be reconstituted with the addition of hemin.

Mutants were eluted from a MonoQ anion exchange FPLC column at approximately 11% buffer B (25 mM TEA pH 7.4, 1 M NaCl) and from the HiTrap chelating column at approximately 80% B. A small percentage of reduced protein (<10%) was found in the initial purification steps and eluted after oxidized protein. With both FPLC columns labelled and unlabelled apo-protein was eluted before the labelled or unlabelled holo protein. Sequential rounds of FPLC (3 to 4 rounds) produced protein preparation, which when viewed by SDS PAGE, were homogenous for most mutants and, with others faint bands due to very low concentrations of other proteins, were seen on overloaded SDS/PAGE gels. Figure Chapter 3-3 shows a 15% SDS/PAGE gel which includes samples of the purified labelled and unlabelled G70H and D73H mutants. The samples were loaded to maximal

concentration and can be seen to be essentially homogenous and at the correct molecular weight with ruthenium labelled samples running slightly above the unlabelled samples.

D Protein Labelling

Labelled protein was eluted from the MonoQ column at 10% B and resolved from unlabelled protein, and was eluted from the HiTrap column at 5% B. Labelling reactions were 30-90% efficient depending on the length of the reaction with 36 hours being optimal for mutants. Purification of labelling reactions by FPLC using MonoQ and HiTrap columns produced samples homogenous for labelled b_{562} as determined by SDS gel electrophoresis (see Figure Chapter 3-3). These labelled samples ran slightly above unlabelled samples on 15% SDS PAGE gels.

Addition of 400 mM imidazole pH 8.0 to $Ru(bpy)_2.H_2O$ labelled protein for 48 hours resulted in formation of the $Ru(bpy)_2(im)$ labelled protein as shown by fluorescence spectra and electron transfer rates. The yields for the imidizolations were similar to those of helix A mutants (approx.> 90%). Addition of imidazole resulted in most of the heme being extracted from the protein and so after removal of the imidazole and precipitated heme, fresh hematin was added dropwise with stirring to reconstitute the protein. Purification of the reconstituted protein by FPLC revealed a small fraction of apo protein.

E Characterization of Expressed Protein

(1) UV Fluorescence and Spectroscopy

The UV/vis spectrum of WT b_{562} and the G70H and D73H mutants are shown in Figure Chapter 3-7 - Figure Chapter 3-9. The spectrum of WT b_{562} is identical to published

spectra. The various non-covalent mutants synthesized have essentially identical spectra to that of WT b_{562}. The spectra do not show the absorption at 695 nm characteristic of a Met - Fe^{3+} ligand. Ruthenation of the WT and mutants did not perturb the UV/vis spectra with the difference spectra appearing identical to those of unlabelled protein.

Figure Chapter 3-10 shows the fluorescence spectra of the labelled D73H and labelled monoaqua mutants. The emissions band ($bpy^{-}\rightarrow Ru^{3+}$) of the labelled D73H mutant is identical to that of the model compound with the emissions peak centred on 670 nm. The monoaqua labelled sample of D73H was purified from a previous labelling reaction and shows some 'contamination' from the imidazole species. The spectra indicates that the protein environment does not appreciably affect the solvation of the ruthenium label.

(2) Circular Dichroism

Figure Chapter 3-11 shows a typical spectrum of a comparison of mutant protein with wild type protein. In this case the ruthenium labelled E86H mutant is compared. The spectra shows that the neither the H63E mutation nor the mutation to form the new labelling site has an appreciable affect on the helical content of the protein. No changes were observed between the spectra of ferric and ferrous proteins as expected for electron transfer proteins.

(3) Electrochemistry

Analysis by Osteryoung square wave voltammetry was carried out to access the effect of the mutations and labelling on the heme potential of the proteins. The values found for unlabelled and labelled WT protein were 165 mV and 143 mV respectively *versus* NHE. The value of 165 mV is 15 mV below that of the reported literature value of approximately 180 mV[8]. This small change could be due to pH differences in the sample or different measurement technique. The reduction of 22 mV for the labelled sample is within the range experienced for labelling of metalloproteins with point charges[9]. Since the UV/vis

absorption spectra of the labelled and unlabelled WT proteins are very similar, it is expected that the electronic structure of the labelled protein is the same as unmodified protein. Despite a nearly identical UV/vis spectra to that of Wt b_{562}, the potential of the D73H mutant is reduced dramatically to a value of 64 mV *versus* NHE, a change of 101 mV to that of the WT protein. Since the ET rate is also below that expected for the distance involved it is difficult to argue that this change is due to a benign alteration in the structure which changes the proteins interaction with the electrode.

(4) Unfolding

The thermal unfolding graphs for ferrous and ferric WT b_{562} are shown in Figure Chapter 3-12. The T_m values recorded for wild-type ferric and ferrous protein were 69°C and 87°C respectively, and are similar to published results of 67°C and 81°C[10]. Figure Chapter 3-12 shows some thermal denaturation curves for WT b_{562} and the UV/vis spectra of the protein in the unfolding region. Above temperatures of T_m the spectra resemble that of free heme.

F Electron Transfer Rate Measurements

The concentration and temperature dependence on the ET rate for WT b_{562} was measured and the results are shown in Figure Chapter 3-14. It can be seen that there is very little concentration dependence for the concentrations used in these experiments (5-139 μM). The addition of NaCl to 150 mM had no effect on the rates. It has been found previously that WT b_{562} dimerizes only at concentrations above 1 mM in the, presence of 100 mM KP_i[11] and so this result is not surprizing. There was very little, if any temperature dependence for the samples measured over the temperature range from 10 °C to 49 °C. This result was also not unexpected since the driving force is close to the estimated reorganization energy, thus placing the energetics near the top of the Marcus curve, and so

rates should be close to their k_{max} values. Rates measured as the sample was cooled were identical to the previous measurements.

To investigate the effect that the ligand binding may have on the ruthenium labelling complex, a sample of Ru labelled apo E86H was prepared. The transient absorption spectra of this species was essentially identical (see Figure Chapter 3-13 upper) to the transient absorption spectra of the Ru(bpy)2.im2 model compound, and showed that ruthenium labelling, at least in this mutant, did not affect the electronic environment of the labelling compound or that no spurious signals were produced from the tyrosine of the protein.

A transient absorption difference spectra for the labelled WT protein were recorded using the flash-quench method. Figure Chapter 3-13 (lower) shows the trace for the flash-quench difference experiment at the milli second time scale. It shows a decrease in the absorption of Fe^{2+} at 430 nm and the increase in the absorption of methyl viologen radical at 400 nm. The increase in Fe^{3+} can be seen at 418 nm as a shoulder of the absorption due to the methyl viologen radical. Monitoring of the absorption at a longer time point revealed a slower component which is seen as the return of the Fe^{2+} absorption and the reduction of the absorption's due to the methyl viologen radical and Fe^{3+}.

The ET rates found for the labelled WT and the G70H mutant were $(6.7\pm0.4)x10^{6}$ s^{-1} and $(2.0\pm0.1)x10^{5}$ s^{-1} respectively. Uncertainties are expressed as standard errors of the mean. The metal-metal distances (R_m) for these proteins are 17 and 19.5 Å. Figure Chapter 3-15 - Figure Chapter 3-17 are typical photo-induced and flash-quench transients for the WT protein and show the absorption of Fe^{2+} and Fe^{3+} at 430 nm and 414 nm respectively, and absorption's for *Ru (excited state) together with RuIII at 315 nm. The emissions transient of the ruthenium excited state was recorded at 670 nm. Fitting of the data using the Kinfit

program provided the above mentioned rates. Both sets of data produced data of the correct relative intensity and sign to confirm the ET between the heme and ruthenium label. The small signal at the start of the WT flash-quench transients is due to a small concentration of oxidized protein. Data processing produced monoexponential rates which showed this low concentration of oxidized protein had a negligible affect on the rates. The WT ET rate at 315 nm was difficult to resolve from the excited state decay rate due to the rates being similar, but starting the data fit at later time points showed a rate that was similar to that found at 430 and 414 nm. Both proteins show an increase in the rates of excited state decay indicating that the heme is effective in quenching this signal. The signal of the G70H mutant at 315 nm is described by a bi-exponential decay, the initial fast phase being that of the excited state decay which also absorbs at 315 nm.

Transients spectra for the D73H mutant are shown in Figure Chapter 3-21 - Figure Chapter 3-23. The emissions rate for the D73H mutant was similar to the model compound showing that in this protein the heme is not efficient at quenching the excited state ruthenium. No signal from the heme was observed in photo-induced experiments. Due to the slow rate found in initial flash-quench experiments using the quencher methyl viologen, the irreversible quencher $Co(NH_3)_5Cl$ was used. The rate was found to be approximately $2x10^3$ s^{-1}. There was some variation between transients, and rates of as low as 5×10^2 s^{-1} were recorded. There was small degree of dependence of the kinetics on the concentration of quencher which may reflect the above mentioned oxidation of the sample by quencher. With consideration of these factors, an approximate rate of $3x10^2$ s^{-1} is proposed for the D73H mutant.

Calculation of k_{max} for these labelled proteins gave the values of $7.9x10^6$ s^{-1}, $2.3x10^5$ s^{-1} and $4.9x10^2$ s^{-1} for the WT and G70H and D73H mutants respectively.

Discussion

The plots of metal-metal distance (R_m) *versus* metal-metal tunnelling length (σl) and edge-edge distance (R_h) *versus* edge-edge tunnelling length (σl heme) are shown in Figure Chapter 3-24. From R_m *versus* σl a distance decay of 1.21 Å-1 is predicted which is in agreement with the decay constant predicted from modelling an ideal α-helix[12]. When the data is plotted as R_h *versus* σl heme, the correlation between tunnelling and distance measurements is much reduced. The predicted decay constant from this graph is 1.56 $Å^{-1}$.

The experimental distance decay factor calculated from the R_m *versus* log k_{max} graph (Figure Chapter 3-25 upper) for WT and the G70H mutant is 1.15 $Å^{-1}$ with a reasonable correlation between rates and the graph with a close contact rate restrained to 10^{13} s^{-1}. Including the D73H mutant in this calculation reduces this value to 1.04 $Å^{-1}$.

Figure Chapter 3-4 - Figure Chapter 3-6 show the sites of labelling and residues involved in the tunnelling pathway (as calculated from the Pathways program analysis) for the helix C labelled residues. The most likely ET pathway for the WT protein is via Gly64 and a through space jump to CBC of the heme. The predicted Pathway for the G70H mutant is via Val69 and Leu68 and a through space jump to CMC of the heme. For the D73H the pathway prediction is from Cδ1 of Ile72 to Cδ2 of Ile10 on helix A, then from Cδ1 of Ile10 to the Met7 ligand sulphur atom. This pathway includes one more through space jump than the others and may be the reason, in addition to the reduced driving force, for the anomalous rate (although the σl *versus* R_m distances correlate well). None of these pathways predict the use of H-bonds and all follow the most direct route to the heme. It is therefore surprizing that the predicted decay of 1.21 $Å^{-1}$ is so close to the theoretical distance decay of 1.26 $Å^{-1}$ for x-helices. The paths in the b_{562} mutant do not maintain an all α-helical route but involve

side chain, inter helix and heme couplings. Since distance decay predictions for small organics are only 0.85-0.95 $Å^{-1}$, the coupling is increased when the heme bonds are utilized and this will tend to compensate for through space jumps. Factoring in the heme bonds distance decay with a value of 0.9 $Å^{-1}$ gives an approximate distance decay for helix C of 1.04 $Å^{-1}$.

The rate *versus* metal-metal tunnelling length (σl) plot for WT and G70H predicts a per C-C sigma bond decay factor of 0.68 which is close to the reported value of 0.6 found in β-sheets[12, 13]. There is no obvious correlation between all the rates of helix C and edge-edge tunnelling lengths (σl heme). Consideration of mutants G70H and D73H alone show that they are on a line separate from WT. This may possibly reflect the axial pathway common to G70H and D73H and the transaxial pathway of WT, although the D73H mutant appears as a separate point on the metal-metal tunnelling graph. The difference in the bond decay rate may reflect differences in the bonding geometry in α-helices to that of β-sheets and/or the possible different affect of multiple pathways in α-helices.

It appears from the graphs of σl *versus* R_m and σl heme *versus* R_h that there is better correlation between the former. The experimental results in considering metal-metal distance and tunnelling give a distance decay rate β of 1.04 Å-1 and a bond decay of 0.66, which seem reasonable considering the direct distances and predicted tunnelling pathways do not follow the axis of the helix. Edge-edge distances and tunnelling analysis yield a β of 1.61 Å-1 and a bond decay of 0.66. This β value appears unreasonably large.

Further discussion of couplings and distances will be reserved for chapter 4.

Bibliography

1. Levinthal, C. 22-24 (Allerton House, Montecillo, Ill., 1969).

2. Schmid, F.X. & Baldwin, R.L. *J. Mol. Biol.* **135**, 199-215 (1979).

3. Kim, P.S. & Baldwin, R.L. *Biochemistry* **19**, 6124-29 (1980).

4. Udgaonkar, J.B. & Baldwin, R.L. *Nature* **335** (1988).

5. Roder, H., Elove, G.A. & Englander, S.W. *Nature* **335**, 700-4 (1988).

6. Kuwajima, K., Yamaya, H., Miwa, H., Sugai, S. & Nagamura, T. *FEBS Lett.* **221**, 115-18 (1987).

7. Hamada, K., Bethge, P.H. & Mathews, F.S. *J. Mol. Biol.* **247**, 947-962 (1995).

8. Moore, G., Williams, R., Perterson, J., Thompson, A. & Mathews, R. *Biochem. Biophys. Acta* **829**, 83-96 (1985).

9. Leitch, F.A., Moore, G.R. & Pettigrew, G.W. *Biochemistry* **23**, 1831 (1984).

10. Fisher, M. *Biochemistry* **30**, 10012-10018 (1991).

11. Wu, J., Gerd, N. & al, e. *Biochemistry* **30**, 2156-2165 (1991).

12. Langen, R. in *Dept. Chemistry and Chemical Engineering* (California Institute of Technology, Pasadena, 1995).

13. Langen, R., *et al. Science* **268**, 1733-1735 (1995).

Figure Chapter 3-1: The backbone structure of wild-type b_{562} and the labelling sites on helix C.

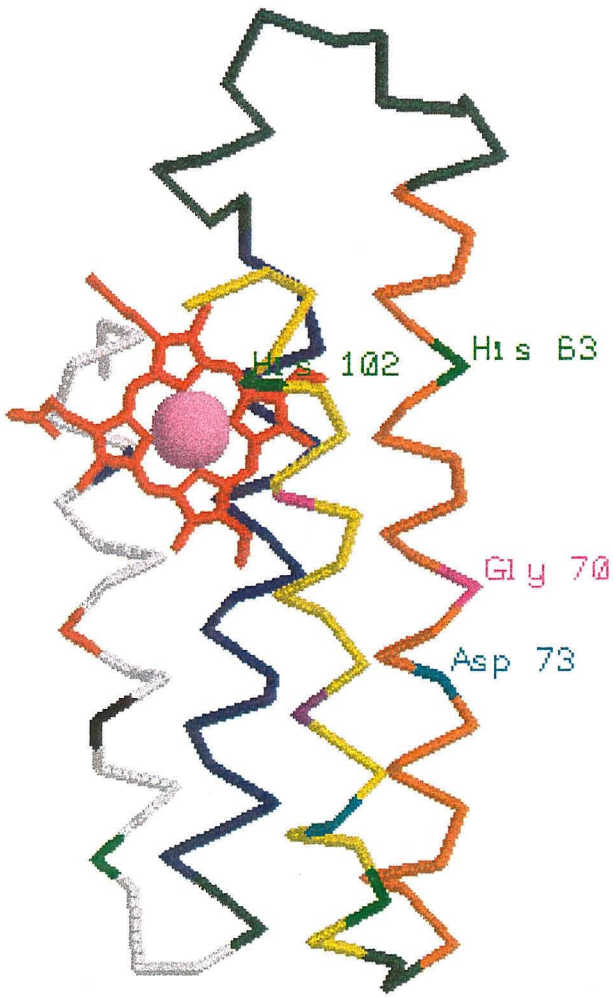
His 102
His 63
Gly 70
Asp 73

Figure Chapter 3-2: Filters used for experiments using the irreversible quencher $Co(NH_3)_5Cl$.

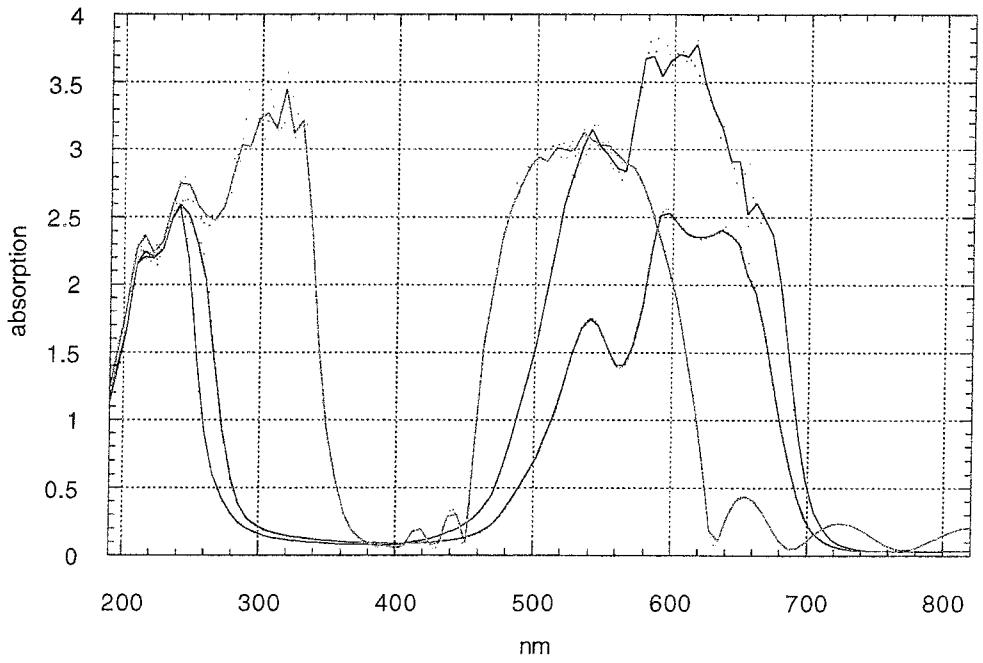
absorption
4
3.5
3
2.5
2
1.5
1
0.5
0
200
300
400
500
600
700
800
nm

Figure Chapter 3-3: SDS PAGE gel of the G70H and D73H mutants of the C α-helix of b_{562}, and the E86H and A89H mutants from helix D.

SDS-PAGE gel of unlabeled and labeled b562 proteins. The molecular weights (in kDa) of protein molecular weight standards are shown.

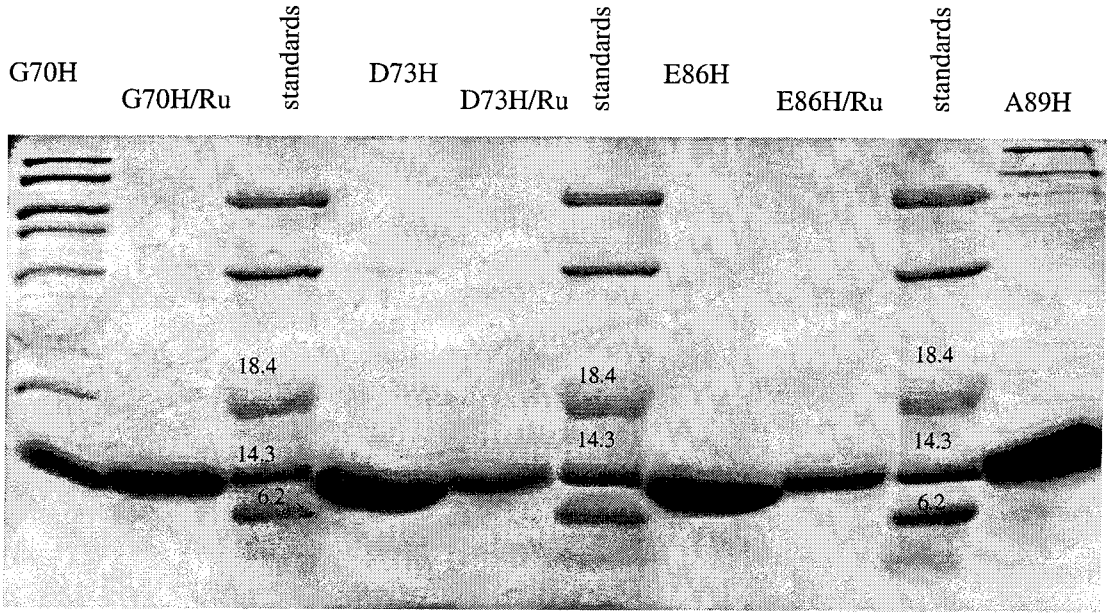

Figure Chapter 3-4: The wild-type b_{562} ruthenium labelling site.

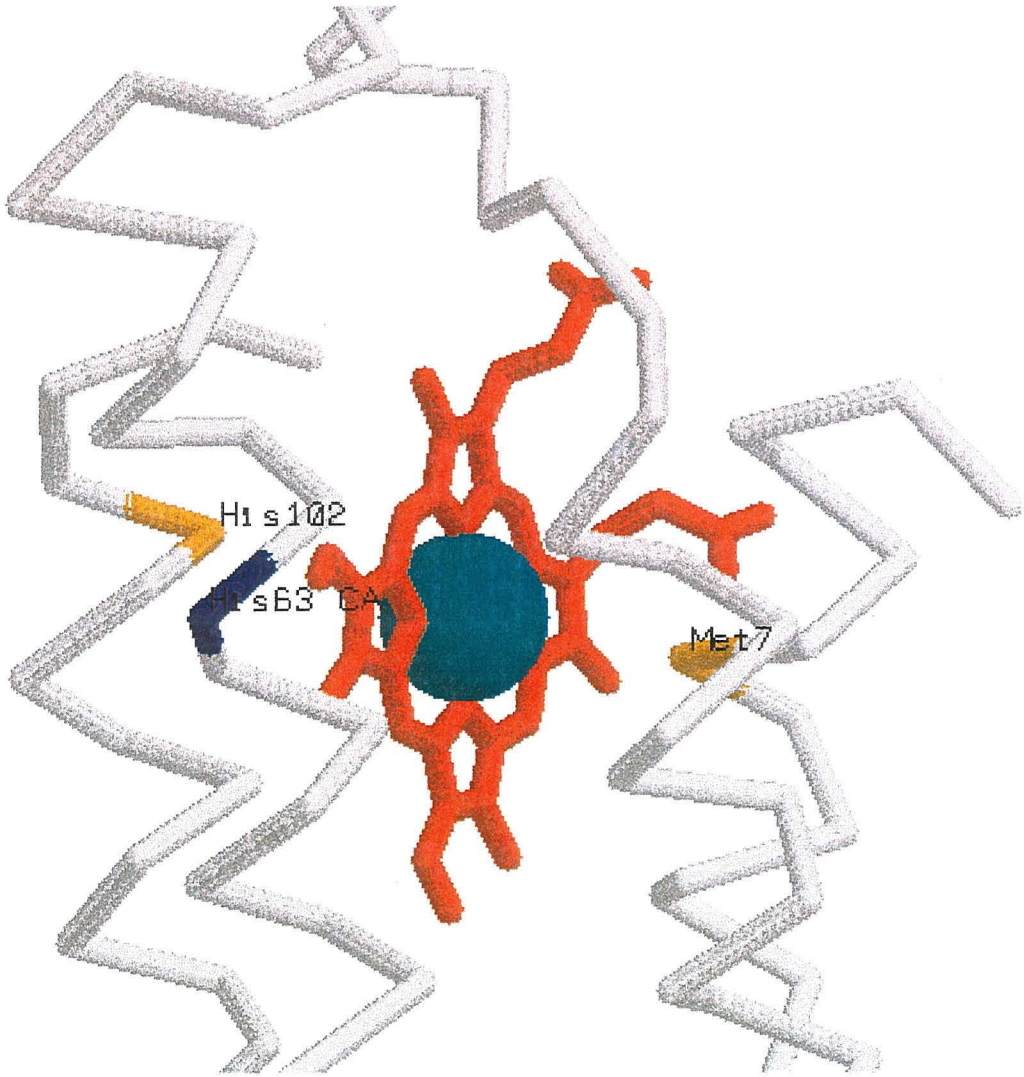
His102
His63 CA
Met7

Figure Chapter 3-5: The ET pathway of the G70H mutant of b_{562} calculated from the Pathways program.

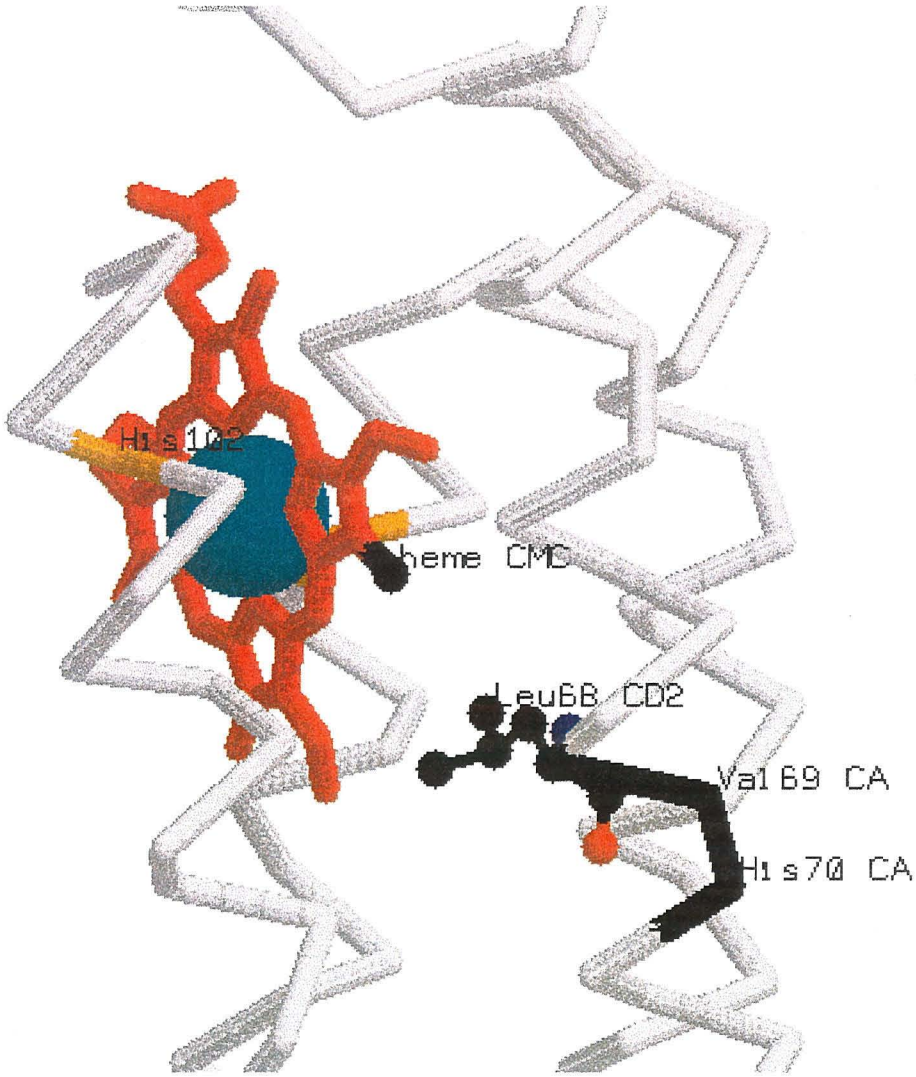
His102
heme CMB
Leu68 CD2
Val69 CA
His70 CA

Figure Chapter 3-6: The ET pathway of the D73H mutant of b_{562} calculated from the Pathways program.

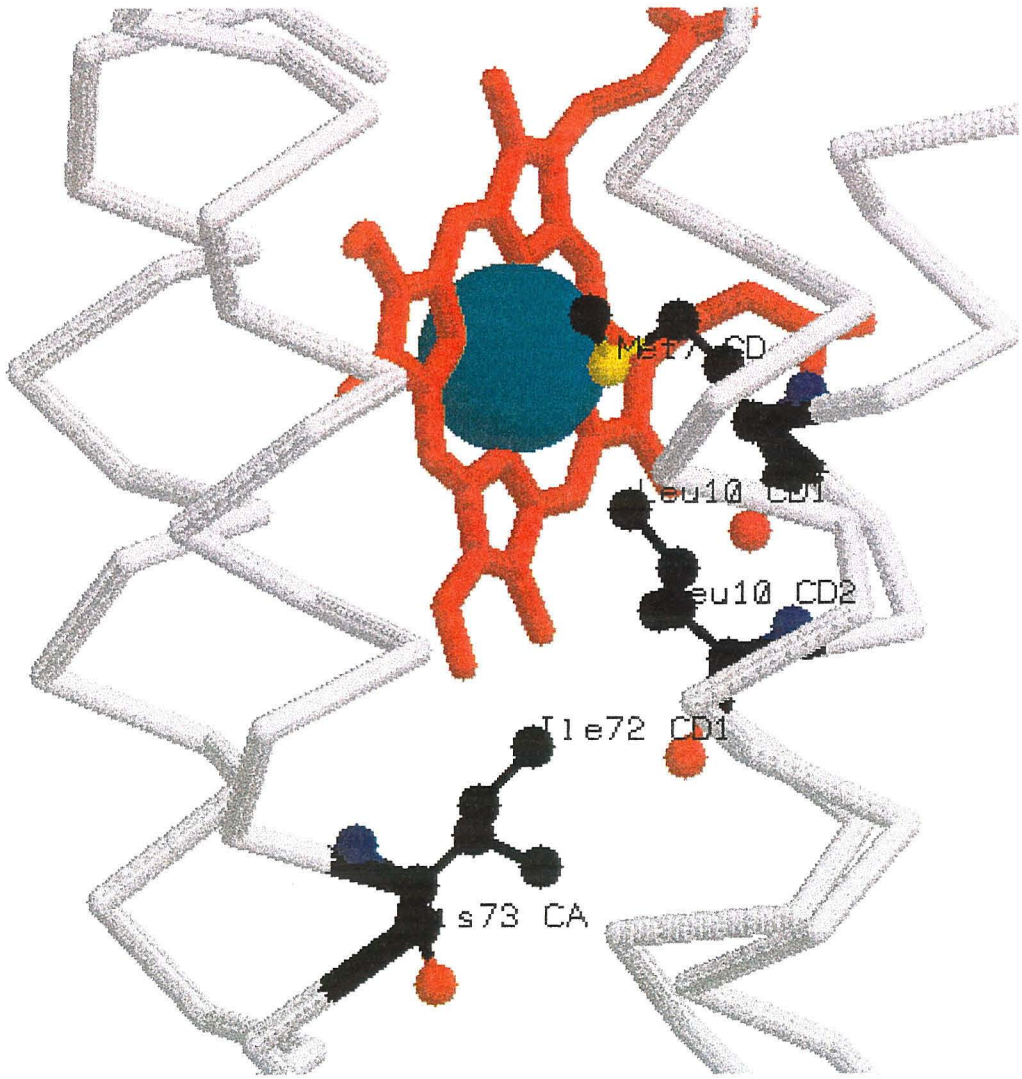
CD
eu10 CD1
eu10 CD2
Ile72 CD1
s73 CA

Figure Chapter 3-7: The UV/vis spectrum of labelled and unlabelled WT b_{562}. Upper: the spectrum of unlabelled b_{562} (thin) and the spectrum of ruthenium labelled WT b_{562} (thick). Lower: the spectrum of WT b_{562} (thick) and the difference spectrum of WT b_{562} and the ruthenium label model compound $Ru(bpy)_2.im_2$.

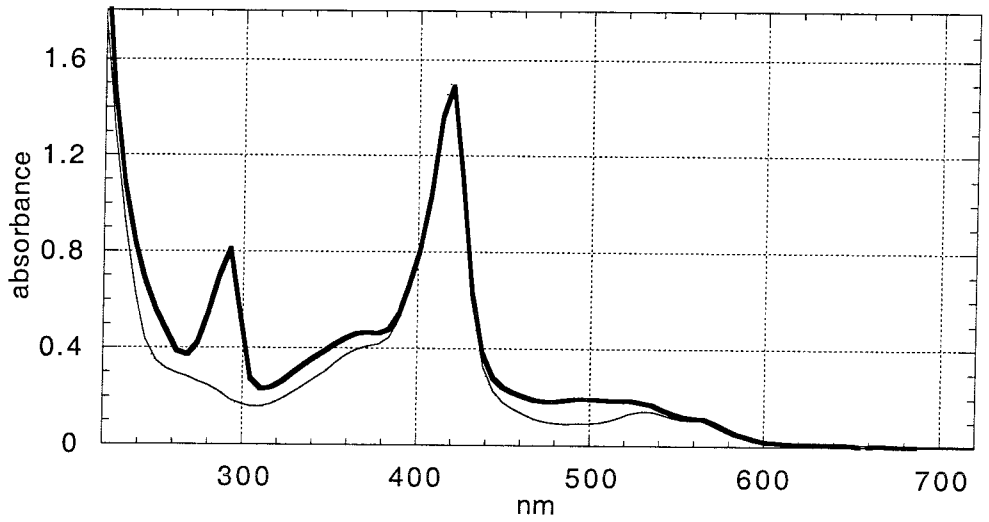
absorbance
1.6
1.2
0.8
0.4
0
300
400
500
600
700
nm

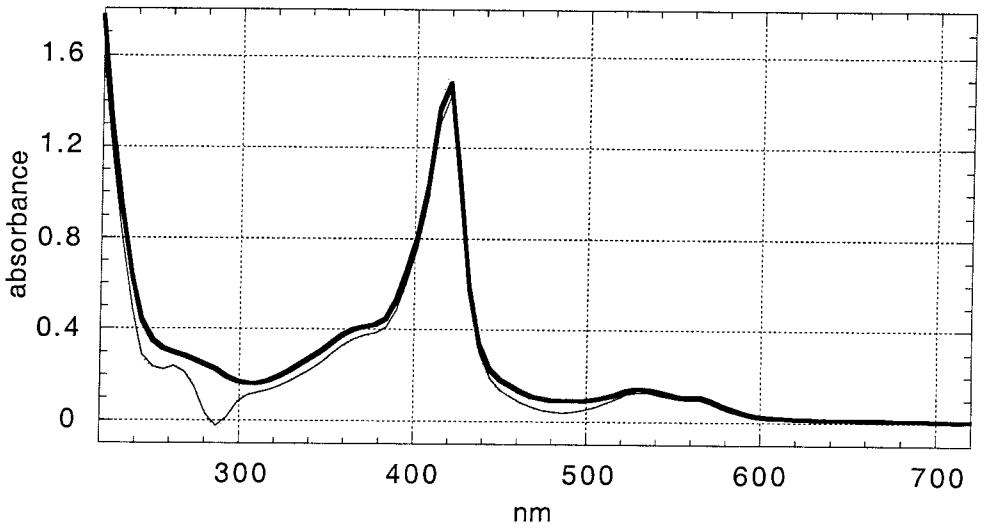
absorbance
1.6
1.2
0.8
0.4
0
300
400
500
600
700
nm

Figure Chapter 3-8: UV/vis absorption spectra of labelled WT b_{562} and the G70H mutant.

WT b_{562} (thick line) and G70H (thin line).

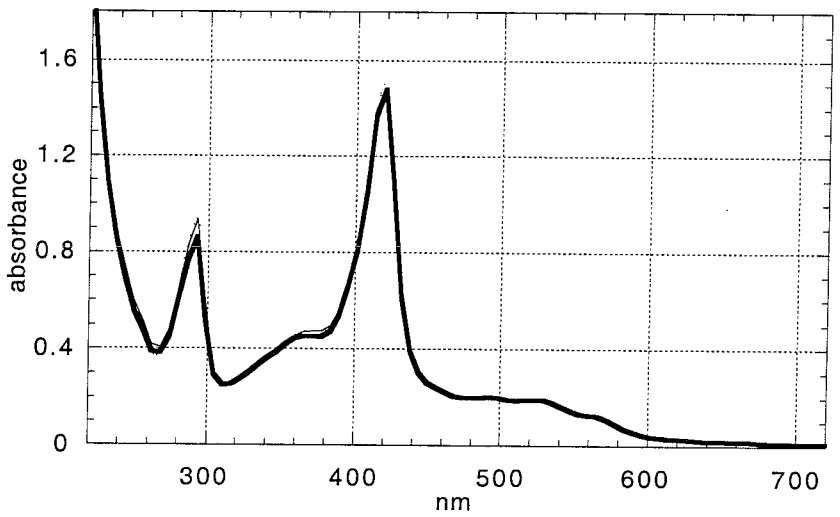
1.6
1.2
0.8
0.4
0
absorbance
300
400
500
600
700
nm

Figure Chapter 3-9: The UV/vis absorption spectra of unlabelled and labelled WT b_{562} and the D73H mutant.

Upper: the spectra of WT b_{562} (thick) and the D73H mutant (thin). Lower: the spectra of labelled WT b_{562} (thick) and labelled D73H (thin).

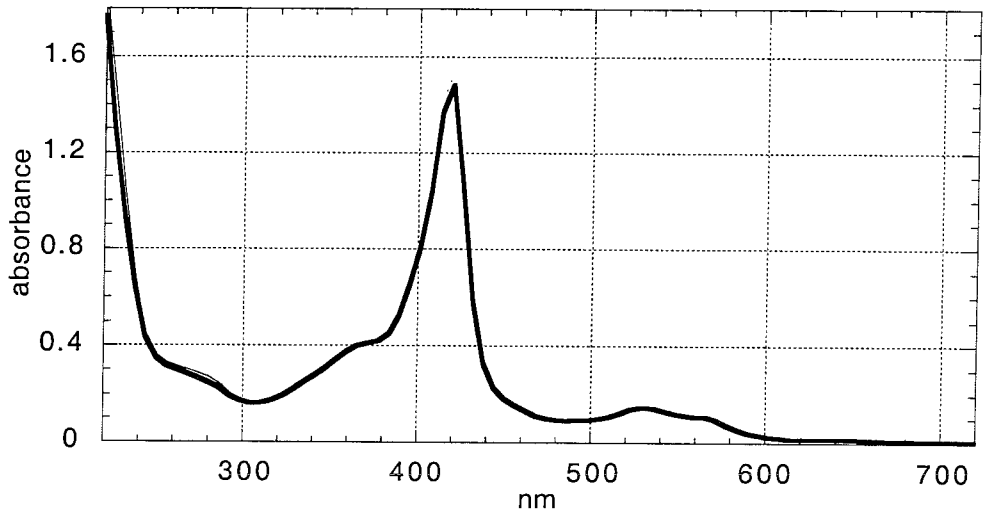
absorbance
1.6
1.2
0.8
0.4
0
300
400
500
600
700
nm

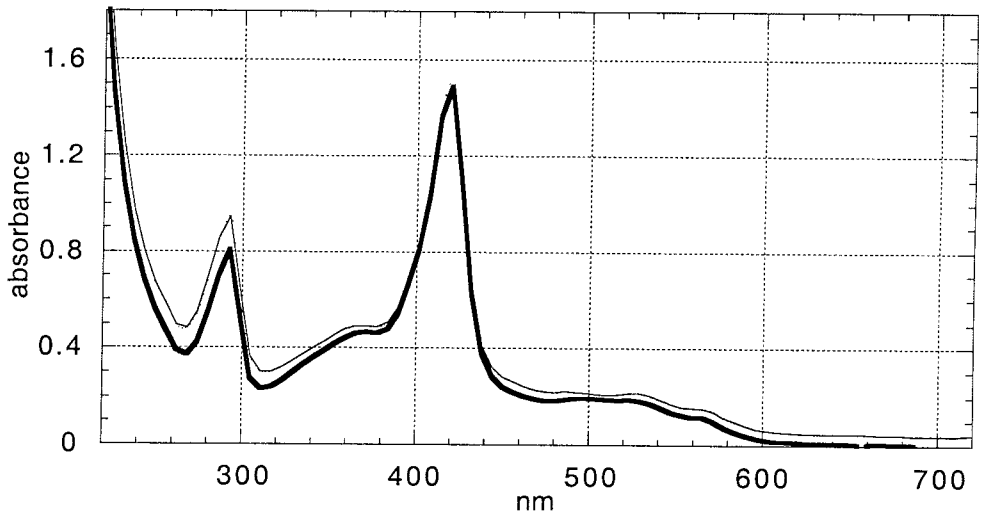
absorbance
1.6
1.2
0.8
0.4
0
300
400
500
600
700
nm

Figure Chapter 3-10: Fluorescence spectra of the D73H mutant.

Fluorescence spectra of the $Ru(bpy)_2$.im-D73H and the Ru(bpy)2.H2O-D73H (monoaqua) mutant. The spectra of the Ru(bpy)2.H2O-D73H mutant contains a small quantity of the $Ru(bpy)_2$.im-D73H form as seen by the emission at 670 nm. Both samples contain 13 μM protein. Also shown is the model compound $Ru(bpy)_2.im_2$ (dashed).

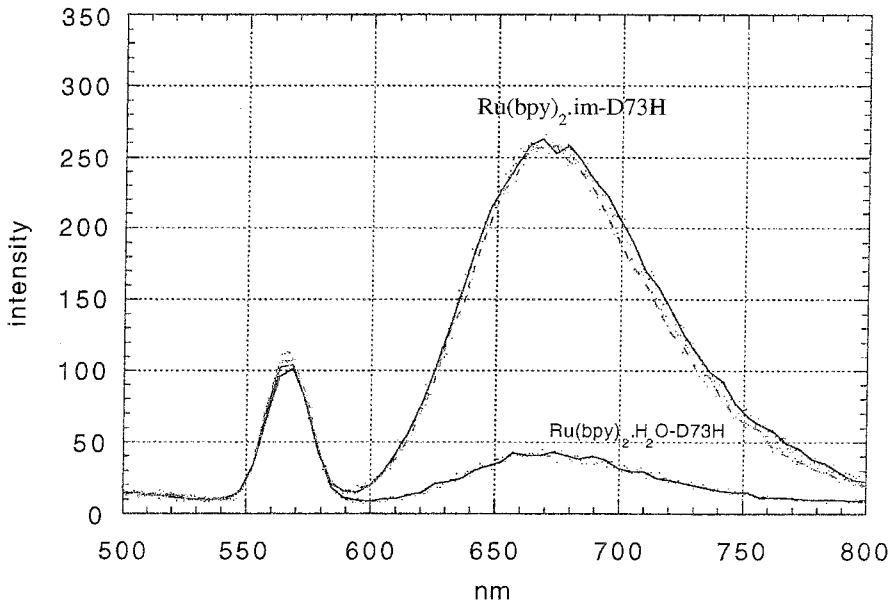
350
300
250
200
150
100
50
0
intensity
500
550
600
650
700
750
800
nm
Ru(bpy)2.im-D73H
Ru(bpy)2.H2O-D73H

Figure Chapter 3-11: CD spectra of WT b_{562} and the ruthenium labelled E86H mutant.

Concentration of WT b_{562} was 12 μM and the labelled E86H mutant 8 μM. The intensity of the E86H sample has been normalized to the concentration of the WT sample.

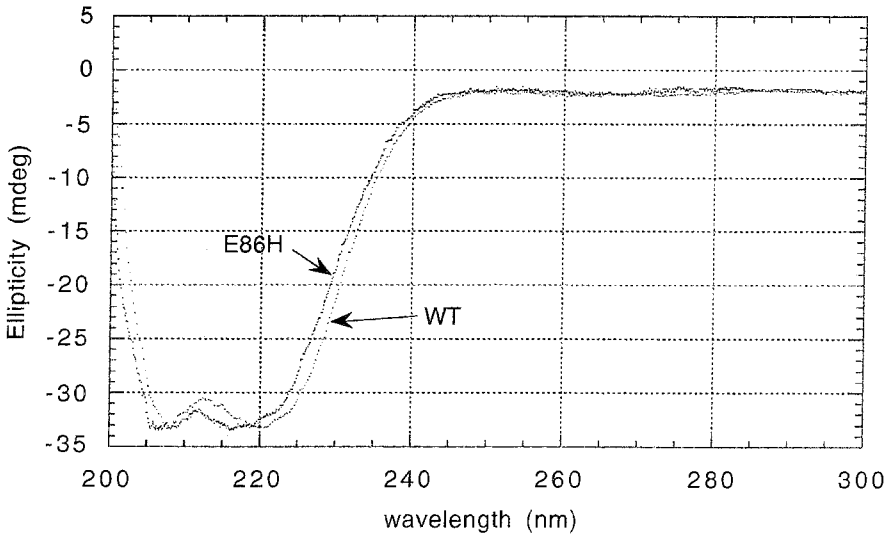
5
0
-5
-10
-15
-20
-25
-30
-35
Ellipticity (mdeg)
E86H
WT
200
220
240
260
280
300
wavelength (nm)

Figure Chapter 3-12: Thermal denaturation curves for ferrous (filled circles) and ferric WT b_{562}.

Also shown (lower) is the UV/vis spectra for ferric protein at various temperatures. Samples were 8.5 μM in 50 mM KP_i.

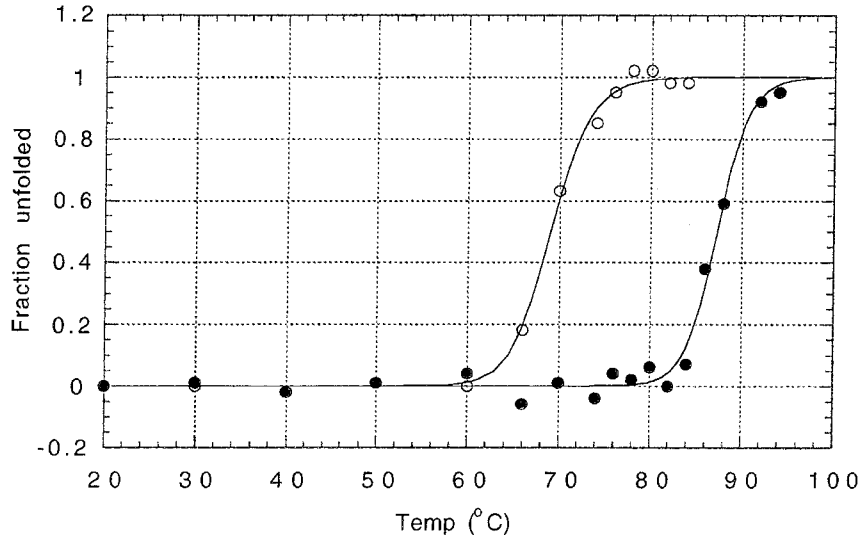
Fraction unfolded
1.2
1
0.8
0.6
0.4
0.2
0
-0.2
20
30
40
50
60
70
80
90
100
Temp (°C)

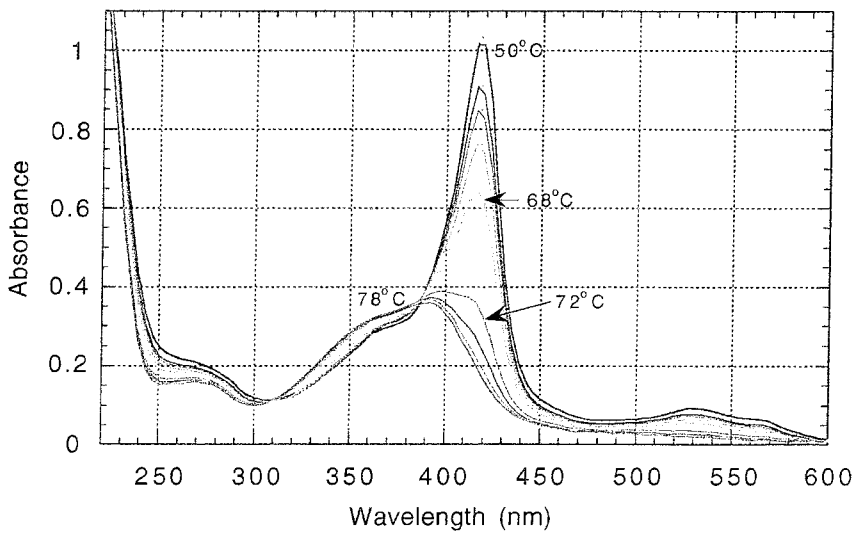
Absorbance
1
0.8
0.6
0.4
0.2
0
50°C
68°C
78°C
72°C
250
300
350
400
450
500
550
600
Wavelength (nm)

Figure Chapter 3-13: Transient absorption difference spectra for apo E86H and WT b_{562}.

Upper: transient absorption spectrum of apo E86H recorded in the μs time scale using the photo-induced method. Lower: transient absorption spectrum from a flash-quench experiment with WT b_{562} showing the initial (circles) post laser pulse decrease in Fe^{2+} at 430 nm and the increase in MV quencher radical at 400 nm. The increase in Fe^{3+} at 414 nm is a shoulder on the MV absorbance. At a later time (squares) the Fe^{2+} increases and the absorption's due to MV radical and Fe^{3+} decrease.

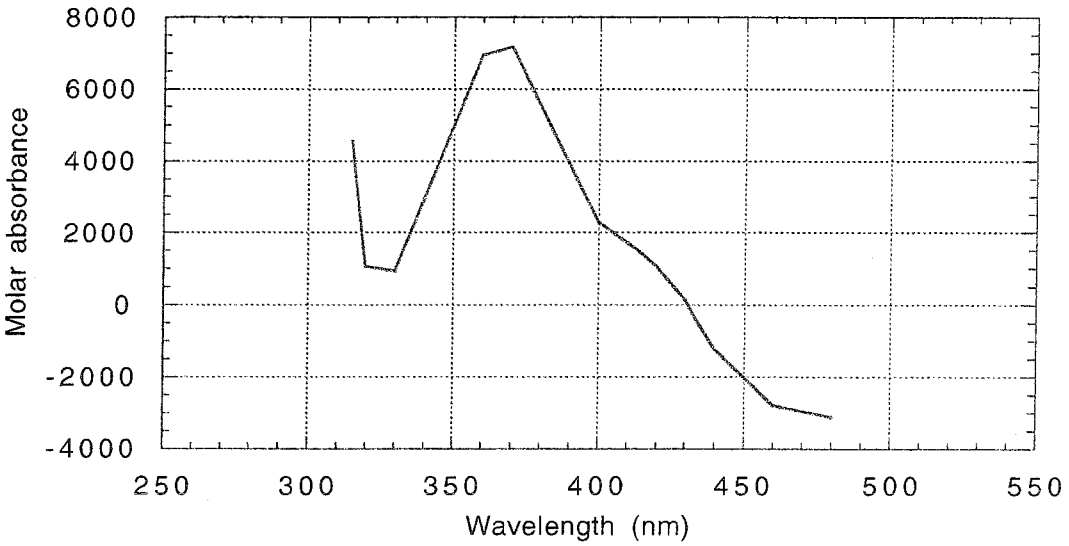
8000
6000
4000
2000
0
-2000
-4000
Molar absorbance
250
300
350
400
450
500
550
Wavelength (nm)

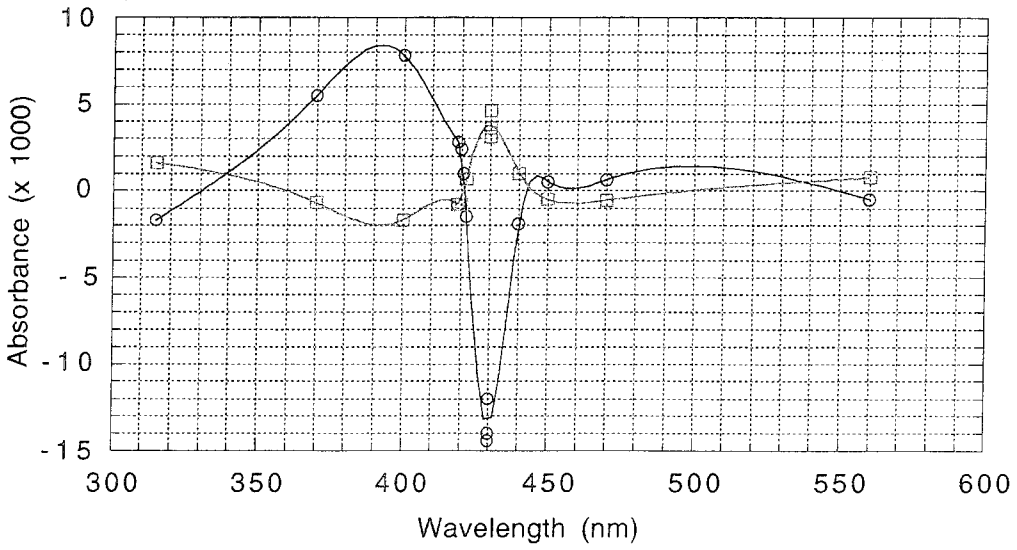
10
5
0
- 5
-10
-15
Absorbance (x 1000)
300
350
400
450
500
550
600
Wavelength (nm)

Figure Chapter 3-14: Concentration and temperature *versus* the ET rate for WT b_{562}.

Upper: the effect of concentration on the rate k^{b}_{ET}. Lower: the effect of temperature on the rate k^{b}_{ET}.

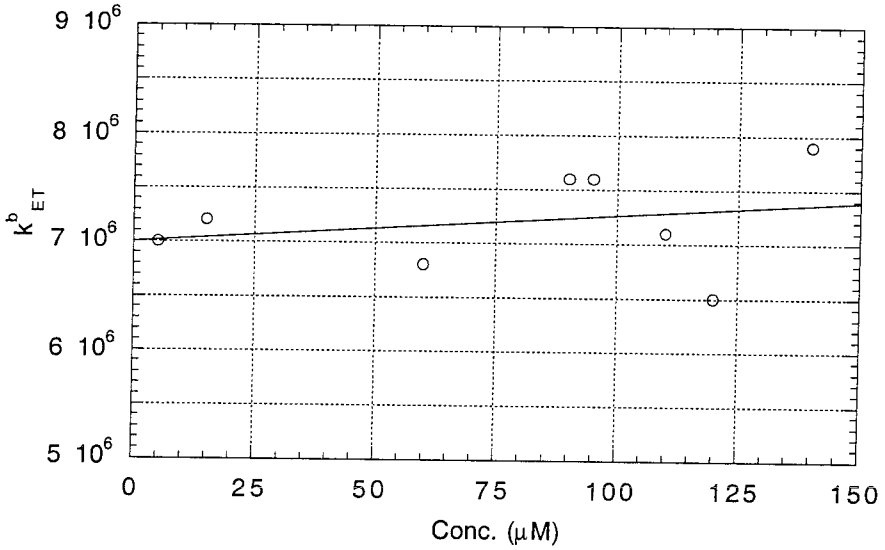
9 10^6
8 10^6
7 10^6
6 10^6
5 10^6
k^b_ET
0
25
50
75
100
125
150
Conc. (μM)

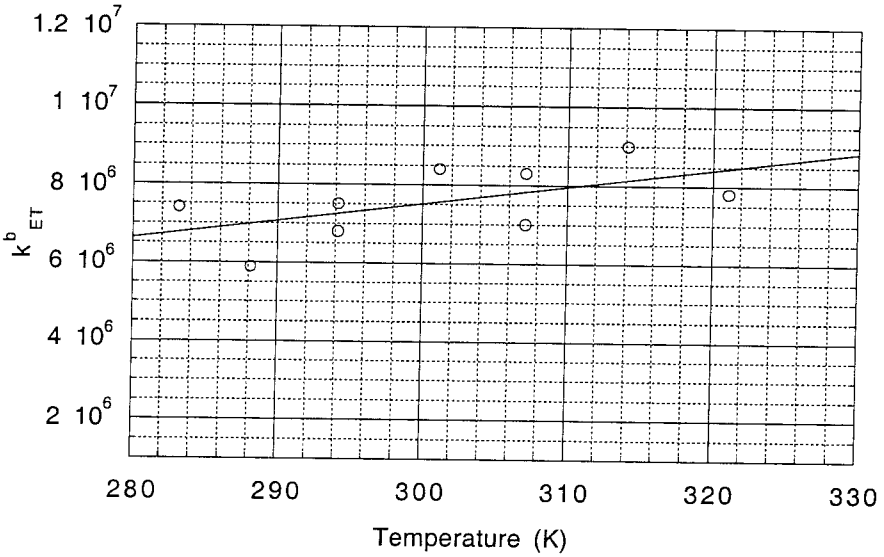
1.2 10^7
1 10^7
8 10^6
6 10^6
4 10^6
2 10^6
k^b_ET
280
290
300
310
320
330
Temperature (K)

Figure Chapter 3-15: WT b_{562} photo induced transient absorbencies.

WT (5.1μM) photoinduced transient absorbance monitored at (A) 430 nm and (B) 414 nm, showing the reduction of Fe^{3+} and the fit to the trace. The residual (signal minus fit) is shown above the traces.

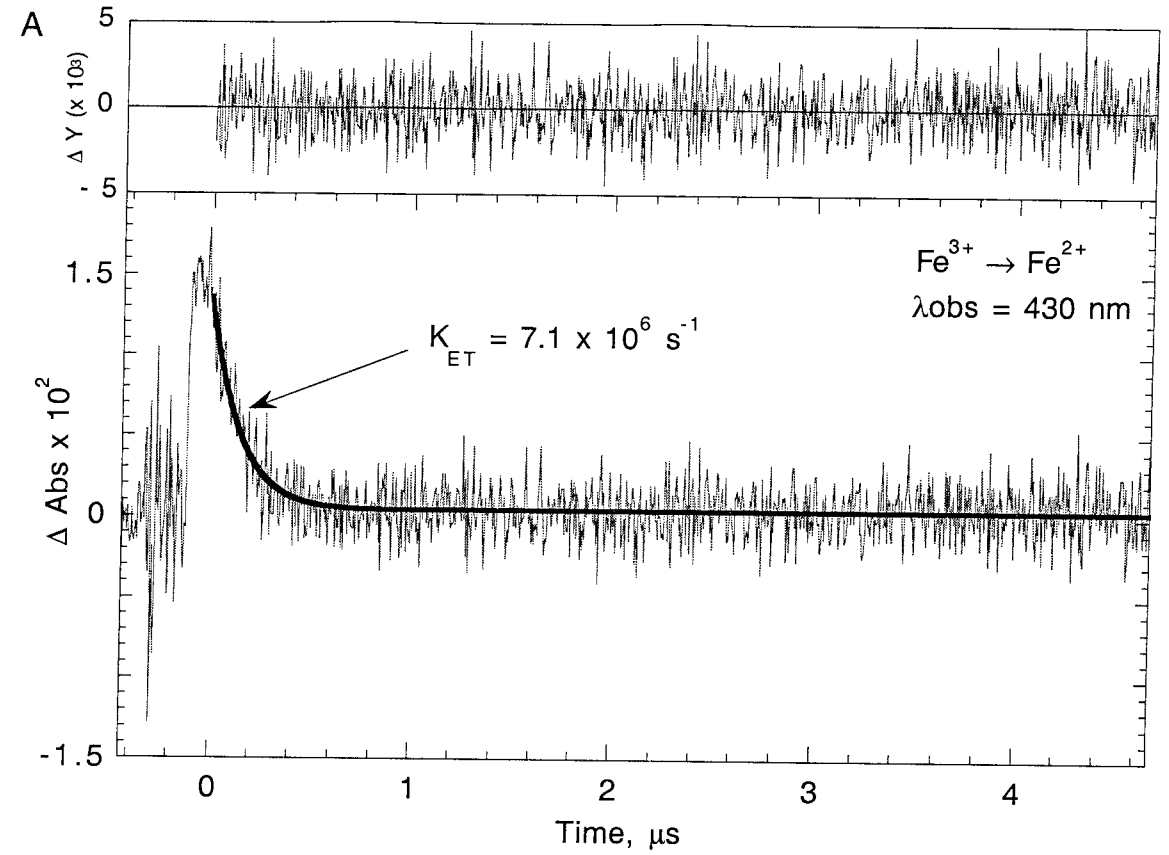
A
5
0
- 5
Δ Y (x 10³)
1.5
0
-1.5
Δ Abs x 10²
$Fe^{3+} \rightarrow Fe^{2+}$
λobs = 430 nm
K_{ET} = 7.1 x 10^6 s^{-1}
0
1
2
3
4
Time, μs

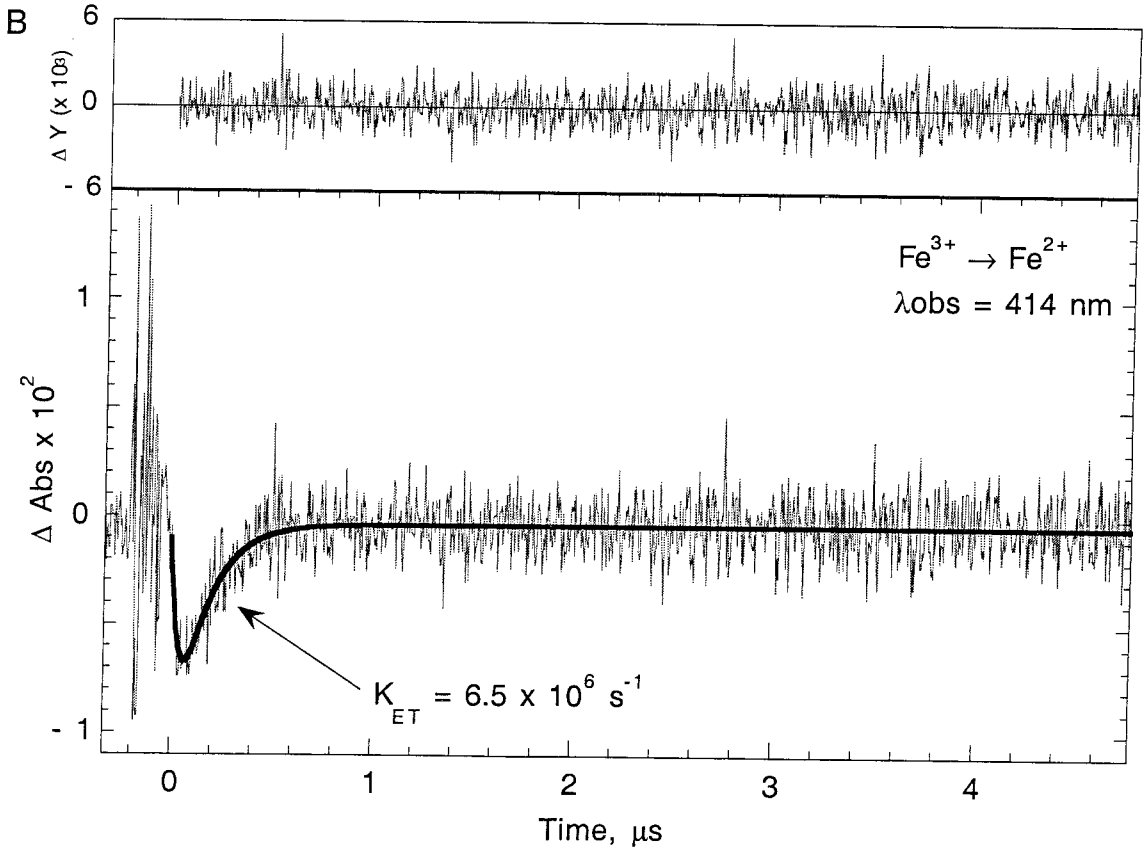
B
6
0
- 6
Δ Y (x 10³)
1
0
- 1
Δ Abs x 10²
$Fe^{3+} \rightarrow Fe^{2+}$
λobs = 414 nm
K_{ET} = 6.5 x 10^6 s^{-1}
0
1
2
3
4
Time, μs

Figure Chapter 3-16: WT b_{562} flash-quench transient absorbencies.

WT (5.1 μM) flash-quenched transient absorbance monitored at (A) 430 nm and (B) 414 nm, showing the oxidation of Fe^{2+} and the fit to the trace. The residual (signal minus fit) is shown above the traces.

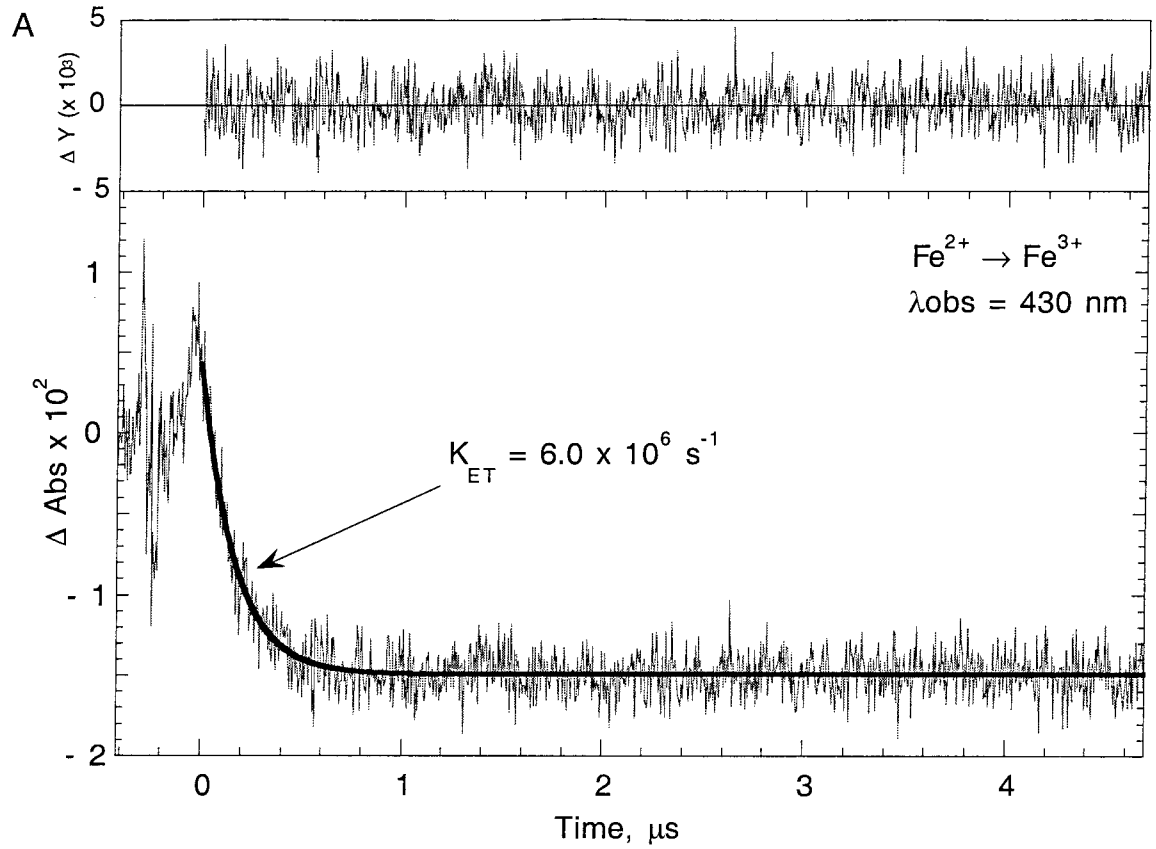
A
5
0
- 5
Δ Y (x 10³)
1
0
- 1
- 2
Δ Abs x 10²
Fe2+ → Fe3+
λobs = 430 nm
K_ET = 6.0 x 10^6 s^-1
0
1
2
3
4
Time, μs

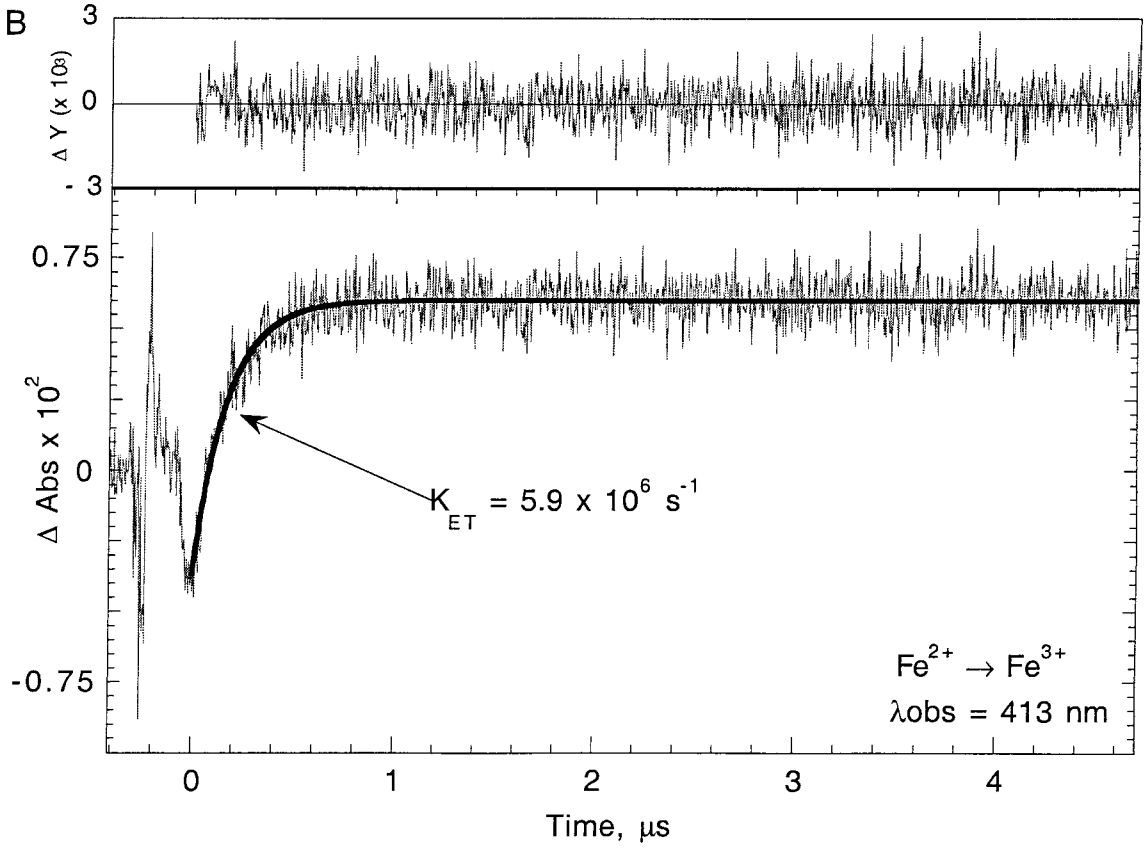
B
3
0
- 3
Δ Y (x 10³)
0.75
0
-0.75
Δ Abs x 10²
K_ET = 5.9 x 10^6 s^-1
Fe2+ → Fe3+
λobs = 413 nm
0
1
2
3
4
Time, μs

Figure Chapter 3-17: WT excited state transient emissions at 670 nm and transient absorption at 315 nm.

WT (14μM) emissions monitored at (A) 670 nm and (B) flash-quenched transient absorbance monitored at 315 nm showing the reduction of Ru^{3+} and *Ru absorbance. The fit to the traces is shown and the residual (signal minus fit) is shown above the traces.

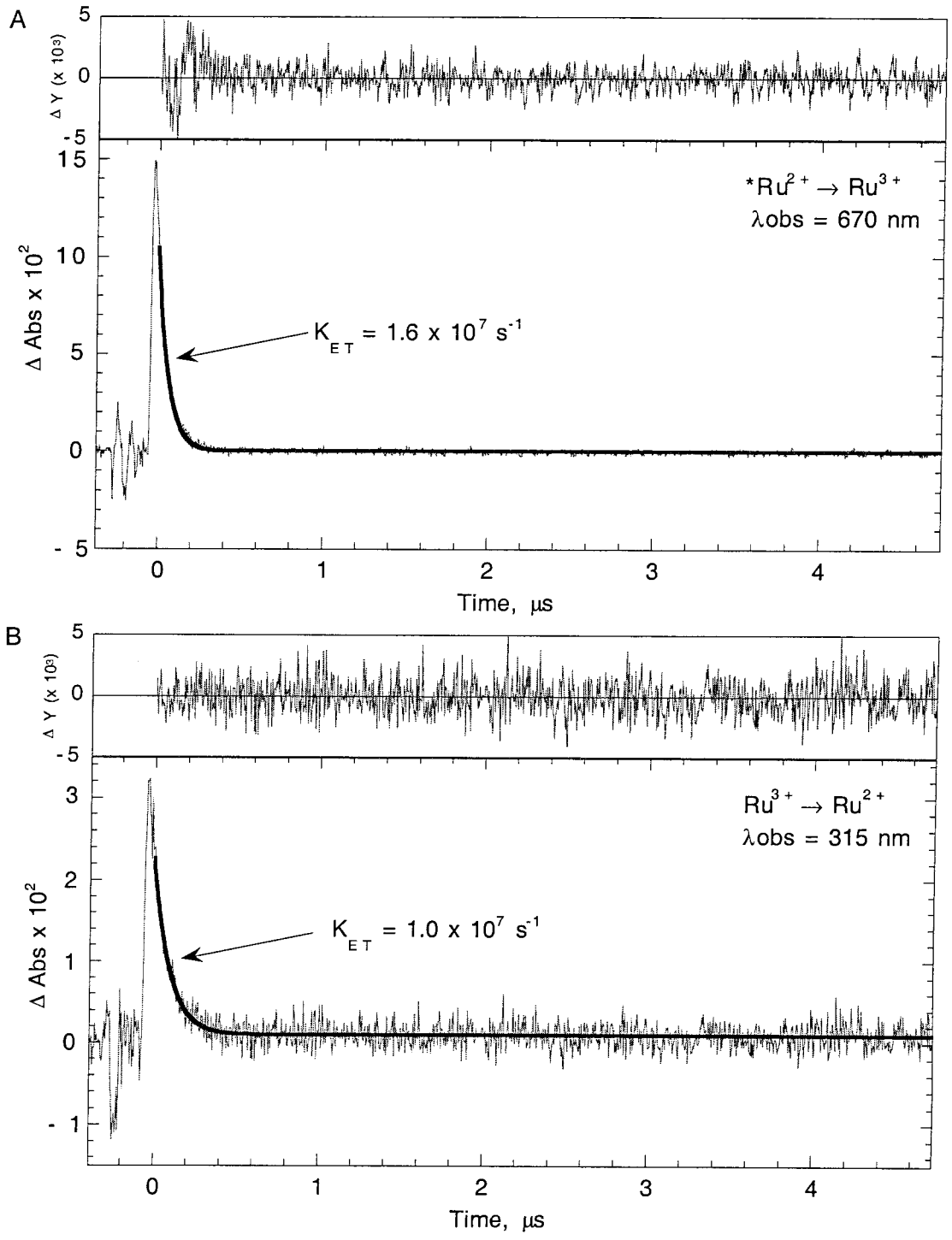
A
Δ Y (x 10³)
5
0
-5
15
10
5
0
- 5
Δ Abs x 10²
*Ru²⁺ → Ru³⁺
λobs = 670 nm
K_ET = 1.6 x 10⁷ s⁻¹
0
1
2
3
4
Time, μs
B
Δ Y (x 10³)
5
0
-5
3
2
1
0
- 1
Δ Abs x 10²
Ru³⁺ → Ru²⁺
λobs = 315 nm
K_ET = 1.0 x 10⁷ s⁻¹
0
1
2
3
4
Time, μs

Figure Chapter 3-18: G70H photo induced transient absorbencies.

G70H (22 μM) photoinduced transient absorbance monitored at (A) 430 nm and (B) 414 nm, showing the reduction of Fe^{3+} and the fit to the trace. The residual (signal minus fit) is shown above the traces.

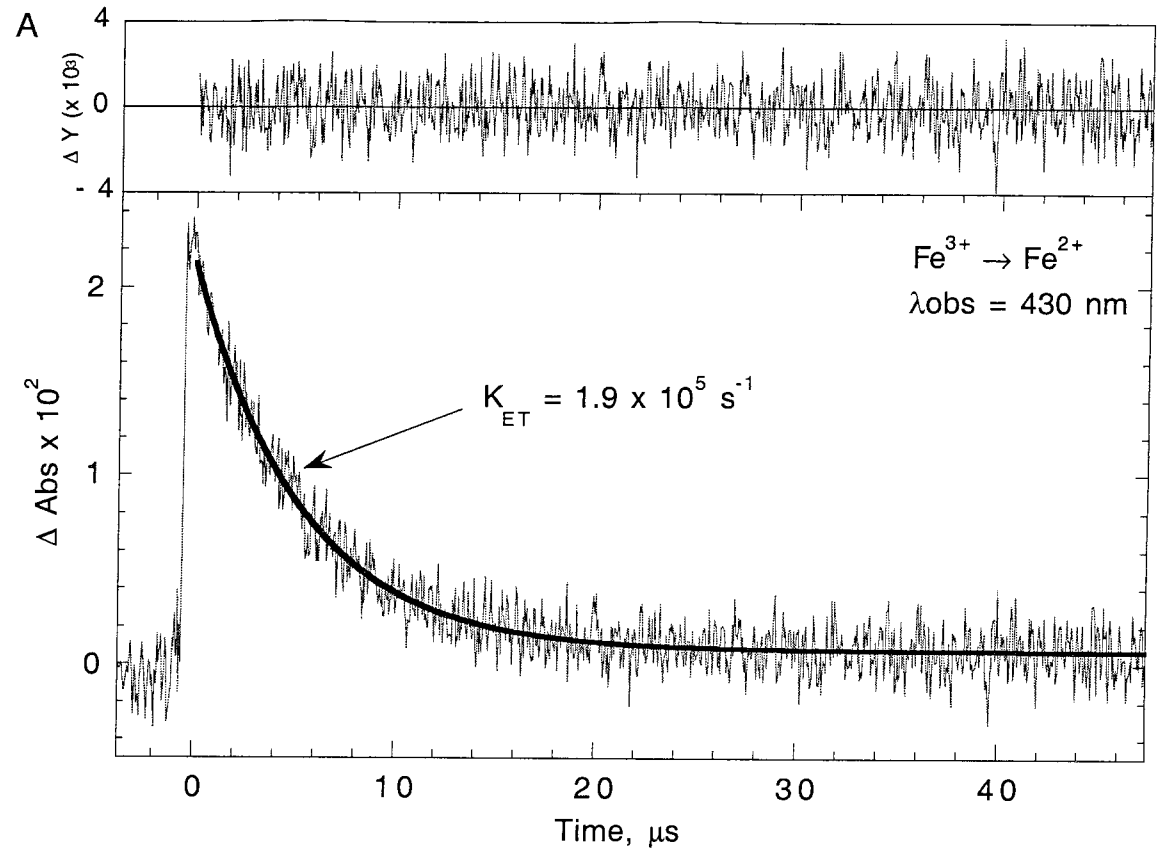
A
4
0
- 4
Δ Y (x 10³)
2
1
0
Δ Abs x 10²
Fe3+ → Fe2+
λobs = 430 nm
K ET = 1.9 x 10⁵ s⁻¹
0
10
20
30
40
Time, μs

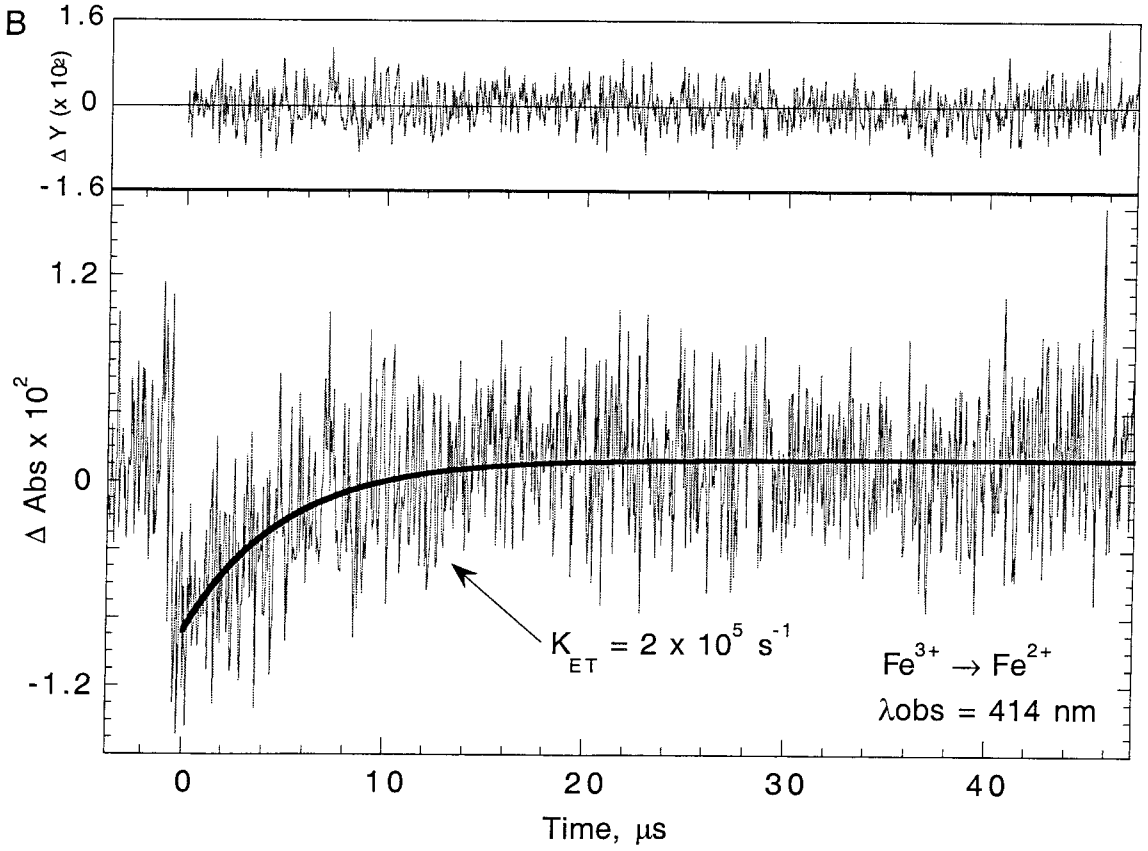
B
1.6
0
-1.6
Δ Y (x 10²)
1.2
0
-1.2
Δ Abs x 10²
K ET = 2 x 10⁵ s⁻¹
Fe3+ → Fe2+
λobs = 414 nm
0
10
20
30
40
Time, μs

Figure Chapter 3-19: G70H flash-quench transient absorbencies.

G70H (7 μM) flash-quenched transient absorbance monitored at (A) 430 nm and (B) 414 nm, showing the oxidation of Fe^{2+} and the fit to the trace. The residual (signal minus fit) is shown above the traces.

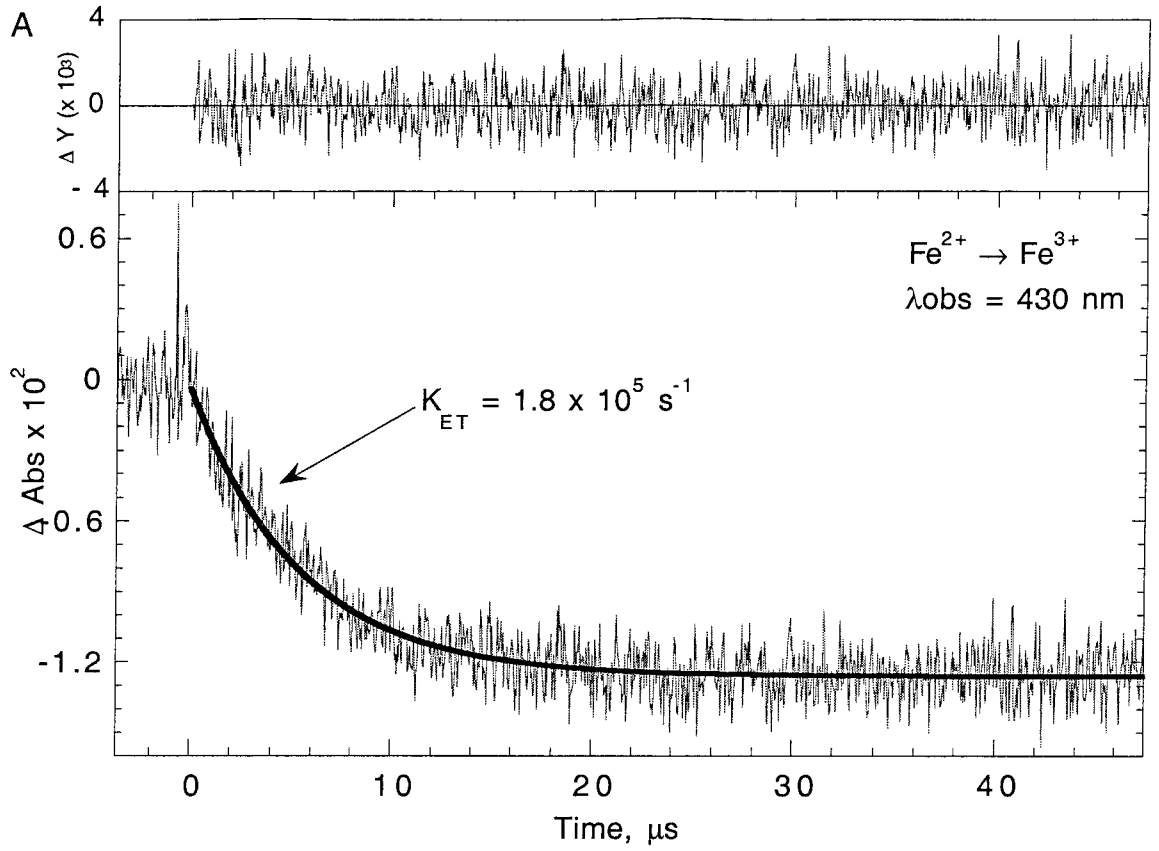
A
4
0
- 4
Δ Y (x 10³)
0.6
0
-0.6
-1.2
Δ Abs x 10²
Fe2+ → Fe3+
λobs = 430 nm
K_ET = 1.8 x 10^5 s^-1
0
10
20
30
40
Time, μs

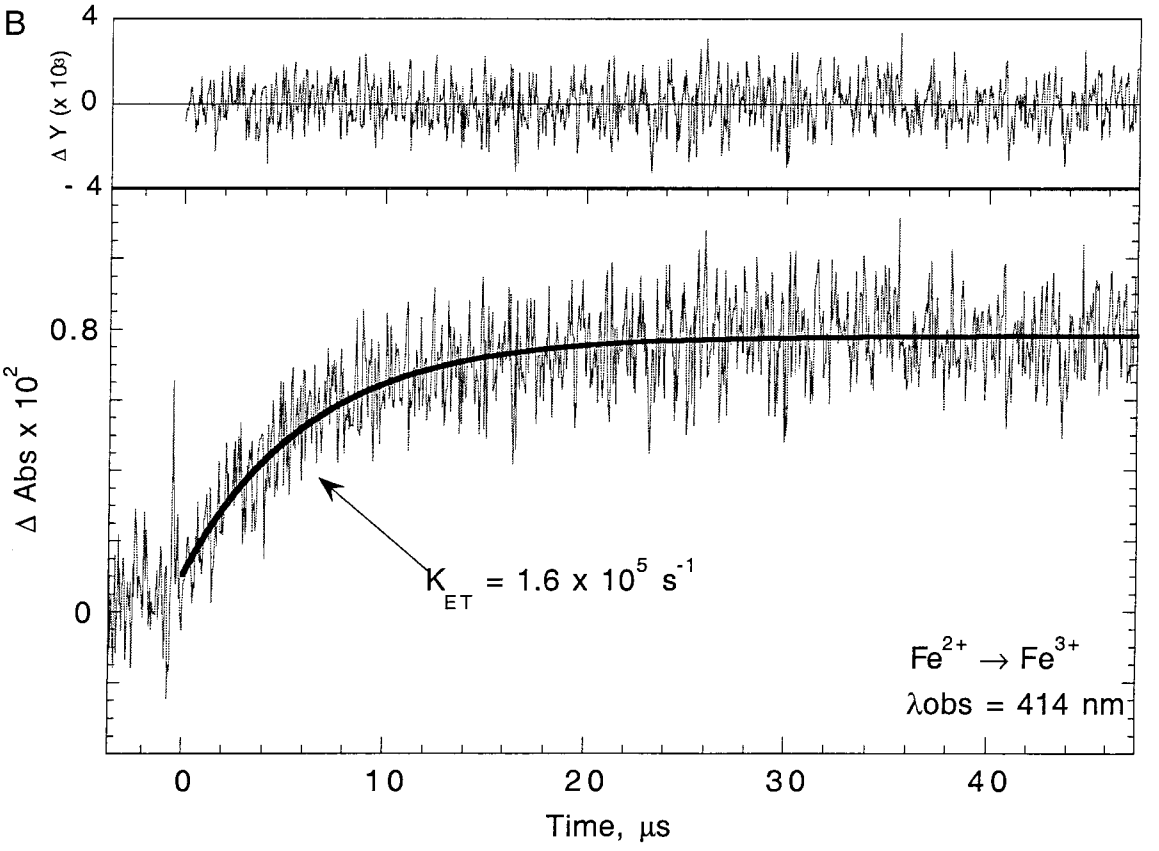
B
4
0
- 4
Δ Y (x 10³)
0.8
0
Δ Abs x 10²
K_ET = 1.6 x 10^5 s^-1
Fe2+ → Fe3+
λobs = 414 nm
0
10
20
30
40
Time, μs

Figure Chapter 3-20: G70H transient emissions at 670 nm and absorption at 315 nm.

G70H (19μM) emissions monitored at (A) 670 nm and (B) flash-quenched transient absorbance monitored at 315 nm showing the reduction of Ru^{3+} and *Ru absorbance. The fit to the traces is shown and the residual (signal minus fit) is shown above the traces.

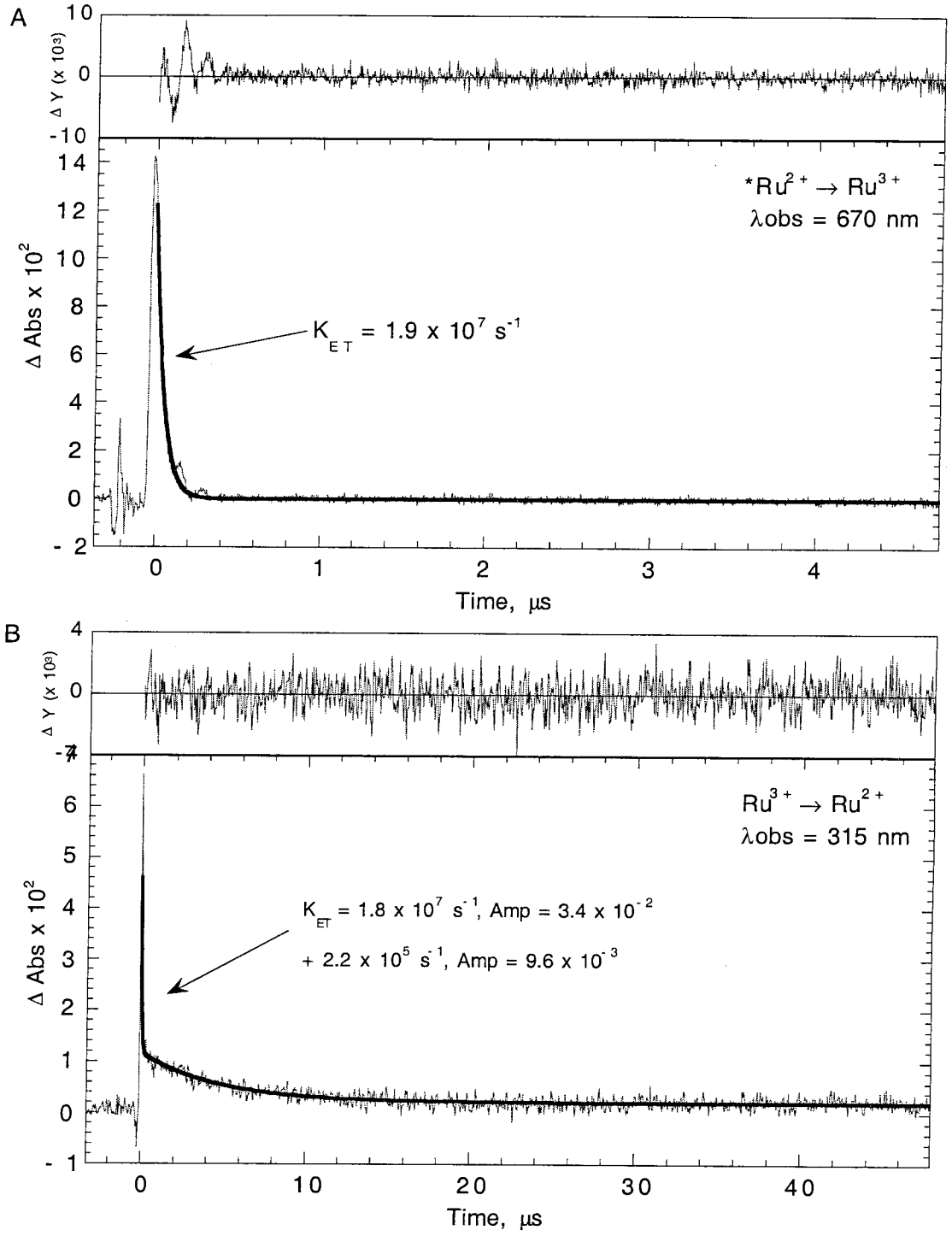
A
Δ Y (x 10³)
Δ Abs x 10²
*Ru²⁺ → Ru³⁺
λobs = 670 nm
K_ET = 1.9 x 10⁷ s⁻¹
Time, μs
B
Δ Y (x 10³)
Δ Abs x 10²
Ru³⁺ → Ru²⁺
λobs = 315 nm
K_ET = 1.8 x 10⁷ s⁻¹, Amp = 3.4 x 10⁻²
+ 2.2 x 10⁵ s⁻¹, Amp = 9.6 x 10⁻³
Time, μs

Figure Chapter 3-21: D73H flash-quench transient absorbencies.

D73H (12 μM) flash-quenched transient absorbance monitored at (A) 430 nm and (B) 414 nm, showing the oxidation of Fe^{2+}. These experiments used the irreversible quencher $Co(NH_3)_5Cl_2$.

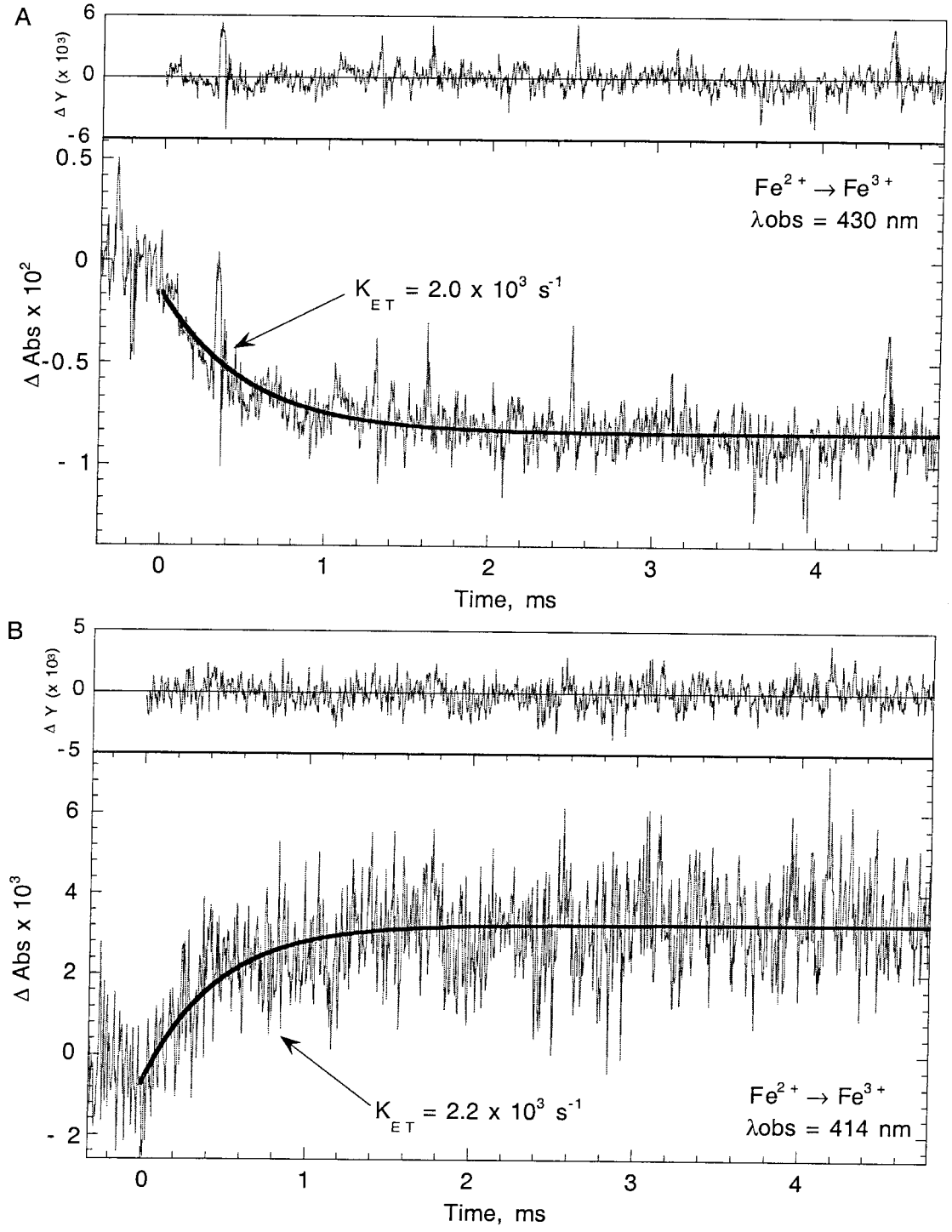
A
Δ Y (x 10³)
6
0
-6
0.5
0
-0.5
- 1
Δ Abs x 10²
Fe²⁺ → Fe³⁺
λobs = 430 nm
K_ET = 2.0 x 10³ s⁻¹
0
1
2
3
4
Time, ms
B
Δ Y (x 10³)
5
0
-5
6
4
2
0
- 2
Δ Abs x 10³
K_ET = 2.2 x 10³ s⁻¹
Fe²⁺ → Fe³⁺
λobs = 414 nm
0
1
2
3
4
Time, ms

Figure Chapter 3-22: D73H flash-quench transient absorbencies.

D73H (12μM) flash-quenched transient absorbance monitored at (A) 430 nm and (B) 414 nm, showing the oxidation of Fe^{2+}. These experiments used the irreversible quencher $Co(NH_3)_5Cl_2$.

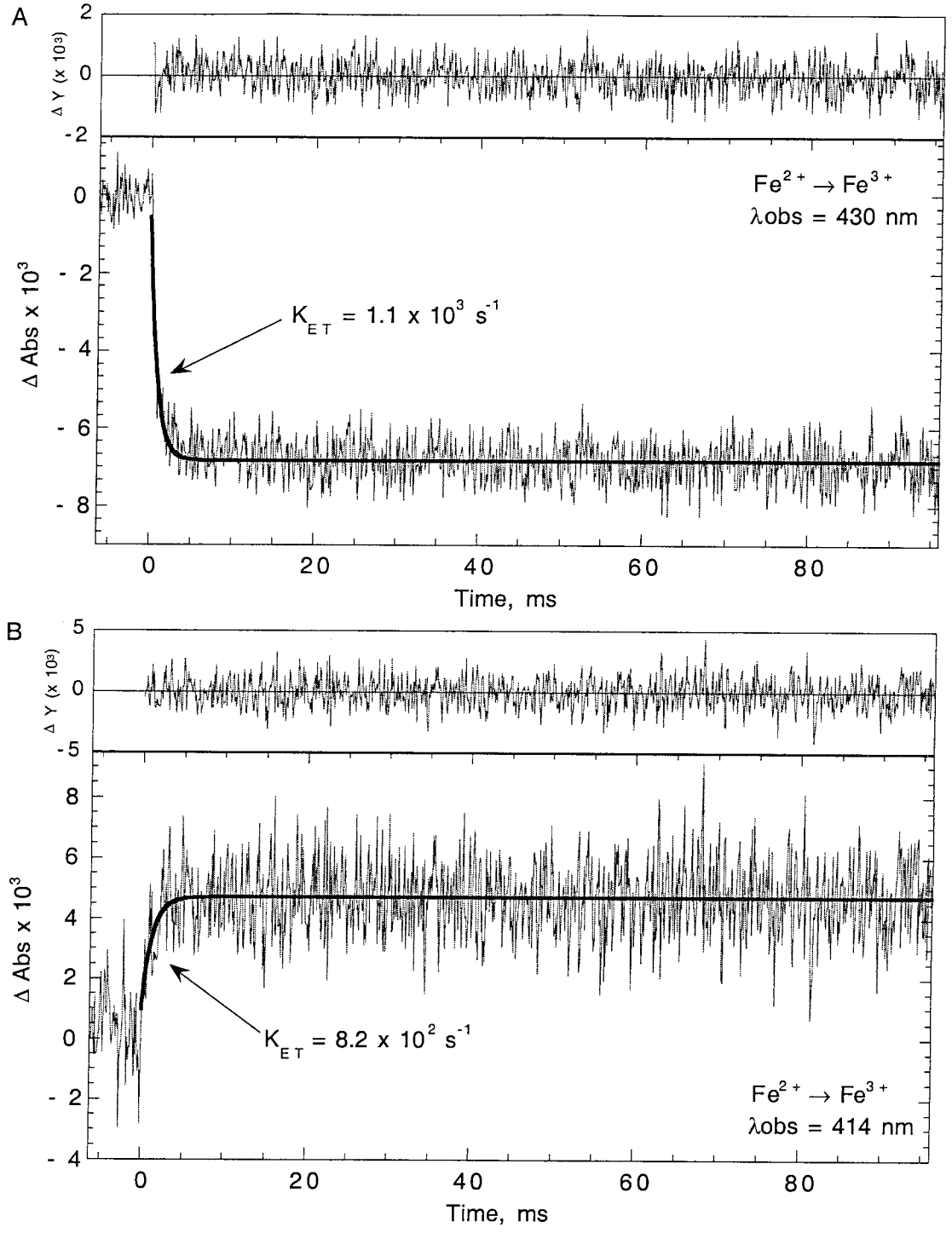
A
Δ Y (x 10³)
2
0
-2
Fe²⁺ → Fe³⁺
λobs = 430 nm
K_ET = 1.1 x 10³ s⁻¹
Δ Abs x 10³
0
- 2
- 4
- 6
- 8
0
20
40
60
80
Time, ms
B
Δ Y (x 10³)
5
0
-5
8
6
4
2
0
- 2
- 4
K_ET = 8.2 x 10² s⁻¹
Fe²⁺ → Fe³⁺
λobs = 414 nm
Δ Abs x 10³
0
20
40
60
80
Time, ms

Figure Chapter 3-23: D73H transient emissions at 670 nm and absorption at 315 nm.

D73H (12.8μM) emissions monitored at (A) 670 nm and (B) flash-quenched transient absorbance monitored at 315 nm showing the reduction of Ru^{3+}. The fit to the traces is shown and the residual (signal minus fit) is shown above the traces.

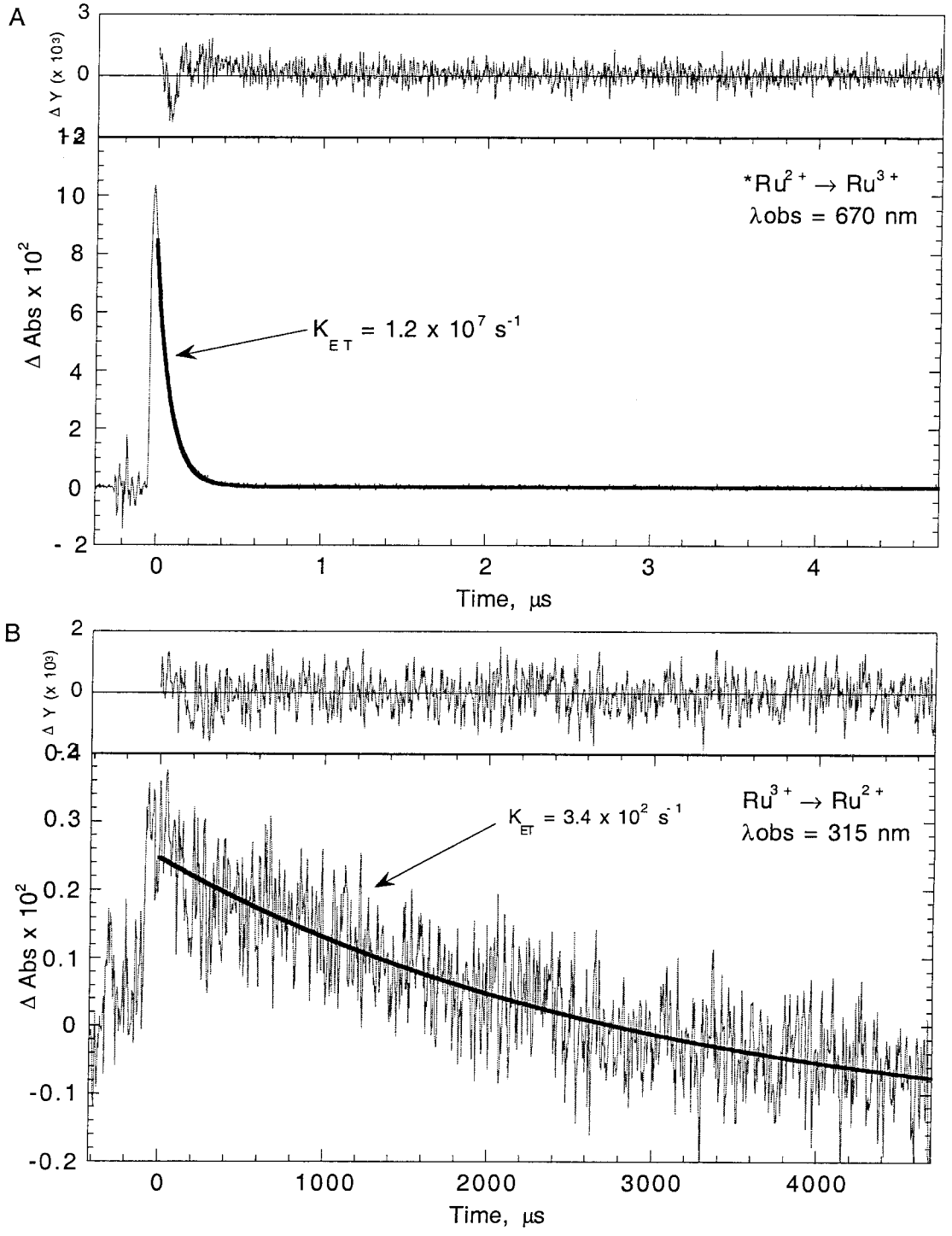
A
Δ Y (x 10³)
3
0
-2
Δ Abs x 10²
10
8
6
4
2
0
- 2
*Ru²⁺ → Ru³⁺
λobs = 670 nm
K_ET = 1.2 x 10⁷ s⁻¹
0
1
2
3
4
Time, μs
B
Δ Y (x 10³)
2
0
-0.2
Δ Abs x 10²
0.3
0.2
0.1
0
-0.1
-0.2
Ru³⁺ → Ru²⁺
λobs = 315 nm
K_ET = 3.4 x 10² s⁻¹
0
1000
2000
3000
4000
Time, μs

Figure Chapter 3-24: Distance *versus* tunneling lengths for helix C of cytochrome b_{562}.

Upper: the metal-metal distance (R_m) *versus* the tunnelling length (σl). Lower: the metal-heme distance (R_h) *versus* the metal-heme tunnelling distance (σl heme) for helix C of b_{562}.

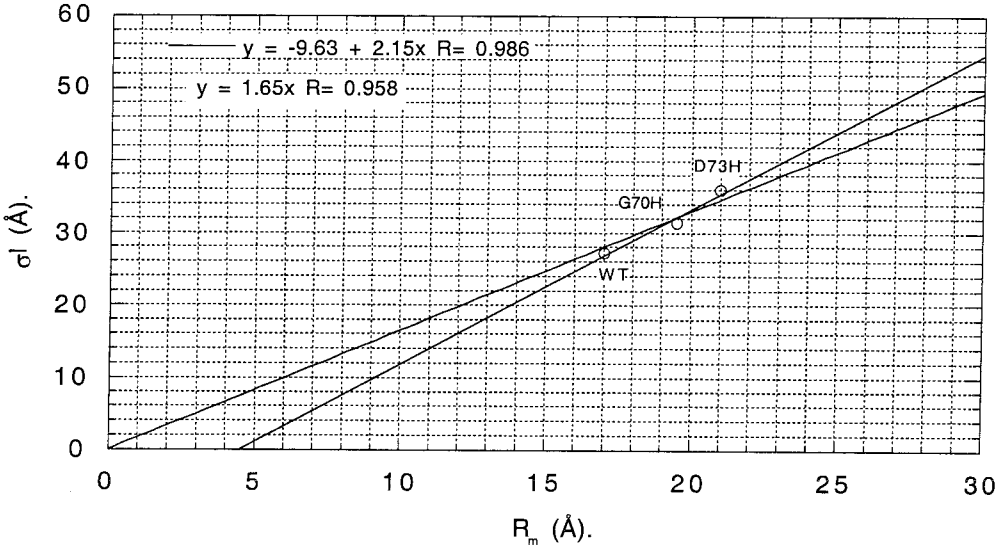
y = -9.63 + 2.15x R= 0.986
y = 1.65x R= 0.958
D73H
G70H
WT
σI (Å).
R_m (Å).
0
10
20
30
40
50
60
0
5
10
15
20
25
30

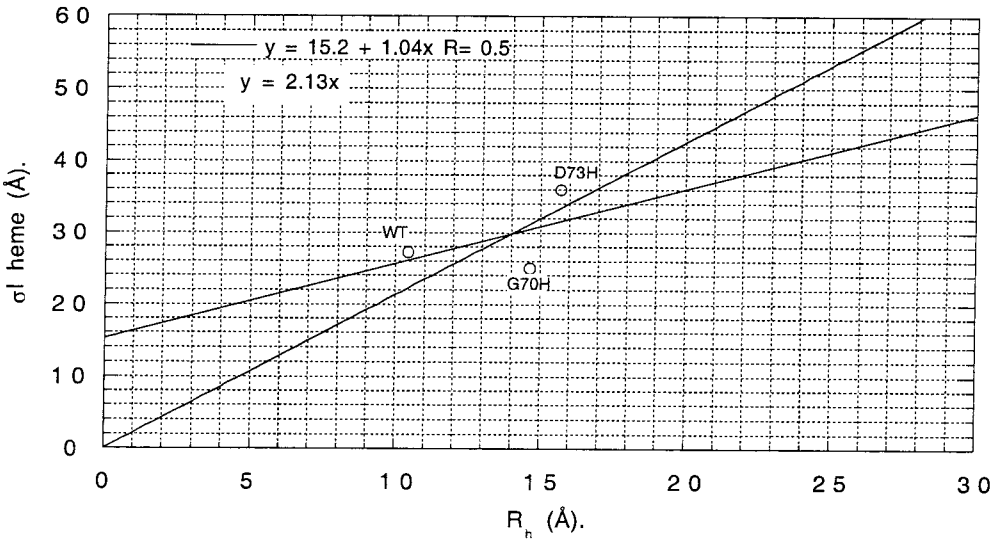
y = 15.2 + 1.04x R= 0.5
y = 2.13x
D73H
WT
G70H
σI heme (Å).
R_h (Å).
0
10
20
30
40
50
60
0
5
10
15
20
25
30

Figure Chapter 3-25: The metal-metal distance (R_m) *versus* log k_{max} (upper) and metal-metal sigma tunneling length (σl) *versus* log k_{max} (lower).

R_m is the distance from the N2 His-X (X = mutation) ruthenium bond to the Fe atom and σl is the His-X Cα-Cβ bond to the Fe ligand bond tunnelling length (as calculated by the Pathways Program) plus 4 bond lengths.

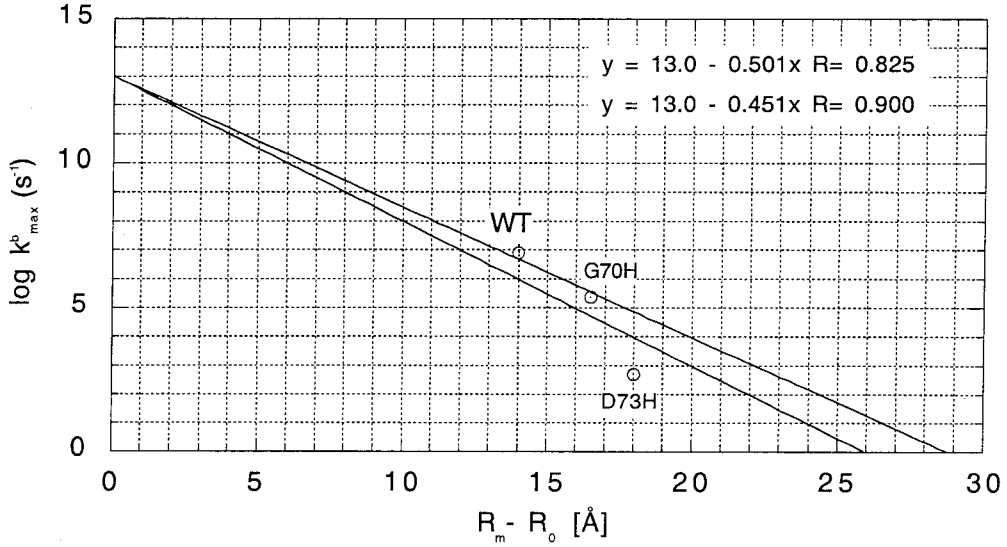
y = 13.0 - 0.501x R= 0.825
y = 13.0 - 0.451x R= 0.900
WT
G70H
D73H
log k^b_{max} (s^{-1})
$R_m - R_0$ [Å]
0
5
10
15
20
25
30

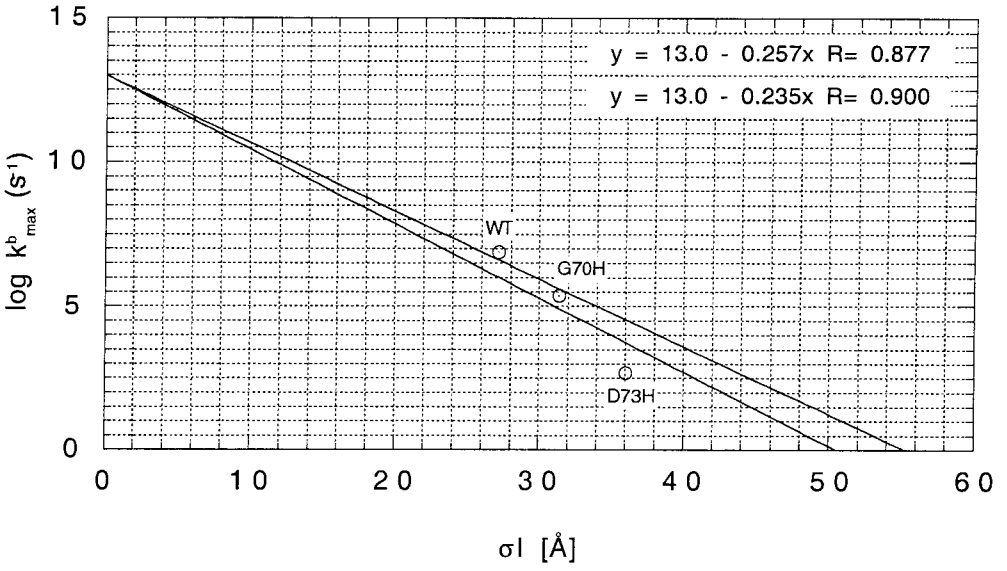
y = 13.0 - 0.257x R= 0.877
y = 13.0 - 0.235x R= 0.900
WT
G70H
D73H
log k^b_{max} (s^{-1})
σI [Å]
0
10
20
30
40
50
60

Figure Chapter 3-26: The metal-heme distance (R_h) *versus* log k_{max} (upper) and the metal-heme tunnelling length (σl heme) *versus* log k_{max} (lower).

R_h is the distance from the N2 His-X (X = mutation) ruthenium bond to the closest porphyrin ring atom and σl heme is the His-X Cα-Cβ bond to the closest porphyrin ring bond tunnelling length (as calculated by the Pathways Program) plus 4 bonds.

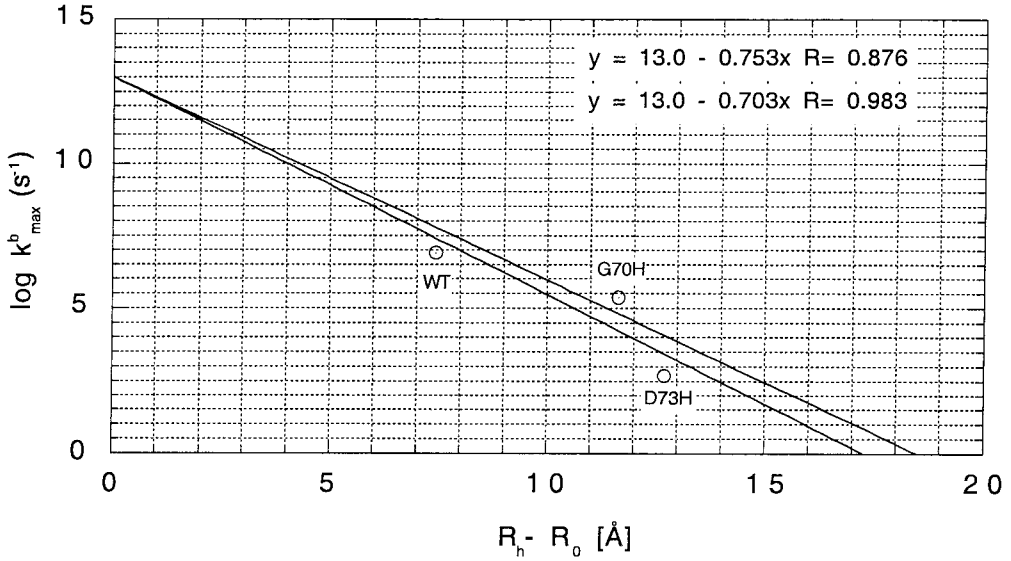
y = 13.0 - 0.753x R= 0.876
y = 13.0 - 0.703x R= 0.983
WT
G70H
D73H
log k^b_{max} (s^{-1})
R_h- R_0 [Å]
0
5
10
15
20

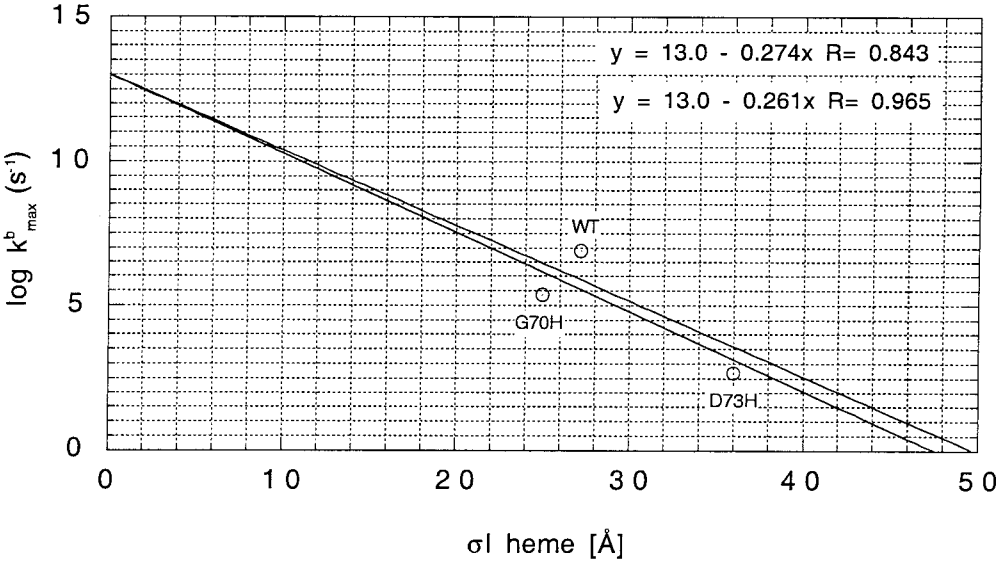
y = 13.0 - 0.274x R= 0.843
y = 13.0 - 0.261x R= 0.965
WT
G70H
D73H
log k^b_{max} (s^{-1})
σI heme [Å]
0
5
10
15
20
30
40
50

Table Chapter 3-1: Distances and tunneling measurements (Å) for wild-type His 63 labelled b_{562} and the G70H and D73H labelled mutants.

labelled residue/mutation	Cα-Fe distance	Cα-heme distance	Ru-Fe distance	Ru-heme distance	Ru-Fe tunnelling distance	Ru-heme tunnelling distance
63His wild-type	13.4	6.9	17.0	10.4	27.2	27.2
Gly70His	16.1	11.3	19.5	14.7	31.4	25.0
Asp73His	18.2	12.9	21.0	15.7	36.0	36.0

b_{562} coupling constants calculated using the Pathways Program.

mutant	Cα-Fe ligand coupling	Cα-heme edge coupling
wild-type	3.8×10^{-4}	na
70	8.2×10^{-5}	8.4×10^{-4}
73	1.5×10^{-5}	1.5×10^{-5}

Table Chapter 3-2: Oligonucleotides used in PCR reactions for the synthesis of the H63E, G70H, D73H, G70H/L68G and D73H/L68G b_{562} mutants.

All mutants were constructed from the H63E gene and this mutation is implied when referring to mutant proteins.

mutation	oligo name	oligo sequence
H63E	H63E top	3' -C TTT CTA AAG GCG *CTT* CCA AAG CTG
	H63E bot	5' -G AAA GAT TTC CGC *GAA* GGT TTC GAC
G70H	G70H top	3'-G CTG TAA GAC CAG *GTG* GTC TAA CTG C
	G70H bot	5' -C GAC ATT CTG GTC *CAC* CAG ATT GAC G
D73H	D73H top	3' -G CCA GTC TAA *GTG* CTG CGC GAC TTC G
	D73H bot	5' -C GGT CAG ATT *CAC* GAC GCG CTG AAG
G70H/L68G	L68G top	3' -CCA AAG CTG TAA *CCC* CAG GTG GTC TAA
	L68G bot	5' -GGT TTC GAC ATT *GGG* GTC CAC CAG ATT
D73H/L68G	L68G top	3' -CCA AAG CTG TAA *CCC* CAG GTG GTC TAA
	L68G bot	5' -GGT TTC GAC ATT *GGG* GTC CAC CAG ATT

Table Chapter 3-2: Observed rates of electron transfer (k^b_{ET}) for wild type b_{562} and the G70H and D73H mutants.

The rates for the D73H mutant were obtained using the irreversible quencher $Co(NH_3)_5Cl^{+2}$.

Mutant	Rate	430 nm PI	414 nm PI	430 nm FQ	414 nm FQ
wild type	$(6.7\pm0.4)\times10^{6}$	$(6.9\pm0.1)\times10^{6}$	$(6.2\pm0.6)\times10^{6}$	$(7.4\pm0.4)\times10^{6}$	$(6.3\pm0.3)\times10^{6}$
G70H	$(2.0\pm0.1)\times10^{5}$	$(1.9\pm0.1)\times10^{5}$	$(2.0\pm0.1)\times10^{5}$	$(2.0\pm0.1)\times10^{5}$	$(1.9\pm0.1)\times10^{5}$
D73H	approx. 3.1×10^{2}				

Mutant	430 mono PI	414 mono PI	670 nm PI	670 nm mono PI
wild type	2e3	nd	$(1.5\pm0.5)\times10^{7}$	8.1×10^{7}
G70H	na	na	$(1.8\pm0.05)\times10^{7}$	$(7.4\pm0.5)\times10^{7}$
D73H	nd	nd	1.1×10^{7}	$(7.6\pm0.4)\times10^{7}$

*average of 430 and 414 nm PI and FQ experiments (where available)

nd - not detected

Chapter 4

Electron Transfer Along Helix D of Cytochrome b_{562}: Labelling of Residues 86, 89 and 92

Introduction

This chapter describes the analysis of electron transfer (ET) between the heme of cytochrome b_{562} and ruthenium(II)bis(2,2'-bipyridine)(imidazole) labelled histidine residues, on the solvent accessible surface of helix D of cytochrome b_{562}, introduced by site-directed mutagenesis. Cytochrome b_{562} (b_{562}) is a well characterized[1-3] soluble 106 amino acid four α-helical bundle protein secreted to the periplasmic space of *Escherichia coli.* The structure of b_{562} is already described in detail in chapters 2 and 3. Helix D, like helix C, contains a short section of 3_{10} helix being located between Ala89 to Gln93.

Materials and Methods

Materials and methods are essentially the same as those of chapters 2 and 3 and so only differences to these methods will be mentioned here.

A DNA

The DNA oligonucleotides used to synthesize the E86H, A89H and E92H mutants are listed in Table Chapter 4-2. Construction of mutants and sequencing of genes was performed as described in chapter 2. All non wild-type mutants were constructed from the H63E gene and this mutation is implied when referring to mutant proteins.

B Electron Transfer Rate Measurements

Rates of intramolecular electron transfer for the A98H and E92H mutants were measured using both the photo-induced and the flash-quench methods by monitoring changes in the transient absorption signal at 430 nm, characteristic of ferrous heme, and also at 414 nm, characteristic of ferric heme. Absorption of the $Ru(bpy)_2(im)$-His label were monitored at 315 nm (RuIII and *RuII) together with the excited state emission at 670 nm. For flash-quench experiments the absorption of the quencher methyl viologen was monitored at 390-400 nm. Figure Chapter 1-2 shows a schematic of the two reaction methods. Samples were approximately 2 ml 8-15 μM protein in 100 mM KP_i and a 1 cm path length laser vacuum cuvette. The samples were degassed and purged with nitrogen for a 5-10 cycles prior to analysis.

The temperature dependence on the rate of ET was analyzed for the A89H mutant. Temperature dependence was monitored with a water jacketed laser cuvette holder and the temperature varied between 5°C and 50°C with 20 minutes for equilibration for each temperature point. After measuring the ET rate at 50°C, the rate was measured at a number of points back towards room temperature (20°C). Multiple sets of laser acquizitions were measured at each temperature point and analyzed using the Kinfit program.

For the E86H mutant the irreversible quencher $Co(NH_3)_5Cl$ was used due to the slow back rate. Under such conditions and using the reversible quencher methyl viologen, the ET back rate was in competition with reduction of Ru^{3+} by methyl viologen radical (see Figure Chapter 1-2). This situation limits the back rate to a maximum of $1 \times 10^3\ s^{-1}$. The dependence of the ET rate on protein concentration was analyzed by measuring the ET rate at concentrations between 0.7 μM and 23 μM. Since photolysis of $Co(NH_3)_5Cl^{2+}$ was observed to promote slow oxidation of the reduced protein used in these experiments, the quencher and proteins samples were mixed just prior to laser excitation by pumping sample

from separate protein and quencher reservoirs into a laser flow cell. Additionally, experiments were carried out in the dark with cut-off and band-pass filters (see Figure Chapter 3-2) to block light of unnecessary wavelengths from the probe light reaching the sample. Data was collected from samples immediately after protein/quencher mixing and the flow cell refilled with another aliquot of fresh sample before averaging of further transients. The concentration of $Co(NH_3)_5Cl^{2+}$ used was 1 mM.

Results

A Design of Mutants

The sites for attachment of ruthenium(II)bis(2,2'-bipyridine)(im) gave the distances listed in Table Chapter 4-1. The ruthenium to heme iron distances (R_m) are seen to range from 18.5 Å to 25 Å. Distances were measured using the molecular modelling programs Insight II and RasMac v2.5 using the 1.4 Å x-ray crystallographic structure 256B[1] downloaded from the Brookhaven data base. χ_1 and χ_2 angles were rotated manually to minimize Van de Waals and electrostatic interactions.

B DNA/Mutagenesis Reactions

The gene used in the mutagenesis reactions was isolated from TB1 cells containing the pNS207 plasmid donated by the Laboratory of Professor Stephen Sligar.

PCR mutagenesis reactions 1, 2 and 3 produced the correct size of gene fragments for each of the mutants. DNA sequencing of the mutant gene confirmed in all cases the correct DNA sequence.

C Protein Expression and Purification

Protein was expressed at 10 -30 mg/L of culture for the mutants. Mutants were eluted from a MonoQ anion exchange FPLC column at approximately 11% buffer B (25 mM TEA pH 7.4, 1 M NaCl) and from the HiTrap chelating column at approximately 80% B. A small percentage of reduced protein (<10%) was found in the initial purification steps and eluted after oxidized protein. With both FPLC columns labelled and unlabelled apo-protein was eluted before the labelled or unlabelled holo protein. Sequential rounds of FPLC (3 to 4 rounds) produced protein preparation which, when viewed by SDS PAGE, were homogenous for most mutants and with others faint bands due to very low concentrations of other proteins were seen on overloaded SDS/PAGE gels. Figure Chapter 3-3 shows a 15% SDS/PAGE gel which includes samples of the purified labelled and unlabelled E86H and A89H mutants. The samples were loaded to maximal concentration and can be seen to be essentially homogenous and at the correct molecular weight with ruthenium labelled samples running slightly above the unlabelled samples.

D Protein Labelling

Protein labelling of the mutant histidine residues with $Ru(bpy)_2(im)$ was similar to that of other mutants and the wild-type with 30-90% yields for the labelling reaction and >90% for the reaction with imidazole.

E Characterization of Expressed Protein

(1) UV Fluorescence and Spectroscopy

The UV/vis spectrum of the labelled and unlabelled E86H, A89H and E92H mutants are shown in Figure Chapter 4-2 - Figure Chapter 4-4. The spectra are identical to that of WT

b_{562} suggesting minimal perturbation of the electronic environment by the mutations and labelling with $Ru(bpy)_2$.im.

(2) Electrochemistry

Potentials for the unlabelled and labelled E86H mutant were 140 mV and 142 mV respectively. Since the E86H mutation is more distal to the heme than the WT labelling site, it would be expected that the coulombic effect of the charged ruthenium label would be reduced as the data shows. The difference between these values and the reported value of 180 mV[4] may be due to the replacement of the wild-type histidine at position 63 with a glutamate residue. With a pk_a of 4.4, this residue will be negatively charged at pH 7 and its coulombic interaction with the heme iron may influence the potential of the heme.

F Electron Transfer Rate Measurements

The temperature dependence on the ET rate for the A89H mutant was measured and the results are shown in Figure Chapter 4-5. It can be seen that there is very little temperature dependence over the range of 5 °C to 50 °C. Rates measured as the sample was cooled were identical to the previous measurements. Since the driving force ($-\Delta G^\circ$) is close to the reorganization energy, the rate is expected to be close to k_{max} and therefore relatively insensitive to temperature changes.

A transient absorption difference spectra for the labelled apo E86H mutant is shown in Figure Chapter 4-6. The transient is identical to that of the model compound $Ru(bpy)_2im_2^{2+}$ and illustrates that the local protein structure has little effect on the electronic environment of the label.

The ET rates found for the E86H, A89H and E92H mutants were $(2.5\pm0.5)x10^{2}$ s^{-1}, $(3.8\pm0.1)x10^{4}$ and $(8.8\pm0.4)x10^{6}$ s^{-1} respectively. Uncertainties are expressed as standard errors of the mean. The metal-metal distances (R_m) for these proteins are 25, 22.5 and 18.5 Å. Figure Chapter 4-7 - Figure Chapter 4-13: E92H show typical photo-induced and flash-quench transients for the mutants at 430 nm, 414 nm and 315 nm. The emissions transients at 670 nm are also shown. Fitting of the data using the Kinfit program provided the above mentioned rates. The rate for the E86H mutant was found by extrapolating the concentration dependence curve to infinite dilution. The flash-quench transients for the A89H mutant was described by a bi-exponential decay: the ET back rate and the re-reduction of the protein by the reduced quencher. Analysis at 315 nm showed that the RuIII also decayed with the same ET back rate.

Calculation of k_{max} gave the values of $(3.0\pm0.5)x10^{2}$ s^{-1}, $(4.4\pm0.1)x10^{4}$ s^{-1} and $(1.0\pm0.4)x10^{7}$ s^{-1} for the E86H, A89H and E92H mutants respectively.

Discussion

The plots of metal-metal distance (R_m) *versus* metal-metal tunnelling length (σl) and edge-edge distance (R_h) *versus* edge-edge tunnelling length (σl heme) are shown in Figure Chapter 4-17. From R_m *versus* σl a distance decay of 1.28 Å-1 is predicted which is in agreement with the decay constant predicted from modelling an ideal α-helix[5]. When the data is plotted as R_h *versus* σl heme, the predicted decay constant increases to 1.60 $Å^{-1}$. Both plots exhibit equally good correlation between points and therefore predict that the ET will decay exponentially with increasing distance.

The experimental distance decay factor β calculated from the R_m *versus* log k_{max} graph (Figure Chapter 4-18 upper) is 1.02 $Å^{-1}$ The correlation between mutants and the graph with a close contact rate of 10^{13} s^{-1} is not ideal, and closer correlation is found for the unrestrained plot, but this has a close contact rate of 10^{18} s^{-1}! The slope of the log k_{max} *versus* σl graph (Figure Chapter 4-18 lower) is 0.205 Å-1 which gives a bond decay rate of 0.72.

Analysis of edge-edge distances for the helix D mutants provides data which is closer to theoretical predictions for the close contact rate of 10^{13} s^{-1}. The plot of log k_{max} *versus* R_h-R_0 (the ruthenium to heme edge distance - 3 Å) gives β as 1.51 Å-1 (Figure Chapter 4-19 upper) and the plot of log k_{max} *versus* σl heme a bond decay factor of 0.67 (Figure Chapter 4-19 lower).

Figure Chapter 4-14 - Figure Chapter 4-16 show the sites of labelling and residues involved in the tunnelling pathway (as calculated from the Pathways program analysis) for the helix D labelled residues. The pathway for the E86H mutant involves a hydrogen bond from the carboxyl of His86 to the Ala90, and then from the carboxyl of Ala91 to the Cδ1 hydrogen of Leu94 and then to the heme CBB carbon. The pathway for A89H and E92H are similar in that it they also use the Leu94 through space jump to reach the heme CBB carbon but no H-bonds are involved. The similarity of the pathways account for the close correlation between R_m and σl and between R_h and σl heme.

It appears from the graphs of σl *versus* R_m and σl heme *versus* R_h that there is better correlation between the latter. Graphs for metal-metal and metal tunnelling *versus* k_{max} give unusually large close contact rates and a high bond decay rate. Graphs for metal-heme and heme tunnelling *versus* log k_{max} give close contact rates in line with theory, a reasonable bond decay rate of 0.67 $Å^{-1}$, but an unusually high β of 1.51 $Å^{-1}$.

Summary

In considering the data grouped by helices, it would appear that helix A and D are better described by both metal-metal tunnelling and metal-metal tunnelling parameters. The rates from both helices correlate well with R_m and σl (except the D73H mutant) with β values of 1.13 and 1.04 and bond decays of 0.69 and 0.68. Helix D is better described by metal-heme and metal-heme tunnelling with a β of 1.51 and a bond decay of 0.67.

The predicted $\sigma l/R_m$ for all the data is 1.28 $Å^{-1}$ (Figure Chapter 4-17 upper), but as already described the predicted pathways are not truly helical: pathways predicted by the Pathways program proceed via the most direct path using side chains, hydrogen bonds and through space jumps, and are not restricted to longitudinal α-helical routes. The size of the heme and the greater efficiency of coupling through its covalent bonds provides all of the mutants with these optimal pathways to the redox centre. Moreover, the rates correlate reasonably well with metal-metal distance with a distance decay rate β of 1.09 $Å^{-1}$. The tunnelling predictions also correlate with the rates but require an adjustment to the sigma bond decay rate from a value of 0.6 to 0.69. The value of 0.6 has been determined by rigorous theoretical and experimental analysis, and adequately describes ET in β-strands of a protein. The adjustment in this analysis may therefore illustrate a weakness in the single pathway model. The experimental structure ratio $\sigma l/R_m$ is 1.49, a value midway between theoretical models which treat hydrogen bonds as covalent bonds for ET (value 1.22) and as through space jumps (value 1.72). H-bonds were predicted to be utilized only if in the direct path to the iron and there treatment in the Pathways model is of an extended covalent bond, approximately equal to two covalent bonds. For the two H-bonds in the pathways (mutant K19H and E86H) this analysis seems reasonable since their rates correlate reasonably well with other mutants in the rate *versus* σl graph (Figure Chapter 4-18).

Analysis of the ET route being from heme edge to ruthenium provides a large distance decay rate β of 1.63 which, using the published bond decay rate of 0.6, gives a σl heme/R_h of 2.23. This value is between the value predicted for α-helices, where ET via H-bonds is facilitated (1.72), and where it is not (2.7)[6]. Since the data is adequately described by metal-metal distances and metal-metal tunnelling lengths (which include H-bonds), this large β appears unreasonable.

A comparison of the R_m and σl *versus* log k_{max} and σl for b_{562} and Azurin[5, 6] is shown in Figure Chapter 4-23. The R_m *versus* log k_{max} graph (upper) shows reasonable agreement between both sets of data (except the D73H mutant) and the distance decay rate for b_{562} is unchanged at 1.09 Å^{-1}. Including data from cytochrome c[7] as shown in Figure Chapter 4-24 also gives good agreement apart from a few rates of cytochrome c(H62 and H72) which have been explained by large through space connectivity's in their pathways. The distance decay rate for these rates is 1.08 Å^{-1}. A comparison of σl *versus* log k_{max} for b_{562} and azurin (Figure Chapter 4-23 lower) shows that the rates for b_{562} do not agree with the bond decay rate of 0.6 with rates in b_{562} being faster than for similar tunnelling distance in azurin. Including cytochrome *c* edge-edge data (Figure Chapter 4-24 lower) shows that the tunnelling rate data for b_{562} is more similar to cytochrome *c* than azurin. A plot of edge-edge distances for both b_{562} and cytochrome *c* shows good correlation between the data sets (Figure Chapter 4-25). It would appear that the disagreement with the bond decay rate is a function of the protein being characteristic of both cytochromes and may indicate that a multiple pathway model would give improved tunnelling lengths as found for some cytochrome *c* rates previously[8].

The distance decay rate found here (1.09 $Å^{-1}$) is far below that found by Dutton in his review of many reaction rates from the bacterial photosynthetic reaction centre and ruthenium labelled cytochrome *c* and myoglobin[9]. Many of the driving forces for these reactions were very low relative to the reorganization energy and so maximal values had to be extrapolated which could have produced the discrepancy between that data and the data presented here.

In conclusion, the α-helices in cytochrome b_{562} provide efficient coupling pathways between redox sites with a β of 1.09 $Å^{-1}$, similar to that of β-strands. The hydrogen bonds predicted to participate in the pathways (mutants 19 and 86) do not appear to reduce the coupling efficiency with data for tunneling rates being very similar to that of cytochrome *c*. The distance dependency of the ET rate in the three proteins, b_{562}, azurin and cytochrome *c*, is adequately described by the same distance decay rate of 1.09 $Å^{-1}$. Since these proteins are comprized of mostly α-helices, β-sheets and a mixture of each, respectively, the one-dimensional barrier model for ET in proteins appears most consistent with the results.

Bibliography

1. Hamada, K., Bethge, P.H. & Mathews, F.S. *J. Mol. Biol.* **247**, 947-962 (1995).

2. Wu, J., Gerd, N. & al, e. *Biochemistry* **30**, 2156-2165 (1991).

3. Mathews, F., Bethge, P. & Czerwinski, E. *J. Biol. Chem.* **254**, 1699-1706 (1979).

4. Moore, G., Williams, R., Perterson, J., Thompson, A. & Mathews, R. *Biochem. Biophys. Acta* **829**, 83-96 (1985).

5. Langen, R. in *Dept. Chemistry and Chemical Engineering* (California Institute of Technology, Pasadena, 1995).

6. Langen, R., *et al. Science* **268**, 1733-1735 (1995).

7. Bjerrum, M.J., *et al. J. Bioenerg. Biomem.* **27**, 295-302 (1995).

8. Casimiro, D.R. in *Divizion of Chemistry and Chemical Engineering* (California Institute of Technology, Pasadena, 1994).

9. Moser, C.C., Keske, J.M. & al, e. *Nature* **355**, 796-802 (1992).

Figure Chapter 4-1: The backbone structure of wild-type b_{562} and the labelling sites on helix D.

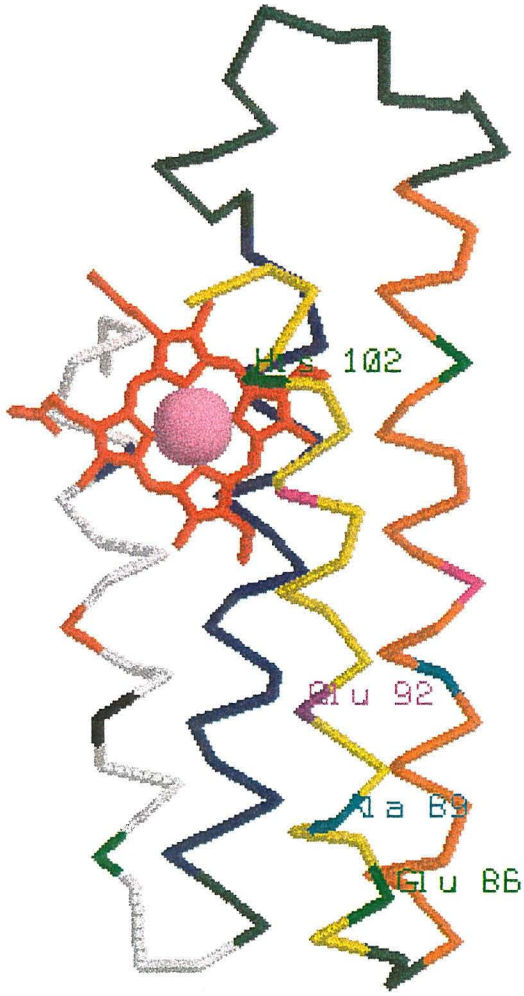
His 102
Glu 92
Ala B9
Glu B6

Figure Chapter 4-2: The UV/vis spectra of unlabelled and labelled E86H *versus* WTb_{562}.

Upper: the spectra of unlabelled E86H (thin) and WT b_{562} (thick). Lower: the spectra of labelled E86H (thick) and labelled WT b_{562}.

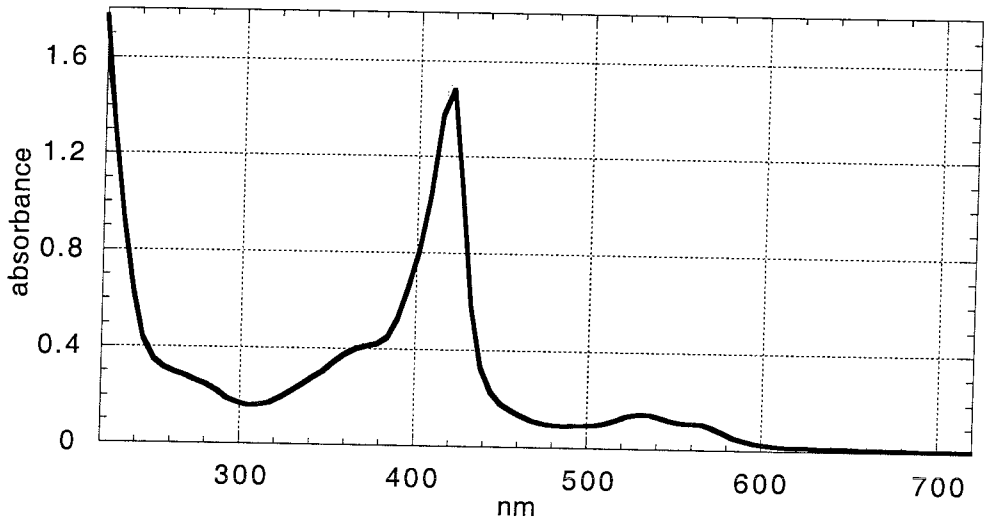
absorbance
1.6
1.2
0.8
0.4
0
300
400
500
600
700
nm

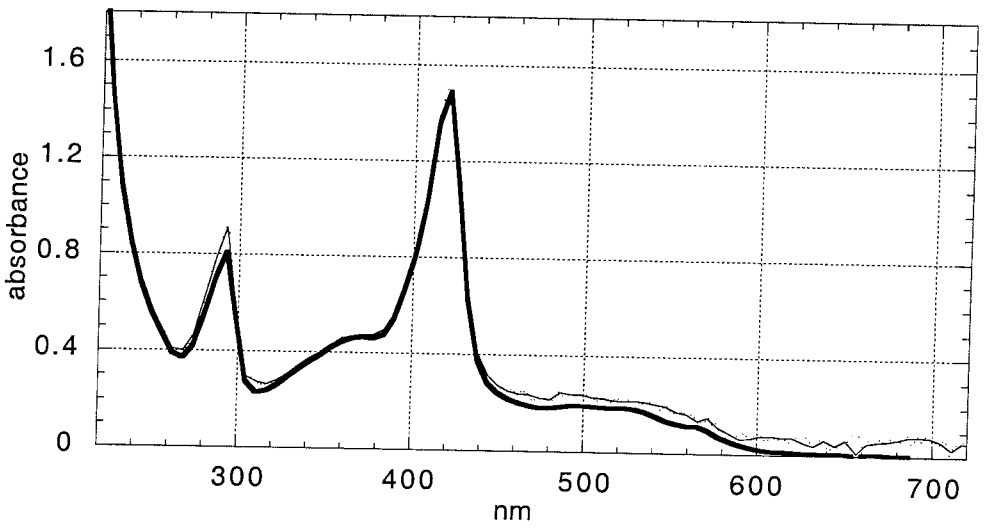
absorbance
1.6
1.2
0.8
0.4
0
300
400
500
600
700
nm

Figure Chapter 4-3: The UV/vis spectrum of labelled A89H *versus* WTb_{562}.

The spectra of labelled A89H (thin) and WT b_{562} (thick).

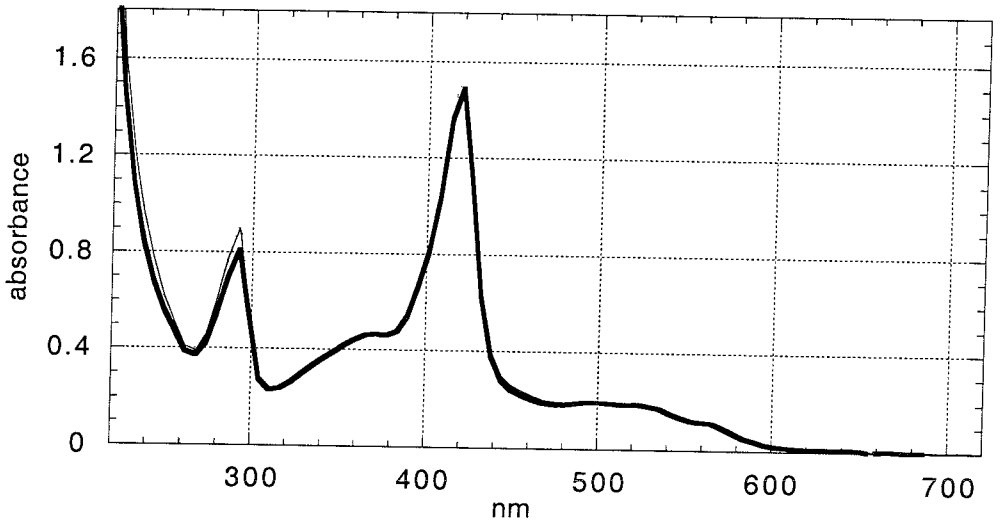
absorbance
1.6
1.2
0.8
0.4
0
300
400
500
600
700
nm

Figure Chapter 4-4: The UV/vis spectra of unlabelled and labelled E92H *versus* WTb_{562}.

Upper: the spectra of unlabelled E92H (thin) and WT b_{562} (thick). Lower: the spectra of labelled E92H (thick) and labelled WT b_{562}.

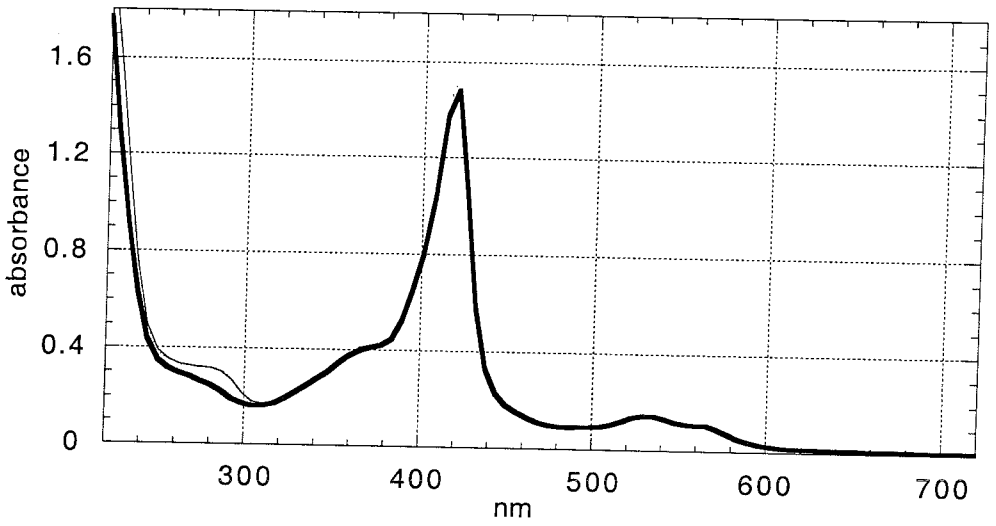
absorbance
1.6
1.2
0.8
0.4
0
300
400
500
600
700
nm

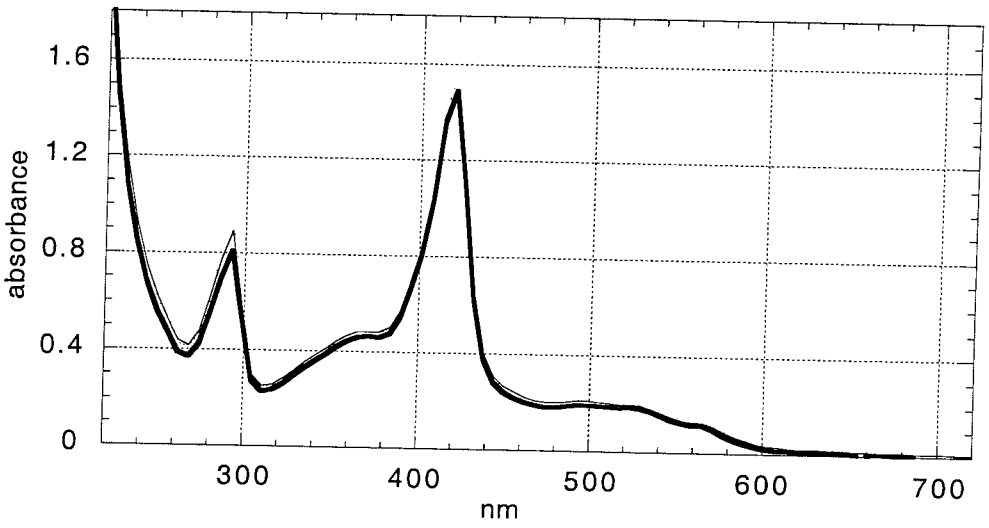
absorbance
1.6
1.2
0.8
0.4
0
300
400
500
600
700
nm

Figure Chapter 4-5: Temperature *versus* the ET rate for the A89H mutant.

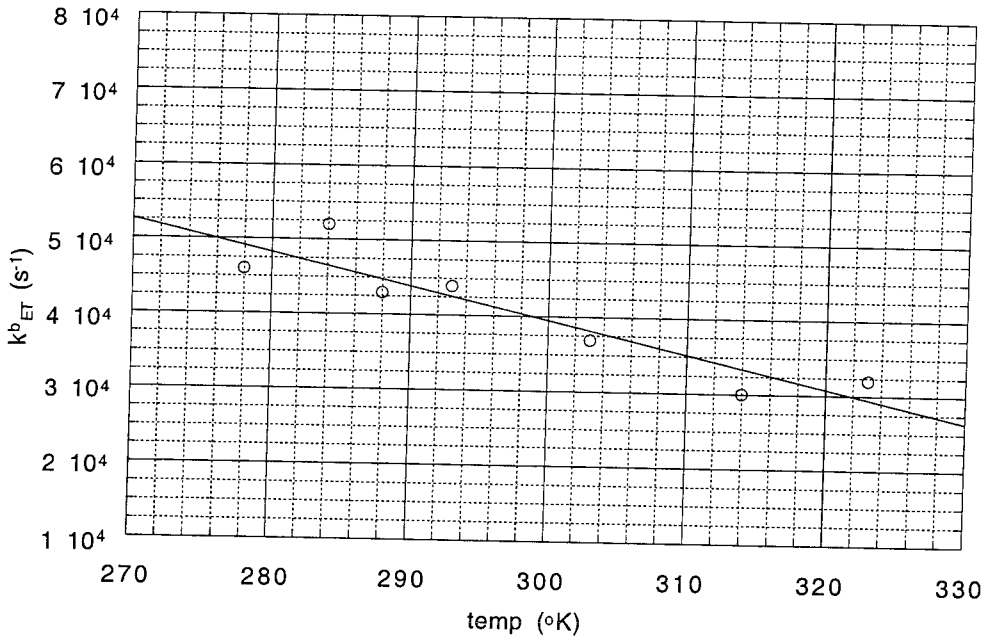
8 10⁴
7 10⁴
6 10⁴
5 10⁴
4 10⁴
3 10⁴
2 10⁴
1 10⁴
k^b_ET (s⁻¹)
270
280
290
300
310
320
330
temp (°K)

Figure Chapter 4-6: Transient absorption spectra for apo E86H.

Transient absorption spectrum of apo E86H recorded in the μs time scale using the photo-induced method.

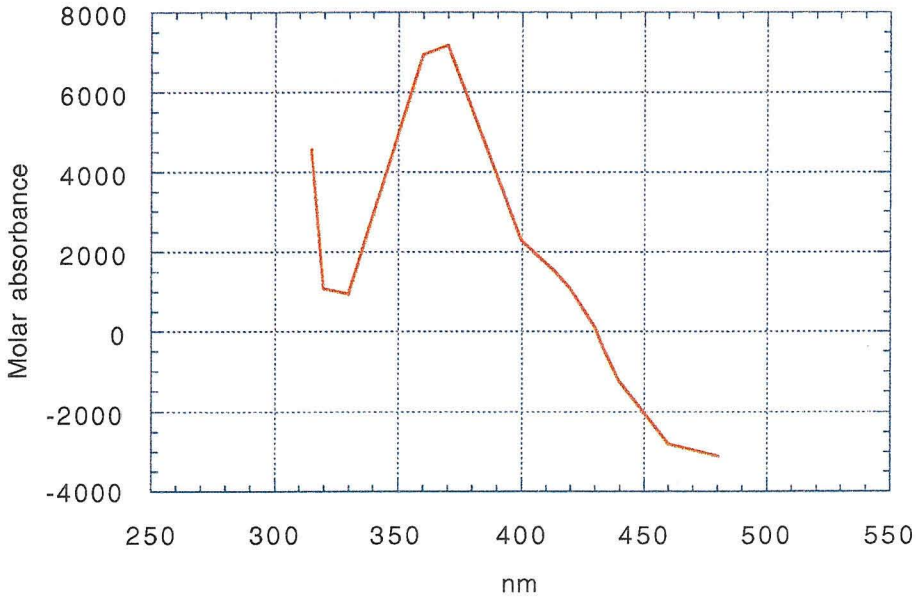
8000
6000
4000
2000
0
-2000
-4000
Molar absorbance
250
300
350
400
450
500
550
nm

Figure Chapter 4-7: E86H flash-quench transient absorbencies.

E86H (16.5 μM) flash-quenched transient absorbance monitored at (A) 430 nm and (B) 414 nm, showing the oxidation of Fe^{2+} and the fit to the trace. These experiments used the irreversible quencher $Co(NH_3)_5Cl_2$.

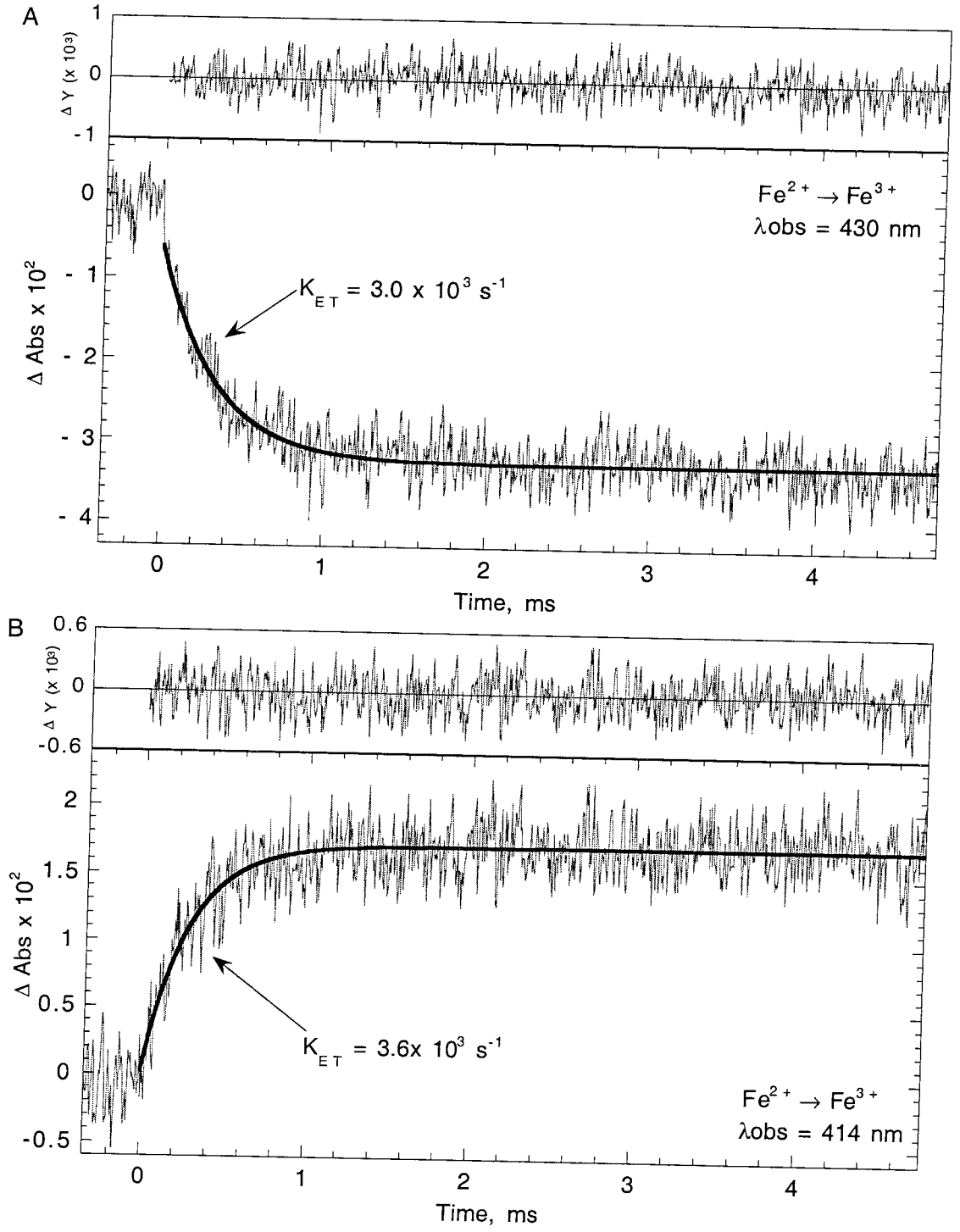
A
Δ Y (x 10³)
Δ Abs x 10²
$Fe^{2+} \rightarrow Fe^{3+}$
λobs = 430 nm
K_{ET} = 3.0 x 10^3 s^{-1}
Time, ms
B
Δ Y (x 10³)
Δ Abs x 10²
K_{ET} = 3.6x 10^3 s^{-1}
$Fe^{2+} \rightarrow Fe^{3+}$
λobs = 414 nm
Time, ms

Figure Chapter 4-8: E86H flash-quench transient absorbencies.

E86H (23 μM) flash-quenched transient absorbance monitored at (A) 430 nm and (B) 414 nm, showing the oxidation of Fe^{2+} and the fit to the trace. These experiments used the irreversible quencher $Co(NH_3)_5Cl_2$.

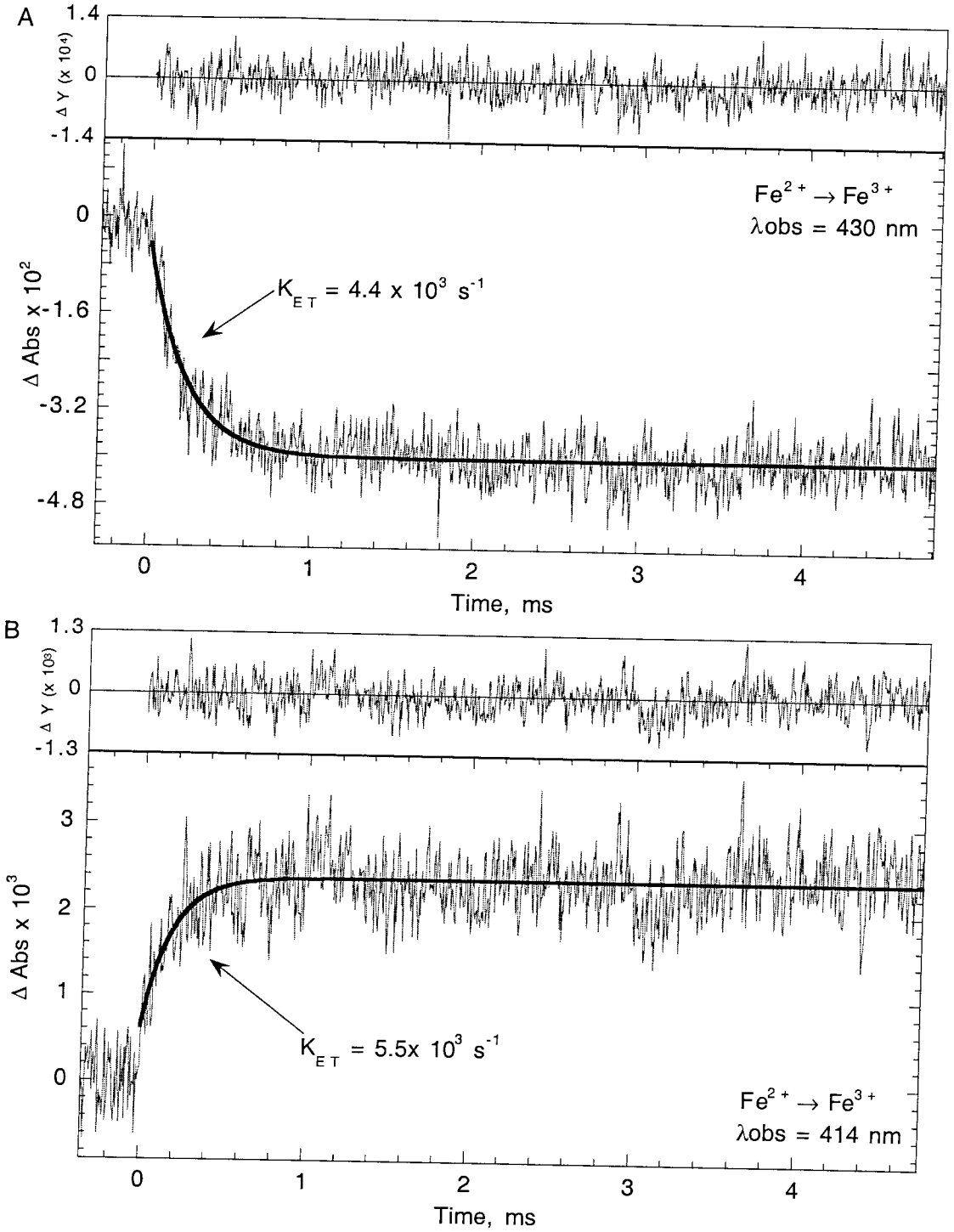
A
1.4
0
-1.4
Δ Y (x 10⁴)
0
-1.6
-3.2
-4.8
Δ Abs x 10²
K_{ET} = 4.4 x 10³ s⁻¹
$Fe^{2+} \rightarrow Fe^{3+}$
λobs = 430 nm
0
1
2
3
4
Time, ms
B
1.3
0
-1.3
Δ Y (x 10⁹)
3
2
1
0
Δ Abs x 10³
K_{ET} = 5.5x 10³ s⁻¹
$Fe^{2+} \rightarrow Fe^{3+}$
λobs = 414 nm
0
1
2
3
4
Time, ms

Figure Chapter 4-9: A89H photo induced transient absorbencies.

A89H (20 μM) photoinduced transient absorbance monitored at (A) 430 nm and (B) 414 nm, showing the reduction of Fe^{3+} and the fit to the trace. The residual (signal minus fit) is shown above the traces.

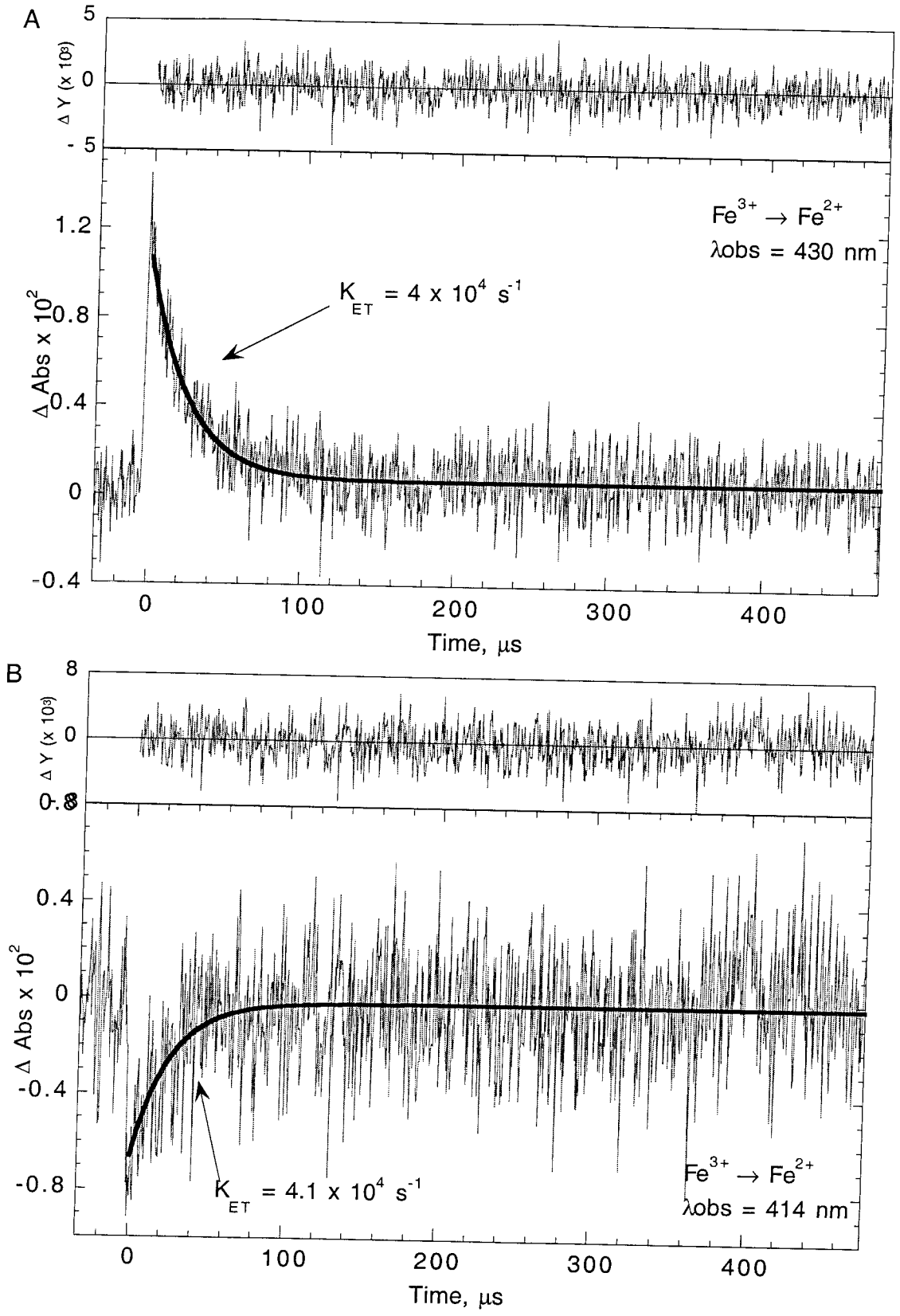
A
5
0
- 5
Δ Y (x 10³)
1.2
0.8
0.4
0
-0.4
Δ Abs x 10²
$Fe^{3+} \rightarrow Fe^{2+}$
λobs = 430 nm
K_{ET} = 4 x 10^4 s^{-1}
0
100
200
300
400
Time, μs
B
8
0
-8
Δ Y (x 10³)
0.4
0
-0.4
-0.8
- Δ Abs x 10²
K_{ET} = 4.1 x 10^4 s^{-1}
$Fe^{3+} \rightarrow Fe^{2+}$
λobs = 414 nm
0
100
200
300
400
Time, μs

Figure Chapter 4-10: A89H flash-quench transient absorbencies.

A89H (7 μM) flash-quenched transient absorbance monitored at (A) 430 nm and (B) 414 nm, showing the oxidation of Fe^{2+} and the fit to the trace. The residual (signal minus fit) is shown above the traces.

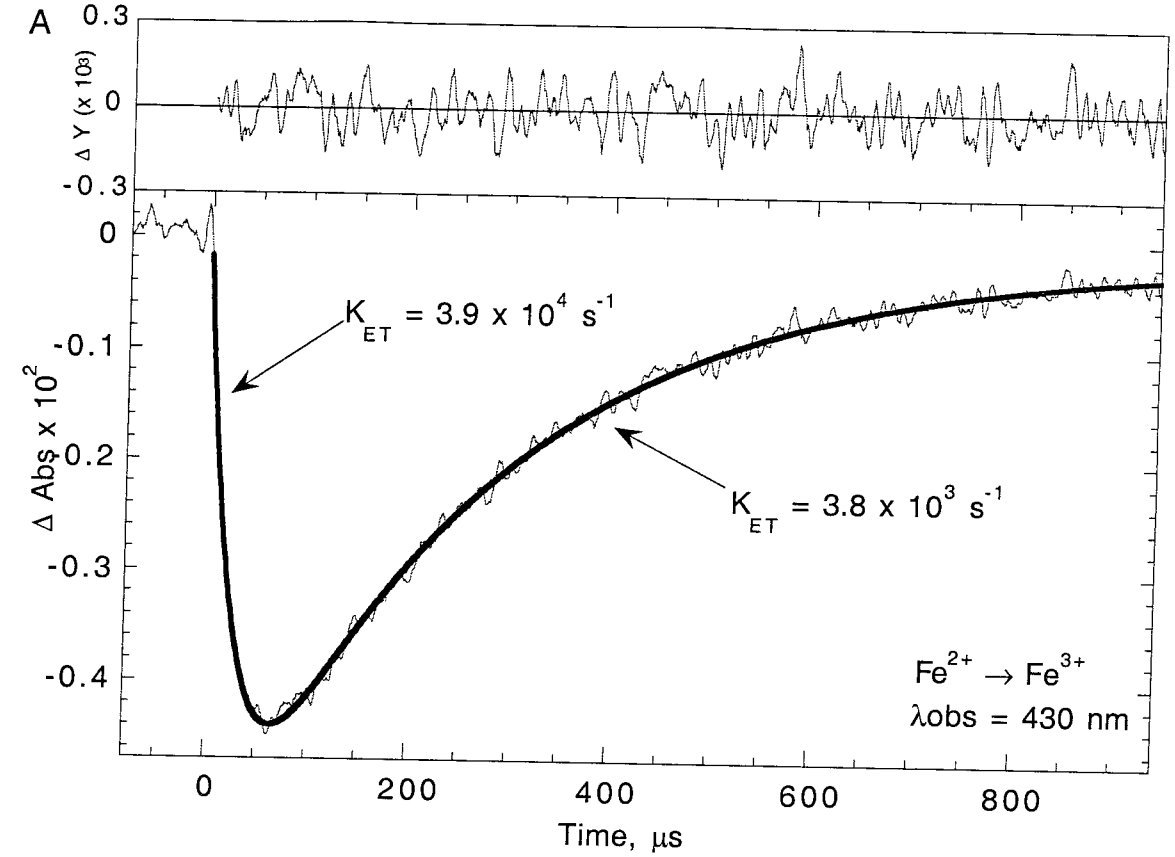
A
0.3
0
-0.3
Δ Y (x 10⁸)
0
-0.1
-0.2
-0.3
-0.4
Δ Abs x 10²
K_ET = 3.9 x 10⁴ s⁻¹
K_ET = 3.8 x 10³ s⁻¹
Fe²⁺ → Fe³⁺
λobs = 430 nm
0
200
400
600
800
Time, μs

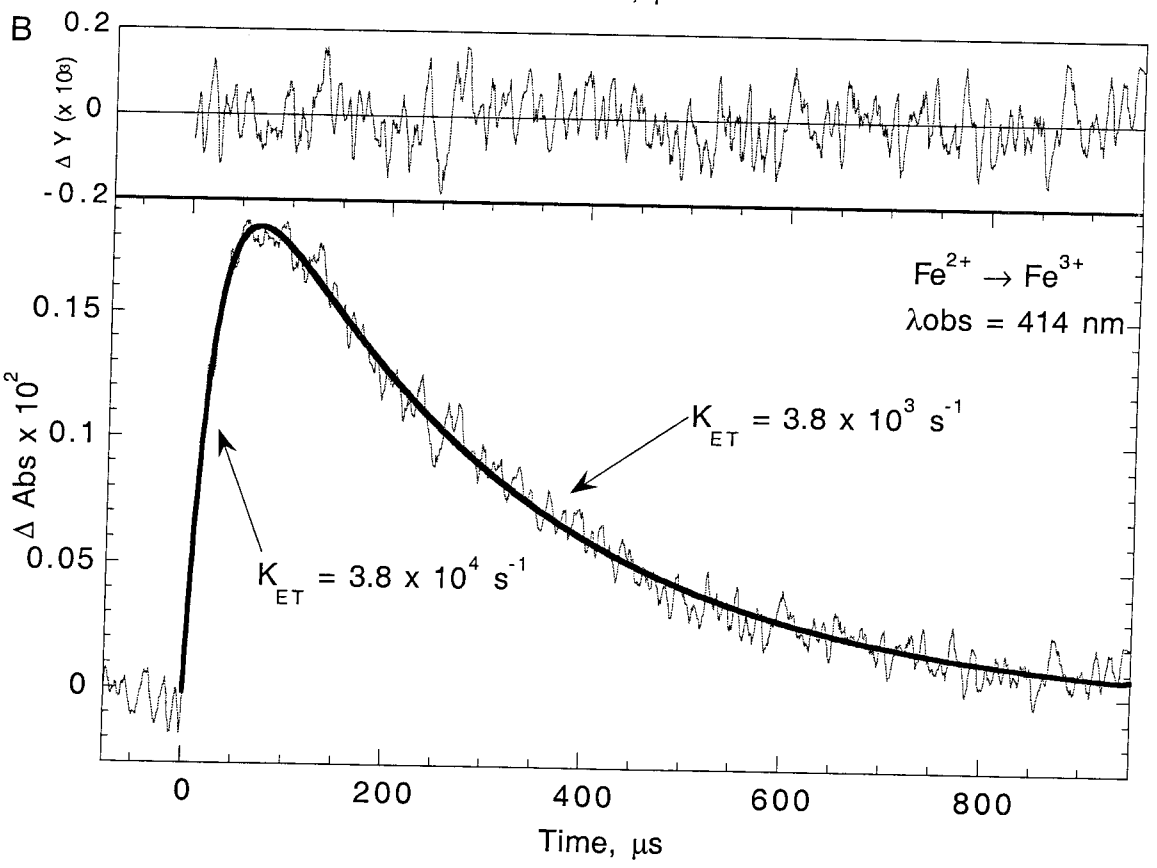
B
0.2
0
-0.2
Δ Y (x 10⁸)
0.15
0.1
0.05
0
Δ Abs x 10²
Fe²⁺ → Fe³⁺
λobs = 414 nm
K_ET = 3.8 x 10³ s⁻¹
K_ET = 3.8 x 10⁴ s⁻¹
0
200
400
600
800
Time, μs

Figure Chapter 4-11: A89H transient emissions at 670 nm and absorption at 315 nm.

A89H (14.5μM) emissions monitored at (A) 670 nm and (B) flash-quenched transient absorbance monitored at 315 nm showing the reduction of Ru^{3+} and *Ru absorbance. The fit to the traces is shown and the residual (signal minus fit) is shown above the traces.

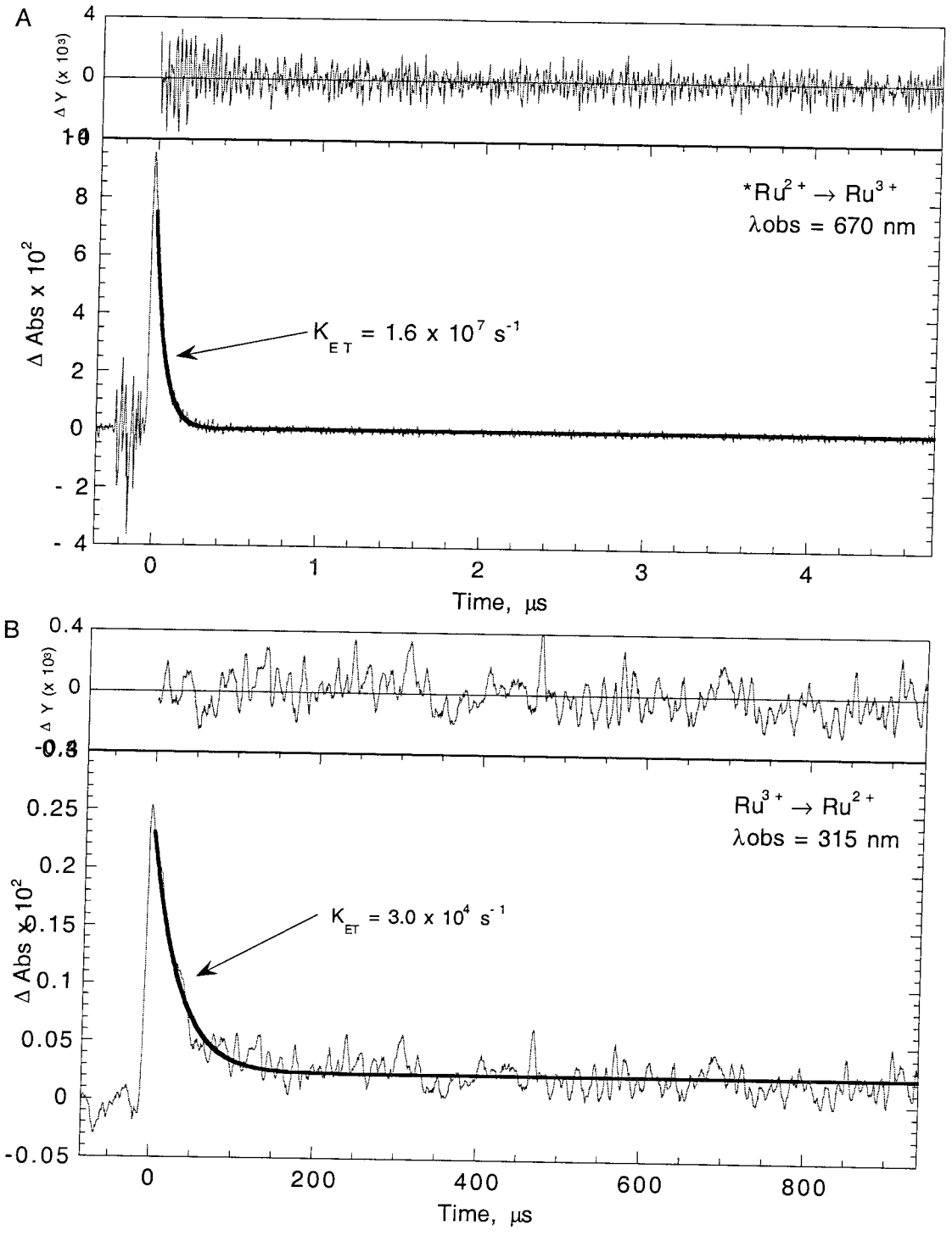
A
Δ Y (x 10³)
4
0
-4
Δ Abs x 10²
8
6
4
2
0
- 2
- 4
*Ru²⁺ → Ru³⁺
λobs = 670 nm
K_ET = 1.6 x 10⁷ s⁻¹
0
1
2
3
4
Time, μs
B
Δ Y (x 10³)
0.4
0
-0.4
Δ Abs x 10²
0.25
0.2
0.15
0.1
0.05
0
-0.05
Ru³⁺ → Ru²⁺
λobs = 315 nm
K_ET = 3.0 x 10⁴ s⁻¹
0
200
400
600
800
Time, μs

Figure Chapter 4-12: E92H photo induced transient absorbencies.

E92H (13 μM) photoinduced transient absorbance monitored at (A) 430 nm and (B) 414 nm, showing the reduction of Fe^{3+} and the fit to the trace. The residual (signal minus fit) is shown above the traces.

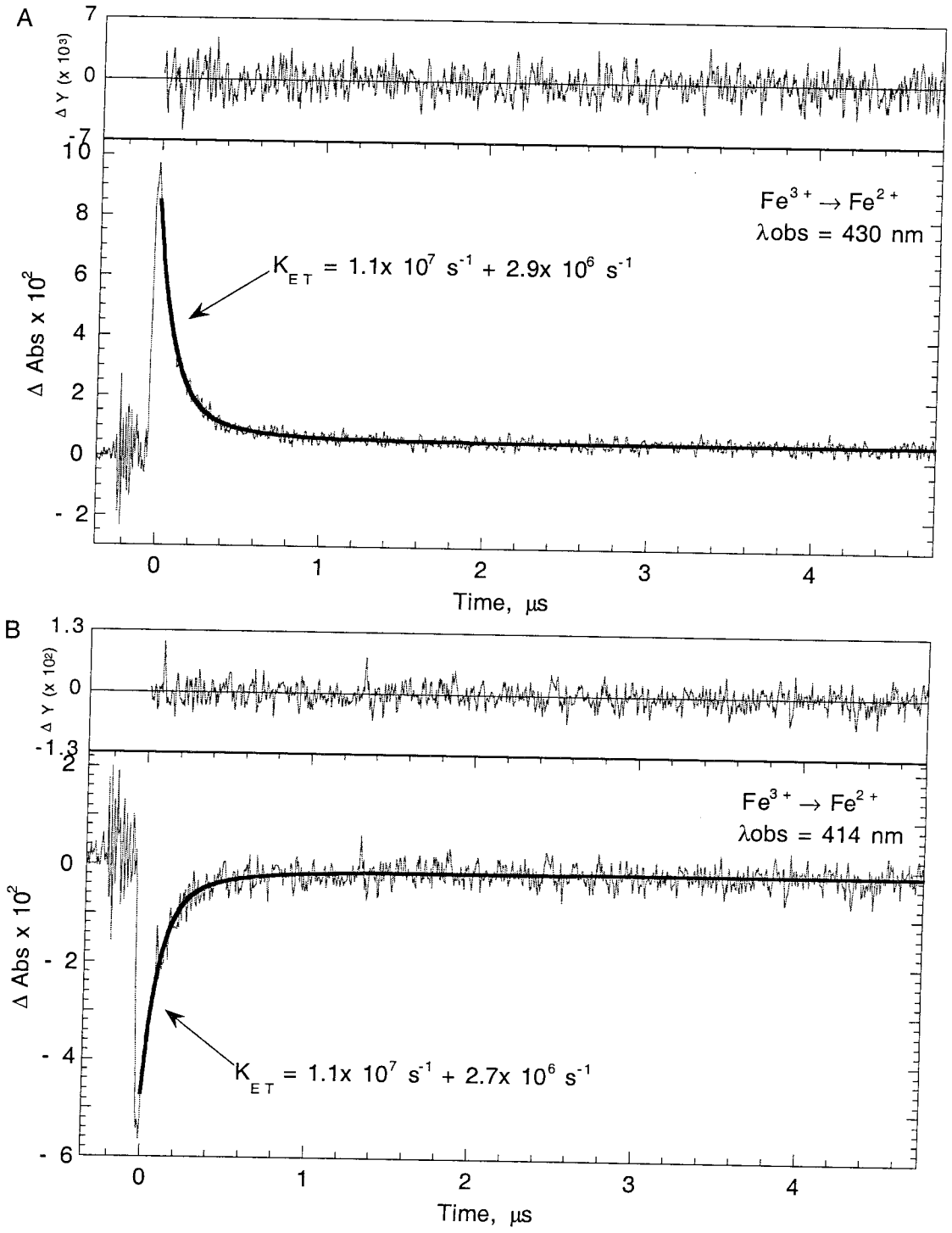
A
Δ Y (x 10³)
7
0
-7
10
8
6
4
2
0
- 2
Δ Abs x 10²
Fe³⁺ → Fe²⁺
λobs = 430 nm
K_ET = 1.1x 10⁷ s⁻¹ + 2.9x 10⁶ s⁻¹
0
1
2
3
4
Time, μs
B
Δ Y (x 10²)
1.3
0
-1.3
2
0
- 2
- 4
- 6
Δ Abs x 10²
Fe³⁺ → Fe²⁺
λobs = 414 nm
K_ET = 1.1x 10⁷ s⁻¹ + 2.7x 10⁶ s⁻¹
0
1
2
3
4
Time, μs

Figure Chapter 4-13: E92H transient emissions at 670 nm and absorption at 315 nm.

E92H (7.8μM) emissions monitored at (A) 670 nm and (B) flash-quenched transient absorbance monitored at 315 nm showing the reduction of Ru^{3+} The fit to the traces is shown and the residual (signal minus fit) is shown above the traces.

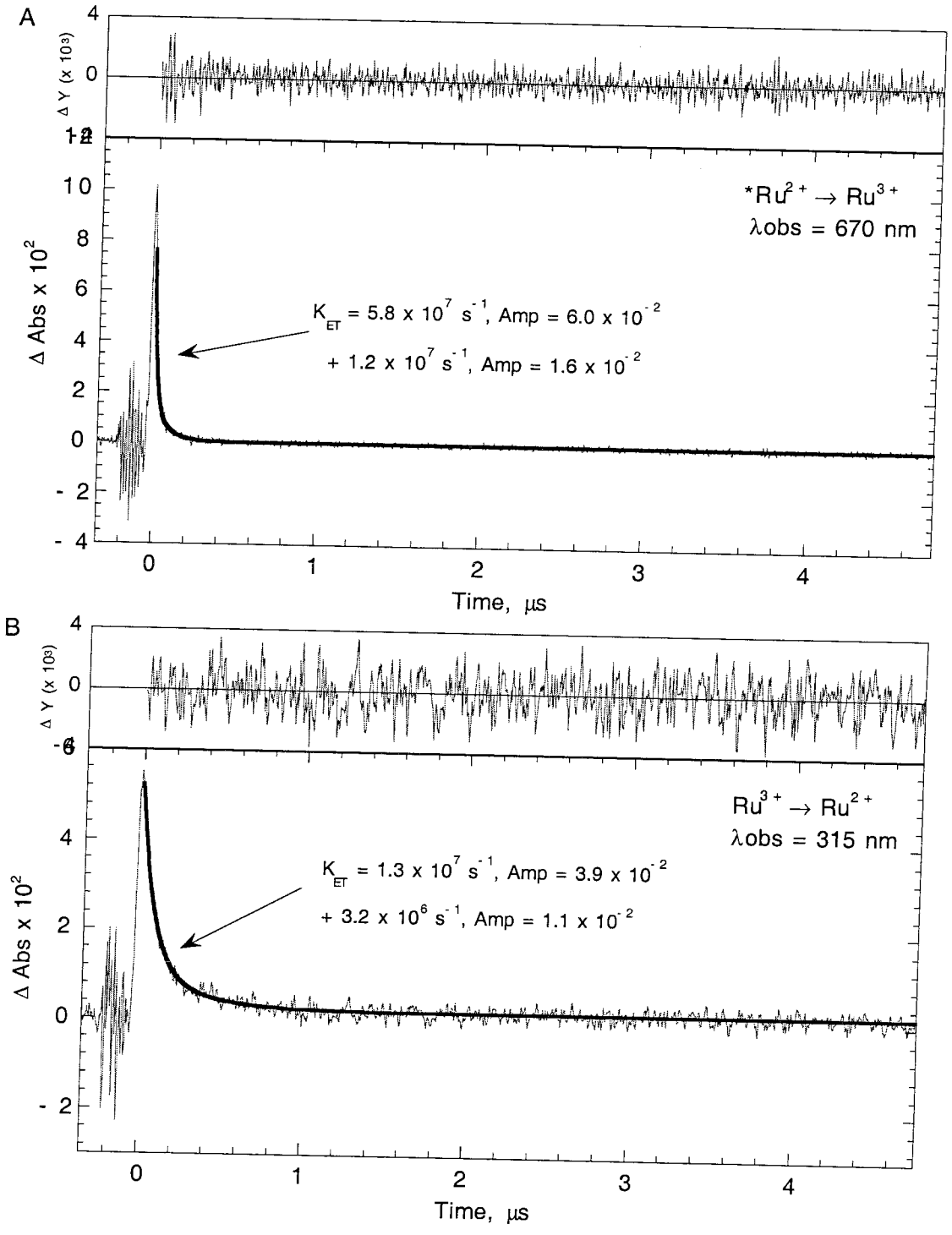
A
Δ Y (x 10³)
Δ Abs x 10²
*Ru²⁺ → Ru³⁺
λobs = 670 nm
K_ET = 5.8 x 10⁷ s⁻¹, Amp = 6.0 x 10⁻²
+ 1.2 x 10⁷ s⁻¹, Amp = 1.6 x 10⁻²
Time, μs
B
Δ Y (x 10³)
Δ Abs x 10²
Ru³⁺ → Ru²⁺
λobs = 315 nm
K_ET = 1.3 x 10⁷ s⁻¹, Amp = 3.9 x 10⁻²
+ 3.2 x 10⁶ s⁻¹, Amp = 1.1 x 10⁻²
Time, μs

Figure Chapter 4-14: The ET pathway of the E86H mutant of b_{562}.

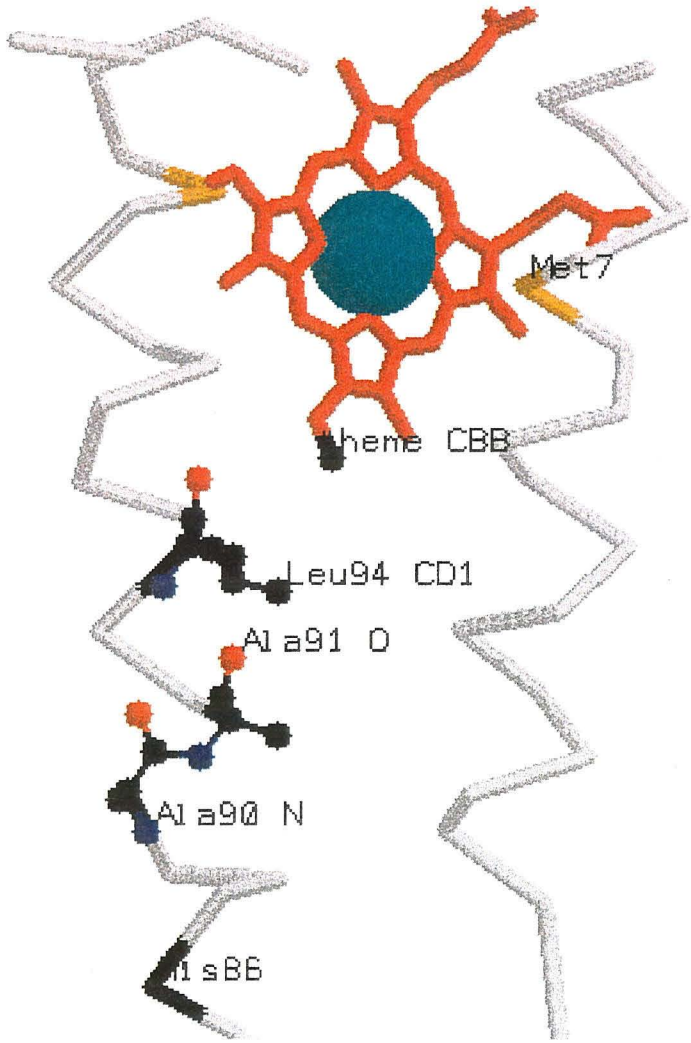
Met7
heme CBB
Leu94 CD1
Ala91 O
Ala90 N
HisBB

Figure Chapter 4-15: The ET pathway of the A89H mutant of b_{562}.

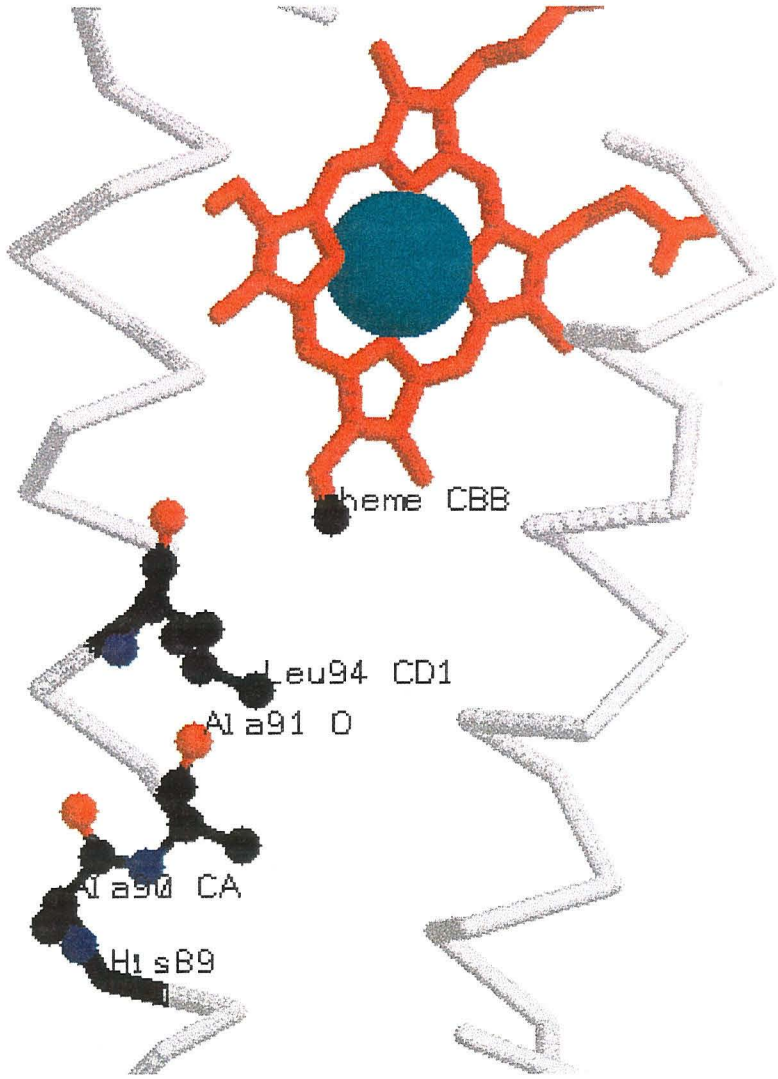
heme CBB
Leu94 CD1
Ala91 O
Ala90 CA
HisB9

Figure Chapter 4-16: The ET pathway of the E92H mutant of b_{562}.

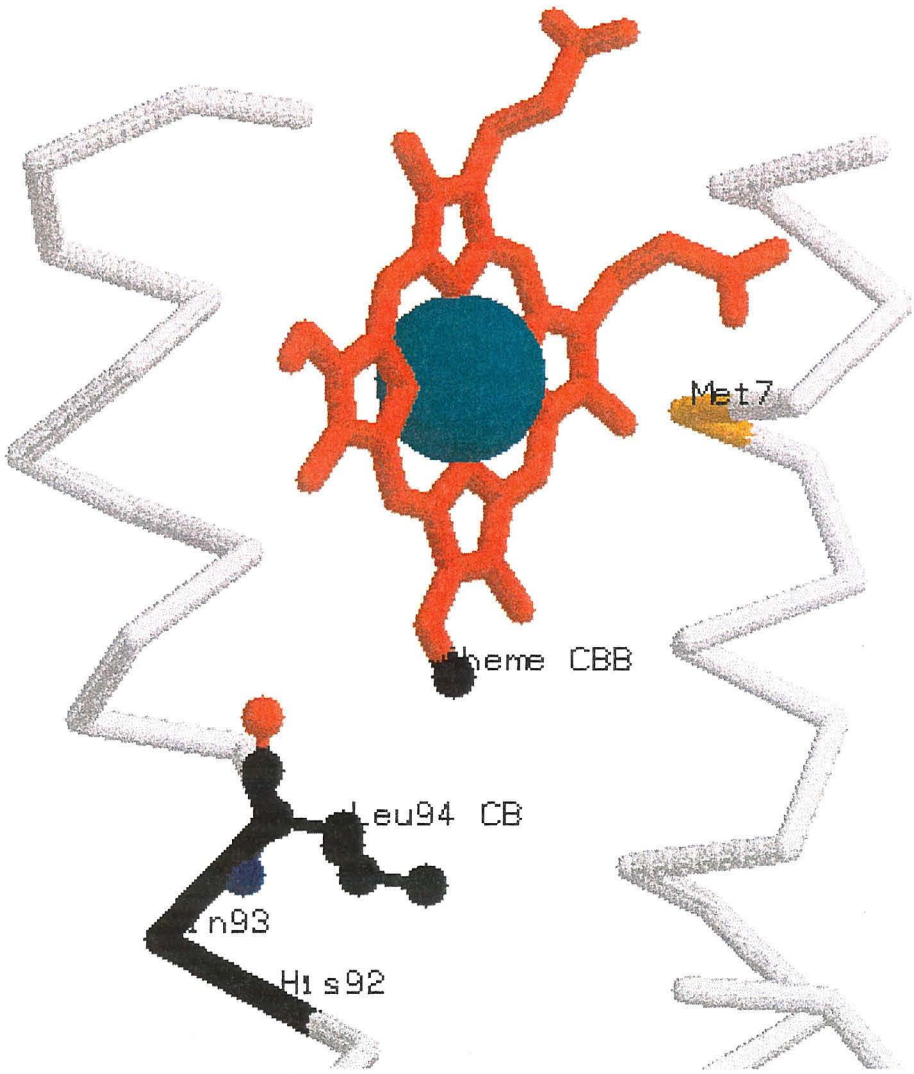
Met7
heme CBB
eu94 CB
n93
His92

Figure Chapter 4-17: Distance *versus* tunnelling lengths for helix D mutants of cytochrome b_{562}.

Upper: the metal-metal distance (R_m) *versus* the tunnelling length (σl). Lower: the metal-heme distance (R_h) *versus* the metal-heme tunnelling distance (σl heme) for helix D of b_{562}.

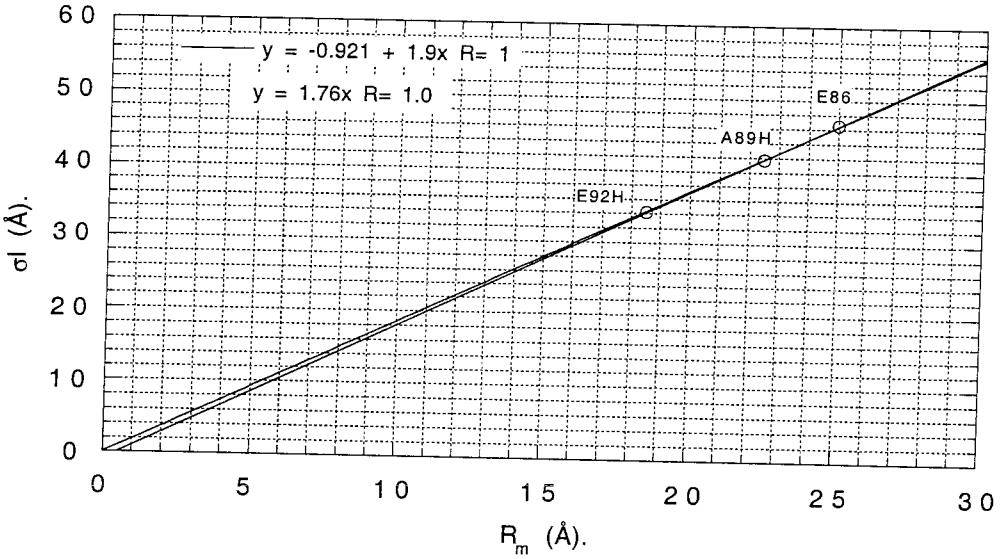
y = -0.921 + 1.9x R= 1
y = 1.76x R= 1.0
E86
A89H
E92H
σI (Å).
0
10
20
30
40
50
60
0
5
10
15
20
25
30
R_m (Å).

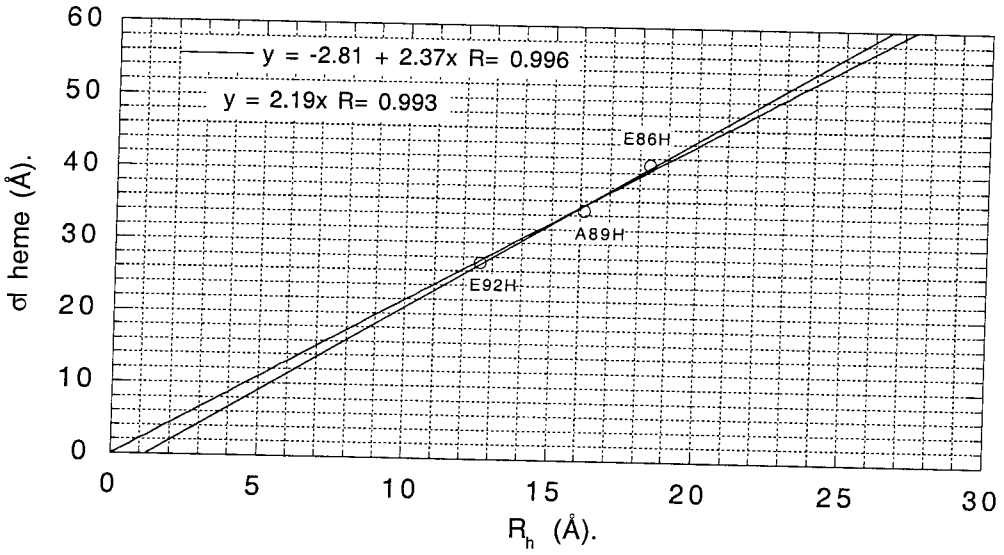
y = -2.81 + 2.37x R= 0.996
y = 2.19x R= 0.993
E86H
A89H
E92H
σI heme (Å).
0
10
20
30
40
50
60
0
5
10
15
20
25
30
R_h (Å).

Figure Chapter 4-18: The metal-metal distance (R_m) *versus* log k_{max} (upper) and metal-metal sigma tunnelling length (σl) *versus* log k_{max} (lower).

R_m is the distance from the N2 His-X (X = mutation) ruthenium bond to the Fe atom and σl is the His-X Cα-Cβ bond to the Fe ligand bond tunnelling length (as calculated by the Pathways program) plus 4 bond lengths.

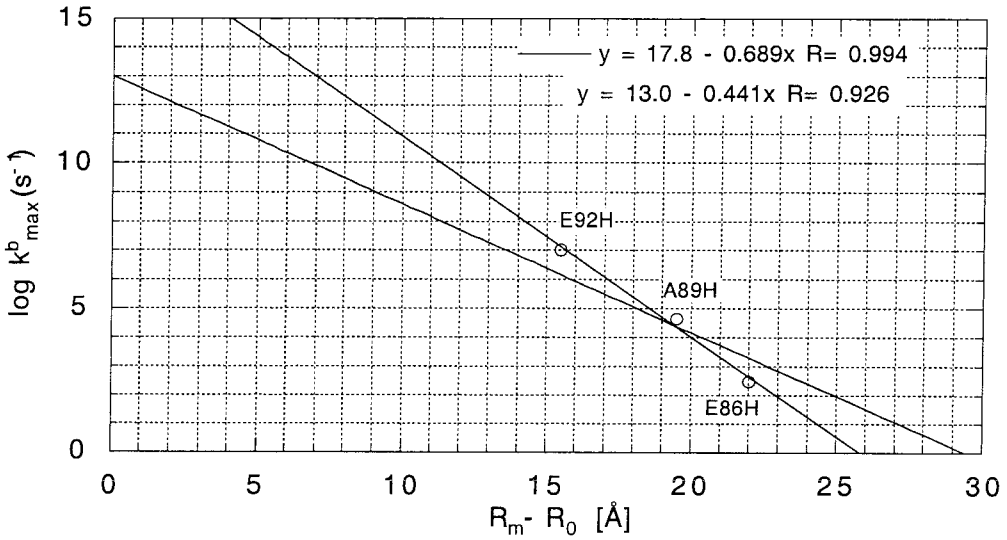
y = 17.8 - 0.689x R= 0.994
y = 13.0 - 0.441x R= 0.926
E92H
A89H
E86H
log k^b_{max} (s^{-1})
R_m- R_0 [Å]
0
5
10
15
20
25
30

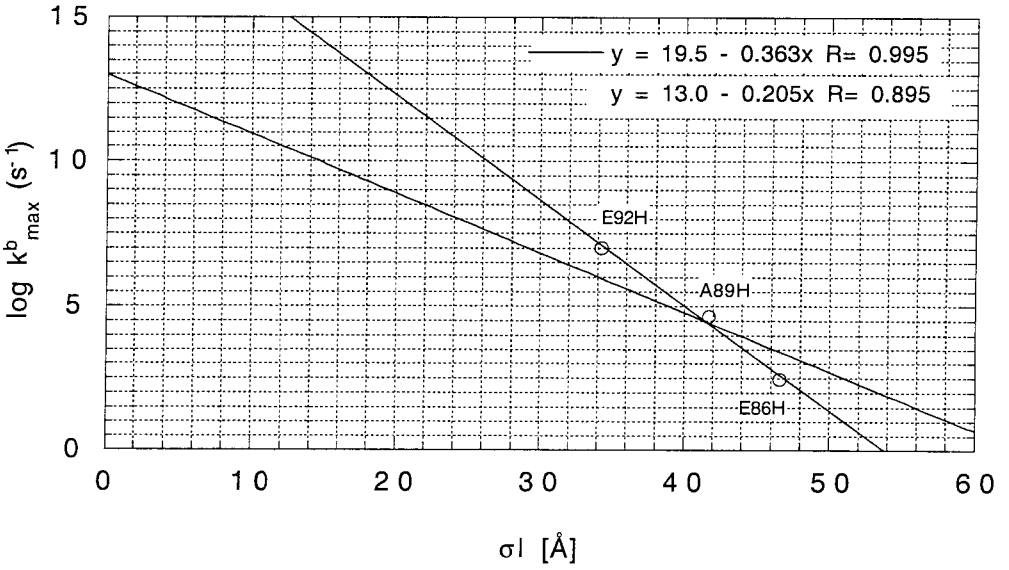
y = 19.5 - 0.363x R= 0.995
y = 13.0 - 0.205x R= 0.895
E92H
A89H
E86H
log k^b_{max} (s^{-1})
σI [Å]
0
10
20
30
40
50
60

Figure Chapter 4-19: The metal-heme distance (R_h) *versus* log k_{max} (upper) and the metal-heme tunnelling length (σl heme) *versus* log k_{max} (lower).

R_h is the distance from the N2 His-X (X = mutation) ruthenium bond to the closest porphyrin ring atom and σl heme is the His-X Cα-Cβ bond to the closest porphyrin ring bond tunnelling length (as calculated by the Pathways program) plus 4 bonds.

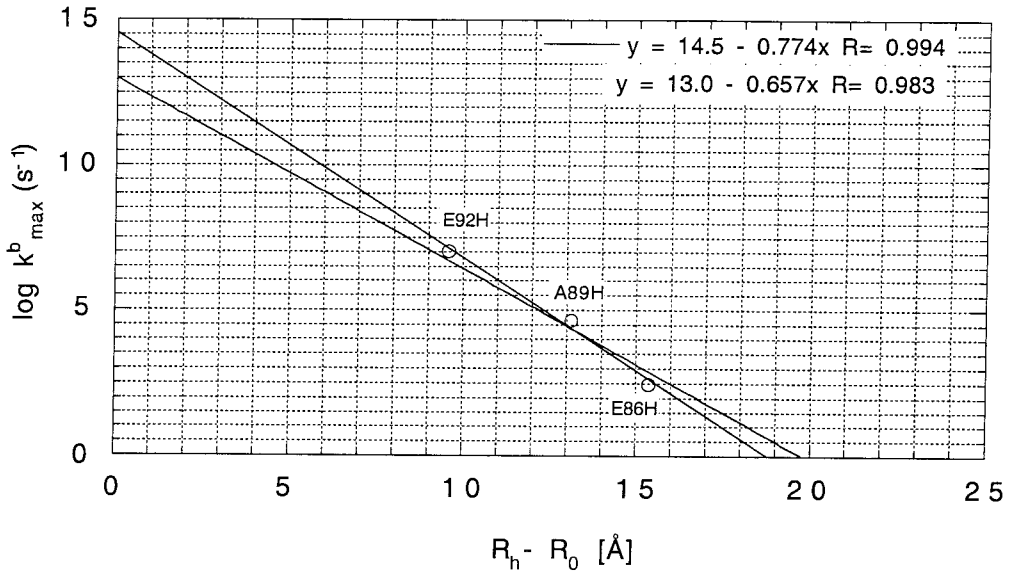
y = 14.5 - 0.774x R= 0.994
y = 13.0 - 0.657x R= 0.983
E92H
A89H
E86H
log k^b_max (s^-1)
R_h - R_0 [Å]
0
5
10
15
20
25

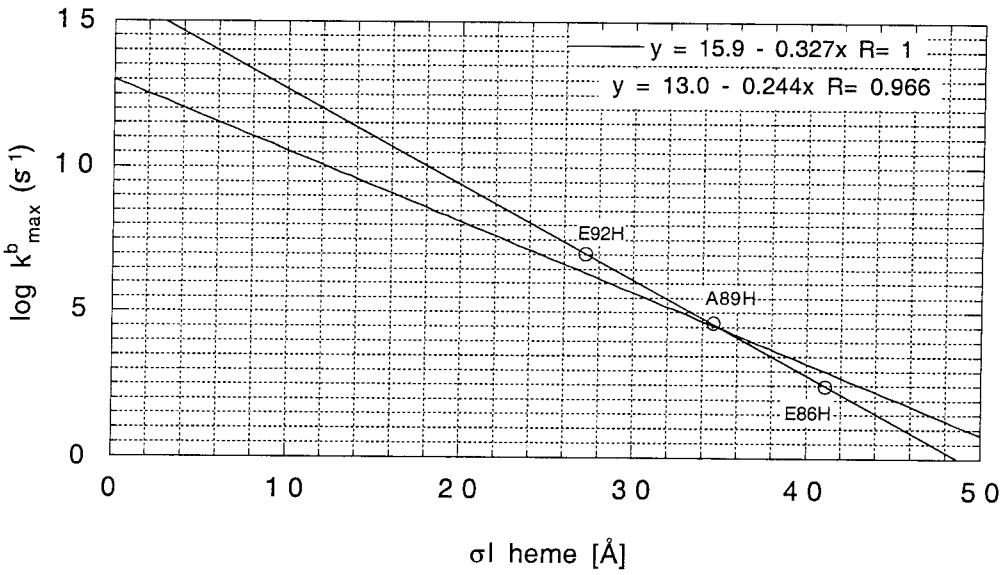
y = 15.9 - 0.327x R= 1
y = 13.0 - 0.244x R= 0.966
E92H
A89H
E86H
log k^b_max (s^-1)
σI heme [Å]
0
5
10
15
20
30
40
50

Figure Chapter 4-20: Distance *versus* tunnelling lengths for all mutants of cytochrome b_{562}.

Upper: the metal-metal distance (R_m) *versus* the tunnelling length (σl). Lower: the metal-heme distance (R_h) *versus* the metal-heme tunnelling distance (σl heme).

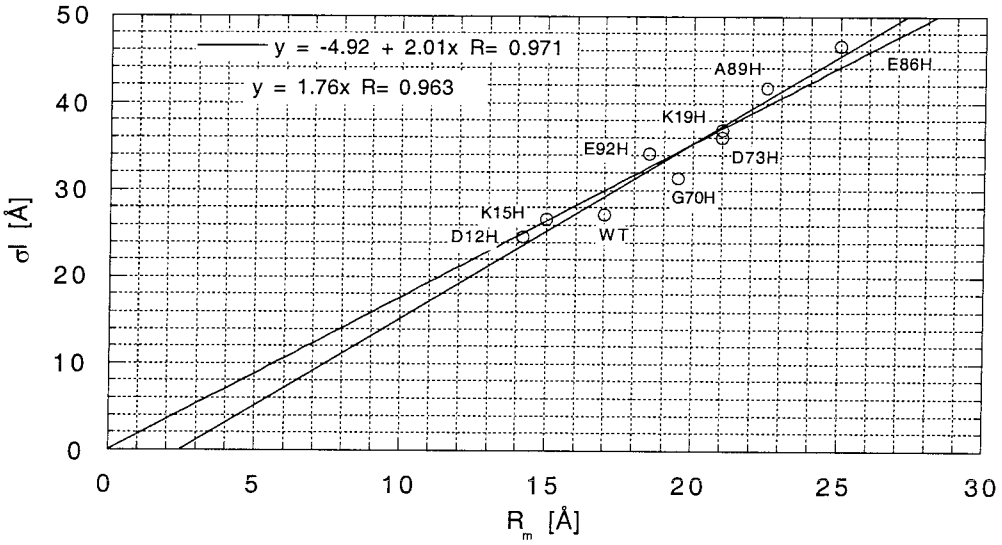
y = -4.92 + 2.01x R= 0.971
y = 1.76x R= 0.963
σI [Å]
R_m [Å]
A89H
E86H
K19H
E92H
D73H
G70H
K15H
D12H
WT
0
5
10
15
20
25
30
40
50

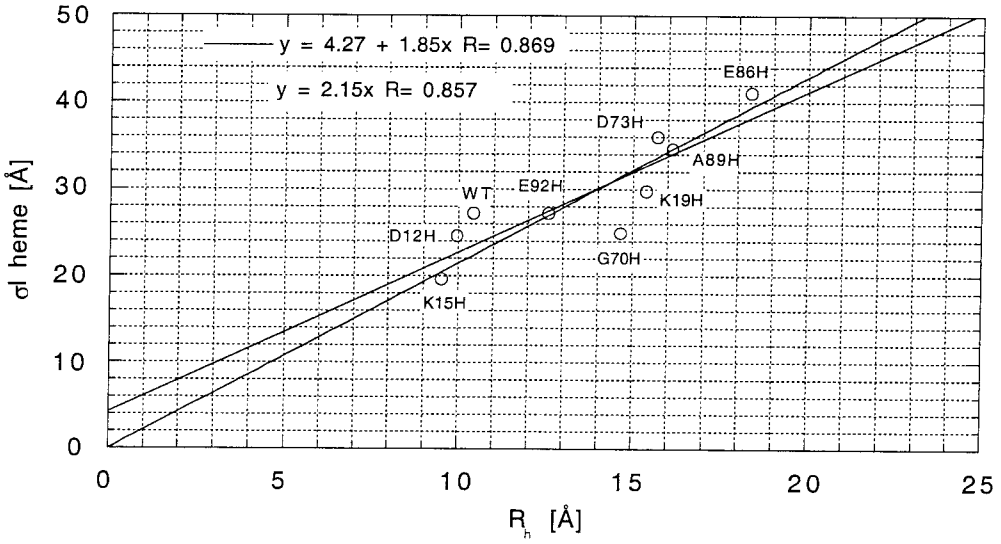
y = 4.27 + 1.85x R= 0.869
y = 2.15x R= 0.857
σI heme [Å]
R_h [Å]
E86H
D73H
A89H
WT
E92H
K19H
D12H
G70H
K15H
0
5
10
15
20
25
30
40
50

Figure Chapter 4-21: The metal-metal distance (R_m) *versus* log k_{max} (upper) and metal-metal sigma tunnelling length (σl) *versus* log k_{max} (lower).

R_m is the distance from the N2 His-X (X = mutation) ruthenium bond to the Fe atom and σl is the His-X Cα-Cβ bond to the Fe ligand bond tunnelling length (as calculated by the Pathways program) plus 4 bond lengths.

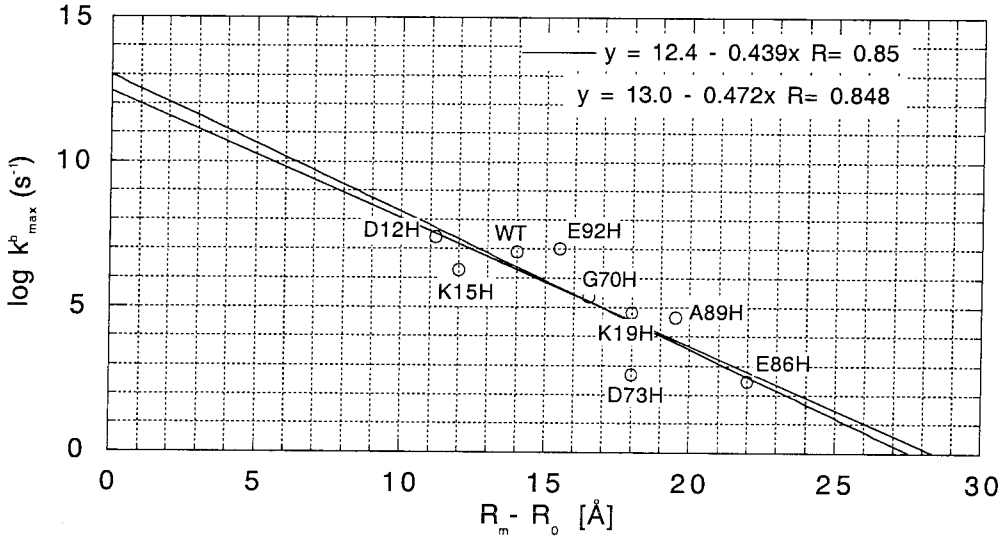
y = 12.4 - 0.439x R= 0.85
y = 13.0 - 0.472x R= 0.848
D12H
WT
E92H
K15H
G70H
A89H
K19H
E86H
D73H
log k^b_max (s^-1)
R_m - R_o [Å]
0
5
10
15
20
25
30

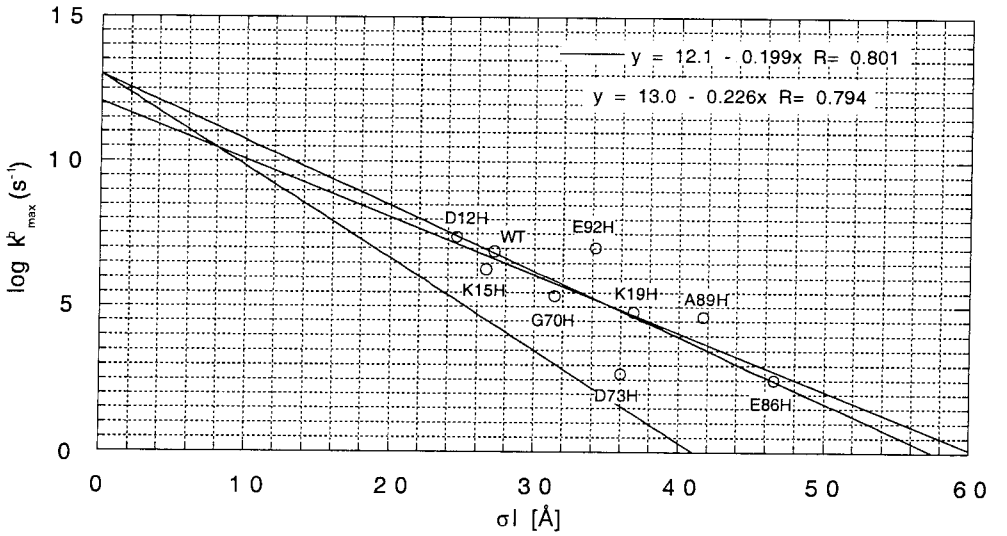
y = 12.1 - 0.199x R= 0.801
y = 13.0 - 0.226x R= 0.794
D12H
WT
E92H
K15H
K19H
A89H
G70H
D73H
E86H
log k^b_max (s^-1)
σl [Å]
0
10
20
30
40
50
60

Figure Chapter 4-22: The metal-heme distance (R_h) *versus* log k_{max} (upper) and the metal-heme tunnelling length (σl heme) *versus* log k_{max} (lower).

R_h is the distance from the N2 His-X (X = mutation) ruthenium bond to the closest porphyrin ring atom and σl heme is the His-X Cα-Cβ bond to the closest porphyrin ring bond tunnelling length (as calculated by the Pathways program) plus 4 bonds.

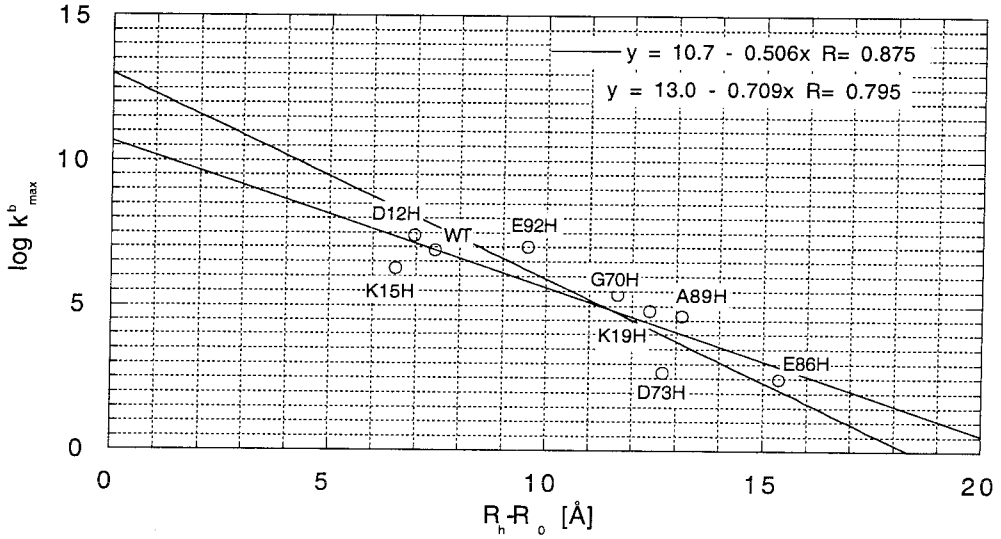
y = 10.7 - 0.506x R= 0.875
y = 13.0 - 0.709x R= 0.795
D12H
WT
E92H
K15H
G70H
A89H
K19H
E86H
D73H
log k^b_max
R_h-R_o [Å]
0
5
10
15
20

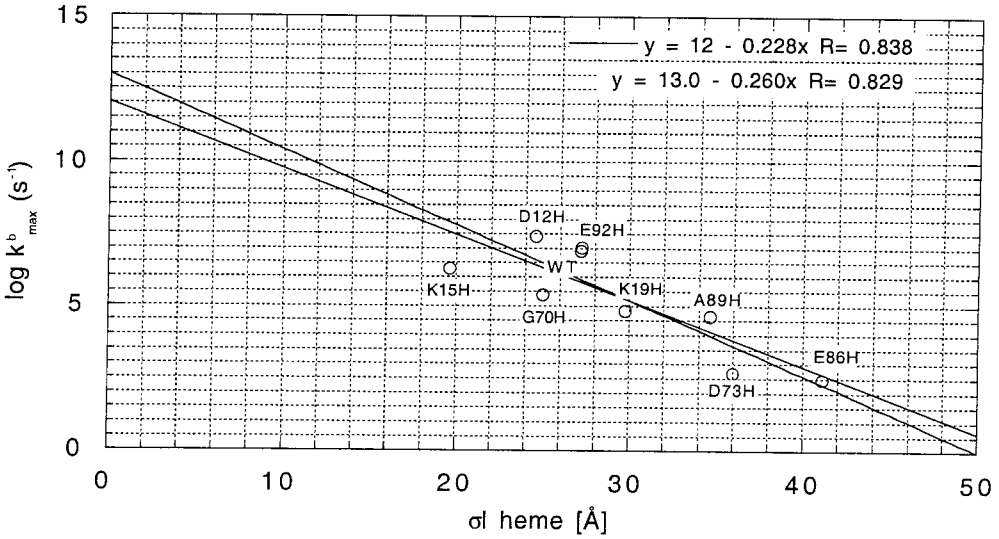
y = 12 - 0.228x R= 0.838
y = 13.0 - 0.260x R= 0.829
D12H
E92H
WT
K15H
K19H
A89H
G70H
E86H
D73H
log k^b_max (s^-1)
σl heme [Å]
0
10
20
30
40
50

Figure Chapter 4-23: A comparison of ET rates and tunnelling data between b_{562} and Azurin.

Plotted are the graphs R_m-R_0 *versus* log k_{max} (upper) and the σl *versus* log k_{max} (lower). Cytochrome b_{562} data points are triangles and azurin circles.

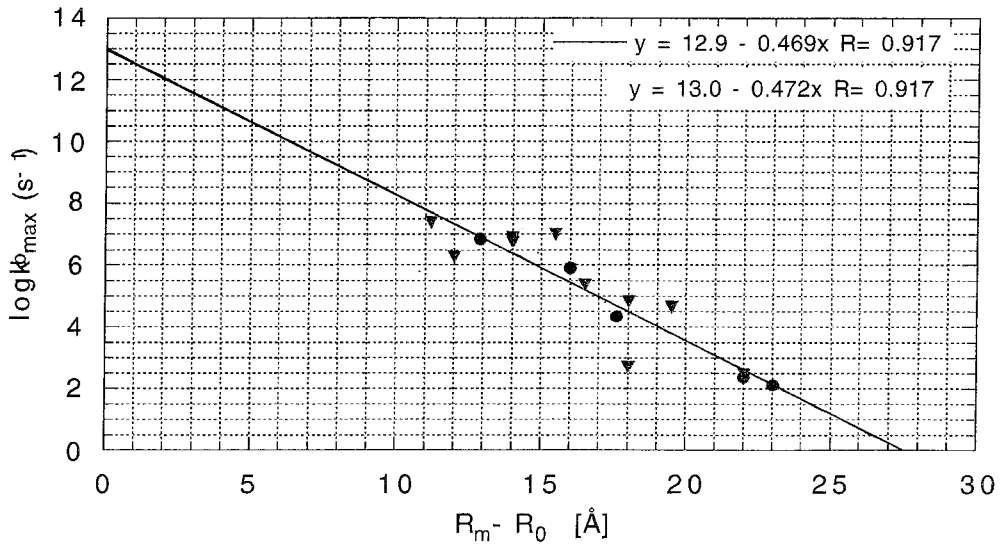
y = 12.9 - 0.469x R= 0.917
y = 13.0 - 0.472x R= 0.917
log k$_{max}$ (s^{-1})
R$_m$- R$_0$ [Å]
0
2
4
6
8
10
12
14
0
5
10
15
20
25
30

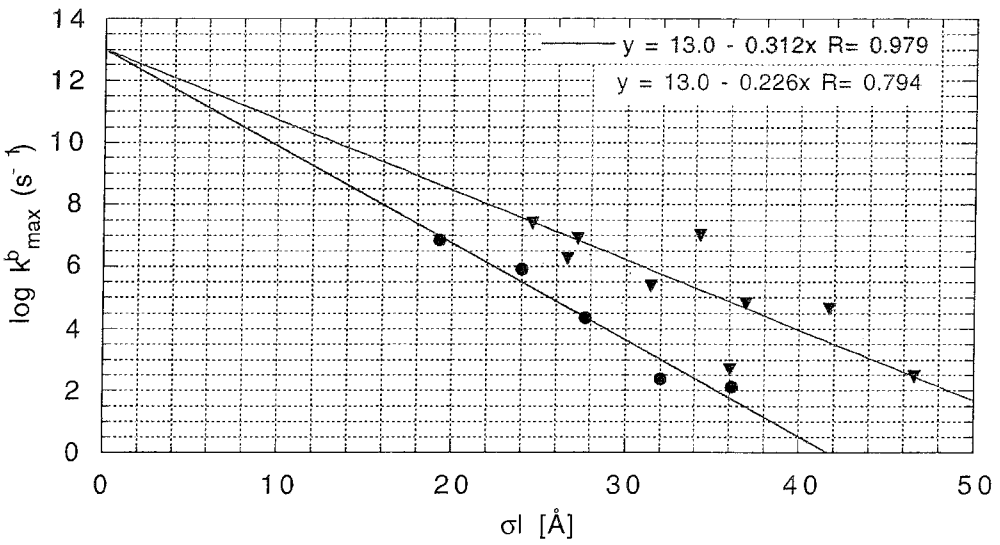
y = 13.0 - 0.312x R= 0.979
y = 13.0 - 0.226x R= 0.794
log k$^b_{max}$ (s^{-1})
σl [Å]
0
2
4
6
8
10
12
14
0
10
20
30
40
50

Figure Chapter 4-24: A comparison of ET rates and tunnelling data between b_{562}, Azurin and cytochrome c.

Plotted are the graphs R_m-R_0 *versus* log k_{max} (upper) and the σl *versus* log k_{max} (lower). Cytochrome b_{562} data points are triangles, azurin circles and cytochrome *c* squares.

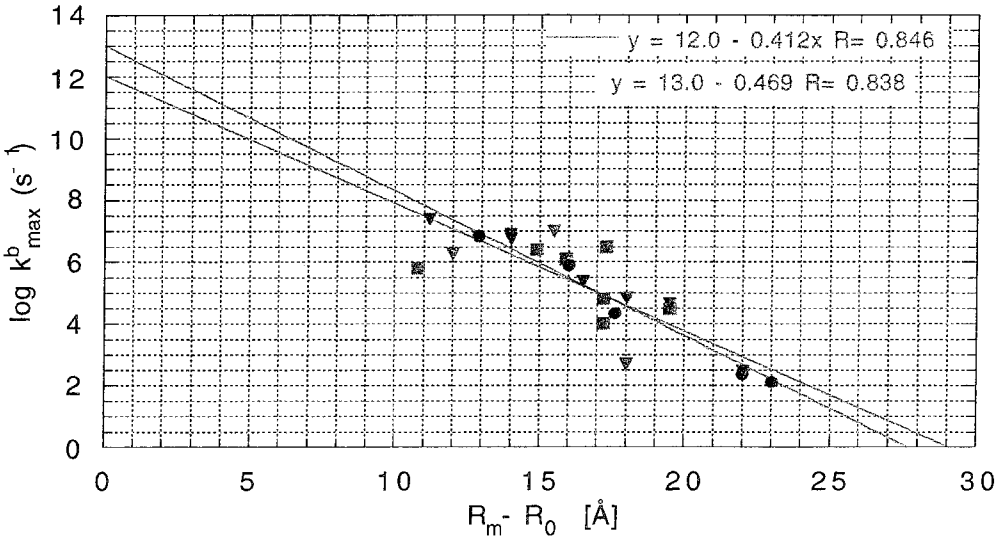
y = 12.0 - 0.412x R= 0.846
y = 13.0 - 0.469 R= 0.838
log k^b_{max} (s^{-1})
R_m- R_0 [Å]
0
2
4
6
8
10
12
14
0
5
10
15
20
25
30

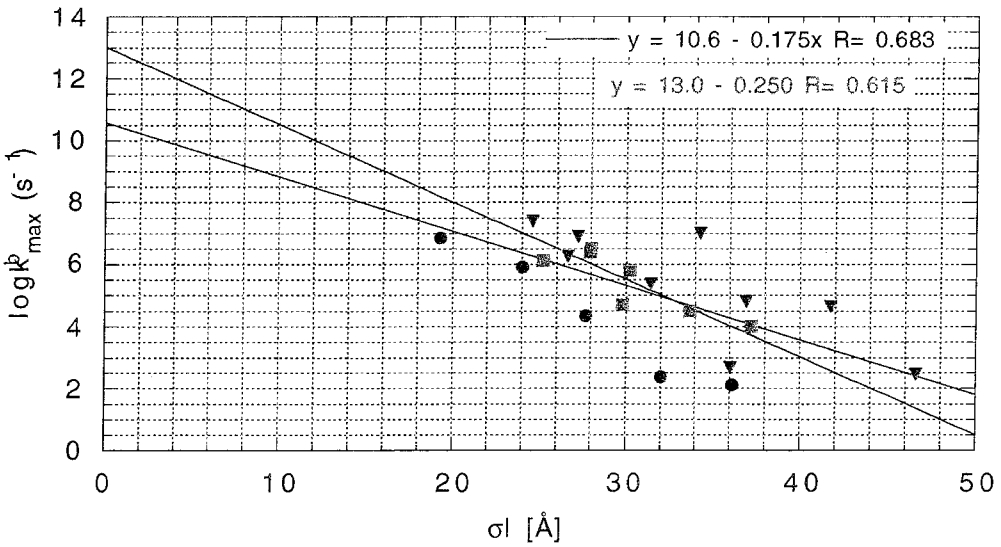
y = 10.6 - 0.175x R= 0.683
y = 13.0 - 0.250 R= 0.615
log k^b_{max} (s^{-1})
σl [Å]
0
2
4
6
8
10
12
14
0
10
20
30
40
50

Figure Chapter 4-25: Edge-edge tunnelling data *versus* log k_{max} for b_{562} and cytochrome *c*.

Cytochrome b_{562} data triangles and cytochrome *c* squares.

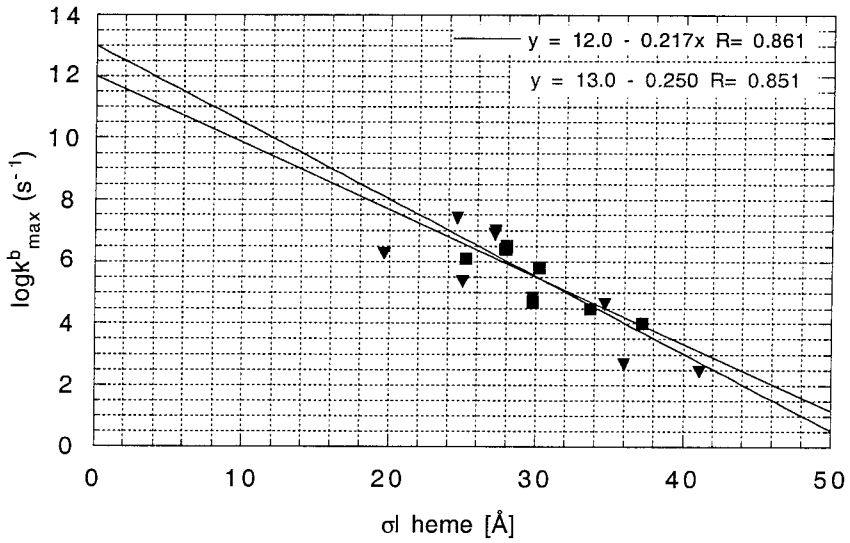
y = 12.0 - 0.217x R= 0.861
y = 13.0 - 0.250 R= 0.851
logk$^{b}_{max}$ (s^{-1})
σl heme [Å]
0
2
4
6
8
10
12
14
0
10
20
30
40
50

Table Chapter 4-1: Distances and tunnelling measurements (Å) for E86H, A89H and E92H labelled mutants.

labelled residue/mutation	Cα-Fe distance	Cα-heme distance	Ru-Fe distance	Ru-heme distance	Ru-Fe tunnelling distance	Ru-heme tunnelling distance
Glu86His	23.7	17.1	25.0	18.4	46.6	41.1
Ala89His	19.8	13.5	22.5	13.5	41.7	34.7
Glu92His	14.7	8.8	18.5	18.5	34.2	27.2

b_{562} coupling constants for helix D mutants calculated using the Pathways Program.

mutant	Cα-Fe ligand coupling	Cα-heme edge coupling
86	3.2×10^{-7}	4.1×10^{-6}
89	$1.9 \times \times 10^{-6}$	2.49×10^{-5}
92	2.9×10^{-5}	3.7×10^{-4}

Table Chapter 4-2: Oligonucleotides used in PCR reactions for the synthesis of the E86H, A89H and E92H b_{562} mutants.

All mutants were constructed from the H63E gene and this mutation is implied when referring to mutant proteins.

mutation	oligo name	oligo sequence
E86H	E86H top	3' -CCA TTT CAT TTT *GTA* CGC GTC CGA CGA
	E86H bot	5' -GGT AAA GTA AAA *CAT* GCG CAG GCT GCT
A89H	A89H top	3' -TTT CTT CGC GTC *GTA* CGA CGT CTC GT
	A89H bot	5' -AAA GAA GCG CAG *CAT* GCT GCA GAG CA
E92H	E92H top	3' -GTC CGA CGA CGT *GTA* GTT GAC TTT TGC
	E92H bot	5' -CAG GCT GCT GCA *CAT* CAA CTG AAA ACG

Table Chapter 4-3: Observed rates of electron transfer (k^b_{ET}) for the E86H, A89H and E92H mutants.

The rates for the E86H mutant were obtained using the irreversible quencher $Co(NH_3)_5Cl^{+2}$.

Mutant	Rate	430 nm PI	414 nm PI	430 nm FQ	414 nm FQ
E86H	$(2.5\pm0.5)\times10^{2}$	-	-	-	-
A89H	$(3.8\pm0.1)\times10^{4}$	$(3.8\pm0.1)\times10^{4}$	$(3.9\pm0.1)\times10^{4}$	3.9×10^{4}	3.6×10^{4}
E92H	$(8.8\pm0.4)\times10^{6}$	$(8.6\pm0.4)\times10^{6}$	$(8.9\pm0.4)\times10^{6}$	-	-

Mutant	430 mono PI	414 mono PI	670 nm PI	670 nm mono PI
E86H	-	-	$(1.4\pm0.1)\times10^{7}$	9.5×10^{7}
A89H	1.4×10^{4}	-	$(1.7\pm0.0)\times10^{7}$	7.1×10^{7}
E92H	$(6.7\pm0.1)\times10^{3}$	$(6.7\pm0.1)\times10^{3}$	$(1.5\pm0.0)\times10^{7}$	8.5×10^{7}

*average of 430 and 414 nm PI and FQ experiments (where available) except E86H where rate were from expts. using the quencher $Co(NH_3)_5Cl^{+2}$.

nd - not detected

Chapter 5

Design of a Mutant of Cytochrome b_{562} Incorporating a Covalently Bound Heme Group

Introduction

Many factors contribute to the magnitude of redox potentials of heme metalloproteins including the charge state and π-acceptor/donor properties of the ligands, spin state of the metal and steric restrictions of the heme binding pocket. Modifications and covalent attachment of the heme group also influence the potential. In this chapter we investigate the effects of covalent ligation of the heme group of cytochrome b_{562}. In the wild-type protein the heme is ligated by a histidine and methionine ligands at positions 102 and 7 respectively. Cytochrome b_{562} (b_{562}), a 106 residue α-helical protein, has been described in detail in chapter 1 of this thesis and investigations of electron transfer reported in chapters 2-4.

It is recognized that axial ligands of cytochromes are the main factor in determining the redox potential of these proteins. Illustrations of these effect are numerous. Cytochrome c557 and c558[1] both have one histidine and one axial ligand to the iron of their heme groups. Their hemes are both ligated by one thioether linkage and the other vinyl group has a substituent group[2]. Redox potential for c557 and c558 are 264 mV and 244 mV respectively which are very similar to the potentials of cytochromes c in which the protoporphyrin IX is bound by two thioether linkages to the vinyl groups. Semisynthesis studies[3, 4] on horse-heart cytochrome c where a cysteine ligand replaces the natural methionine ligand decreases the reduction potential to -390 mV from 262 mV. The ligands of b_{562} have been probed using site directed mutagenesis by Barker et al. to investigate the effects of mutant ligands. Both the bis-methionine mutant[5] and the bis-methionine mutant (H102M) with a covalently attached heme have been characterized. The covalent attachment of the heme is via a thioether linkage and a mutant R98C site. The ferric form of the bis-methionine mutant is high-spin with only one methionine ligand whilst the reduced protein

has bis-methionine ligation. The ferrous form of the covalent heme protein is also bi-methionine ligated, but the ferric protein appears to show spin-disorder with a low-spin bis-methionine ligated state and a high-spin state similar to the single mutant protein. The same group also characterized the single R98C mutant and showed that the heme in this protein was covalently attached but that the protein was present as two species which differed in mass by 32 Da[6]. The potential of the bis-methionine mutant was found to be increased from a WT value of 180 mV to 440 mV at pH 4.8.

As well as probing the electron transfer properties of the b_{562} with a covalent heme, this protein will reveal the effects, if any, of the heme orientational disorder. It has been shown that the heme group in b_{562} has two orientations differing by 180° about the α,γ-meso axis with a 2:1 ratio of conformers. Covalent ligation of the heme may remove this disorder and reveal any effects of the equilibrium on the ET rate.

Materials and Methods

A Design of Mutant

Design of the site for covalent attachment of the heme to the protein was carried out using RasMac v2.5 with the criteria that the ligation site, introduced by replacement of a residue by a cysteine whose thiol can then react by electrophillic addition to one of the heme vinyl groups, be close to and have its Cα-Cβ bond as collinear as possible with one of the vinyl moieties of the protoporphyrin IX Fe(III). Attachment of the heme is by electrophillic attack of the heme vinyl to form a thioether linkage. This method has been proposed to be spontaneous or mediated by an as yet unknown lyase. The site chosen was the same as that

reported previously, the R98C mutants, which is in close proximity to the heme 2-vinyl group.

Figure Chapter 5-1 shows the locations of the proposed R98C mutation in the heme pocket. The oligos used to introduce the mutation are shown below:

R98C top	3' -C TTT TGC TGG *ACG* TTG CGG ATA GTG G
R98C bot	5' -G AAA ACG ACC *TGC* AAC GCC TAT CAC C

Mutagensis was performed as previously described with the same primer and terminator oligos.

B Protein Expression/Purification

Expression of mutants with the covalently attached heme was carried out under semi aerobic conditions by growing 3 l cell cultures in 4 l flasks. In addition, purification of these mutants was modified by the addition of 2 mM sodium ascorbate to the extrusion buffer and 2 mM DTT in buffers used to process the samples further, including chromatography (FPLC) buffers. The samples were also stored in solutions containing DTT.
All other steps including labelling of protein with ruthenium(II)bis(2,2'-bipyridine)imidazole and laser analysis were as described for the non-covalent heme proteins in chapter 1.

Results

A DNA/Mutagenesis Reactions and Protein Expression and Purification

The identity of the mutant gene was confirmed by DNA sequencing. Protein yields of holoprotein were typically 4 mg/ml with a large quantity of apoprotein also produced. No attempts were made to reconstitute this apoprotein. It was found if the protein was left for greater than 24 h under aerobic conditions, then a green protein solution developed.

B Characterization of Expressed Protein

An SDS-PAGE protein gel of the R98C mutant is shown in Figure Chapter 5-2 and an unstained gel in Figure Chapter 5-3 (upper). A brown band at the correct molecular weight, and same location as seen in the comassie blue stained gels, is seen. This brown band was not seen with the WT protein or any of the mutant proteins in which the heme is removed by the SDS and electrophoresis procedure. The R98C mutants are also seen to have a slightly higher molecular weight also indicating that the heme is covalently attached. Mass spectral analysis of the protein revealed a protein of the correct molecular weight as shown in Figure Chapter 5-3 (lower). A sample with internal molecular mass standards gave a mass of 12,344 Da. The peak at 11,714 is attributed to apo protein. Interestingly, the species seen by Barker with an additional mass of 32 Da was not observed. The UV/vis spectra of the R98C mutant had identical properties to that reported by Barker with a shift of the Soret to 416 nm as shown in Figure Chapter 5-5 - Figure Chapter 5-6. The spectra of unlabelled and ruthenium labelled R98C are very similar to WT b_{562} except for the shift of the Soret to 416 nm. The reduced protein does not exhibit a large increase in intensity and

the Soret moves to 423 nm. A brief investigation into the stability of the protein relative to WT by guanidinium hydrochloride (GuHCl) denaturation monitored by circular dichroism showed the R98C mutant to be more stable than the WT protein (Figure Chapter 5-4 upper). The graphs marked as Fe^{2+} were for Fe^{3+} samples to which a small volume of sodium dithionite solution was added. Samples which were reduced before denaturation had midpoint unfolding points of 7.0 M GuHCl which is the same value as for WT b_{562}. The CD spectra of the ferric and ferrous R98C exhibited the same degree of helical content as WT protein (Figure Chapter 5-4 lower).

C Rate Measurements

Transient absorption photo-induced spectra for R98C are shown in Figure Chapter 5-7 and Figure Chapter 5-8. Observation at 414 nm and 428 nm gave the rate (k^b_{ET}) of 4.6 x 10^6 s^{-1} which is within the experimental error of the rate found for WT of 6.7 x 10^6 s^{-1}.

Discussion

It has been found that the rate of electron transfer in a mutant of b_{562} with a covalently attached heme is the same as that found in the WT protein. Although no electrochemical data is presented for this mutant, the close similarity in rates indicates that any change in potential would be small. This result is not unexpected since it is known that the effects of axial ligands determine the redox potential to the large part. This example illustrates this point succinctly since, although now a c-type cytochrome, the potential would still appear to be 100 mV lower than that of cytochrome *c*.

The result that covalent ligation of the heme gives a protein with a similar electron transfer rate to WT protein also suggests that the heme reorientation does not affect the rate of ET.

The reduction potential of b_{562} is pH dependent and can be explained by the presence of three groups with differing pK_a values in the ferric and ferrous states[7]. Two of these groups are proposed to be the His102 ligand and a heme propionate group. The other had been proposed to be either the carboxylate side chain of Glu4 or Glu8. The His102 has a reduced pK_a of 9.0 and stabilization of the histidinate102 has been proposed to be via the side chain of Arg98[7] or the side chain of the carboxyl terminal residue Arg106[8]. Since Arg98 is no longer available in the covalent mutant and the rate has not changed, it provides evidence that Arg106 stabilizes the histidinate102 negative charge.

Bibliography

1. Pettigrew, G.W. *Nature* **241**, 531-533 (1973).

2. Pettigrew, G.W. *FEB Lett.* **22**, 64-66 (1970).

3. Raphael, A.L. & Gray, H.B. *J. Am. Chem. Soc.* **113**, 1038-1040 (1991).

4. Raphael, A.L. & Gray, H.B. *Proteins: Struct., Funct., Genet.* **6**, 338-340 (1989).

5. Barker, P.D. & Freund, S.M.V. *Biochemistry* **35**, 13627-13635 (1996).

6. Barker, P.D., Nerou, E.D., Freund, S.M.V. & Fearnley, I.M. (1995).

7. Moore, G., Williams, R., Perterson, J., Thompson, A. & Mathews, R. *Biochem. Biophys. Acta* **829**, 83-96 (1985).

8. Hamada, K., Bethge, P.H. & Mathews, F.S. *J. Mol. Biol.* **247**, 947-962 (1995).

Figure Chapter 5-1: The R98C mutant of b_{562}.

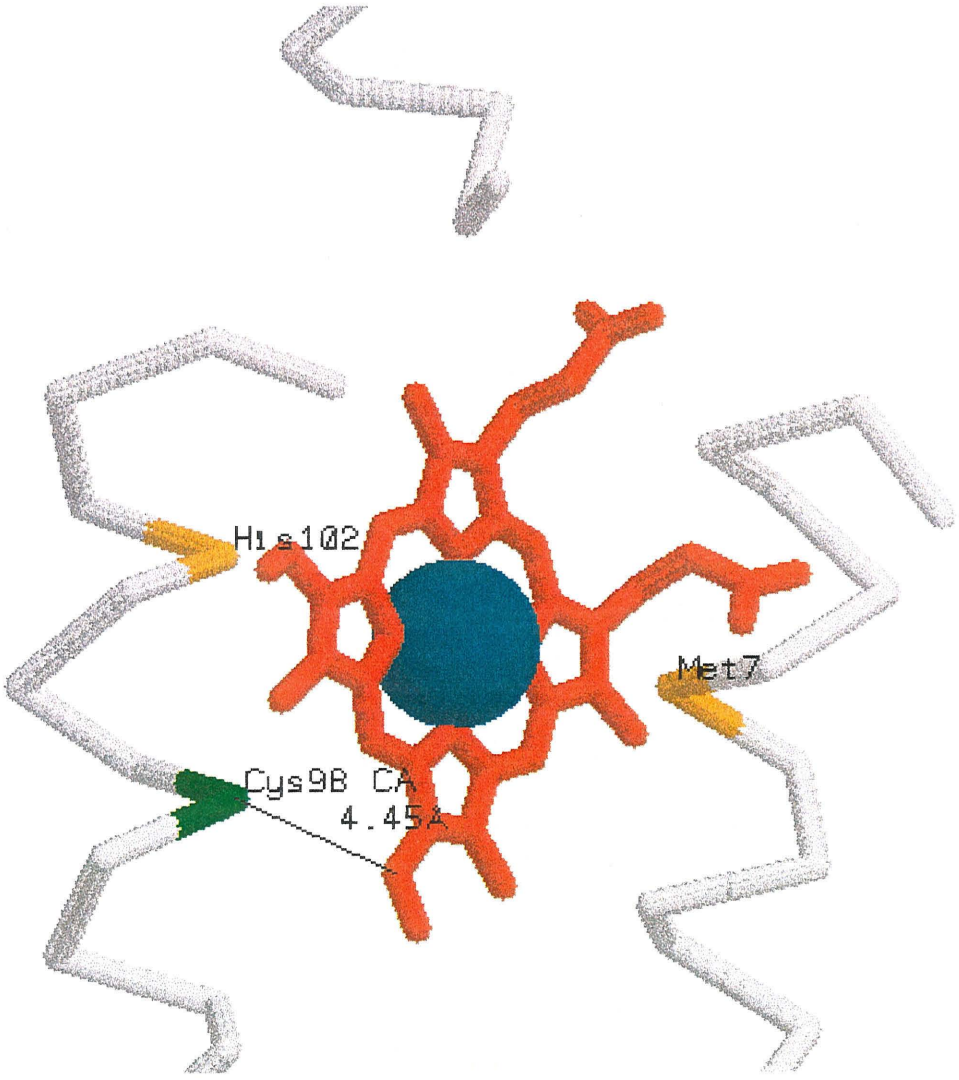
His102
Met7
Cys9B CA
4.45A

Figure Chapter 5-2: SDS/Page protein gel of labelled and unlabelled R98C and WT b_{562}.

A

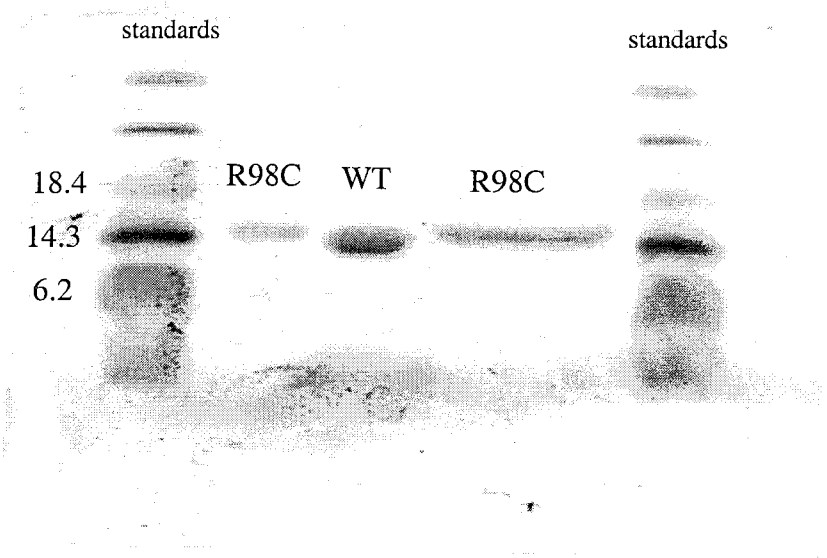
standards
standards
18.4
14.3
6.2
R98C
WT
R98C

B

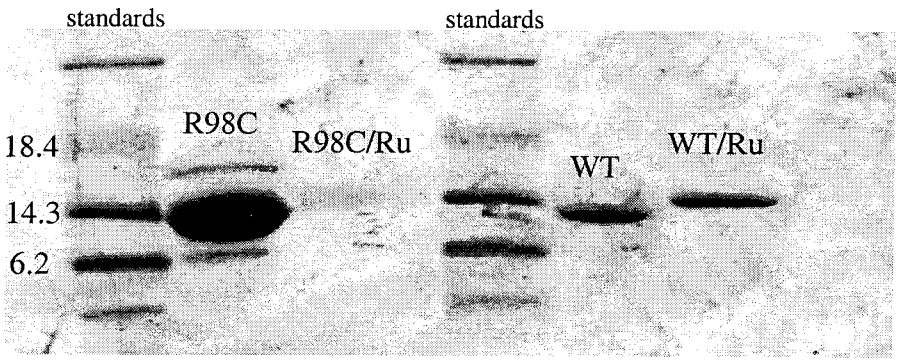
standards
standards
18.4
14.3
6.2
R98C
R98C/Ru
WT
WT/Ru

Figure Chapter 5-3: Unstained SDS/PAGE protein gel of R98C and WT b_{562} and mass spec. Data for R98C.

Approximately 40 μg of the R98C mutant and WT b_{562} were loaded onto the gel. The arrow indicates a band of brown stain due to heme. The same sample was submitted for mass spectral analysis (lower). Peak at approx. 14 kDa is an instrumental 'glitch'.

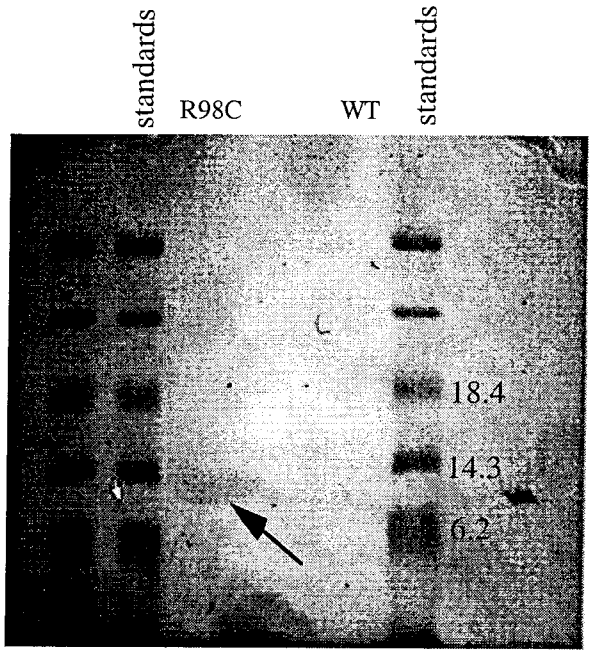
standards
R98C
WT
standards
18.4
14.3
6.2

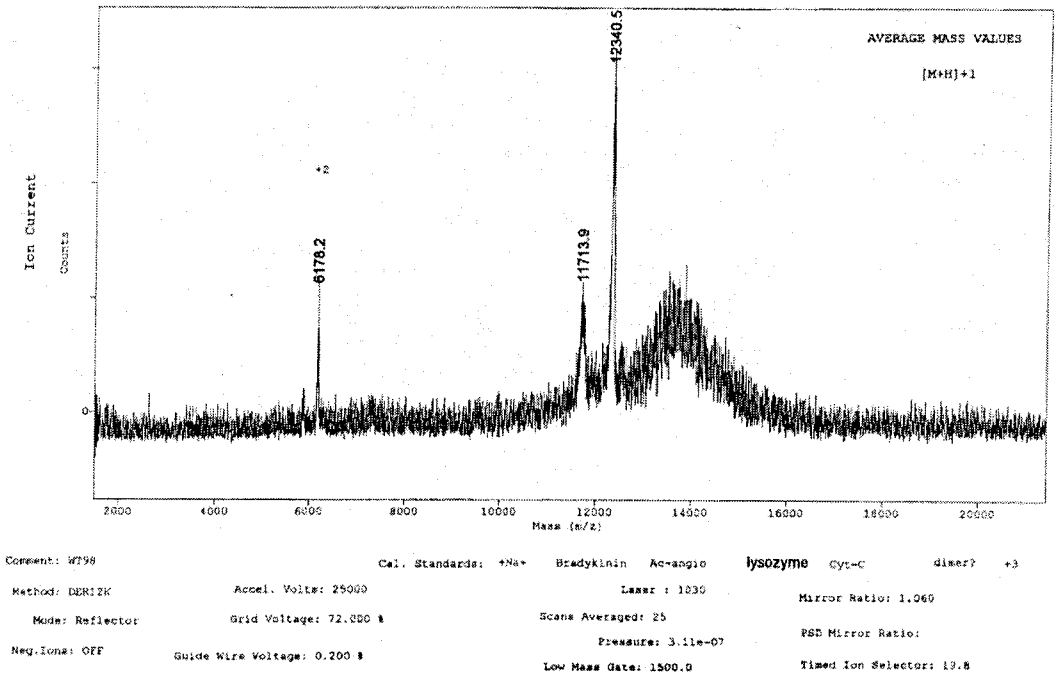
AVERAGE MASS VALUES
[M+H]+1
42340.5
+2
6178.2
11713.9
Ion Current
Counts
0
2000
4000
6000
8000
10000
12000
14000
16000
18000
20000
Mass (m/z)
Cal. Standards: +Na+ Bradykinin Ac-angio lysozyme Cyt-C dimer? +3
Laser : 1830
Mirror Ratio: 1.069
Scans Averaged: 25
Pressure: 3.11e-07
PSD Mirror Ratio:
Low Mass Gate: 1500.0
Timed Ion Selector: 19.8

Figure Chapter 5-4: Comparison of CD and GuHCl unfolding data for R98C and WT b_{562}.

Upper: unfolding of 10 μM samples of the R98C mutant and Wt b_{562}. Reduction of Fe^{3+} was by addition of a small volume of fresh sodium dithionate soln. Lower: CD spectra of ferric WT b_{562} (12 μM) and 10 μM ferric and ferrous R98C. The R98C concentrations have been normalized to that of the WT sample.

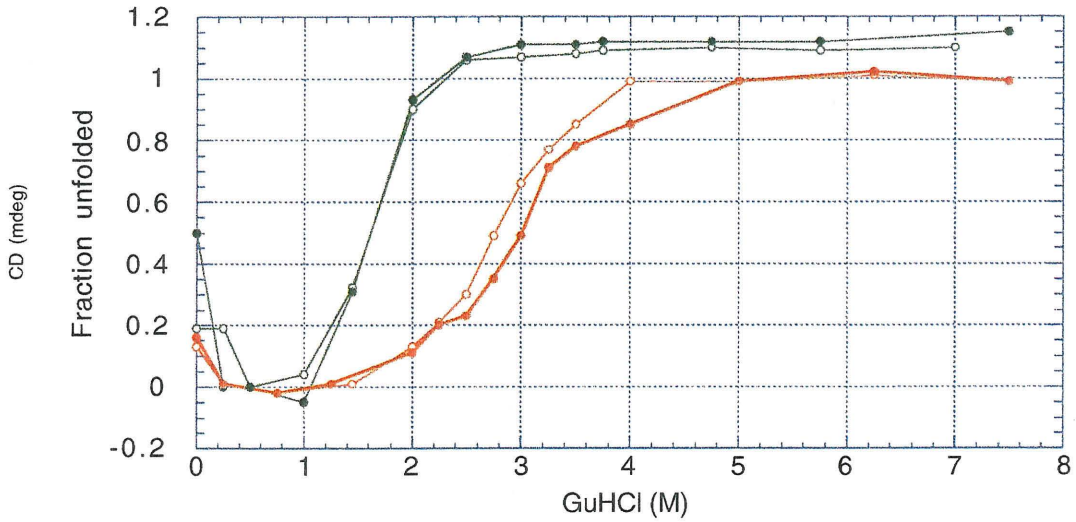
CD (mdeg)
Fraction unfolded
1.2
1
0.8
0.6
0.4
0.2
0
-0.2
0
1
2
3
4
5
6
7
8
GuHCl (M)

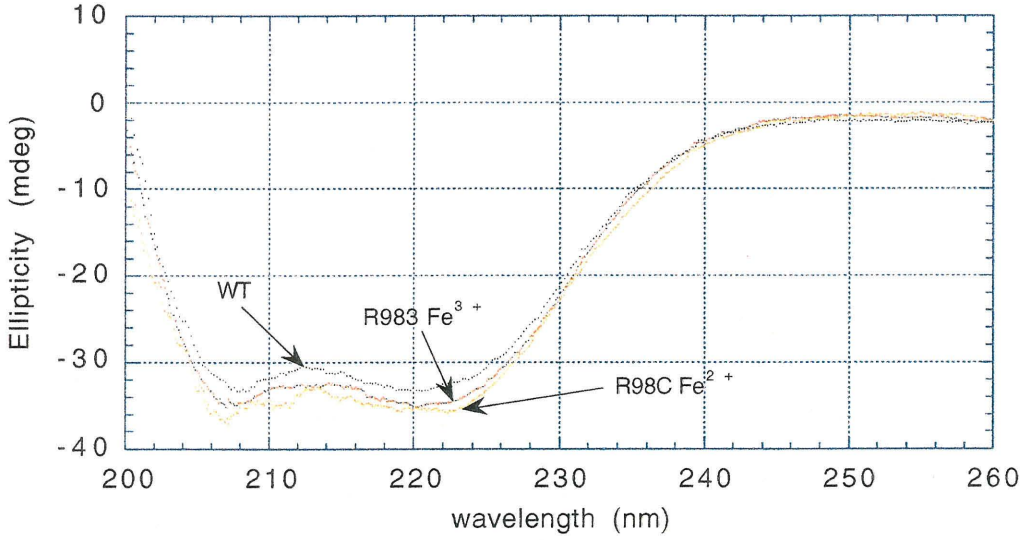
Ellipticity (mdeg)
10
0
-10
-20
-30
-40
200
210
220
230
240
250
260
wavelength (nm)
WT
R983 Fe3+
R98C Fe2+

Figure Chapter 5-5: UV/vis spectra of ferrous and ferric R98C.

UV/vis spectra of ferrous (thin) and ferric (thick). The large peak at 315 nm is sodium dithionite.

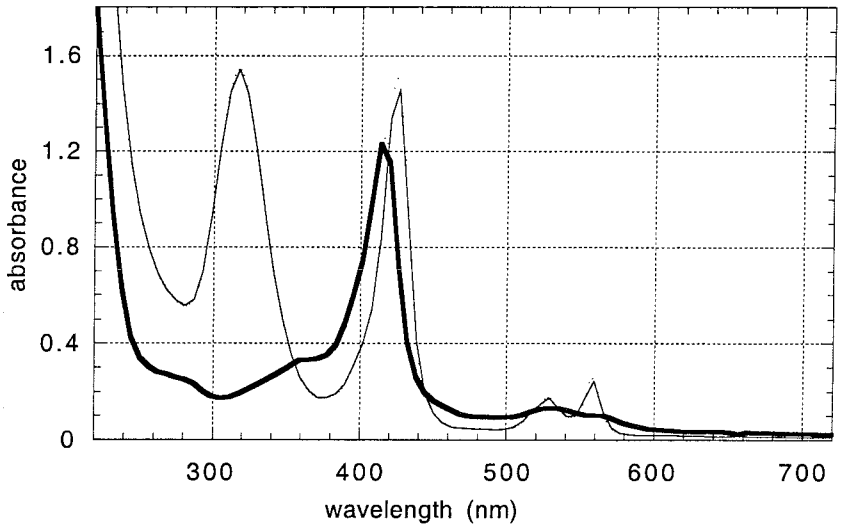
absorbance
1.6
1.2
0.8
0.4
0
300
400
500
600
700
wavelength (nm)

Figure Chapter 5-6: UV/vis spectra of unlabelled and labelled R98C and WT b_{562}. Unlabelled (upper) R98C covalent mutant (thin) and WT b_{562} (thick). Lower spectra of ruthenium labelled R98C (thin) and WT b_{562} (thick).

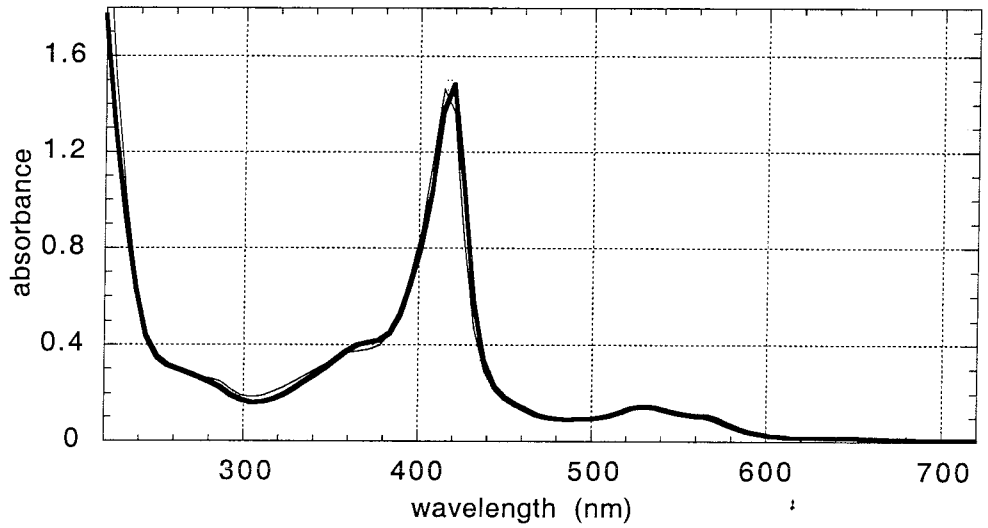
absorbance
1.6
1.2
0.8
0.4
0
300
400
500
600
700
wavelength (nm)

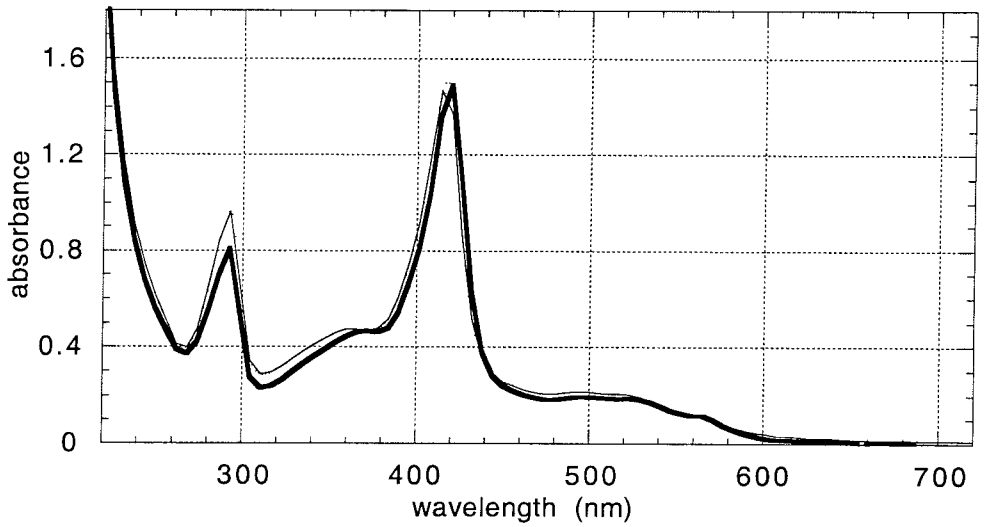
absorbance
1.6
1.2
0.8
0.4
0
300
400
500
600
700
wavelength (nm)

Figure Chapter 5-7: R98C photo induced transient absorbencies.

R98C (13 μM) photoinduced transient absorbance monitored at (A) 428 nm and (B) 412 nm, showing the reduction of Fe^{3+} and the fit to the trace. The residual (signal minus fit) is shown above the traces.

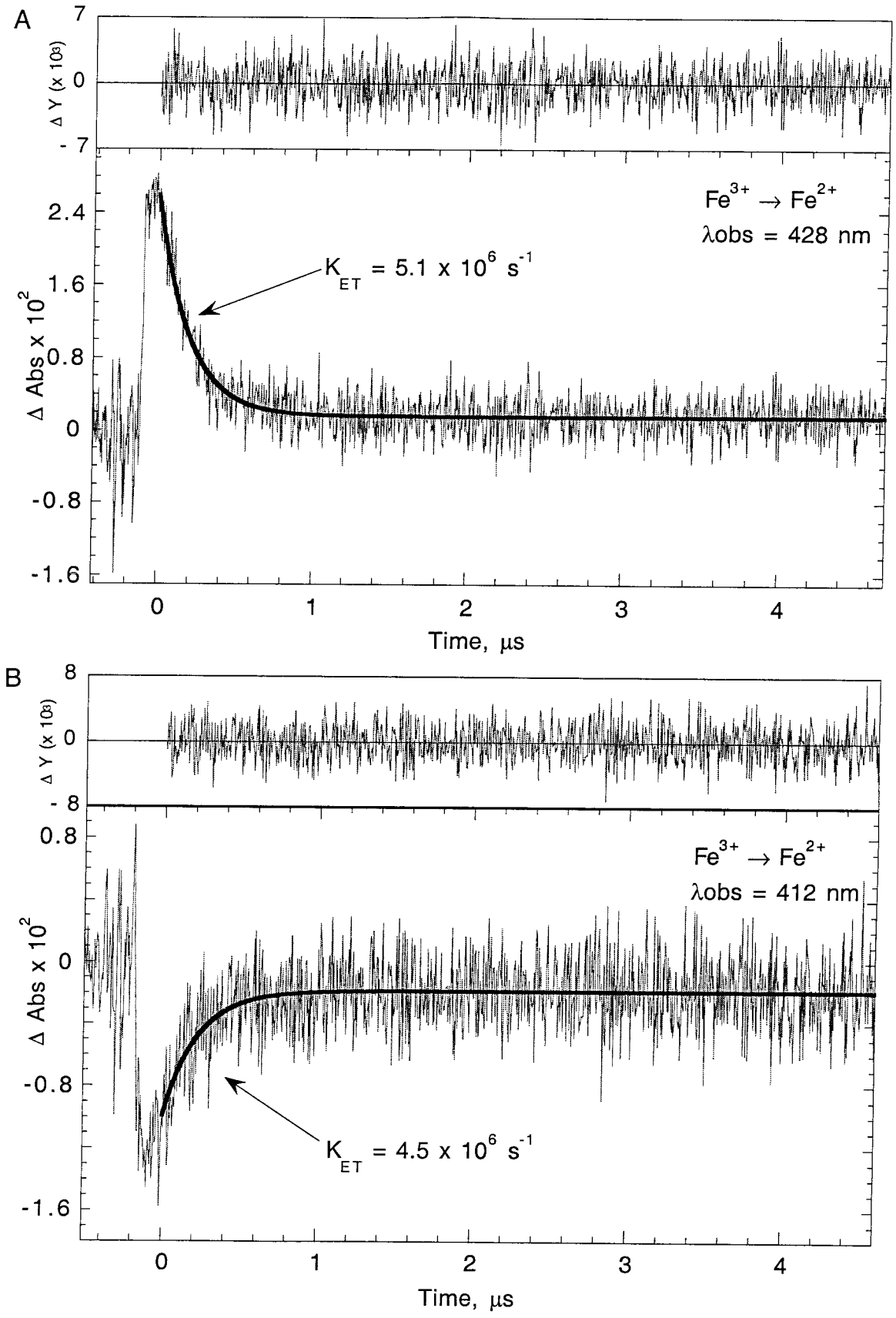
A
7
0
- 7
Δ Y (x 10⁸)
2.4
1.6
0.8
0
-0.8
-1.6
Δ Abs x 10²
Fe³⁺ → Fe²⁺
λobs = 428 nm
K_ET = 5.1 x 10⁶ s⁻¹
0
1
2
3
4
Time, μs
B
8
0
- 8
Δ Y (x 10⁸)
0.8
0
-0.8
-1.6
Δ Abs x 10²
Fe³⁺ → Fe²⁺
λobs = 412 nm
K_ET = 4.5 x 10⁶ s⁻¹
0
1
2
3
4
Time, μs

Figure Chapter 5-8: R98C transient emissions at 670 nm and absorption at 315 nm.

R98C (13μM) emissions monitored at (A) 670 nm and (B) flash-quenched transient absorbance monitored at 315 nm showing the oxidation of Ru^{2+}. The fit to the traces is shown and the residual (signal minus fit) is shown above the traces.

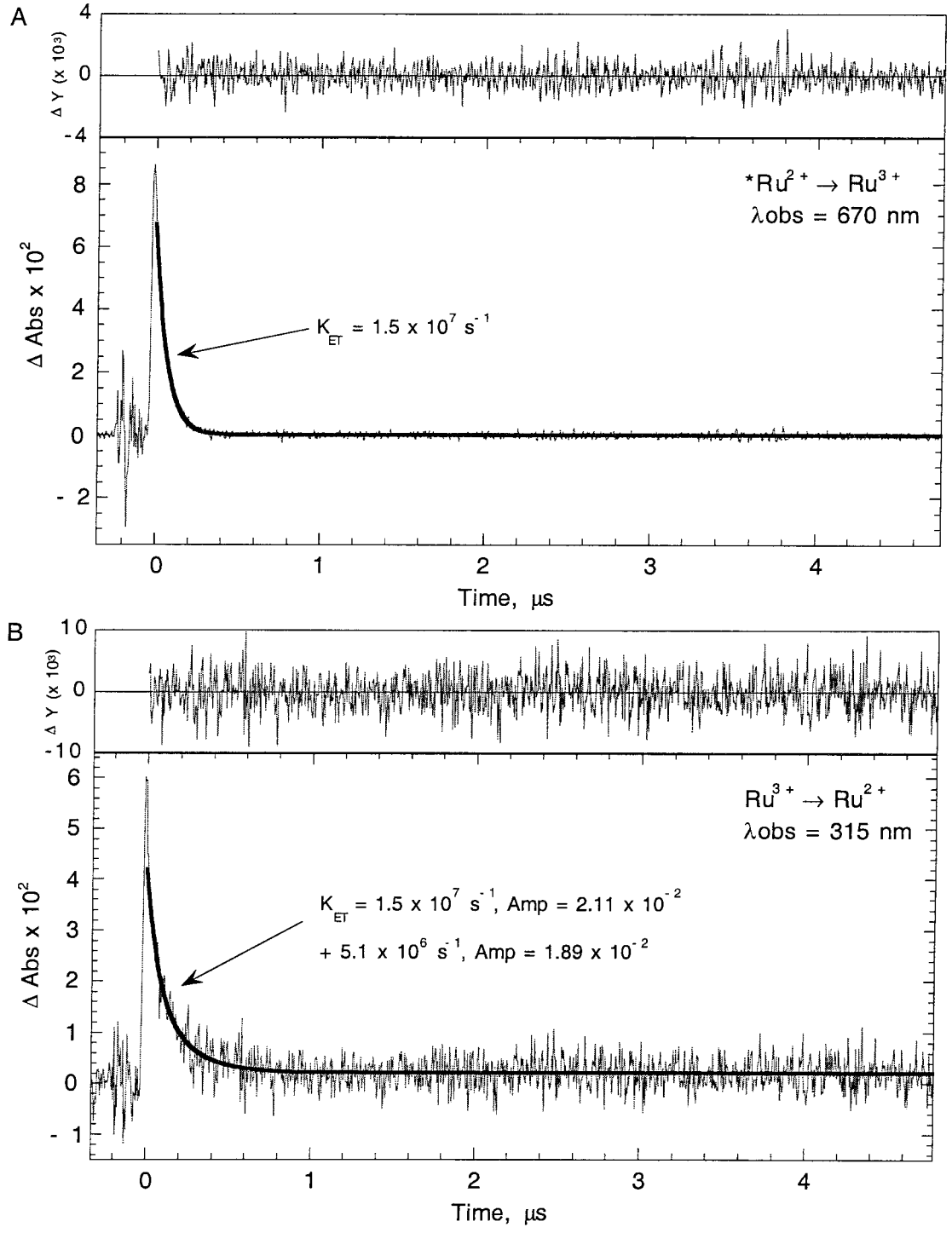
A
Δ Y (x 10³)
4
0
-4
Δ Abs x 10²
8
6
4
2
0
- 2
*Ru²⁺ → Ru³⁺
λobs = 670 nm
K_ET = 1.5 x 10⁷ s⁻¹
0
1
2
3
4
Time, μs
B
Δ Y (x 10³)
10
0
-10
Δ Abs x 10²
6
5
4
3
2
1
0
- 1
Ru³⁺ → Ru²⁺
λobs = 315 nm
K_ET = 1.5 x 10⁷ s⁻¹, Amp = 2.11 x 10⁻²
+ 5.1 x 10⁶ s⁻¹, Amp = 1.89 x 10⁻²
0
1
2
3
4
Time, μs